UNIVERSITÀ DEGLI STUDI DI TRIESTE

XXVIII CICLO DELLA SCUOLA DI DOTTORATO DI RICERCA
IN INGEGNERIA E ARCHITETTURA
INDIRIZZO INGEGNERIA DELL'INFORMAZIONE

Time of arrival estimation of LTE signals for positioning: bounds and algorithms

Settore scientifico-disciplinare: ING-INF/03

Dottorando:
Marco Driusso
Marco Driusso

Coordinatore:
Prof. Roberto Vescovo
Università degli Studi di Trieste
Roberto Vescovo

Supervisore di tesi:
Prof. Fulvio Babich
Università degli Studi di Trieste

Co-supervisore di tesi:
Dr. Chris Marshall
u-blox UK LTD

Anno Accademico 2014-2015

"I've seen things you people wouldn't believe.
Attack ships on fire off the shoulder of Orion.
I watched C-beams glitter in the dark near the Tannhauser gate.
All those moments will be lost in time, like tears in rain.
Time to die."

Rutger Hauer as Roy Batty
Blade Runner, Ridley Scott, 1982.

Abstract

This thesis presents a research work on the estimation of the time of arrival (TOA) of modern cellular signals for positioning purposes. The Third Generation Partnership Project (3GPP) Long Term Evolution (LTE) signals are analyzed, and the underlying orthogonal frequency division multiplexing (OFDM) based physical layer used in the cellular downlink is exploited. The original contribution presented in the thesis is twofold.

Firstly, a framework has been developed for assessing the TOA estimation performance achievable with OFDM signals. The signals are realistically modeled, and different power distributions of the available OFDM sub-carriers have been carefully defined. This allowed new exploration of the TOA estimation performance both in the asymptotic and in the threshold root mean square error (RMSE) regions. Moreover, a novel performance metric based on the shape of the Ziv-Zakai bound curve has been defined, and used to precisely evaluate the boundaries between the threshold and asymptotic RMSE regions. The analysis revealed a trade-off between the threshold RMSE, which is related in practice to sensitivity, and the asymptotic RMSE, which determines the ultimate accuracy. This shows that not only the Gabor bandwidth but also the threshold signal-to-noise ratio (SNR) should be considered when designing reference signals.

Secondly, a TOA estimation algorithm has been developed and applied to real LTE OFDM signals collected in multipath indoor and outdoor propagation environments. The new algorithm, referred to as ESPRIT and Kalman filter for time of Arrival Tracking (EKAT), combines a super-resolution algorithm, which performs the multipath separation, with a Kalman filter, which tracks the estimated direct path TOA. In addition, techniques have been extended for combining the received LTE pilot tones in the time, frequency, spatial and also cell ID domains. This exploits the intrinsic diversity offered by the LTE cell specific reference signal (CRS), and showed an improvement in the robustness and in the quality of the TOA estimates. The pseudoranges evaluated with the proposed EKAT algorithm have been used to feed a positioning filter, delivering position estimates with an error smaller than 8 m (50% CEP) in the indoor scenario.

Acknowledgements

This PhD thesis is part of a wider project, which was conceived by the mind of Dr. Chris Marshall from u-blox UK. Hence, the first acknowledgement goes to Chris, for his patience and competence in guiding me through this beautiful field of research, which was unknown to me before starting this challenging journey. And since this has been a long journey, several people travelled with me during the different seasons. My sincerest gratitude goes to Fabian, Mischa, and Nicola from the Hochschule für Technik Rapperswil, for their help and their wide competence in several fields. A lot of the work reported in this thesis wouldn't have been possible without their contribution. I want to thank also Andrea and Federico from u-blox Italia, who worked with Chris and me on this subject on different occasions, and who now are my new colleagues. Finally, a big thank you to my supervisor Prof. Fulvio Babich, for having always supported me and accorded me freedom and trust.

During these last three years my life mostly happened in the "Microonde" lab at the University of Trieste. Thanks to "my students", who actually became dear friends, Tommaso, Flavio and Maurizio, and to the other mates I met recently at the university, Francesco and Dario. Moreover, thanks to the lab-mates Giulia, Riccardo, Alessandro, Max and Amir, and to the *dudes* Alessandro and Aljosa.

Another thing I found during these last three years is rock climbing, and all the people related to that world here in Trieste. Hence, I want to thank my *rampighezzi*'s friends, especially Mauro, Denis, Luca, Davide and Michele.

Then, I want to thank my parents Loris and Anna, my grandma Amelia, my uncle Bruno, my brother Simone and my sister Eugenia, and all my old friends. Thanks for being always at my side.

Finally, my deepest thank you goes to my love Elsona. Thank you for letting every moment we spend together become the best moment ever. I think you are the only person who really understands me, and who is capable of supporting me with the right words at the right time, always. I think that nothing contributed to this work more than your presence in my life.

Summary

The contributions presented in this dissertation are the result of a three-year study period as a Ph.D. student in information engineering at the Telecommunication Group of the Department of Engineering and Architecture at the University of Trieste. The presented work has been realized with the support of the company u-blox UK Ltd and in close collaboration with the Hochschule für Technik Rapperswil (HSR), Switzerland, where several technical workshops and meetings were held during the study period.

Nowadays, positioning and navigation technologies are commonly used in a large variety of contexts [1–6]. One of the most popular applications is in the field of transportation, where positioning systems are frequently used to ease the navigation in maritime, air, and terrestrial vehicles. Localization systems are also used in robotics for guiding autonomous devices, in cartography, in various context such as telecommunications, finance, and other time critical applications for clock synchronization, in the sports field for monitoring and analyzing the athletes' training. Other applications include assent management, and the tracking systems for vehicles, people and pets. More safety critical scenarios include disaster relief, emergency services, and search and rescue operations [7]. Positioning technologies are also strongly exploited in the military field, in procedures such as target tracking and missile guidance.

In addition to these aspects, emerging technologies such as the concept of Internet of Things (IOT), and the growing ubiquitous availability of broadband mobile connections, increasingly lead to the need for communication networks to offer location awareness features. Indeed, data collected or exchanged through a communication network should often be supplied together with the corresponding location information. Examples are personalized advertisements, social networking, and all the applications related to the wireless sensor networks such as environment monitoring and intrusion detection [5].

In the majority of these applications, the localization task is accomplished by exploiting global navigation satellite systems (GNSSs), since these are a very precise and effective mean for positioning, thanks to their global coverage, high precision, and relatively low cost end-user receiver devices. However, there are multiple situations in which the GNSSs may not work effectively [8]. Devices often move to environments where sky view is limited, such as subterranean and indoor areas, narrow urban canyons, dense forests, etc. There, it may be impossible to obtain a position fix due to satellite reception being limited in angle and power. GNSSs

are also vulnerable to jamming and spoofing, which appear to be growing in frequency and severity [9, 10], and to bad space weather conditions. In addition, the development and deployment of a GNSS infrastructure has extremely high costs, which are not sustainable by the majority of the countries. Consequently, addressing the problem of positioning without relying on satellite systems is of fundamental importance.

Several methods have been proposed to tackle positioning in critical scenarios. Examples include inertial navigation systems, fingerprint based positioning, and localization via wireless terrestrial signals. While the former have the disadvantage of cumulative errors and extensive calibration campaigns, respectively, the latter may provide good performance and coverage with the advantage of no or limited additional infrastructure deployment [11–13]. In this context, localization by means of the cellular systems base stations (BSs) downlink signals is a promising approach, because of their wide availability and coverage, also bearing in mind the future deployments of micro/pico-cells. Consequently, positioning using Third Generation Partnership Project (3GPP) Long Term Evolution (LTE) downlink signals has become a subject of recent research and industrial interest.

The 3GPP started the development of LTE in 2004, and released the first version of the standard in 2008. LTE offers increased capacity, data rates, and user mobility in respect to the previous standard for the cellular mobile systems, thanks to an improved core network and radio interface. According to the data reported in [14] and updated to September 2015, the countries with at least one commercial LTE network are 140, with time coverage values[1] going from the 51% of Italy, to the 80% of the Netherlands (Europe's best), from the 78% of the United States, to the 97% of the South Korea (World's best). Together with its rising global coverage, the LTE system is an attractive option to be considered for positioning also because of the characteristics of its radio interface. Indeed, multi-carrier wideband waveforms such as the orthogonal frequency division multiplexing (OFDM) based LTE downlink signals are an ideal candidate for being used as reference signals in time of arrival (TOA) estimation, especially for range estimations in harsh propagation environments [15–17].

Against this background, this thesis work addresses the problem of estimating, for positioning purposes, the time of arrival of real 3GPP LTE signals, by exploiting their underlying OFDM based physical layer. The original contribution of the presented work is twofold.

Firstly, a theoretical analysis has been developed, based on the Cramér-Rao bound and on the Ziv-Zakai bound, and aimed at assessing the root mean square error (RMSE) behaviour of realistically modeled OFDM signals when used for TOA estimation in an additive white Gaussian noise (AWGN) channel. This permitted to identify a trade-off between threshold and asymptotic RMSE behaviour of the

---

[1] The time coverage is a metric for holistically assessing the coverage of a network. It consists in the average percentage of time that users spent connected to that particular network in respect to the total time spend connected [14].

employed OFDM signals, which is a useful achievement from the TOA reference signals design point of view, and to compare different LTE signals to be used in positioning applications.

Secondly, a TOA estimation and tracking algorithm has been developed, to be used to estimate time based pseudoranges in real world multipath environments. The developed algorithm, referred to as ESPRIT and Kalman filter for time of Arrival Tracking (EKAT), has been tested on real LTE signals, collected during in the field measurements in outdoor vehicular and indoor environments. The algorithm is based on the use of super-resolution algorithms (SRAs), which naturally exploit the OFDM physical layer of the LTE signals, and of a modified Kalman filter (KF), which is able to manage the discontinuities typical of real datasets. Furthermore, EKAT features a bound-based measurement reliability estimation, and combining methods of the received LTE signals in the time, frequency, spatial, and cell ID domains, for improving performance and robustness. The obtained ranges have been then employed in a positioning filter, for evaluating the effectiveness of EKAT from a positioning perspective. This part of the research work has been developed in collaboration with the Institute for Communication Systems (ICOM) team of the HSR, who performed the measurements and implemented the positioning engine.

The remainder of the thesis is divided in two main parts, with the first describing the background topics analyzed at the beginning of the Ph.D. study period, and with the second part presenting the original contributions.

In Chapter 1, the basic principles of a positioning system are explained, with particular attention to the positioning systems based on time based distance measurements. Firstly, some classifications of the positioning systems are briefly proposed. Then, the remaining sections focus on the description of the physical quantities measured for obtaining a distance estimate, to be later used for performing the localization. The systems that are based on time measurements are explained more in detail, since these are the ones exploited throughout this thesis work.

In Chapter 2, the LTE downlink physical layer is briefly described, with particular attention to the OFDM transmission technique, and to the LTE reference signals exploited throughout the rest of the thesis work. Moreover, the chapter also explains how LTE manages its frequency reuse factor of one, and how this enables the simultaneous reception of reference signals from multiple cells controlled by the same BS, which is a feature exploited in the experimental part of the presented work.

Chapter 3 describes the most popular SRAs, with particular attention to the multiple signal classification (MUSIC) and the estimation of signal parameters via rotational invariance techniques (ESPRIT), which is the one used throughout this thesis work.

Chapter 4 briefly presents the theoretical performance bounds used for assessing the effectiveness of the various considered TOA reference signals. The used bounds are the Cramér-Rao bound and the Ziv-Zakai bound.

Chapter 5, which constitutes the first part of the original results, presents a study of the performance of the OFDM signals when used as reference signals for time of arrival estimation. A model for physically realizable signals is described and used to address the RMSE performance of realistic OFDM waveforms. Thanks to the adoption of different sub-carriers power distributions and of a new performance figure, the results of a study on the estimation RMSE both in the threshold and asymptotic signal-to-noise ratio regions is presented. The results of a comparison of different LTE OFDM reference signals are also reported, which permitted to establish the best signal to use for time based ranging purposes.

Chapter 6 presents the second part of the original results. The developed EKAT algorithm is described, and used for evaluating time-based pseudoranges from datasets of real LTE signals collected from the commercial network of the town of Rapperswil, Switzerland. Different measurement environments have been tested, including an outdoor vehicular and an indoor scenario, both characterized by strong multipath propagation. The different combining algorithms developed for improving the quality of the TOA estimates are explained, and the effectiveness of the proposed approach in separating multipath and tracking the direct path TOA is demonstrated. Finally, the positioning results obtained by using the ranges estimated with the developed EKAT algorithm are presented.

Contents

List of acronyms

3GPP	Third Generation Partnership Project
AD	analog-to-digital
ADSL	asymmetric digital subscriber line
AWGN	additive white Gaussian noise
BS	base station
CDF	cumulative density function
CEP	circular error probability
CFR	channel frequency response
CIR	channel impulse response
CP	cyclic prefix
CRB	Cramér-Rao bound
CRS	cell specific reference signal
DA	digital-to-analog
DAB	digital audio broadcasting
DAC	digital-to-analog converter
DC	direct current
DFT	discrete Fourier transform
DOA	direction of arrival
DP	direct path
DRSS	differential received signal strength
DVB-T	terrestrial digital video broadcasting
EKAT	ESPRIT and Kalman filter for time of Arrival Tracking
EKF	extended Kalman filter
ENU	east-north-up coordinates
ESPRIT	estimation of signal parameters via rotational invariance techniques
FD	frequency domain
FDD	frequency domain duplexing
FFT	fast Fourier transform
GB	Gabor bandwidth
GNSS	global navigation satellite system
GPS	Global Positioning System
HSR	Hochschule für Technik Rapperswil
ICIC	inter-cell interference coordination

ICOM	Institute for Communication Systems
IDFT	inverse discrete Fourier transform
IFFT	inverse fast Fourier transform
IOT	Internet of Things
KF	Kalman filter
LHS	left hand side
LORAN	LOng RAnge Navigation
LOS	line of sight
LS	least squares
LTE	Long Term Evolution
MDL	minimum descriptive length
MIMO	multiple input multiple output
ML	maximum likelihood
MS	mobile station
MSE	mean square error
MUSIC	multiple signal classification
NLOS	non line of sight
OFDM	orthogonal frequency division multiplexing
OFDMA	orthogonal frequency division multiple access
OTDOA	observed time difference of arrival
PCI	physical cell identity
PCIG	physical cell identity group
PDF	probability density function
PDP	power delay profile
PE	positioning engine
PRS	positioning reference signal
PSS	primary synchronization signal
R95	95% radius
RB	resource block
RE	resource element
RHS	right hand side
RMS	root mean square
RMSE	root mean square error
RSS	received signal strength
RV	random variable
SDR	software defined radio
SNR	signal-to-noise ratio
SRA	super-resolution algorithm
SSS	secondary synchronization signal
SVD	singular values decomposition
TDD	time domain duplexing
TDOA	time difference of arrival
TOA	time of arrival
UE	user equipment

USRP	universal software radio peripheral
UTC	Coordinated Universal Time
WLAN	wireless local area network
WPAN	wireless personal area network
ZZB	Ziv-Zakai bound

List of symbols

Matrices and vectors are generally denoted as bold upper case and bold italic lower case letters, respectively, e.g. $\mathbf{A} \in \mathbb{C}^{M \times N}$ and $\boldsymbol{a} \in \mathbb{C}^{M}$. Generally, $\hat{a}, \hat{\boldsymbol{a}}$ and $\hat{\mathbf{A}}$ denote the estimates of $a, \boldsymbol{a}$ and $\mathbf{A}$, respectively. A length M discrete time sequence is represented as $x[n]$, $n = 0, \ldots, M-1$, or with the vector representation $\boldsymbol{x} = [x[0], \ldots, x[M-1]]^{\mathrm{T}} \in \mathbb{C}^{M}$. Moreover, $x[n]$ identifies either the n^{th} element of the sequence or the entire sequence, and which of the two will be clear by the context. The discrete frequency domain representation of $x[n]$ is generally denoted with the corresponding capital letter, and the k index, i.e., $X[k] = \mathrm{DFT}\{x[n]\}$. Below are listed the most commn symbols and operators used throughout the thesis.

$(\cdot)^{\mathrm{T}}$	transpose of a matrix
$(\cdot)^{-1}$	inverse of a matrix
$(\cdot)^{\mathrm{H}}$	Hermitian transpose of a complex matrix
$(\cdot)^{\dagger}$	Moore-Penrose pseudoinverse of a matrix
$(\cdot)^{*}$	complex conjugate of a scalar, vector, or matrix
$\langle\cdot\rangle_x$	modulo x operation, $x \in \mathbb{N}$
$\lfloor\cdot\rfloor$	floor function
$*$	linear convolution between discrete or continuous time sequences
$\circledast_N$	circular convolution between discrete time length N sequences
$\mathbf{I}_P$	$P \times P$ eye matrix
$\mathbf{0}_{P \times Q}$	$P \times Q$ all-zero matrix
$\mathbf{0}_P$	length P all-zero vector
$\mathrm{Var}(\cdot)$	variance of a random variable (or of an estimator)
$\mathrm{MSE}(\cdot)$	mean square error of an estimator
$\mathrm{RMSE}(\cdot)$	root mean square error of an estimator
$\mathcal{F}\{\cdot\}$	continuous time Fourier transform
$\mathcal{F}^{-1}\{\cdot\}$	inverse continuous time Fourier transform
$\mathrm{DFT}\{\cdot\}$	discrete Fourier transform
$\mathrm{IDFT}\{\cdot\}$	inverse discrete Fourier transform
$\mathbb{E}[\cdot]$	expected value of a random variable
$\mathbb{E}_x[\cdot]$	expected value in respect to the random variable x
$\lvert\cdot\rvert$	absolute value of a complex number
$\arg\{\cdot\}$	argument of a complex number

$\mathfrak{Re}\{\cdot\}$	real part of a complex number
$\mathfrak{Im}\{\cdot\}$	imaginary part of a complex number
$\mathrm{n}[\cdot]$	cardinality of a set
$\varnothing$	the empty set
$\Vert\cdot\Vert$	norm of a vector
$\delta(t)$	continuous time Dirac delta function
$\delta[n]$	discrete time Dirac delta function
$\delta_{ll'}$	Kronecker delta
c	speed of light, assumed equal to 299792458 m/s
v	relative speed between transmitter and receiver
$t^{(\mathrm{U})}$	UTC epoch corresponding to the discrete measurement time t
$h(t)$	channel impulse response
$H(f)$	channel frequency response
$h[n]$	discrete channel impulse response
$H[k]$	discrete channel frequency response
h_l	channel gain of the l^{th} path of a multipath channel
τ_l	delay corresponding to the l^{th} path of a multipath channel
$\hat{\tau}_l^{i,p}(t)$	l^{th} estimated multipath TOA from cell i antenna port p at time t with the ESPRIT algorithm
$\hat{\tau}_x^{i,p}(t)$	CIR based TOA estimation with the algorithm $x \in \{\mathrm{IM}, \mathrm{IL}\}$ at time t from cell i antenna port p
$\hat{\tau}_x^{i}(t)$	CIR based TOA estimation with the algorithm $x \in \{\mathrm{IM}, \mathrm{IL}\}$ at time t from both antenna ports of cell i
$\hat{L}^{i,p}(t)$	number of multipath components estimated from cell i antenna port p at time t with the MDL algorithm
$\Upsilon^{i,p}(t)$	set of multipath TOA estimated from cell i antenna port p at time t with the ESPRIT algorithm
$\Theta^{i,p}(t)$	set of multipath TOA estimated from cell i antenna port p at time t which do not imply a receiver movement with a speed higher than $v_{\max}^{(1)}$
$\mathcal{K}_j(t)$	set of cell IDs of BS j that are visible by the receiver at the time t
$\Lambda_j(t)$	sub-set of cell IDs of BS j visible at time t having corresponding pseudoranges that do not imply a receiver movement with a speed higher than $v_{\max}^{(2)}$
$\hat{\boldsymbol{\zeta}}^{i}(t)$	EKAT KF estimated state at time t pertaining to cell i
$\hat{\zeta}_0^{i}(t)$	first component of $\hat{\boldsymbol{\zeta}}^{i}(t)$, corresponding to the tracked DP TOA
$\hat{\mathbf{P}}^{i}(t)$	EKAT KF estimated state covariance matrix at time t pertaining to cell i
$\hat{P}_{0,0}^{i}(t)$	upper left element of the matrix $\hat{\mathbf{P}}^{i}(t)$, corresponding to the variance of the tracked DP TOA
$\mathbf{Q}$	EKAT KF constant process noise covariance matrix
$\boldsymbol{z}_{\mathrm{E}}(t)$	EKAT KF measurement vector

$z_{\mathrm{E}}^{p}(t)$	p^{th} element of $\boldsymbol{z}_{\mathrm{E}}(t)$, corresponding to the TOA measurement from antenna port p
$\mathbf{R}(t)$	EKAT KF measurement noise covariance matrix at time t
$R^{p}(t)$	p^{th} element of the diagonal of $\mathbf{R}(t)$, corresponding to the variance of the TOA measurement from antenna port p
D_{init}	maximum time to wait for a second measurement to be used for initializing the EKAT KF
D_{max}	maximum time to wait for a new measurement before reinitilizing EKAT KF
γ_0	EKAT KF scaling factor for increasing the unreliability of a measurement implying a receiver speed higher than $v_{\mathrm{max}}^{(1)}$
γ_1	EKAT KF scaling factor for increasing the unreliability due to the use of a previous measurement
γ_2	EKAT KF scaling factor for increasing the unreliability due to the use of a predicted measurement
$\boldsymbol{\xi}(t)$	state of the positioning EKF
$\mathbf{Q}_{\mathrm{p}}$	constant process noise covariance matrix of the positioning EKF
$\boldsymbol{z}_{\mathrm{p}}(t)$	measurement vector of the positioning EKF
$\mathbf{R}_{\mathrm{p}}(t)$	measurement noise covariance matrix of the positioning EKF
P_x^{r}	experimental probability of the algorithm $x \in \{\mathrm{E}, \mathrm{IL}\}$ of producing a range estimate
P_x^{p}	experimental probability of producing a position fix with the ranges evaluated with algorithm $x \in \{\mathrm{E}, \mathrm{IL}\}$
$P(\mathcal{E}_{\mathrm{d}}^{\mathrm{est}} < \varepsilon)$	experimental CDF of the ranging error
$P(\mathcal{E}_{\mathrm{p}}^{\mathrm{est}} < \varepsilon)$	experimental CDF of the positioning error
$P(\mathcal{E}_{\mathrm{d}}^{\mathrm{in}} < \varepsilon)$	experimental CDF of the ranging error as a percentage of the common number of input elements
$P(\mathcal{E}_{\mathrm{p}}^{\mathrm{in}} < \varepsilon)$	experimental CDF of the positioning error as a percentage of the common number of input elements
$S[k]$, $\boldsymbol{S}$	sequence containing an OFDM symbol sub-carriers' content
$\tilde{S}[k]$, $\tilde{\boldsymbol{S}}$	sequence containing an OFDM symbol sub-carriers' content shifted with FFT-shift
$S_{l,n_s}^{p}[k]$	LTE RE carried by sub-carrier k, OFDM symbol l, slot n_s, antenna port p, or entire sequence containing the sub-carriers' content of the corresponding OFDM symbol
$\kappa_l^{i,p}$	FD shift that characterizes each CRS mapping depending on the cell ID i, antnna port p, and symbol in the slot l
$\mathcal{C}_{t,l,n_s}^{i,p}$	set of equispaced sub-carriers occupied by the CRS of OFDM symbol l, slot n_s, antenna port p, received from cell i at time t
$r_{t,l,n_s}^{i}[n]$	time domain samples of the received LTE OFDM symbol l, slot n_s, from cell i at time t
$R_{t,l,n_s}^{i}[k]$	sub-carrier content of the received LTE OFDM symbol l, slot n_s, from cell i at time t

$\hat{H}^{i,p}_{t,l,n_s}[k]$	CFR sampling using the LTE CRS of OFDM symbol l, slot n_s, antenna port p, cell i, measured at time t
$\hat{H}^{i,p}_{t,n_s}[k]$	merged CFR sampling using the LTE CRSs of slot n_s, antenna port p, cell i, measured at time t
$\hat{H}^{i,p}_{t}[k]$	CFR estimate after combining of the slots received at time t from antenna port p, cell i
$\mathbf{X}^{i,p}_{t}$	data matrix used in EKAT for ESPRIT based TOA estimation at time t using the signals from antenna port p of cell i
$\hat{h}^{i,p}_{t}[n]$	estimated CIR from antenna port p, cell i at time t
$s_{\mathrm{c}}(t)$	result of the realistic DA conversion of the OFDM signal samples $s[n]$
$s_{\mathrm{cp}}(t)$	result of the ideal DA conversion of the OFDM signal samples $s[n]$ preceded by the CP
L_{cp}	CP length in samples
N_{dft}	length of the DFT operator used for the implementation of the OFDM modulation
$N^{\mathrm{cp}}_{\mathrm{tot}}$	total number of samples corresponding to the OFDM symbol included the CP
N_{sc}	number of used sub-carriers in an OFDM symbol
N_{a}	number of non-null sub-carrier in an OFDM power distribution
$I_{N_{\mathrm{sc}}}(d)$	number of empty sub-carriers determined by the adopted N_{sc} sub-carriers power distribution around the DC
β	Gabor bandwidth
γ_{f}, $\gamma_{\mathrm{f,dB}}$	SNR at which the ZZB has a convex to concave point of inflection
γ_{th}, $\gamma_{\mathrm{th,dB}}$	novel SNR threshold quantifying the border between threshold and asymptotic RMSE region
δ_2	SNR threshold quantifying the border between threshold and asymptotic RMSE region according to [18]
$\Xi(\gamma_{\mathrm{dB}})$	ZZB as a function of the SNR expressed in dB
B	LTE system bandwidth
$N^{\mathrm{DL}}_{\mathrm{RB}}$	number of downlink LTE resource blocks
$N^{\mathrm{DL}}_{\mathrm{symb}}$	number of OFDM symbols in an LTE slot
N_{tot}	number of pilot tones (either CRS of PRS) in an LTE OFDM symbol
$N^{\mathrm{cell}}_{\mathrm{ID}}$	physical cell identity or cell ID
$N(t)$	number of BSs received at time t
$\hat{d}^{\mathrm{BS}}_{j}(t)$	estimated distance from BS j using signals of all the BS's cells
$\hat{d}_{i}(t)$	estimated distance using the signals of cell i
$\hat{\rho}^{\mathrm{BS}}_{j}(t)$	estimated pseudorange from BS j using signals of all the BS's cells
$\hat{\rho}_{i}(t)$	estimated pseudorange using the signals of cell i
$\mathfrak{D}_j$	clock bias of BS j expressed as a distance
$\mathfrak{d}_j$	clock drift of BS j expressed as a distance
$\varrho_j(t)$	instantaneous clock offset of BS j expressed as a distance
f_{C}	carrier's frequency

f_{D}	Doppler shift
f_s	sampling frequency used in the DA conversion for generating an OFDM signal
σ_w^2	complex noise variance
$\mathcal{N}_0$	bi-lateral power spectral density of the complex thermal noise, $\mathcal{N}_0/2$ per dimension
$\mathcal{E}_s$	energy of the reference signal $s(t)$
$\mathcal{CN}(\mu, \sigma^2)$	complex Gaussian noise distribution with μ mean and $\sigma^2/2$ variance per dimension
$Z(\gamma)$	value of the Ziv-Zakai bound as a function of the SNR γ
$C(\gamma)$	value of the Cramér-Rao bound as a function of the SNR γ
$\eta(\gamma, \Delta)$	auxiliary function for the evaluation of the ZZB integral
$\xi(\gamma_{\mathrm{dB}}, \Delta)$	auxiliary function for the evaluation of the derivatives of the ZZB
$\rho_s(\Delta)$	single sided autocorrelation function of a signal, expressed as a function of the lag Δ
Δf	frequency separation between the sub-carriers of an OFDM symbol
Δf_{CRS}	frequency separation between two adjacent CRS pilots
Δf_{PRS}	frequency separation between two adjacent PRS pilots
Δf_{mCRS}	frequency separation between two adjacent CRS pilots after pilot frequency merging
Δf_{SRA}	sample separation of a frequency domain sequence that feed a SRA for TOA estimation
Δt_{r}	retransmission time in two way TOA ranging
Δt_{s}^i	delay introduced for achieve symbol synchronization on cell i
Δt_{p}	elapsed time since the last position estimate
Δt_{z}	elapsed time since the last measurement available for a certain cell
$\boldsymbol{p}(t)$	receiver position vector at time t
$\dot{\boldsymbol{p}}(t)$	receiver speed vector at time t
$\ddot{\boldsymbol{p}}(t)$	receiver acceleration vector at time t
T	interval between two subsequent measurements in the datasets of Chapter 6
$T_{\mathrm{cp},l}$	duration of the CP of the l^{th} LTE OFDM symbol
T_s	duration of an OFDM symbol or of a whichever reference symbol
$T_{s,0}$	base time unit in LTE
T_ω	length of the windowing function that limits the sinc-shaped impulse response of physically realizable DACs
T_{c}	duration of a physically realizable OFDM signal
T_{o}	observation interval for a reference signal
$\omega(t)$	windowing function that limits the sinc-shaped impulse response of physically realizable DACs
$p_\omega(t)$	impulse response of a physically realizable DAC

Part I

Background

Chapter 1

Distance measurements for positioning

In this introductory chapter, the basic principles of a positioning system are explained, with particular attention to the positioning systems based on distance measurements. Firstly, some classifications of the positioning systems are briefly proposed. Then, the remaining sections focus on the description of the physical quantities measured for obtaining a distance estimate, to be later used for performing the localization. The systems that are based on time measurements are explained more in detail, since these are the ones exploited throughout this thesis work.

1.1 Radio positioning systems

There are several types of positioning systems. One of the widest classes of positioning systems is constituted by all the systems based on the measurements of the wireless signals' properties. As an example, the global navigation satellite systems (GNSSs), including the well known Global Positioning System (GPS), the European Galileo, the Russian GLONASS, the Chinese BeiDou, and others, belong to this class. As explained in the summary of the thesis, GNSSs are by far the most popular and used localization systems. They exploit distance measurements from the satellites of an orbiting constellation, which are equipped with tightly synchronized atomic clocks and which periodically transmit ephemerides in order to enable the receiver to calculate each satellite position. The distances between the receiver and the satellites are estimated by measuring the time of arrival of the transmitted signals, and by exploiting the signals' transmission time, which is timestamped in the transmitted signals themselves.

The localization systems that exploit radio signals are not limited to the satellite systems, but include also the class of the terrestrial systems. In the past decades, terrestrial positioning systems were mainly used for maritime and air navigation, and include, e.g., the LOng RAnge Navigation (LORAN) system and the Decca

Navigator System. Recently, terrestrial wireless positioning systems have gained improved interest also for less specific application fields. This is mainly motivated by the fact that those systems constitute a valid alternative to the satellite systems, to be used in environments where the GNSSs performance falter, or in case of GNSSs failures. Moreover, because of the rising ubiquitous connectivity offered by the recent broadband mobile systems such as the Third Generation Partnership Project (3GPP) Long Term Evolution (LTE), terrestrial positioning systems are often integrated, at various levels, with a wireless communication network. In this case, the terrestrial positioning system is referred to as a cellular-based positioning system.

A wireless terrestrial positioning system involves several devices called nodes, which are assumed to be connected to some wireless communications network. These nodes can be divided in two categories: the anchor nodes have a known location, while the agents have unknown location and are the nodes to be located. Both anchors and agents can have a fixed or mobile position. In cellular-based positioning, anchors are usually the base stations (BSs) of the mobile system, which have a fixed position, while agents are the users' mobile terminals, which are referred to as mobile stations (MSs).

The positioning process consists of two main steps [6]. In the first step, referred to as the measurement phase, agents and anchors measure any physical signal property which carries information about the relative positions of the other nodes, by exploiting the signals received from the network. The most common quantities measured in this phase are described in Section 1.2. In the second step, referred to as the location update phase, the location of the agents is determined by using the information acquired in the first step in conjunction with *a priori* information such as the anchors' positions. The positioning techniques exploited through this research work are described in Section 1.3.

1.1.1 Classifications

A positioning method can be classified according to several criteria [1]. If the system topology is considered, a positioning method may be: a self-positioning method, if measurements and processing are done by the MS; a remote positioning method, if the measurements and processing are made by the BS or by the network; an indirect positioning method, if both the BS and the MS contribute to measurements and processing needed for positioning.

A positioning system may also be classified according to the physical coverage that ensures. Indeed, a localization method may be classified as satellite, terrestrial or short-range positioning. The first method involves satellite communications and provide positioning on a global scale. Terrestrial positioning systems are based on signals sent or received by terrestrial stations, which may be the BSs of a cellular communication system, or specific transmitting stations, like in the case of navigation systems such as the LORAN system. Terrestrial systems provide positioning services within the range of the exploited communication technology, in dependence also of the carrier frequency used. Coverages may vary from the thousands of kilo-

Measurement	Physical quantity	Description
TOA	Time	Reception time of a reference signal
TDOA	Time	Difference of times between the reception of two synchronous reference signals
RSS	Power	Received reference signal power
DRSS	Power	Difference of received power between the two reference signals
DOA	Angle	Angle of arrival of the received reference signal in respect to a fixed orientation
Node ID	-	Identifier of the node that transmitted the reference signal
PDP	Power vs delay	Shape of the multipath power delay profile

Table 1.1 – Overview of signal properties used in positioning.

meters of the hyperbolic navigation systems such as the LORAN, to the tens of kilometers of the cellular systems. Finally, short-range positioning concerns wireless local area networks (WLANs) and wireless personal area networks (WPANs), provides positioning within the range of the tens of meters, and is used mainly for indoor positioning.

Another useful classification divides positioning systems in integrated, opportunistic or hybrid systems. In the case of integrated systems, the positioning framework is implemented together with the wireless communication technology, while in the case of opportunistic systems the wireless communication protocol is exploited to opportunistically determine the position. In hybrid systems, a mixture of integrated and opportunistic approaches is used in combination or alternately depending on the environment and on the positioning requirements.

1.2 Measurements

A terrestrial radio positioning system exploits the position-dependent parameters of a received signal which are later used in the location phase for evaluating a position estimate [2]. The signals exploited for such purpose are referred to as reference signals. The position-dependent parameters measured from a received reference signal include its time of arrival (TOA), its received signal strength (RSS), its direction of arrival (DOA), or some identifier of the particular node that transmitted the signal. Moreover, differential measurements may be employed, such as time difference of arrival (TDOA) measurements or the differential received signal strength (DRSS) between two reference signals. Finally, the shape of the multipath power delay profile (PDP) measured thanks to the exploitation of the reference signal may also be exploited as a position dependent parameter. An overview of some of the position-dependent signal parameters is presented in Table 1.1, with each entry described in the following.

The node identifier is an unambiguous identifier of a transmitting node. Usually, node identifiers are used in the so called cell ID based positioning systems, where the cell ID transmitted from a cellular system BS is exploited by the MS for obtaining an estimation of its position. In a wireless communication system where a cell ID localization service is available, all the BS positions associated with their unique ID are stored in a database. A MS can query the localization service sending the cell IDs of the received BSs. If just one BS is received, the position of the MS is usually approximated with the position of the BS, with a maximum error equal to the radius of the cell covered by that particular BS. Conversely, if more than one BS is received, and if the database stores positions associated with the reception of sets of specific BSs, a more precise estimate can be generated.

Multipath PDP are exploited in a similar way, in positioning systems which adopt the so called fingerprinting techniques. Such methods are based on a database that is built in a preliminary calibration phase. This database associates the particular PDP measured in a certain point, and other signal parameters, to the position coordinates of that point. In the positioning phase, the agent node that wants to obtain an estimation of its position, measures the received PDP thanks to the reception of reference signals, and then query the database sending the measured PDP. The database answers with the coordinates that correspond to the PDP which is the most similar to the one measured [1].

DOA measurements are performed in order to assess the angle of arrival of the received reference signal in respect to a fixed orientation. This type of measurements require the node to be equipped with a directional antenna, such as an adaptive phased array of two or more antenna elements, and to run some signal processing algorithm for DOA estimation. These facts make DOA estimation complex and expensive in terms of implementation, and hence usually less attractive as a positioning technique intended for being implemented in consumer devices.

Finally, RSS and TOA measurements permit the estimation of the distance between the transmitting and the receiving node. The process of estimating the distance between two nodes is often referred to as ranging. These type of measurements are analyzed more in detail in the following sections.

1.2.1 Received signal strength

Received signal strength (RSS) measurements exploit the dependence on the distance of the received signal power. Indeed, if the power of the received reference signal can be measured, and under the assumption of knowing the transmission power, the path loss can be easily evaluated. Then, if a propagation model has been fixed, which establishes a dependence between path loss and distance between transmitter and receiver, an estimate of the distance can be obtained. A simple propagation model which is frequently used in RSS measurements quantifies the instantaneous received power $P_{\mathrm{r,dB}}(t)$ expressed in dB as [19]:

$$P_{\mathrm{r,dB}}(t) = P_{\mathrm{t,dB}} - 10 \cdot \alpha \cdot \log_{10}(d) - K - X_{\mathrm{f}}(t) - X_{\mathrm{s}}, \tag{1.1}$$

where: $P_{\mathrm{t,dB}}$ is the transmitted power; K is a constant gain factor which depends on the antenna gains and on the carrier frequency; $X_{\mathrm{f}}(t)$ is a random variable (RV) that models the small scale multipath fading, which is the attenuation due to the recombination at the receiver of different replicas of the same signals, with different attenuations and phase shifts; X_{s} is the shadowing term, which corresponds to the large scale attenuation due to obstacles in the propagation environment, and is usually modeled as a log-normal RV; and $10 \cdot \alpha \cdot \log_{10}(d)$ is the attenuation due to the distance d according to the path loss exponent α. The fading term presents fast variations in time, and can be easily removed by averaging a certain number of measurements over time, obtaining the average received power $\bar{P}_{\mathrm{r,dB}}$. Then, after having fixed a certain path loss exponent α, and with the assumption of the knowledge of the parameters K and P_{t}, the distance can be estimated as [1]:

$$\hat{d} = 10^{-\frac{\bar{P}_{\mathrm{r,dB}} - P_{\mathrm{t}} + K}{10 \cdot \alpha}}. \tag{1.2}$$

As one can see from (1.2), the estimated distance is highly dependent on the choice of the particular path loss exponent α, which ultimately determines how the propagation environment is modeled. The path loss exponent may be fixed in a previous calibration phase, according to measurement campaigns [19, 20], or determined dynamically according to different strategies [21, 22].

The main advantage of using RSS measurements for performing range estimations is constituted by the implementation simplicity. Indeed, the only requirement for the transmitting and receiving nodes is the ability of measuring the power, which is a common feature of almost every communication module, and no synchronization is required. The drawback of this technique is the sensitivity in respect to modeling mismatches. Indeed, the correctness of the estimated distance is highly dependent on how closely the fixed propagation model fits the actual propagation environment.

1.2.2 Time of arrival

In a radio positioning system, the distance between two nodes may be estimated by measuring the time that a signal takes for propagating from the transmitter to the receiver. Then, assuming then that the electromagnetic wave that constitutes the reference signal travels at a speed approximately equal to the speed of light in the vacuum, i.e., at $c = 299792458\,\mathrm{m/s}$, the distance can be easily retrieved. There are different types of TOA based ranging techniques, which differ on the base of the different requirements on the synchronization of the nodes' clocks.

Consider the most ideal case, in which all the nodes of the system share the same clock, i.e., their clocks are assumed to be perfectly synchronized. Moreover, suppose that the nodes that transmit the reference signals insert in the signal itself the timestamp t_{t} of the transmission time. Then, once the receiver has estimated the TOA $\hat{t}_{\mathrm{r}}$ of the reference signal, and read the transmission timestamp, the distance between the two nodes can be calculated according to the procedure depicted in Figure 1.1a, i.e.:

$$\hat{d} = \left(\hat{t}_{\mathrm{r}} - t_{\mathrm{t}}\right) \cdot c. \tag{1.3}$$

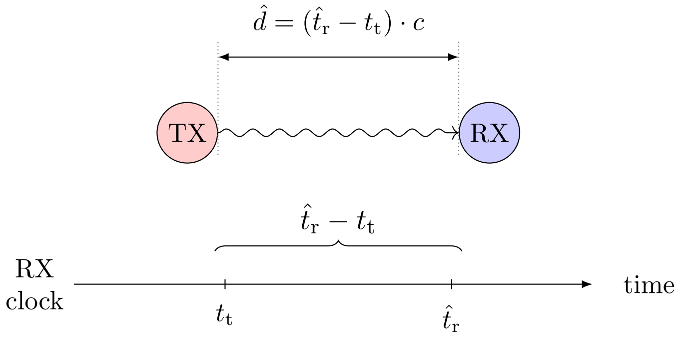

(a) TOA ranging in case of synchronized nodes.

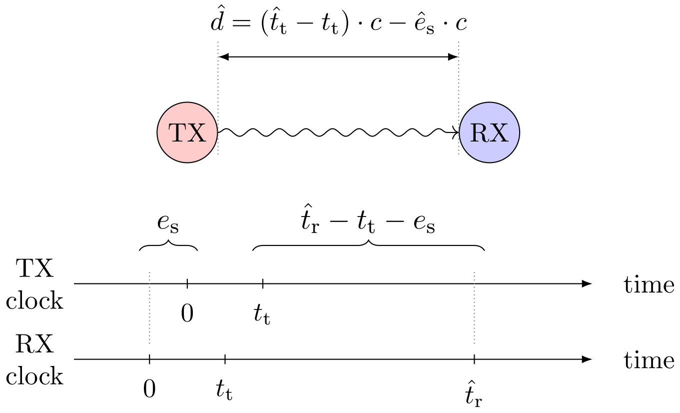

(b) TOA ranging in case of non synchronized nodes.

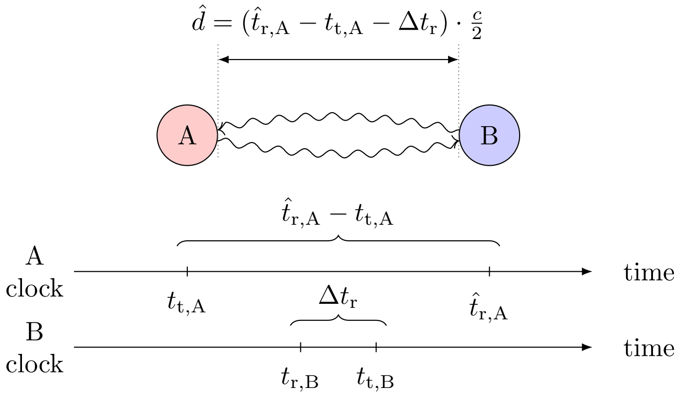

(c) Two way TOA ranging. The reference signal is transmitted from A to B, and then back from B to A, after a delay of Δt_r.

Figure 1.1 – Different ranging techniques based on TOA measurements.

The clock synchronization of all the network's nodes is often a challenging task. Hence, some systems accepts the mis-synchronization of the receiver node. Suppose that the receiver clock has an offset of e_{s} in respect to the transmitter clock, as depicted in Figure 1.1b. Once the reference signal, transmitted at time t_{t} according to the transmitter's clock, reaches the receiver, the TOA $\hat{t}_{\mathrm{r}}$ can be evaluated, according to the receiver's clock. In this case, the quantity $\hat{\rho} = c \cdot (\hat{t}_{\mathrm{r}} - t_{\mathrm{t}})$, which is referred to as pseudorange, is not directly related to the distance between the nodes. For evaluating the correct distance, the clock offset has to be estimated with some technique, obtaining $\hat{e}_{\mathrm{s}}$. Then, the actual distance can be obtained by correcting the pseudorange $\hat{\rho}$ as:

$$\hat{d} = \left(\hat{t}_{\mathrm{r}} - t_{\mathrm{t}}\right) \cdot c - e_{\mathrm{s}} = \hat{\rho} - \hat{e}_{\mathrm{s}} \cdot c. \tag{1.4}$$

There are several techniques for the estimation of the clock offset. The GPS estimates the receiver's clock offset together with the receiver's position coordinates $\boldsymbol{p} = [x, y, z]^{\mathrm{T}} \in \mathbb{R}^3$, treating e_{s} as an additional unknown in the solution of the positioning equations [3]. In the approach developed in the work presented in this thesis and explained in Chapter 6, the clock offsets are estimated in a preliminary phase exploiting the knowledge of the receiver position.

Finally, the TOA based ranging solution that requires the smallest costs in terms of nodes' synchronization, is the so called two-way TOA ranging. According to this approach, which is depicted in Figure 1.1c, a node A transmits a reference signal at time $t_{\mathrm{t,A}}$, which is received by the node B and retransmitted after Δt_{r}. The node A receives again the reference signal, and estimates the TOA as $\hat{t}_{\mathrm{r,A}}$. Under the assumption that the retransmission time Δt_{r} is known, the distance between the nodes A and B can be estimated with no constraints on the nodes' clocks, as:

$$\hat{d} = \left(\hat{t}_{\mathrm{r,A}} - t_{\mathrm{t,A}} - \Delta t_{\mathrm{r}}\right) \cdot \frac{c}{2}. \tag{1.5}$$

The drawbacks of this approach are the overhead due to the doubled transmission times, and the fact that all the network's nodes must have an active role, i.e., they must all transmit. Moreover, another drawback is represented by the fact that the retransmission time Δt_{r} may vary and cannot always be accurately known.

Distance estimations based on TOA measurements may be very accurate. As explained in Chapter 4, the accuracy grows with the bandwidth of the reference signal, provided that the receiver band is sufficiently large to correctly reconstruct the received signal after the analog-to-digital (AD) conversion. The drawbacks related to the TOA based ranging techniques are mostly related to the propagation environment. Indeed, the propagation time of the received signal is related to the actual distance between two nodes only if the signal considered for the TOA estimation propagates through the line of sight (LOS). This is the case of the GNSSs, where, in open sky situations, the signals transmitted from the satellites reach the mobile receiver through the direct path. Conversely, if the TOA estimation occurs in environments characterized by non line of sight (NLOS) and multipath propagation, the resulting distance estimate may be severely biased, e.g., in the case the receiver estimates a multipath component TOA as the direct path TOA. This is the reason

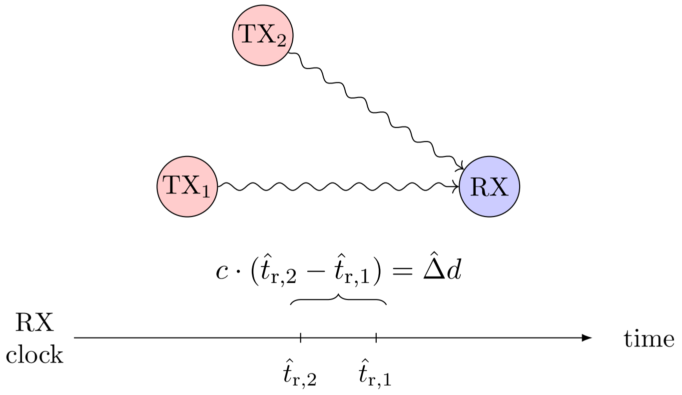

Figure 1.2 – TDOA measurements. $\hat{\Delta} d$ is the estimate of the difference of the distances between the two nodes and the receiver $\Delta d = d_2 - d_1$.

why, when TOA based ranging is performed in such propagation environments, appropriate signal processing is needed at the receiver for separating multipath and identifying the direct path. Chapter 6 of this thesis work tackles this problem in the case of real LTE signals measured in outdoor vehicular and indoor environments.

1.2.3 Time difference of arrival

A time based ranging technique that partly relaxes the constraint on the synchronization of the network's nodes is constituted by the time difference of arrival (TDOA) approach. Following this approach, only the anchor nodes must share the same clock reference, i.e., they must be synchronized. Under this assumption, suppose that the anchors transmit a reference signal at the same time. The mobile receiver that has to estimate its position can measure the various TOA according to its local clock. Then, for all the possible couples of received anchors, the difference between the times of arrival of the corresponding reference signals can be evaluated, as depicted in Figure 1.2. The TDOA measurement $\hat{t}_{\mathrm{r},2} - \hat{t}_{\mathrm{r},1}$ is related to the difference of distances between the two nodes and the receiver as:

$$\hat{\Delta} d = c \cdot (\hat{t}_{\mathrm{r},2} - \hat{t}_{\mathrm{r},1}). \tag{1.6}$$

This is not an actual distance measurement, but constitutes a differential measurement that can be employed in hyperbolic localization techniques, which are explained in Section 1.3.2. Similarly to the TOA techniques, also the TDOA approach suffer multipath and NLOS propagation.

The TDOA measurements constitutes the basis for the so called observed time difference of arrival (OTDOA) approach, which is the technique chosen for positioning by mean of the positioning reference signal (PRS) in the 3GPP LTE standard. Further details on positioning in the LTE standard are available in [23–26].

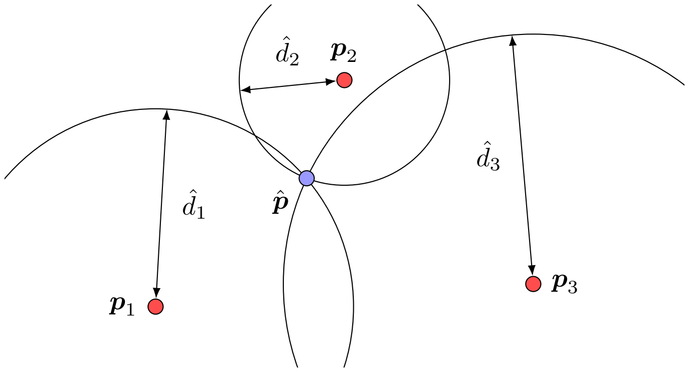

Figure 1.3 – Example of trilateration with 3 anchors having positions equal to $\boldsymbol{p}_1$, $\boldsymbol{p}_2$, $\boldsymbol{p}_3$. The estimated distances are $\hat{d}_1$, $\hat{d}_2$, $\hat{d}_3$, and the estimated position is $\hat{\boldsymbol{p}}$.

1.3 Positioning

In this section, some of the most common techniques used for positioning are briefly explained. Usually, the choice of a certain positioning technique highly depends on the type of position dependent parameters measured in the measurement phase. In the following, only the concepts of lateration and hyperbolic positioning are described, which can be used for estimating the position when ranging or differential range measurements are performed in the measurement phase, respectively. Further details about positioning techniques can be found in [1–6, 27].

1.3.1 Trilateration

The trilateration technique exploit distance estimates between the agent and multiple anchors for localizing the agent. Those distances may be estimated with a ranging technique, such as the TOA or RSS measurements described in the previous section. In a scenario with M anchors, the trilateration consists in finding the point of intersection of a set of M circles centered on the anchors' positions $\boldsymbol{p}_j \in \mathbb{R}^D$, $j = 1, \ldots, M$, and having a radius equal to the measured distances $\hat{d}_j$, $j = 1, \ldots, M$, where $D \in \{2, 3\}$ denotes the number of spatial dimensions to consider. Figure 1.3 depicts a simple case of 2D trilateration. The system of equations corresponding to the trilateration problem is:

$$\begin{cases} \|\boldsymbol{p} - \boldsymbol{p}_1\| = \hat{d}_1 \\ \|\boldsymbol{p} - \boldsymbol{p}_2\| = \hat{d}_2 \\ \quad \cdots \\ \|\boldsymbol{p} - \boldsymbol{p}_M\| = \hat{d}_M \end{cases}, \tag{1.7}$$

which is a non linear system of equations to be solved in respect to the unknown position of the receiver $\boldsymbol{p} \in \mathbb{R}^D$. Since (1.7) is a system in $D \in \{2, 3\}$ unknown, at least D equations are required for obtaining a finite number of solutions, which determines the constraint $M \geq D$. This means that in a 2D scenario, the ranging measurements from at least 2 anchors are needed, while in a 3D scenario, the ranging measurements from at least 3 anchors are needed. Moreover, for obtaining a unique solution, at least 3 and 4 anchors are needed in the 2D and 3D case, respectively.

A rigorous solution of (1.7) exists and is unique only if the distance estimates $\hat{d}_i$ are all correct. However, in a real scenario with non-exact distance estimates, the system of (1.7) does not have an exact solution. Several approaches are available for finding solutions of (1.7) that minimize appropriate metrics. The most popular methods are the least squares (LS) algorithms [1], and Bayesian methods such as the extended Kalman filter (EKF) [28] or the particle filters [29,30]. As an example, in Chapter 6 of the thesis work, an EKF is used for solving the positioning problem exploiting TOA based range estimations.

A well-known class of positioning systems that make use of trilateration techniques for the positioning phase is the class of the GNSSs. As mentioned in Section 1.2.2, GNSSs exploit TOA based ranging techniques, accepting a mis-synchronization of the receiver clock. Since all the satellites are equipped with very precise synchronized atomic clocks, there is only one clock offset e_s to estimate, i.e., the offset of the receiver clock in respect to the satellites' common clock. This receiver clock offset is estimated in the positioning phase, by adding a fourth unknown to the system of (1.7). Indeed, if the measured pseudoranges can be expressed as:

$$\hat{\rho}_j = d_j + e_\mathrm{s} \cdot c \tag{1.8}$$

then the following system of equations can be defined [3]:

$$\begin{cases} \|\boldsymbol{p} - \boldsymbol{p}_1\| + c \cdot e_\mathrm{s} = \hat{\rho}_1 \\ \|\boldsymbol{p} - \boldsymbol{p}_2\| + c \cdot e_\mathrm{s} = \hat{\rho}_2 \\ \quad \cdots \\ \|\boldsymbol{p} - \boldsymbol{p}_M\| + c \cdot e_\mathrm{s} = \hat{\rho}_M \end{cases}, \tag{1.9}$$

which can be solved with the techniques mentioned above. As one can note from (1.9), the unknown are $D+1$, i.e., the receiver position $\boldsymbol{p} \in \mathbb{R}^D$ and its clock offset e_s. Hence, pseudorange measurements from at least $M \geq D+1$ anchors must be available in this case. That is the reason why, for obtaining a GPS position fix, at least four satellites are required to be visible. In this case, four satellites permit to isolate two possible solutions, and the one closer to the Earth surface is usually chosen.

1.3.2 Hyperbolic positioning

Hyperbolic positioning techniques are used when differential measurements are available, such as in the case of TDOA measurements. As Figure 1.4 depicts, every measurement computed by the agent in respect to a couple of anchors permit to evaluate a difference of distances $\hat{\Delta} d_{i,j}$, $i \neq j$, which corresponds to a branch of an

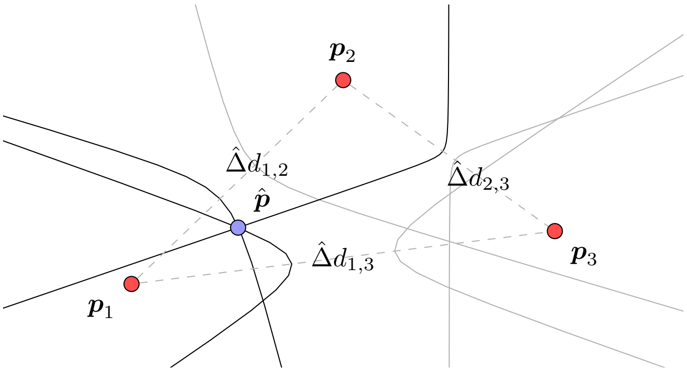

Figure 1.4 – Example of hyperbolic positioning with 3 anchors having positions equal to $\boldsymbol{p}_1$, $\boldsymbol{p}_2$, $\boldsymbol{p}_3$. The estimated difference of distances are $\hat{\Delta} d_{1,2}$, $\hat{\Delta} d_{2,3}$, $\hat{\Delta} d_{1,3}$, and the estimated position is $\hat{\boldsymbol{p}}$.

hyperbola with the two anchors in the focal points. This is because the hyperbola is the locus of points where the absolute value of the difference of the distances to two points called foci is constant, where the sign of the difference of distances permits to identify the two branches. The intersection of all the hyperbolas corresponds to the position of the node to be located. Mathematically, if M anchors are available, this problem corresponds to the non linear system of $\frac{1}{2}M(M-1)$ equations in the unknown $\boldsymbol{p} \in \mathbb{R}^D$ given by:

$$\begin{cases} \|\boldsymbol{p}-\boldsymbol{p}_1\| - \|\boldsymbol{p}-\boldsymbol{p}_2\| = \hat{\Delta} d_{1,2} \\ \|\boldsymbol{p}-\boldsymbol{p}_1\| - \|\boldsymbol{p}-\boldsymbol{p}_3\| = \hat{\Delta} d_{1,3} \\ \quad \cdots \\ \|\boldsymbol{p}-\boldsymbol{p}_{M-1}\| - \|\boldsymbol{p}-\boldsymbol{p}_M\| = \hat{\Delta} d_{M-1,M} \end{cases}, \tag{1.10}$$

which can be solved with one of the methods mentioned in Section 1.3.1. In this case, measurements from a minimum of $M \geq 3$ anchors are required both in the cases of 2D and 3D positioning for obtaining a finite number of solutions.

Chapter 2

The 3GPP Long Term Evolution

The Third Generation Partnership Project (3GPP) Long Term Evolution (LTE) is the standard for the fourth generation cellular mobile communication systems. In respect to the previous generations' standards for the broadband wireless access, it offers increased capacity, data rates, and user mobility, thanks to various improvements in the core network and to a different radio interface, which also adopts beamforming and multiple input multiple output techniques for user separation and increased transmission throughput and reliability. In this chapter, the LTE downlink physical layer is briefly described, with particular attention to the orthogonal frequency division multiplexing transmission technique, and to the LTE reference signals exploited throughout the rest of the thesis work. Moreover, the final section explains how LTE manages its frequency reuse factor of one, and how this enables the reception of reference signals from multiple cells controlled by the same base station.

2.1 Orthogonal frequency division multiplexing

The Long Term Evolution (LTE) downlink physical layer is based on the orthogonal frequency division multiplexing (OFDM) modulation principle. The OFDM modulation is a technique widely used in wireless and wired communications since it allows high bandwidth transmissions in dispersive channels with a reduced implementation and equalization complexity. The asymmetric digital subscriber line (ADSL) system is an example of wired OFDM based standard. However, OFDM gained the most of its popularity in the field of the wireless communications [31], and is exploited in various communication standards such as the IEEE 802.11 a/g/n/ac for the WLANs, the terrestrial digital video broadcasting (DVB-T), the digital audio broadcasting (DAB), and the aforementioned LTE.

The basic idea behind OFDM is to transmit several orthogonal parallel streams in the frequency domain (FD), where each stream's symbol rate is sufficiently low to avoid distortion due to the wireless multipath channel. The data rate is maintained high thanks to the FD parallel transmission, and the distortion is avoided due to the low symbol rate of each stream. In other words, the overall signal transmitted is a wideband signal, but the symbols carrying information are transmitted with parallel narrowband transmissions. Hence, OFDM is capable of treating a frequency selective channel as a set of parallel adjacent narrowband flat channels. This peculiarity of the OFDM modulation permits a straightforward FD symbol-wise equalization of the transmitted data. Finally, a key aspect of the OFDM principle is its implementation: the typical complexity of multi-carrier systems, i.e., the need of generating several carriers, is avoided thanks to an handy discrete Fourier transform (DFT) based base-band generation of the overall signal to be transmitted. Further and in-depth informations on OFDM can be found in [19, 20, 31, 32] and references therein.

In this section, the basic concepts for understanding an OFDM physical layer are explained. Then, a brief motivation for understanding why OFDM signals and super-resolution algorithms (SRAs) for time of arrival estimation can be successfully combined is given.

2.1.1 OFDM transmission

An OFDM signal can be specified by defining the content of its sub-carriers, i.e., by defining the modulation symbols to be transmitted on each sub-carrier. Indeed, consider an OFDM system with a total number N_{dft} of available sub-carriers. The sub-carrier content of the transmitted reference signal is specified by the length N_{dft} sequence:

$$\boldsymbol{S} = \Big[S[-\tfrac{N_{\mathrm{dft}}}{2}],\ \dots,\ S[-1],\ S[0],\ S[1],\ \dots,\ S[-\tfrac{N_{\mathrm{dft}}}{2}-1]\Big]^{\mathrm{T}} \in \mathbb{C}^{N_{\mathrm{dft}}}. \qquad (2.1)$$

Each of the symbols $S[k]$ is taken from a PSK/QAM constellation, and usually the symbol corresponding to the center frequency is left empty, i.e., $S[0] = 0$. Usually, not all the available sub-carriers are filled with modulations symbols, since a certain number of peripherals sub-carriers are left empty, i.e.:

$$S[k] = \begin{cases} \text{some modulated symbol} & \text{if } k \in \big[-\frac{N_{\mathrm{sc}}}{2}, \frac{N_{\mathrm{sc}}}{2}\big] \smallsetminus \{0\} \\ 0 & \text{otherwise} \end{cases}, \qquad (2.2)$$

where $N_{\mathrm{sc}} \leq N_{\mathrm{dft}}$ is the number of actual occupied sub-carriers. Then, the OFDM signal can be defined as:

$$s(t) = \sum_{k=-N_{\mathrm{sc}}/2}^{N_{\mathrm{sc}}/2} g(t) \cdot S[k] \cdot e^{j2\pi k \Delta f t}, \quad t \in [0, T_s[, \qquad (2.3)$$

where T_s is the OFDM symbol duration, Δf is the separation between adjacent sub-carriers, and $g(t)$ is the shaping impulse, which ideally should match a rectangular signal of duration equal to T_s. A frequency separation of $\Delta f = 1/T_s$ together with a perfectly rectangular shaping impulse ensure orthogonality between the sub-carriers [31]. If the signal of (2.3) is sampled with a sampling period of T_s/N_{dft}, then

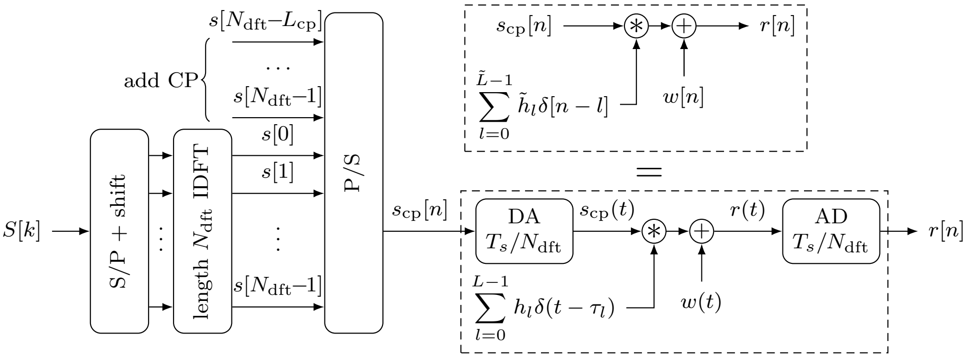

Figure 2.1 – Block scheme of an OFDM transmitter working on a multipath fading channel. The equivalent discrete time system is also shown, where the continuous convolution with the channel $h(t)$ is replaced by the discrete convolution with its discrete time version $h[n]$. The base band representation of the system is depicted.

the discrete time signal $\boldsymbol{s} = [s[0], \dots, s[N_{\rm dft}-1]]^{\rm T} \in \mathbb{C}^{N_{\rm dft}}$ can be obtained, as:

$$\begin{aligned} s[n] = s(t)\big|_{t=n\frac{T_s}{N_{\rm dft}}} &= \sum_{k=-N_{\rm sc}/2}^{N_{\rm sc}/2} S[k] \cdot e^{j2\pi k \frac{1}{T_s}\frac{nT_s}{N_{\rm dft}}} = \sum_{k=-N_{\rm sc}/2}^{N_{\rm sc}/2} S[k] \cdot e^{j\frac{2\pi}{N_{\rm dft}}kn} \\ &= \sum_{k=-N_{\rm dft}/2}^{N_{\rm dft}/2-1} S[k] \cdot e^{j\frac{2\pi}{N_{\rm dft}}kn} = \sum_{k=0}^{N_{\rm dft}-1} \tilde{S}[k] \cdot e^{j\frac{2\pi}{N_{\rm dft}}kn} \\ &= N_{\rm dft} \cdot \mathrm{IDFT}\left\{\tilde{S}[k]\right\}, \quad n = 0, \dots, N_{\rm dft}-1, \end{aligned} \tag{2.4}$$

where $\tilde{S}[k]$ is the sequence obtained by applying the FFT-shift operation on the sequence $S[k]$, i.e.:

$$\tilde{\boldsymbol{S}} = \left[0, S[1] \dots, S[N_{\rm sc}/2], \mathbf{0}^{\rm T}_{N_{\rm dft}-N_{\rm sc}-1}, S[-N_{\rm sc}/2], \dots, S[-1]\right]^{\rm T} \in \mathbb{C}^{N_{\rm dft}}. \tag{2.5}$$

As one can see, $\tilde{S}[k]$ is the same sequence as $S[k]$, with the left and right halves swapped. The procedure above demonstrates that the OFDM signal can be obtained through a digital-to-analog (DA) conversion of the discrete time signal of (2.4), which can be generated using a simple inverse discrete Fourier transform (IDFT) operation. This procedure is depicted in the left part of Figure 2.1, where the base band OFDM transmission scheme is represented.

Before DA conversion and transmission, the OFDM scheme requires a length $L_{\rm cp}$ cyclic prefix (CP) to be inserted before the samples of (2.4), which consists of the tail samples of $s[n]$. Upon defining $N_{\rm tot}^{\rm cp} = N_{\rm dft} + L_{\rm cp}$, the discrete time sequence with the CP that feeds the DA converter before transmission can be written as:

$$s_{\rm cp}[n] = \begin{cases} s[N_{\rm dft} - L_{\rm cp} + n] & n = 0, \dots, L_{\rm cp}-1 \\ s[n - L_{\rm cp}] & n = L_{\rm cp}, \dots, N_{\rm tot}^{\rm cp} \end{cases}, \tag{2.6}$$

which becomes $s_{\mathrm{cp}}(t)$ after DA conversion. The role of the CP is twofold. Firstly, as will be explained in the next section, the CP enables a simple FD equalization, thanks to the fact that the CP transforms the linear convolution between the OFDM symbol and the channel in a circular convolution. Secondly, the time interval occupied by the CP acts as a guard interval between subsequent OFDM symbols that permits to avoid inter-symbol interference caused by the dispersivity of the channel.

As demonstrated, the base band version of the multi-carrier signal can be obtained by simple signal processing techniques. As mentioned in the introduction of the chapter, this is one of the reasons why OFDM is particularly attractive. After the DA conversion, the signal $s_{\mathrm{cp}}(t)$ is ready for being up-converted to the carrier frequency f_{C} and transmitted in the wireless channel as a single carrier transmission.

2.1.2 OFDM demodulation

As represented in the transmission scheme of Figure 2.1, the received signal is given by the convolution between the transmitted signal $s_{\mathrm{cp}}(t)$ and the channel impulse response (CIR) $h(t)$ plus the noise $w(t)$. If the signal is transmitted in an L paths wireless multipath channel having CIR:

$$h(t) = \sum_{l=0}^{L-1} h_l \delta(t - \tau_l), \tag{2.7}$$

then, upon the assumption of constant channel during the duration of $s_{\mathrm{cp}}(t)$, the received signal is:

$$r(t) = h(t) * s_{\mathrm{cp}}(t) + w(t) = \sum_{l=0}^{L-1} h_l s_{\mathrm{cp}}(t - \tau_l) + w(t). \tag{2.8}$$

The assumption of constant channel during the duration of the OFDM symbol is crucial for the OFDM system to work properly without any performance loss. In the case of the LTE standard with a normal CP configuration (the most common configuration, used throughout this paper and found during the measurements used), the duration of an OFDM symbol with the longest possible CP is $T_s + T_{\mathrm{cp},0} \simeq 66.6\,\mu\mathrm{s} + 5.21\,\mu\mathrm{s} = 71.81\,\mu\mathrm{s}$. Typically, in wireless communication theory, the amplitude of a fading channel is considered correlated in the interval Δt if the product $f_{\mathrm{D}}\Delta t$ is smaller than 0.1, where $f_{\mathrm{D}} = f_{\mathrm{C}} \cdot v/c$ is the Doppler shift and v is the relative speed between transmitter and receiver [20]. At a carrier frequency of $f_{\mathrm{C}} = 2\,\mathrm{GHz}$, this means that:

$$f_{\mathrm{D}}\Delta t \leq 0.1 \;\Leftrightarrow\; v \leq \frac{0.1c}{f_{\mathrm{C}}\Delta t} \simeq 208\,\frac{\mathrm{m}}{\mathrm{s}}, \tag{2.9}$$

which is a speed considerably higher than the maximum speed supported by the LTE standard (which is 500 km/h).

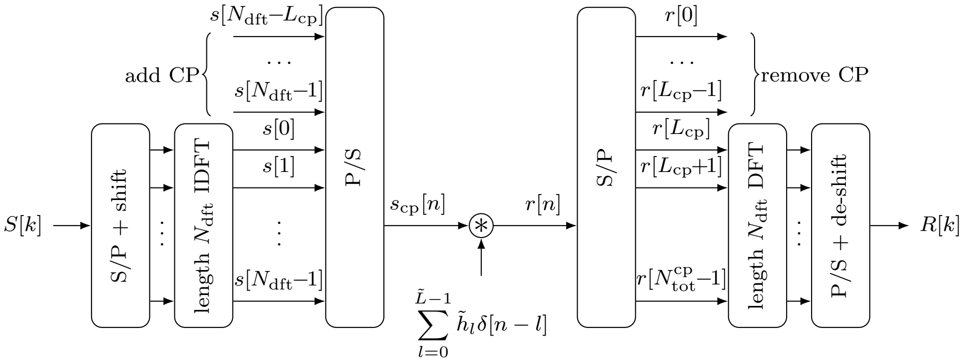

Figure 2.2 – Block scheme of an OFDM transceiver working on the discrete time dispersive channel of (2.11). The additive noise which is present at the receiver is omitted in this scheme.

By sampling $r(t)$ with an analog-to-digital (AD) converter employing the same sampling interval used at the transmitter side, i.e., T_s/N_{dft}, one obtains the discrete time signal $r[n]$, which is given by:

$$r[n] = h[n] * s_{\mathrm{cp}}[n] + w[n] = \sum_{l=0}^{\tilde{L}-1} \tilde{h}_l s_{\mathrm{cp}}[n-l] + w[n], \quad n = 0, \ldots, N_{\mathrm{tot}}^{\mathrm{cp}} - 1, \tag{2.10}$$

where $h[n]$ is the discrete time equivalent of $h(t)$, given by:

$$h[n] = \sum_{l=0}^{\tilde{L}-1} \tilde{h}_l \delta[n-l]. \tag{2.11}$$

The equivalence between the discrete time channel $h[n]$ and the continuous time channel $h(t)$ is also depicted in the right part of Figure 2.1.

In [19] and references therein, it is demonstrated that the linear convolution between $s_{\mathrm{cp}}[n]$ and $h[n]$ is equal to the circular convolution between $s[n]$ and $h[n]$, provided that the first L_{cp} samples of $r[n]$ are discarded. As mentioned before, this is one of the reasons why the CP is used. Hence, by discarding the first L_{cp} samples of (2.10), one obtains:

$$r[n] = h[n] \circledast_{N_{\mathrm{dft}}} s[n] + z[n], \tag{2.12}$$

where $\circledast_{N_{\mathrm{dft}}}$ is the length N_{dft} circular convolution operator. Finally, the reception procedure depicted in Figure 2.2 is performed, which basically consists of the inverse of the tasks performed at the transmitter side. By applying to $r[n]$ the DFT operator and using the convolution property of the DFT (the DFT of a circular convolution between two sequences is equal to the element-wise product of the DFTs of the two sequences), one can retrieve the content of each sub-carrier. More particularly:

$$\begin{aligned} R[k] &= \mathrm{DFT}\{r[n]\} = \mathrm{DFT}\{h[n] \circledast_{N_{\mathrm{dft}}} s[n]\} + \mathrm{DFT}\{z[n]\} \\ &= \mathrm{DFT}\{h[n]\} \cdot \mathrm{DFT}\{s[n]\} + \text{noise} \\ &= N_{\mathrm{dft}} H[k] \tilde{S}[k] + \text{noise}, \quad k = 0, \ldots, N_{\mathrm{dft}} - 1. \end{aligned} \tag{2.13}$$

In (2.13), the discrete time sequence $H[k]$ corresponds to the length N_{dft} DFT of $h[n]$, which ultimately is a sampled version of the band limited channel frequency response (CFR). Hence, using the received frequency domain samples $R[k]$ and exploiting the knowledge of the sub-carrier content $S[k]$, one can recover the samples $H[k]$ of the CFR. This demonstrates that the transmission of an OFDM reference signal, that is, a signal for which the sub-carrier content $S[k]$ is *a priori* known at the receiver, offers a simple means for sampling the channel in the frequency domain. This, in conjunction with the SRAs, has been exploited in the presented work on time of arrival (TOA) estimation.

As will be shown in Section 3.1, the input of a SRA used for multipath TOA estimation is a sampled version of the CFR. There are several ways for sampling a CFR $H(f)$. Suppose that one wants to estimate the CFR value at $f = f_k$ for some values of k, i.e. the values of $H(f_k)$ have to be estimated. This can be achieved by performing a frequency sweeping and transmitting subsequently a sounding signal on each of the values of f_k, or by using multiple transmitters each having a carrier frequency equal to f_k. However, all these methods require dedicated hardware and are not suitable to be realized in low cost consumer devices. As demonstrated above, an OFDM physical layer provides a simple means for realizing a sampling of a channel response in the FD, without the need of additional dedicated hardware.

An example of channel estimation may be the least squares channel estimator [33], which is the simplest estimator possible, and estimates the channel samples as:

$$\hat{H}[k] = \frac{R[k]}{\tilde{S}[k]} = N_{\mathrm{dft}} \cdot H[k] + \text{noise}. \tag{2.14}$$

There are several more accurate OFDM channel estimators. The interested reader may refer to [19, 31, 33] and references therein for further details.

2.2 The LTE downlink physical layer

In the LTE standard, a base station (BS) is referred to as an eNodeB, and a sector pertaining to a certain eNodeB is identified by the cell ID $N_{\mathrm{ID}}^{\mathrm{cell}}$, that is referred to as a physical cell identity (PCI). A mobile receiver is referred to as user equipment (UE), and an eNodeB provides resources to each UE through the use of an orthogonal frequency division multiple access (OFDMA) scheme. OFDMA exploits the OFDM principle to efficiently multiplex users in FD by assigning to each of them a set of the sub-carriers that constitutes the OFDM symbol.

2.2.1 Time-frequency structure

The LTE downlink physical layer has two main possible configurations, the type 1 downlink physical layer, designed for frequency domain duplexing (FDD), and the type 2 downlink physical layer, designed for time domain duplexing (TDD). The LTE type 1 downlink physical layer is the most common, and is the one that will

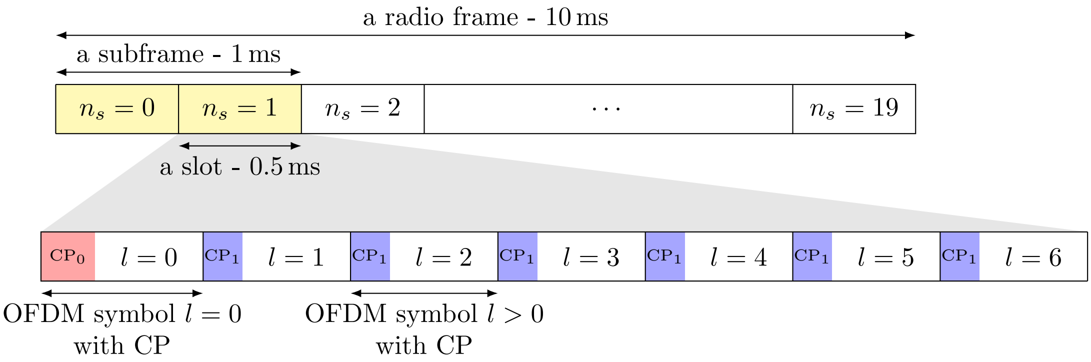

Figure 2.3 – Type 1 LTE downlink physical layer time structure for the normal CP configuration. As one can see, the duration of the CP of the OFDM symbol $l = 0$ is larger than the other symbols' CPs. Each OFDM symbol carries N_{sc} sub-carriers in the frequency domain.

B	1.4MHz	3MHz	5MHz	10MHz	15MHz	20MHz
$N_{\text{RB}}^{\text{DL}}$	6	15	25	50	75	100
N_{sc}	72	180	300	600	900	1200
N_{tot}	12	30	50	100	150	200

Table 2.1 – List of possible downlink bandwidth configurations.

be considered throughout the presented work, also because is the only configuration observed in the measurements.

The LTE type 1 downlink physical layer is organized in 10 ms long radio frames. Each radio frame corresponds to 10 sub-frames, each made of 2 slots (20 slots per frame, 0.5 ms each). As Figure 2.3 depicts, each slot is composed of $N_{\text{symb}}^{\text{DL}}$ OFDM symbols in the time domain. Each OFDM symbol is made by the actual symbol (having a duration of $T_s = 1/\Delta f$) preceded by its own CP, which has a slight longer duration in the first OFDM symbol of the slot.

There are two LTE CP configurations, the normal CP configuration, and the extended CP configuration. The latter is intended to be used in large sub-urban and rural cells, where a large delay spread has to be supported. Conversely, the former is the most common configuration, which is the one that has been considered throughout the presented work. In the normal CP configuration, $N_{\text{symb}}^{\text{DL}} = 7$, and the spacing between the OFDM sub-carrier is set to $\Delta f = 15\,\text{kHz}$. Consequently, each OFDM symbol has a duration of $T_s = 1/\Delta f \simeq 66.7\,\mu\text{s}$, and is preceded by its CP. The CP of the first OFDM symbol of a slot has a duration of $160 \cdot T_{\text{s},0}$ while the CPs of the remaining symbols have a duration of $144 \cdot T_{\text{s},0}$, being $T_{\text{s},0} = T_s/2048 \simeq 32.55\text{ns}$ the basic time unit of LTE. In the frequency domain, each OFDM symbol corresponds to $N_{\text{sc}} = N_{\text{sc}}^{\text{RB}} N_{\text{RB}}^{\text{DL}}$ sub-carriers, spaced of $\Delta f = 15\text{kHz}$ when the normal cyclic prefix configuration is adopted, for which $N_{\text{sc}}^{\text{RB}} = 12$. The number of total sub-carriers used in each OFDM symbol (and ultimately the LTE signal bandwidth B) is determined

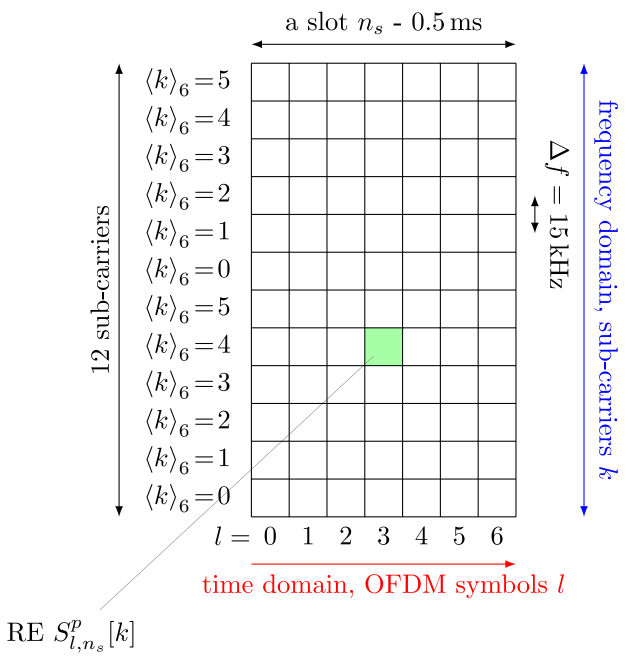

Figure 2.4 – Representation of a resource block (RB) with the time-frequency grid concept for the antenna port p. The generic resource element (RE) $S^p_{l,n_s}[k]$ is also indicated.

by the parameter $N_{\mathrm{RB}}^{\mathrm{DL}}$. There are 6 possible configurations, which are summarized in Table 2.1.

The definition of the LTE downlink physical layer in both the time and frequency domains leads to the time-frequency grid concept depicted in Figure 2.4. This grid is used to define the mapping of the transmit resources to particular OFDM symbols and sub-carriers within the OFDM symbol. The basic resource unit of LTE, corresponding to the k^{th} sub-carrier of a certain OFDM symbol in a slot, is referred to as resource element (RE). REs are grouped in resource blocks (RBs), each corresponding to $N_{\mathrm{sc}}^{\mathrm{RB}}$ adjacent sub-carriers in the FD, for the duration of one slot. Resources are allocated to users within a cell in terms of RBs. The number of RBs carried by the LTE signal in the frequency domain depends on the particular channel bandwidth configuration, and ultimately on the parameter $N_{\mathrm{RB}}^{\mathrm{DL}}$. Only one RB is depicted in the grid of Figure 2.4. The complete representation of the LTE signal across all the LTE channel bandwidth can be obtained repeating the grid $N_{\mathrm{RB}}^{\mathrm{DL}}$ times vertically.

LTE addresses the spatial domain with the concept of antenna port [26]. Each antenna port is identified by the index p, and corresponds to a single physical antenna or to a set of antennas that are treated from the communication point of view as a single physical antenna (this is the case of antenna arrays used for beamforming). For extending the above time-frequency grid concept to the spatial domain, a different grid is employed for every antenna port.

Finally, an LTE signal transmitted from a particular antenna port p is defined by the collection of the REs $S^p_{l,n_s}[k]$ defined on the signal's time-frequency grid. Every element $S^p_{l,n_s}[k]$ corresponds to the content of a particular sub-carrier k in the OFDM symbol l of the slot n_s. Then, the actual base band analog signal is obtained with a classical OFDM modulation with empty DC sub-carrier, as [26]:

$$\begin{aligned} s^p_{l,n_s}(t) = &\sum_{k=-N_{\mathrm{sc}}/2}^{k=-1} S^p_{l,n_s}[k+N_{\mathrm{sc}}/2]\, e^{j2\pi k \Delta f t} + \\ + &\sum_{k=0}^{k=N_{\mathrm{sc}}/2-1} S^p_{l,n_s}[k+N_{\mathrm{sc}}/2]\, e^{j2\pi (k+1) \Delta f t},\ t \in]-T_{\mathrm{cp},l}, T_{\mathrm{s}}]. \end{aligned} \tag{2.15}$$

As one can note from the above definition, the sequence $S^p_{l,n_s}[k]$, $k = 0, \ldots, N_{\mathrm{sc}} - 1$, defined for the LTE standard does not take into account the DC sub-carrier, which is mandatory to be left empty. Hence, for generating the signal of (2.15) with the low complexity DFT based implementation described in Section 2.1, the sequence $S^p_{l,n_s}[k]$ must be modified in order to contain a zero element in the DC sub-carrier position. This, after a zero padding to the length N_{dft} of the IDFT operator used at the transmitter and an fast Fourier transform (FFT)-shift operation, produces the sequence $\tilde{S}^p_{l,n_s}[k]$ given by:

$$\begin{aligned} \tilde{\boldsymbol{S}}^p_{l,n_s} = \Big[&0, S^p_{l,n_s}[N_{\mathrm{sc}}/2], \ldots, S^p_{l,n_s}[N_{\mathrm{sc}}-1], \mathbf{0}^{\mathrm{T}}_{N_{\mathrm{dft}}-N_{\mathrm{sc}}-1}, \\ &S^p_{l,n_s}[0], \ldots, S^p_{l,n_s}[N_{\mathrm{sc}}/2-1]\Big]^{\mathrm{T}} \in \mathbb{C}^{N_{\mathrm{dft}}}, \end{aligned} \tag{2.16}$$

where N_{dft} is the length of the DFT operator, which is an implementation design parameter. Afterwards, the discrete time version of the signal in (2.15) can be evaluated as $s^p_{l,n_s}[n] = N_{\mathrm{dft}} \cdot \mathrm{IDFT}\{\tilde{S}^p_{l,n_s}[k]\}$.

For presentation simplicity, the sequence manipulation showed in (2.16) is not repeated for every LTE sequence used in the presented work. The notation $s^p_{l,n_s}[n] = \mathrm{IDFT}\{S^p_{l,n_s}[k]\}$ (note the $S^p_{l,n_s}[k]$ with no tilde) and its inverse $S^p_{l,n_s}[k] = \mathrm{DFT}\{s^p_{l,n_s}[n]\}$ will imply a correct sequence manipulation, that, together with the DFT/IDFT, realizes exactly the empty DC modulation of (2.15).

2.2.2 Exploited reference signals

LTE offers two downlink reference signals that are indicated for range measurements, i.e., the positioning reference signal (PRS) and the cell specific reference signal (CRS). The PRS is specifically designed for the acquisition of multiple simultaneous range measurements and is transmitted in dedicated time intervals [26]. However, operators generally tend to avoid its transmission in order to save bandwidth for user data. On the other hand, although the CRS is primarily designed for channel estimation and coherent data demodulation, it may be opportunistically exploited for range measurements, particularly because it is always transmitted. Both

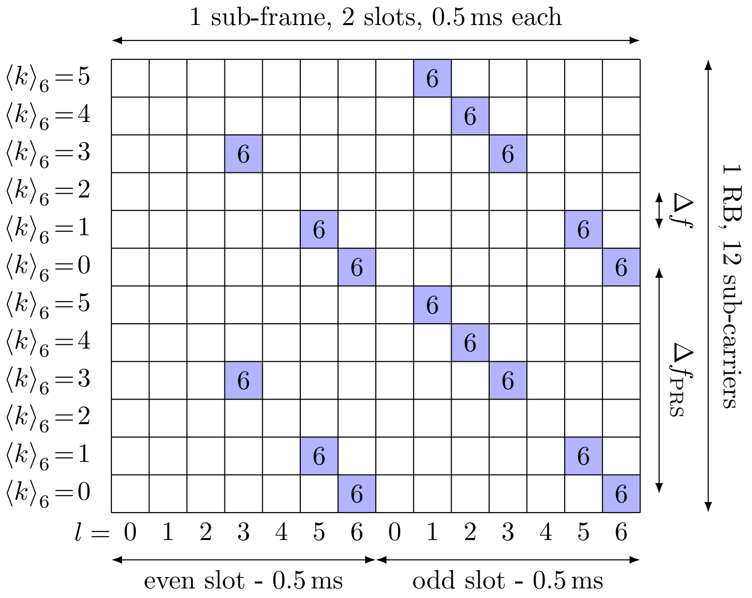

Figure 2.5 – PRS stairway shaped mapping to resource elements. Since the PRS is transmitted on low interference sub-frames, there is no data transmission from any other antenna port in any other empty RE. The index $p = 6$ in each colored square identifies the antenna port from which the symbol is transmitted.

the PRS and the CRS are cell-specific: this means that the definition of the signal sequence and the mapping of this sequence to the REs depend on the cell ID $N_{\mathrm{ID}}^{\mathrm{cell}}$.

The PRS is defined as a QPSK modulated length-31 Gold sequence. The PRS is transmitted from antenna port $p = 6$ and mapped to the REs with the stairway shaped pattern depicted in Figure 2.5. Since the PRS pilot tones occupy one sub-carrier every six through all the available bandwidth (with a spacing of $\Delta f_{\mathrm{PRS}} = 6\Delta f = 90\,\mathrm{kHz}$), the total number of transmitted pilot tones is $N_{\mathrm{tot}} = N_{\mathrm{sc}}/6$ per OFDM symbol. The PRS is configured to be transmitted on specific positioning sub-frames, which are designed as low interference sub-frames, that is, without transmission on data channels [23].

Similarly to the PRS, the CRS is defined as a QPSK modulated length-31 Gold sequence. Multiple CRSs are transmitted from the BS for a particular sector with a mapping to REs that depends on the antenna port configuration. When a configuration with 2 antenna ports is adopted, a CRS transmission occurs twice per slot, on symbols $l = 0$ and $l = 4$: each time, a different CRS is transmitted from each antenna port on the same OFDM symbol in non-overlapping sub-carriers, as Figure 2.6 depicts. Again, since the CRS pilot tones occupies one sub-carrier every six through all the available bandwidth (with a spacing of $\Delta f_{\mathrm{CRS}} = 6\Delta f = 90\,\mathrm{kHz}$), the total number of transmitted pilot tones is $N_{\mathrm{tot}} = N_{\mathrm{sc}}/6$ per antenna port per OFDM symbol. Since the CRS is intended as a reference signal for channel estimation and data demodulation, it is always transmitted. The user data allocated to a particular set of RBs is distributed on all the REs not reserved to the CRS (or to other control

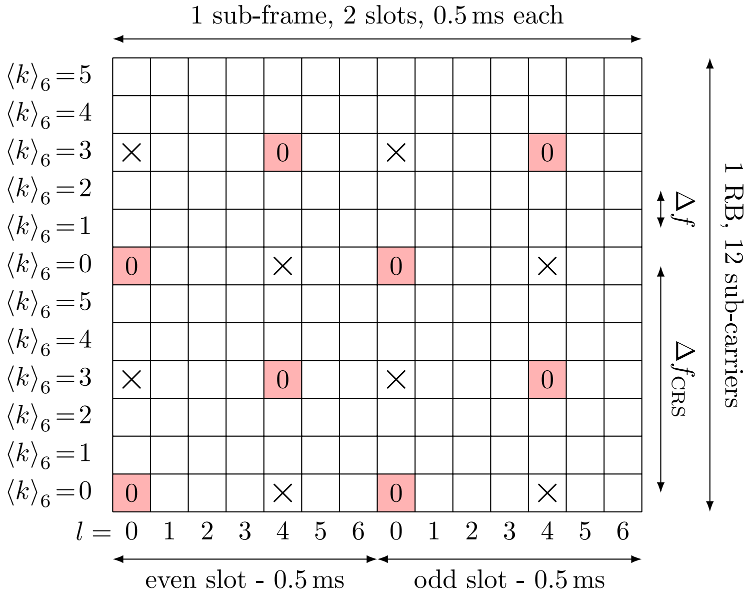

(a) Antenna port $p = 0$.

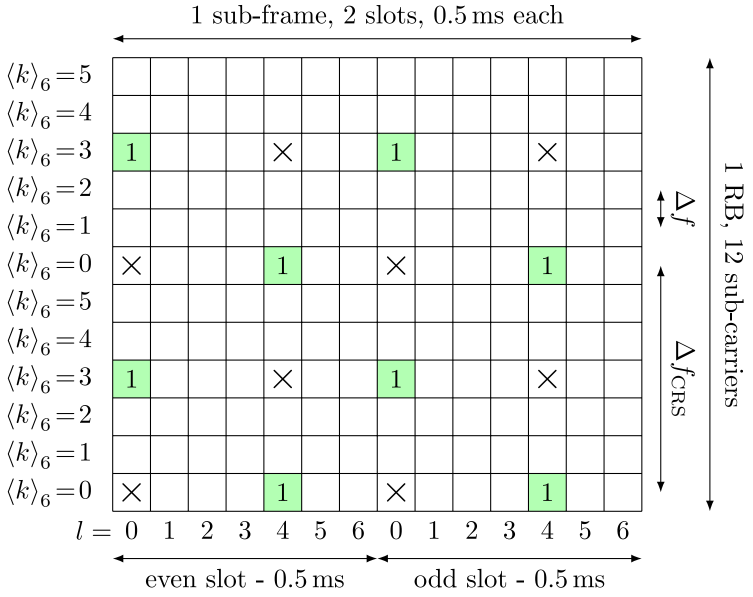

(b) Antenna port $p = 1$.

Figure 2.6 – CRS diamond shaped mapping to resource elements for a 2 antenna port configuration (namely, CRS transmission occurs from $p = \{0, 1\}$). The empty REs may be filled by user data if the corresponding RB is allocated to data transmission. The index p in each colored square identifies the antenna port from which the symbol is transmitted. The × in a RE means that nothing can be transmitted on that RE from the considered antenna port.

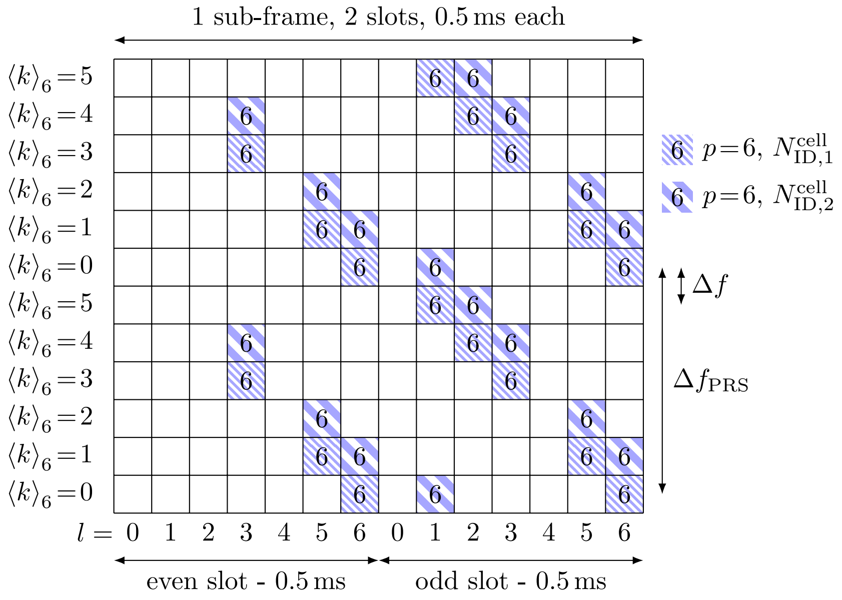

(a) A transmission of up to six orthogonal PRSs from different cells is possible, provided that the corresponding cell IDs have different values of $\langle N_{\mathrm{ID}}^{\mathrm{cell}}\rangle_6$.

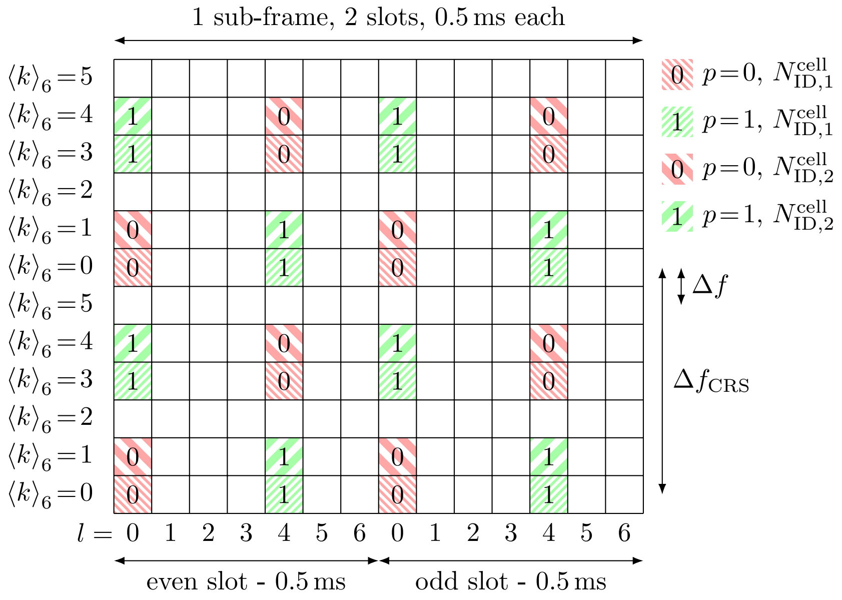

(b) For a 2 antenna port configuration a transmission of up to three orthogonal CRSs from different cells is possible. In the represented case, the FD shift corresponding to the two cell IDs are $\kappa_l^{i_1,p}$ and $\kappa_l^{i_2,p}$, with $|\kappa_l^{i_1,p}-\kappa_l^{i_2,p}|=1$.

Figure 2.7 – Mapping to resource elements of the used reference signals for two cell IDs $N_{\mathrm{ID},1}^{\mathrm{cell}}$ and $N_{\mathrm{ID},2}^{\mathrm{cell}}$. The index p in each colored square identifies the antenna port from which the symbol is transmitted.

or synchronisation signals). This means that in OFDM symbols $l = 0$ and $l = 4$, the empty REs between the CRS pilots may be filled with user data.

The mapping to REs of PRSs transmitted from different cells differs by a FD shift of $\langle N_{\mathrm{ID}}^{\mathrm{cell}} \rangle_6$, as represented in Figure 2.7a. This enables the transmission of up to six orthogonal PRS from sectors having cell IDs $\{N_{\mathrm{ID}}^{\mathrm{cell}}, N_{\mathrm{ID}}^{\mathrm{cell}} + 1, \ldots, N_{\mathrm{ID}}^{\mathrm{cell}} + 5\}$, and ultimately permits the simultaneous reception of reference signals from different sectors.

Similarly, the CRS transmitted from different BS sectors is mapped to REs using a FD shift which depends on the cell ID $N_{\mathrm{ID}}^{\mathrm{cell}}$ and is denoted with $\kappa_l^{i,p}$ (the super script i identifies the particular cell). Assuming that a 2 antenna port configuration is adopted, and hence that two different CRS are transmitted from the two antenna ports in the same instant, the transmission of up to three orthogonal CRS from sectors having cell IDs $\{N_{\mathrm{ID}}^{\mathrm{cell}}, N_{\mathrm{ID}}^{\mathrm{cell}} + 1, N_{\mathrm{ID}}^{\mathrm{cell}} + 2\}$ is possible, as Figure 2.7b shows.

2.2.3 Frequency reuse factor

LTE is designed to operate with a frequency reuse factor of one. Indeed, the measurement campaign described in Section 6.3 showed that operators tends to deploy LTE base stations with sectors all using the same carrier frequency. By transmitting on the same channel, neighbour cells suffer of strong inter-cell interference, which has to be faced adopting inter-cell interference coordination (ICIC) strategies.

Consider a simplified system with two adjacent cells using the same channel, each controlled by a different eNodeB, and two UEs, each connected to a different cell. Suppose that the two users are provided by the eNodeB with resources on the same slots and sub-carriers. Then, the total system downlink achievable rate is given by:

$$R_{\mathrm{tot}} = B\left[\log_2\left(1+\frac{P_{s,1}|H_{1,1}|^2}{P_n+P_{s,2}|H_{2,1}|^2}\right) + \log_2\left(1+\frac{P_{s,2}|H_{2,2}|^2}{P_n+P_{s,1}|H_{1,2}|^2}\right)\right], \tag{2.17}$$

being $P_n = \mathcal{N}_0 B$ the noise power, $\mathcal{N}_0$ the bi-lateral power spectral density of the complex thermal noise, B the system channel bandwidth, $P_{s,x} < P_{\max}$ the power transmitted from the BS $x \in \{1, 2\}$, $P_{\max}$ the maximum power available at the BS for the particular user, and $|H_{i,j}|^2$, $i, j \in \{1, 2\}$, the channel gain between the transmitter i and the receiver j. In this scenario, two opposite situations may occur, depending on the UEs positions [34, p.287].

1. Each UE is close to its eNodeB, as represented in Figure 2.8a: in this situation, $|H_{1,1}| >> |H_{2,1}|$ and $|H_{2,2}| >> |H_{1,2}|$; hence, the best total throughput is obtained if the eNodeBs transmit all the available power on the allocated resources to both the UEs, namely $P_{s,1} = P_{s,2} = P_{\max}$.

2. The UEs are close, nearby the cell border, as represented in Figure 2.8b: in this situation, $|H_{1,1}| \simeq |H_{2,1}|$ and $|H_{2,2}| \simeq |H_{1,2}|$; hence, the best total throughput is obtained allowing just one UE to transmit, e.g., $P_{s,1} = P_{\max}$ and $P_{s,2} = 0$.

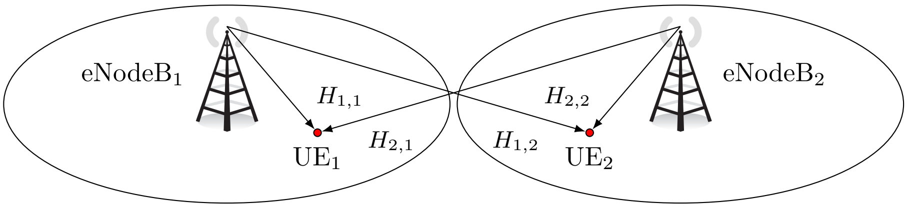

(a) UEs close to the corresponding eNodeB.

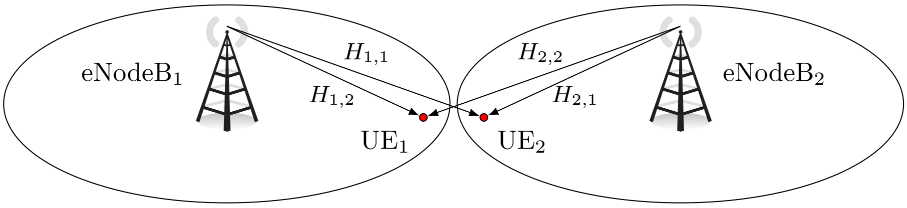

(b) Close UEs, nearby the cell edge.

Figure 2.8 – Different inter-cell interference situations in a 2-eNodeBs 2-UEs system with a frequency reuse factor of 1, depending on the UEs position in respect to the eNodeBs.

In practical situations, as these scenarios illustrate, resources should be allocated to users depending on their position in respect to the eNodeB. For users close to the BS (cell-centre users), an actual frequency reuse factor of one can be employed, and hence the same sub-carriers can be allocated in the same time slots to users of different neighbour cells. For users close to the cell border (cell-edge users), resource scheduling must be applied:

- different cells may allocate orthogonal RBs to their cell-edge users; this is optimal, but limits the number of users;
- while a cell is serving on a certain RB a user close to the cell edge, a neighbour cell may only transmit at low power on that RB (e.g., with the aim of serving a UE close to its cell centre); this is referred to as soft frequency reuse.

When different cells are controlled by different eNodeBs, these ICIC policies require inter-eNodeB communication. However, we are interested in cells controlled by the same eNodeB. In this case, the eNodeB can implement autonomously its ICIC policy, which may still be based on a full frequency reuse for cell-centre users, and a soft frequency reuse for cell-edge users, as depicted in Figure 2.9.

It is important to stress that ICIC strategies affect only the user data, and not the reference signals such as the CRS, which are always transmitted from each sector. Hence, the frequency reuse factor of one adopted by the LTE enables CRSs from adjacent cells to be transmitted on the same channel, and to be received simultaneously, since the ICIC policy does not affect their power, and since the CRS pilots of neighbour cells are generally orthogonal. This aspect is further clarified in the next section.

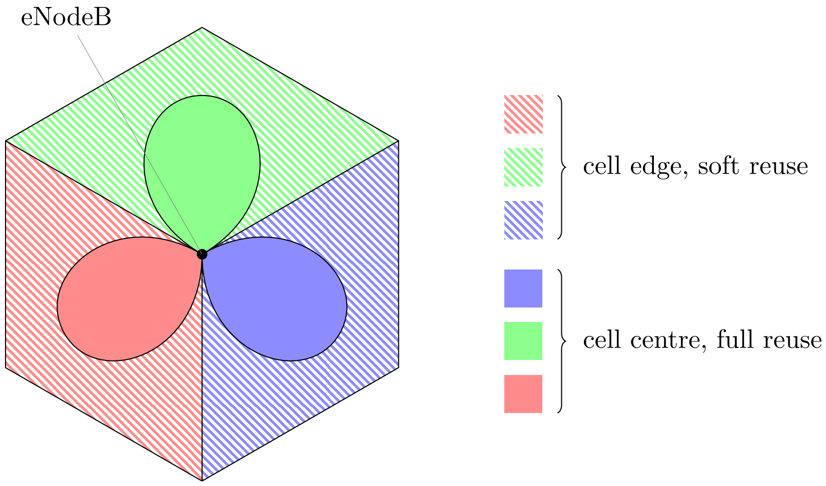

Figure 2.9 – Possible inter-cell interference coordination scheme for cells controlled by the same eNodeB. The different colors identify different cells, while the different patterns identity different cell zones, corresponding to different ICIC strategies.

2.2.4 Physical cell identities

Each cell ID $N_{\mathrm{ID}}^{\mathrm{cell}}$ is referred to as a physical cell identity (PCI). There are 504 PCIs, grouped into 168 physical cell identity groups (PCIGs), each made of three identities. A PCI is hence defined as $N_{\mathrm{ID}}^{\mathrm{cell}} = 3N_{\mathrm{ID}}^{(1)} + N_{\mathrm{ID}}^{(2)}$, where $N_{\mathrm{ID}}^{(1)} \in \{0, \dots, 167\}$ identifies the PCIG and $N_{\mathrm{ID}}^{(2)} \in \{0, 1, 2\}$ correspond to a particular cell ID within the PCIG. The three identities within a group, identified by the cell IDs $\{N_{\mathrm{ID}}^{\mathrm{cell}}, N_{\mathrm{ID}}^{\mathrm{cell}} + 1, N_{\mathrm{ID}}^{\mathrm{cell}} + 2\}$, are usually assigned to the cells under the control of the same eNodeB [35, p.155]. Hence, as a consequence of the mapping scheme described in Section 2.2.2, the three CRSs (as well as the PRSs) of the cells of the same PCIG (controlled, as said above, by the same eNodeB), are associated with three consecutive cell IDs, and hence are orthogonal in the frequency domain.

The multiple sectors controlled by the same eNodeB are usually multiplexed only by means of directional antennas. However, while served from the predominant cell, reception of other cells from the same BS is still possible, due to antenna back lobes and multipath. This fact, together with the orthogonal transmission of the reference symbols (CRS or PRS) pertaining to the PCIs of the same group (i.e., of the same eNodeB), and together with the fact that LTE adopts a frequency reuse factor of one, enables the simultaneous reception of reference signals from multiple sectors of the same base station. This fact is exploited in the presented work for positioning purposes, as explained in Section 6.7.

Chapter 3

Super resolution algorithms

Super-resolution algorithms constitute a class of methods for the estimation of frequencies in harmonic models. They have been mainly used for direction of arrival estimation of planar waveforms on linear uniform arrays. Few works in the literature recognize that super-resolution algorithms can also be used for multipath time of arrival estimation. This chapter describes the most popular super-resolution algorithms, with particular attention to the ones used throughout this thesis work.

3.1 Super-resolution algorithms for TOA estimation

Consider the channel impulse response (CIR) of a multipath fading channel, which is given by [20]:

$$h(t;\tau) = \sum_{l=0}^{L-1} h_l(t)\delta(\tau - \tau_l(t)), \tag{3.1}$$

where $\tau_0 < \cdots < \tau_{L-1}$ and each of the coefficient $h_l(t) \in \mathbb{C}$ represents the complex gain pertaining to each of the L paths that reaches the receiver. Suppose that the observation interval is small enough that the delays $\tau_l(t)$ and the channel gains $h_l(t)$ can be considered constant, leading to the time-invariant CIR:

$$h(\tau) = \sum_{l=0}^{L-1} h_l\delta(\tau - \tau_l). \tag{3.2}$$

Consider now a system that transmits through the channel of (3.2) a reference signal $s(t)$, that is known at the receiver. The received signal is:

$$r(t) = \sum_{l=0}^{L-1} h_l s(t - \tau_l) + w(t), \tag{3.3}$$

where $w(t)$ is a complex noise process, that is assumed to be un-correlated and to have a zero mean $\sigma_w^2/2$ per-dimension variance Gaussian distribution. The aim of a system that has to estimate the time of arrival (TOA) of the signal $s(t)$ is the estimation of the delay τ_0 given the received signal $r(t)$. As will be shown in the next sections, the super-resolution algorithms (SRAs) can be exploited for achieving such a goal.

Consider the Fourier transform of (3.2), which constitutes the so called channel frequency response (CFR):

$$H(f) = \mathcal{F}\left\{h(\tau)\right\} = \sum_{l=0}^{L-1} h_l e^{-j2\pi f \tau_l} \in \mathbb{C}. \tag{3.4}$$

As one can note, (3.4) constitutes an harmonic model, since the signal $H(f)$ is composed by the sum of L complex sinusoids (in the frequency domain) having a period of $\frac{1}{\tau_l}$. In other words, $H(f)$ can be seen as a continuous time signal in the variable f, made of L sinusoids of frequency τ_l (which actually have the dimensions of time since they represent time-delays).

Super resolution algorithms are a powerful tool that can be used to estimate the frequencies contained in an harmonic model-like signal. Their name is due to their ability to resolve complex exponentials closely spaced in frequency [36]. Since the CFR of a multipath channel is an harmonic model, SRAs can be employed for the estimation of the time of arrival of a reference signal. In particular, SRAs can be used for the estimation of the frequencies of the complex sinusoids that compose $H(f)$, namely the delays τ_l. The use of SRAs for estimating the multipath TOA of a wireless channel has been previously reported in the literature in works such as [15, 16, 33, 37–42] and references therein.

Suppose that the receiver is able to produce a rough estimate of the CFR. This estimate will likely be a sampled and noisy version of $H(f)$, where the frequency domain (FD) sampling interval is Δf_{SRA}:

$$\begin{aligned} x[n] &= H(f = n\Delta f_{\text{SRA}}) + w[n] = \sum_{l=0}^{L-1} h_l e^{-2\pi n \Delta f_{\text{SRA}} \tau_l} + w[n] \\ &= \sum_{l=0}^{L-1} h_l e^{-2\pi n f_l} + w[n] \ \in \mathbb{C},\ \forall n. \end{aligned} \tag{3.5}$$

According to the sampling theorem, the inverse of the sampling interval $1/\Delta f_{\text{SRA}}$ must be at least two times bigger than the maximum delay $\tau_{\max} = \tau_{L-1} - \tau_0$, i.e.:

$$\frac{1}{\Delta f_{\text{SRA}}} \geq 2\tau_{\max} \quad \Leftrightarrow \quad \Delta f_{\text{SRA}} \leq \frac{1}{2\tau_{\max}}. \tag{3.6}$$

Hence, the parameters $f_l = \Delta f_{\text{SRA}} \tau_l$ assume values in the interval $\left[-\frac{1}{2}, \frac{1}{2}\right]$ and represent the discrete time frequencies that the receiver has to estimate.

3.1.1 Sub-space based approach

In the following section, the sub-space approach on which super-resolution techniques rely is explained. The interested reader may refer to [36] and [43] for further details about super resolution algorithms. Consider a set of $M > L$ adjacent samples of $x[n]$ collected in the vector $\boldsymbol{x}[n]$, which is referred to as a snapshot:

$$\boldsymbol{x}[n] = [x[n], x[n+1], \ldots, x[n+M-1]]^{\mathrm{T}} \in \mathbb{C}^M. \tag{3.7}$$

Each snapshot $\boldsymbol{x}[n]$ can be written as:

$$\begin{aligned}
\boldsymbol{x}[n] &= \sum_{l=0}^{L-1} h_l e^{-2\pi n f_l} \left[1, e^{-2\pi f_l}, e^{-2\pi f_l 2}, \ldots, e^{-2\pi f_l (M-1)}\right]^{\mathrm{T}} + \boldsymbol{w}[n] \\
&= \sum_{l=0}^{L-1} h_l e^{-2\pi n f_l} \boldsymbol{v}(f_l) + \boldsymbol{w}[n] \\
&= \mathbf{V}\boldsymbol{h}[n] + \boldsymbol{w}[n] = \boldsymbol{s}[n] + \boldsymbol{w}[n], \qquad (3.8)
\end{aligned}$$

where:

$$\boldsymbol{s}[n] = \sum_{l=0}^{L-1} h_l e^{-2\pi n f_l} \boldsymbol{v}(f_l) = \mathbf{V}\boldsymbol{h}[n] \in \mathbb{C}^M, \tag{3.9}$$

$$\mathbf{V} = [\boldsymbol{v}(f_0), \boldsymbol{v}(f_1), \ldots, \boldsymbol{v}(f_{L-1})] \in \mathbb{C}^{M \times L}, \tag{3.10}$$

$$\boldsymbol{v}(f) = \left[1, e^{-2\pi f}, e^{-2\pi f 2}, \ldots, e^{-2\pi f (M-1)}\right]^{\mathrm{T}} \in \mathbb{C}^M, \tag{3.11}$$

$$\boldsymbol{w}[n] = [w[n], w[n+1], \ldots, w[n+M-1]]^{\mathrm{T}} \in \mathbb{C}^M, \tag{3.12}$$

$$\boldsymbol{h}[n] = \left[h_0 e^{-2\pi n f_0}, h_1 e^{-2\pi n f_1}, \ldots, h_{L-1} e^{-2\pi n f_{L-1}}\right]^{\mathrm{T}} \in \mathbb{C}^L, \tag{3.13}$$

are respectively the signal vector, the time-window frequency matrix, the time-window frequency vector, the noise vector and the channel coefficients vector. Each element of $\boldsymbol{w}[n]$ is assumed to be a complex Gaussian random variable with zero mean and $\sigma_w^2/2$ variance per dimension, and to be independent from all the other noise samples. Hence, the auto-correlation matrix of the vector $\boldsymbol{w}[n]$ is $\mathbf{R}_w = \mathbb{E}[\boldsymbol{w}[n]\boldsymbol{w}^{\mathrm{H}}[n]] = \sigma_w^2 \mathbf{I}_M$. Moreover, the complex channel gains $h_l = |h_l| \, e^{\arg\{h_l\}}$ are assumed to be random variables having independent identically distributed phases $\arg\{h_l\}$ with a uniform distribution in the interval $[0, 2\pi)$ [15]. Finally, assume that the modulus $|h_l|$ and the phase $\arg\{h_l\}$ of each channel gain are independent.

Upon these assumptions, consider the auto-correlation matrix of the snapshot vector $\boldsymbol{x}[n]$, which is given by:

$$\begin{aligned}
\mathbf{R}_x &= \mathbb{E}\left[\boldsymbol{x}[n]\boldsymbol{x}^{\mathrm{H}}[n]\right] \\
&= \mathbb{E}\left[\boldsymbol{s}[n]\boldsymbol{s}^{\mathrm{H}}[n]\right] + \mathbb{E}\left[\boldsymbol{w}[n]\boldsymbol{w}^{\mathrm{H}}[n]\right] \\
&= \mathbb{E}\left[\left(\sum_{l=0}^{L-1} h_l e^{-j2\pi n f_l} \boldsymbol{v}(f_l)\right)\left(\sum_{l'=0}^{L-1} h_{l'}^* e^{j2\pi n f_{l'}} \boldsymbol{v}^{\mathrm{H}}(f_{l'})\right)\right] + \sigma_w^2 \mathbf{I}_M \\
&= \sum_{l=0}^{L-1} \sum_{l'=0}^{L-1} \mathbb{E}\left[h_l h_{l'}^*\right] e^{-j2\pi n (f_l - f_{l'})} \boldsymbol{v}(f_l) \boldsymbol{v}^{\mathrm{H}}(f_{l'}) + \sigma_w^2 \mathbf{I}_M. \qquad (3.14)
\end{aligned}$$

Since $|h_l|$ and $\arg\{h_l\}$ are independent, the term $\mathbb{E}[h_l h_{l'}^*]$ becomes:

$$\begin{aligned}
\mathbb{E}\left[h_l h_{l'}^*\right] &= \mathbb{E}\left[|h_l||h_{l'}^*|\right]\mathbb{E}\left[e^{\arg\{h_l\}}e^{-\arg\{h_{l'}\}}\right] \\
&= \begin{cases} \mathbb{E}\left[|h_l|\right]\mathbb{E}\left[|h_{l'}^*|\right]\mathbb{E}\left[e^{\arg\{h_l\}}\right]\mathbb{E}\left[e^{-\arg\{h_{l'}\}}\right] & \text{if } l \neq l' \\ \mathbb{E}\left[|h_l|^2\right] & \text{if } l = l' \end{cases} \\
&= \begin{cases} \mathbb{E}\left[|h_l|\right]\mathbb{E}\left[|h_{l'}^*|\right]\int_0^{2\pi}\frac{1}{2\pi}e^{jh}dh\int_0^{2\pi}\frac{1}{2\pi}e^{-jh'}dh' & \text{if } l \neq l' \\ \mathbb{E}\left[|h_l|^2\right] & \text{if } l = l' \end{cases} \\
&= \alpha_l^2\delta_{ll'}, \qquad (3.15)
\end{aligned}$$

where $\alpha_l^2 = \mathbb{E}[|h_l|^2]$ and $\delta_{ll'}$ is the Kronecker delta. Hence, Eq. (3.14) becomes:

$$\begin{aligned}
\mathbf{R}_x &= \sum_{l=0}^{L-1}\alpha_l^2\boldsymbol{v}(f_l)\boldsymbol{v}^{\mathrm{H}}(f_l) + \sigma_w^2\mathbf{I}_M \\
&= \mathbf{V}\mathbf{A}\mathbf{V}^{\mathrm{H}} + \sigma_w^2\mathbf{I}_M \qquad (3.16) \\
&= \mathbf{R}_s + \mathbf{R}_w \in \mathbb{C}^{M\times M}, \qquad (3.17)
\end{aligned}$$

where $\mathbf{A} = \operatorname{diag}\{[\alpha_0^2, \dots, \alpha_{L-1}^2]^{\mathrm{T}}\} \in \mathbb{C}^{L\times L}$ and $\mathbf{R}_s = \mathbf{V}\mathbf{A}\mathbf{V}^{\mathrm{H}} \in \mathbb{C}^{M\times M}$ is referred to as signal auto-correlation matrix. The noise auto-correlation matrix $\mathbf{R}_w$ is full rank since it is diagonal, i.e., the rank $\mathbf{R}_w$ is equal to M. Moreover, since $M > L$, the signal auto-correlation matrix $\mathbf{R}_s$ is rank deficient. This can be seen from the dimensions of the matrices that generate $\mathbf{R}_s$:

$$\mathbf{R}_s = \underbrace{\mathbf{V}}_{M\times L}\,\underbrace{\mathbf{A}}_{L\times L}\,\underbrace{\mathbf{V}^{\mathrm{H}}}_{L\times M}, \qquad (3.18)$$

where it is evident that $\mathbf{R}_s$ takes vectors from $\mathbb{C}^M$, projects them to $\mathbb{C}^L$ (through the matrix $\mathbf{A}\mathbf{V}^{\mathrm{H}}$), and finally maps them back to $\mathbb{C}^M$ (using $\mathbf{V}$). Hence, $\mathbf{R}_s$ has rank equal to L and hence it has $M-L$ null eigenvalues.

Since $\mathbf{R}_x$ is a normal matrix (i.e. $\mathbf{R}_x\mathbf{R}_x^{\mathrm{H}} = \mathbf{R}_x^{\mathrm{H}}\mathbf{R}_x$), then it exists an eigendecomposition of $\mathbf{R}_x$ with an orthonormal basis of eigenvectors, i.e.:

$$\begin{aligned}
\mathbf{R}_x &= \mathbf{Q}\boldsymbol{\Lambda}\mathbf{Q}^{\mathrm{H}} \\
&= \begin{bmatrix}\boldsymbol{q}_0 & \boldsymbol{q}_1 & \cdots & \boldsymbol{q}_{M-1}\end{bmatrix}\begin{bmatrix}\lambda_0 & 0 & \dots & 0 \\ 0 & \lambda_1 & \dots & 0 \\ \vdots & \vdots & \ddots & \vdots \\ 0 & 0 & \dots & \lambda_{M-1}\end{bmatrix}\begin{bmatrix}\boldsymbol{q}_0^{\mathrm{H}} \\ \boldsymbol{q}_1^{\mathrm{H}} \\ \vdots \\ \boldsymbol{q}_{M-1}^{\mathrm{H}}\end{bmatrix} \\
&= \sum_{m-0}^{M-1}\lambda_m\boldsymbol{q}_m\boldsymbol{q}_m^{\mathrm{H}}, \qquad (3.19)
\end{aligned}$$

where $\lambda_m \in \mathbb{R}^+$ are the eigenvalues of $\mathbf{R}_x$ and $\boldsymbol{q}_m \in \mathbb{C}^M$ are the corresponding eigenvectors, $\boldsymbol{\Lambda} = \operatorname{diag}\{[\lambda_0, \dots, \lambda_{M-1}]^{\mathrm{T}}\}$ and $\mathbf{Q}\mathbf{Q}^{\mathrm{H}} = \mathbf{I}_M$ (i.e. $\boldsymbol{q}_m^{\mathrm{H}}\boldsymbol{q}_{m'} = \delta_{mm'}$). The eigenvalues of $\mathbf{R}_x = \mathbf{R}_s + \sigma_w^2 \mathbf{I}_M$ can be calculated recalling that, if $\lambda_i(\mathbf{A})$ is the i^{th} eigenvector of the matrix $\mathbf{A} \in \mathbb{C}^{M \times M}$, then $\lambda_i(\mathbf{A} + \alpha \mathbf{I}_M) = \lambda_i(\mathbf{A}) + \alpha$, obtaining:

$$\lambda_m\left(\mathbf{R}_x\right) = \lambda_m\left(\mathbf{V}\mathbf{A}\mathbf{V}^{\mathrm{H}}\right) + \sigma_w^2. \tag{3.20}$$

Using (3.18), one can note that the signal auto-correlation matrix $\mathbf{R}_s = \mathbf{V}\mathbf{A}\mathbf{V}^{\mathrm{H}}$ has $M - L$ null eigenvalues. Moreover, it can be demonstrated (see [36]) that the L non-null eigenvalues of $\mathbf{R}_s$ are equal to $M\alpha_l^2$, $l = 0, \ldots, L-1$. Hence, the eigenvalues of $\mathbf{R}_x$ are:

$$\left.\begin{array}{l} \lambda_0 = M\alpha_0^2 + \sigma_w^2 \\ \ldots \\ \lambda_{L-1} = M\alpha_{L-1}^2 + \sigma_w^2 \end{array}\right\} \text{eigenvalues corresponding to the signal,} \tag{3.21}$$

$$\left.\begin{array}{l} \lambda_L = \sigma_w^2 \\ \ldots \\ \lambda_{M-1} = \sigma_w^2 \end{array}\right\} \text{eigenvalues corresponding to the noise.} \tag{3.22}$$

Hence, (3.19) can be written splitting the summation in two terms, one corresponding to the signal eigenvalues, and the other corresponding to the noise eigenvalues, obtaining:

$$\begin{aligned} \mathbf{R}_x &= \sum_{m=0}^{M-1} \lambda_m \boldsymbol{q}_m \boldsymbol{q}_m^{\mathrm{H}} = \sum_{m=0}^{L-1} \lambda_m \boldsymbol{q}_m \boldsymbol{q}_m^{\mathrm{H}} + \sum_{m=L}^{M-1} \sigma_w^2 \boldsymbol{q}_m \boldsymbol{q}_m^{\mathrm{H}} \\ &= \mathbf{Q}_s \mathbf{\Lambda}_s \mathbf{Q}_s^{\mathrm{H}} + \sigma_w^2 \mathbf{Q}_w \mathbf{Q}_w^{\mathrm{H}}, \end{aligned} \tag{3.23}$$

where:

$$\mathbf{Q}_s = \left[\boldsymbol{q}_0, \ldots, \boldsymbol{q}_{L-1}\right] \in \mathbb{C}^{M \times L}, \tag{3.24}$$

$$\mathbf{Q}_w = \left[\boldsymbol{q}_L, \ldots, \boldsymbol{q}_{M-1}\right] \in \mathbb{C}^{M \times (M-L)}, \tag{3.25}$$

$$\mathbf{\Lambda}_s = \operatorname{diag}\left\{[\lambda_0, \ldots, \lambda_{L-1}]^{\mathrm{T}}\right\} \in \mathbb{C}^{L \times L}. \tag{3.26}$$

This procedure demonstrates that the auto-correlation matrix $\mathbf{R}_x$ of the snapshot vector $\boldsymbol{x}[n]$ can be decomposed in two matrices, one generated by an orthonormal basis of vectors (namely the columns of $\mathbf{Q}_s$) that corresponds to the signal sub-space, and the other generated by another orthonormal basis of vectors (namely the columns of $\mathbf{Q}_w$) that corresponds to the noise sub-space, which spans a space that is orthogonal to the signal sub-space. In other words, the sub-spaces spanned by $\mathbf{Q}_s$ and $\mathbf{Q}_w$ are orthogonal. Since the time-window frequency vectors $\boldsymbol{v}(f)$ lie in the signal sub-space if $f = f_l$, then the vectors $\boldsymbol{v}(f_l)$ are orthogonal to the noise sub-space, i.e.:

$$\boldsymbol{v}^{\mathrm{H}}(f_l)\boldsymbol{q}_m = 0 \quad \forall l,\ \forall m \geq L. \tag{3.27}$$

This property is exploited by super-resolution algorithms for understanding if a particular discrete time frequency $f \in \left[-\frac{1}{2}, \frac{1}{2}\right]$ is contained in the signal $x[n]$. In particular, a SRA checks if the vector $\boldsymbol{v}(f)$ is orthogonal or not to the noise sub-space, which is equivalent to checking if it belongs or not to the signal sub-space.

3.1.2 Estimation of the auto-correlation matrix

The first problem to be faced in a real implementation is that a limited number of samples of the signal $x[n]$ is known and hence the ideal auto-correlation matrix $\mathbf{R}_x$ is unknown at the estimator side. The matrix $\mathbf{R}_x$ can only be estimated using the limited number of snapshots that is usually available in a real system, leading to the estimated auto-correlation matrix $\hat{\mathbf{R}}_x$, which is more reliable as the number of available snapshot $\boldsymbol{x}[n]$ increases.

There are several methods for the estimation of $\mathbf{R}_x$ [15]. If a number of N non overlapping length M snapshots of the discrete time signal $x[n]$ are available, namely:

$$\boldsymbol{x}_0, \ldots, \boldsymbol{x}_{N-1}, \quad \boldsymbol{x}_n \in \mathbb{C}^M, \ \forall n, \tag{3.28}$$

they can be used for the estimation of $\mathbf{R}_x$ as:

$$\hat{\mathbf{R}}_x = \frac{1}{N} \sum_{n=0}^{N-1} \boldsymbol{x}_n \boldsymbol{x}_n^{\mathrm{H}} = \frac{1}{N} \begin{bmatrix} \boldsymbol{x}_0 & \ldots & \boldsymbol{x}_{N-1} \end{bmatrix} \begin{bmatrix} \boldsymbol{x}_0^{\mathrm{H}} \\ \ldots \\ \boldsymbol{x}_{N-1}^{\mathrm{H}} \end{bmatrix} = \mathbf{X}_{\mathrm{no}} \mathbf{X}_{\mathrm{no}}^{\mathrm{H}}, \tag{3.29}$$

where the non overlapping snapshots collection matrix $\boldsymbol{X}_{\mathrm{no}}$ is defined as:

$$\mathbf{X}_{\mathrm{no}} = \frac{1}{\sqrt{N}} [\boldsymbol{x}_0, \ldots, \boldsymbol{x}_{N-1}] \in \mathbb{C}^{M \times N}. \tag{3.30}$$

When $x[n] = H(f = n\Delta f_{\mathrm{SRA}}) + w[n]$, i.e., when the super-resolution algorithm is used for channel estimation purposes, the non overlapping snapshots $\boldsymbol{x}_p$ may be FD samples of the channel in different instants (this is valid only for static channels), or FD samples of the channel acquired in different frequency bands. On the other hand, if just a long single snapshot of $x[n]$ is available, say a length $N_{\mathrm{tot}} > M$ snapshot:

$$[x[0], x[1], \ldots, x[N_{\mathrm{tot}} - 1]], \tag{3.31}$$

then $N = N_{\mathrm{tot}} - M + 1$ overlapping snapshots can be defined as:

$$\boldsymbol{x}[n] = [x[n], x[n+1], \ldots, x[n+M-1]]^{\mathrm{T}} \in \mathbb{C}^M, \ n = 0, \ldots, N-1, \tag{3.32}$$

and the auto-correlation matrix can be estimated as:

$$\hat{\mathbf{R}}_x = \frac{1}{N} \sum_{n=0}^{N-1} \boldsymbol{x}[n] \boldsymbol{x}[n]^{\mathrm{H}} = \frac{1}{N} \begin{bmatrix} \boldsymbol{x}[0] & \ldots & \boldsymbol{x}[N-1] \end{bmatrix} \begin{bmatrix} \boldsymbol{x}^{\mathrm{H}}[0] \\ \ldots \\ \boldsymbol{x}^{\mathrm{H}}[N-1] \end{bmatrix} = \mathbf{X}_{\mathrm{o}} \mathbf{X}_{\mathrm{o}}^{\mathrm{H}}, \tag{3.33}$$

where the overlapping snapshots collection matrix $\boldsymbol{X}_{\mathrm{o}}$ is defined as:

$$\boldsymbol{X}_{\mathrm{o}} = \frac{1}{\sqrt{N}} [\boldsymbol{x}[0], \ldots, \boldsymbol{x}[N-1]] \in \mathbb{C}^{M \times N}. \tag{3.34}$$

Again, when the SRA is used for channel estimation purposes, the case of long overlapping snapshot is the most common, especially when time variant channels are considered.

Once the estimated auto-correlation matrix is computed, its eigendecomposition is performed, obtaining a set of M eigenvectors $\hat{\boldsymbol{q}}_m, m = 0, \dots M-1$, each associated with the corresponding eigenvalue λ_m. The L eigenvectors corresponding to the L largest eigenvalues are assumed to be the signal eigenvectors, while the other $M-L$ eigenvectors are assumed to be the noise eigenvectors. If the eigenvalues are $\lambda_0 > \lambda_1 > \cdots > \lambda_{M-1}$, then the signal sub-space is assumed to be spanned by the columns of:

$$\hat{\mathbf{Q}}_s = \left[\hat{\boldsymbol{q}}_0, \dots, \hat{\boldsymbol{q}}_{L-1}\right] \in \mathbb{C}^{M \times L}, \tag{3.35}$$

while the noise sub-space is assumed to be spanned by the columns of:

$$\hat{\mathbf{Q}}_w = \left[\hat{\boldsymbol{q}}_L, \dots, \hat{\boldsymbol{q}}_{M-1}\right] \in \mathbb{C}^{M \times (M-L)}. \tag{3.36}$$

3.2 The MUSIC algorithm

The multiple signal classification (MUSIC) algorithm determines the frequencies contained in the analysed signal $x[n]$ through the following procedure. First, the pseudospectrum $R_{\text{MUSIC}}(f)$ is computed according to:

$$R_{\text{MUSIC}}(f) = \frac{1}{\left|\sum_{m=L}^{M-1} \boldsymbol{v}^{\text{H}}(f)\hat{\boldsymbol{q}}_m\right|^2} \tag{3.37}$$

As stated in (3.27), if $\hat{\boldsymbol{q}}_m$ is a noise eigenvector, then it should be orthogonal to the vector $\boldsymbol{v}(f_l)$. Hence, the spectrum of (3.37) should present L peaks in correspondence of the discrete time frequencies $f = f_l$, which are the L frequencies contained in the harmonic signal $x[n]$. As a consequence, the second phase of the MUSIC algorithm consists in finding the L highest peaks of $R_{\text{MUSIC}}(f)$, which appear at a discrete time frequency that corresponds to the estimate $\hat{f}_l$.

In real implementations, it is impossible to calculate a continuous version of the function $R_{\text{MUSIC}}(f)$, hence a discretization in $N_{\text{d}} > M$ samples is needed. In particular, the discretized pseudospectrum $R_{\text{MUSIC}}[n]$ can be easily computed through the discrete Fourier transform (DFT) operator using the following observations. First, suppose that the vector $\hat{\boldsymbol{q}}_m \in \mathbb{C}^M$ is:

$$\hat{\boldsymbol{q}}_m = [\hat{q}_m[0],\, \hat{q}_m[1],\, \dots,\, \hat{q}_m[M-1]]^{\text{T}} \in \mathbb{C}^M \tag{3.38}$$

Then, observe that:

$$\begin{aligned}\boldsymbol{v}^{\text{H}}\left(f = -\frac{1}{2} + \frac{n}{N_{\text{d}}}\right)\hat{\boldsymbol{q}}_m &= \sum_{k=0}^{M-1} \hat{q}_m[k]\, e^{j2\pi k f}\Bigg|_{f=-\frac{1}{2}+\frac{n}{N_{\text{d}}}} \\ &= \sum_{k=0}^{M-1} \hat{q}_m[k]\, e^{-j\pi k} e^{j\frac{2\pi}{N_{\text{d}}}nk} \\ &= \left[\text{IDFT}_{N_{\text{d}}}\left\{\hat{q}_m[k]\right\}\right]_{\text{shift}}, \quad n = 0, \dots, N_{\text{d}}-1. \end{aligned} \tag{3.39}$$

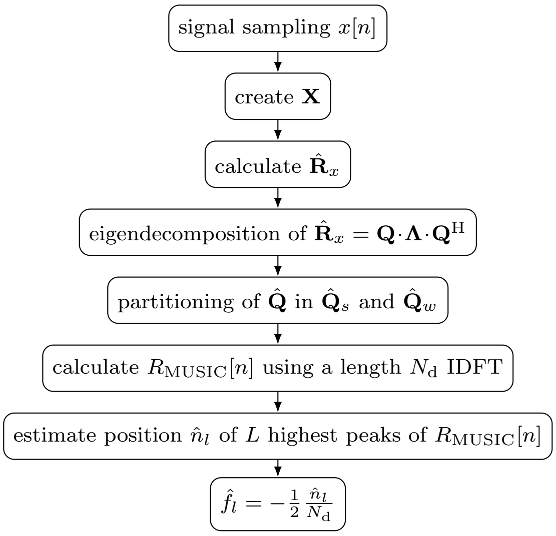

Figure 3.1 – Flowgraph of the implementation of the MUSIC algorithm.

In (3.39), the $[\cdot]_{\mathrm{shift}}$ operator applies the FFT-shift function to a vector, which performs a swapping between the left and right halves of the input vector.

Finally, the discretized MUSIC pseudospectrum can be obtained as:

$$R_{\mathrm{MUSIC}}[n] = \frac{1}{\left|\sum_{m=L}^{M-1} \left[\mathrm{IDFT}_{N_{\mathrm{d}}}\left\{\hat{q}_m[k]\right\}\right]_{\mathrm{shift}}\right|^2}, \quad n = 0, \ldots, N_{\mathrm{d}} - 1, \tag{3.40}$$

and the frequency estimates can be obtained by selecting the sample indexes that correspond to the L highest peaks of $R_{\mathrm{MUSIC}}[n]$. If $\hat{n}$ is the sample corresponding to a peak of $R_{\mathrm{MUSIC}}[n]$, then the frequency estimate will be:

$$\hat{f} = -\frac{1}{2} + \frac{\hat{n}}{N_{\mathrm{d}}}, \tag{3.41}$$

which corresponds to the delay estimate:

$$\hat{\tau} = \frac{1}{\Delta f_{\mathrm{SRA}}}\left(-\frac{1}{2} + \frac{\hat{n}}{N_{\mathrm{d}}}\right). \tag{3.42}$$

As one can see, the accuracy of the estimation depends on the discretization interval that is adopted in the calculation of $R_{\mathrm{MUSIC}}[n]$, which ultimately corresponds to the length N_{d} of the IDFT operator used in (3.40). Higher values of N_{d} corresponds to higher estimation precision for the MUSIC algorithm, but determine an higher complexity from the implementative point of view. Finally, Figure 3.1 shows the actual implementation of the MUSIC algorithm.

3.3 The ESPRIT algorithm

The estimation of signal parameters via rotational invariance techniques (ESPRIT) algorithm relies on the data matrix $\mathbf{X} \in \mathbb{C}^{M \times N}$ of (3.34), which is given by:

$$\mathbf{X} = [\boldsymbol{x}[0], \ldots, \boldsymbol{x}[N-1]] \in \mathbb{C}^{M \times N}. \tag{3.43}$$

Note that the sub-script $(\cdot)_{\mathrm{o}}$ has been dropped from $\mathbf{X}$ for notational simplicity. In (3.43), M is the length of a single data snapshot and $N = N_{\mathrm{tot}} - M + 1$ is the number of overlapping snapshots used in $\mathbf{X}$. The ESPRIT derivation is formulated here as in [36]. Consider the vector defined in (3.8), which can be also written as:

$$\begin{aligned}
\boldsymbol{x}[n] &= \boldsymbol{s}[n] + \boldsymbol{w}[n] = \sum_{l=0}^{L-1} h_l e^{-j2\pi n f_l} \boldsymbol{v}(f_l) + \boldsymbol{w}[n] \\
&= [\boldsymbol{v}(f_0), \ldots, \boldsymbol{v}(f_{L-1})] \begin{bmatrix} e^{-j2\pi f_0} & \ldots & 0 \\ \vdots & \ddots & \vdots \\ 0 & \ldots & e^{-j2\pi f_{L-1}} \end{bmatrix}^n \begin{bmatrix} h_0 \\ \vdots \\ h_{L-1} \end{bmatrix} + \boldsymbol{w}[n] \\
&= \mathbf{V} \cdot \mathbf{\Phi}^n \cdot \boldsymbol{h} + \boldsymbol{w}[n],
\end{aligned} \tag{3.44}$$

where $\mathbf{V} \in \mathbb{C}^{M \times L}$ is the same matrix defined in (3.10), $\boldsymbol{h} = [h_0, \ldots, h_{L-1}]^{\mathrm{T}} \in \mathbb{C}^L$ collects the L channel gains and:

$$\mathbf{\Phi} = \begin{bmatrix} e^{-j2\pi f_0} & \ldots & 0 \\ \vdots & \ddots & \vdots \\ 0 & \ldots & e^{-j2\pi f_{L-1}} \end{bmatrix} \in \mathbb{C}^{L \times L}, \tag{3.45}$$

is referred to as rotational matrix. The ESPRIT algorithm estimates the discrete time frequencies f_l through the estimation of the matrix $\mathbf{\Phi}$. More particularly, the estimation of $\mathbf{\Phi}$ using the data $\mathbf{X}$ can be performed exploiting the particular structure of the harmonic signal $\boldsymbol{s}[n]$. As an example, consider the signal $s_0[n] = \alpha \cdot e^{j2\pi f n}$, which has the following property:

$$s_0[n+1] = \alpha \cdot e^{j2\pi f(n+1)} = s_0[n] \cdot e^{j2\pi f}. \tag{3.46}$$

As one can see, the samples $s_0[n+1]$ and $s_0[n]$ are related through a phase shift of $2\pi f$ radiants, which corresponds to a rotation of $2\pi f$ radiants on the unitary circle. Hence, if one knows $s_0[n+1]$ and $s_0[n]$, the discrete time frequency f can be easily determined. Consider now the vector $\boldsymbol{s}[n] \in \mathbb{C}^M$, and note that it can be expressed as a combination of two partially overlapped vectors:

$$\boldsymbol{s}_{M-1}[n] = [s[n], \ldots, s[n+M-2]]^{\mathrm{T}} \in \mathbb{C}^{M-1}, \tag{3.47}$$

$$\boldsymbol{s}_{M-1}[n+1] = [s[n+1], \ldots, s[n+M-1]]^{\mathrm{T}} \in \mathbb{C}^{M-1}, \tag{3.48}$$

as:

$$\boldsymbol{s}[n] = \begin{bmatrix} \boldsymbol{s}_{M-1}[n] \\ s[n+M-1] \end{bmatrix} = \begin{bmatrix} s[n] \\ \boldsymbol{s}_{M-1}[n+1] \end{bmatrix} \in \mathbb{C}^M. \tag{3.49}$$

The length $M-1$ vector $\boldsymbol{s}_{M-1}[n]$ can be written as:

$$\boldsymbol{s}_{M-1}[n] = \mathbf{V}_{M-1} \cdot \boldsymbol{\Phi}^n \cdot \boldsymbol{h}, \tag{3.50}$$

and the matrix $\mathbf{V}_{M-1}$ is constructed in the same way as the matrix $\mathbf{V}$ of (3.10), except that the time-window frequency vectors $\boldsymbol{v}_{M-1}(f)$ have length equal to $M-1$, i.e.:

$$\mathbf{V}_{M-1} = [\boldsymbol{v}_{M-1}(f_0), \boldsymbol{v}_{M-1}(f_1), \ldots, \boldsymbol{v}_{M-1}(f_{L-1})] \in \mathbb{C}^{(M-1)\times L}, \tag{3.51}$$

$$\boldsymbol{v}_{M-1}(f) = \left[1, e^{-2\pi f}, e^{-2\pi f 2}, \ldots, e^{-2\pi f (M-2)}\right]^{\mathrm{T}} \in \mathbb{C}^{M-1}. \tag{3.52}$$

As one can see from (3.50), the vectors $\boldsymbol{s}_{M-1}[n]$ and $\boldsymbol{s}_{M-1}[n+1]$ can be generated respectively as $\boldsymbol{s}_{M-1}[n] = \boldsymbol{V}_1 \boldsymbol{\Phi}^n \boldsymbol{h}$ and $\boldsymbol{s}_{M-1}[n+1] = \boldsymbol{V}_2 \boldsymbol{\Phi}^n \boldsymbol{h}$, where:

$$\mathbf{V}_1 = \mathbf{V}_{M-1}, \tag{3.53}$$

$$\mathbf{V}_2 = \mathbf{V}_{M-1}\boldsymbol{\Phi} = \mathbf{V}_1\boldsymbol{\Phi}, \tag{3.54}$$

i.e. the "generating" matrices $\mathbf{V}_1$ and $\mathbf{V}_2$ are related through a "rotation" determined by the phase shift described in the matrix $\boldsymbol{\Phi}$. Moreover, the $M-1$ dimensional subspaces spanned by the columns of $\mathbf{V}_1$ and $\mathbf{V}_2$ lie in the signal sub-space, since:

$$\begin{aligned} \mathbf{V} &= \begin{bmatrix} \mathbf{V}_1 \\ e^{j2\pi f_0 (M-1)}, \ldots, e^{j2\pi f_{L-1}(M-1)} \end{bmatrix} = \begin{bmatrix} 1, \ldots, 1 \\ \mathbf{V}_{M-1}\boldsymbol{\Phi} \end{bmatrix} = \begin{bmatrix} 1, \ldots, 1 \\ \mathbf{V}_2 \end{bmatrix} \\ &= \begin{bmatrix} \mathbf{V}_1 \\ ** \end{bmatrix} = \begin{bmatrix} ** \\ \mathbf{V}_2 \end{bmatrix}. \end{aligned} \tag{3.55}$$

Finally, it can be said that $\boldsymbol{s}[n]$ has a rotational invariance property since it can be decomposed in portions which can be related through simple phase shifts, i.e. rotations on the unitary circle.

The ESPRIT algorithm exploits this relation for the estimation of the discrete time frequencies f_l. In particular, consider the singular values decomposition (SVD) of $\mathbf{X}$, which results in:

$$\mathbf{X} = \mathbf{U} \cdot \boldsymbol{\Sigma} \cdot \mathbf{L}^{\mathrm{H}}, \tag{3.56}$$

where $\mathbf{L} \in \mathbb{C}^{N \times N}$ and $\mathbf{U} \in \mathbb{C}^{M \times M}$ are unitary matrices (i.e. $\mathbf{L} \cdot \mathbf{L}^{\mathrm{H}} = \mathbf{I}_N$, $\mathbf{U} \cdot \mathbf{U}^{\mathrm{H}} = \mathbf{I}_M$), and $\boldsymbol{\Sigma} \in \mathbb{C}^{M \times N}$ is a diagonal matrix containing the $\mathrm{rank}(\mathbf{X}) = M_r \leq \min\{M, N\}$ non-null singular values of $\mathbf{X}$, i.e.:

$$\boldsymbol{\Sigma} = \begin{bmatrix} \boldsymbol{\Sigma}_{M_r} & \mathbf{0}_{M_r \times (N-M_r)}, \\ \mathbf{0}_{(M-M_r)\times M_r} & \mathbf{0}_{(M-M_r)\times(N-M_r)} \end{bmatrix} \in \mathbb{C}^{M \times N} \tag{3.57}$$

$$\hat{\boldsymbol{\Sigma}}_{M_r} = \mathrm{diag}\left\{[\sigma_0, \ldots, \sigma_{M_r-1}]^{\mathrm{T}}\right\} \in \mathbb{C}^{M_r \times M_r}, \tag{3.58}$$

where $\sigma_0 > \cdots > \sigma_{M_r-1} > 0$. Upon observing that the eigendecomposition of $\hat{\mathbf{R}}_x$ can be obtained using the SVD of $\mathbf{X}$ as:

$$\hat{\mathbf{R}}_x = \mathbf{X} \cdot \mathbf{X}^{\mathrm{H}} = \mathbf{U} \cdot \boldsymbol{\Sigma} \cdot \mathbf{L} \cdot \mathbf{L}^{\mathrm{H}} \cdot \boldsymbol{\Sigma}^{\mathrm{H}} \cdot \mathbf{U}^{\mathrm{H}} = \mathbf{U} \cdot \boldsymbol{\Sigma} \cdot \boldsymbol{\Sigma}^{\mathrm{H}} \cdot \mathbf{U}^{\mathrm{H}}, \tag{3.59}$$

one can note that the square root of the eigenvalues of $\hat{\mathbf{R}}_x$ are the singular values of $\mathbf{X}$. Moreover, the columns of $\mathbf{U}$ are an estimation for the eigenvectors of $\mathbf{R}_x$ and hence it can be assumed that they span the signal and the noise sub-spaces. Hence, $\mathbf{U}$ can be decomposed as:

$$\mathbf{U} = [\mathbf{U}_s \, \mathbf{U}_w] \, , \tag{3.60}$$

where the matrix $\mathbf{U}_s \in \mathbb{C}^{M \times L}$ collects the estimates for the signal space eigenvectors (which correspond to the L largest singular values) and the matrix $\mathbf{U}_w \in \mathbb{C}^{M \times (M-L)}$ collects the estimates for the noise sub-space eigenvectors.

The matrix $\mathbf{U}_s$ can be split into two sub-matrices $\mathbf{U}_{s,1} \in \mathbb{C}^{(M-1) \times L}$ and $\mathbf{U}_{s,2} \in \mathbb{C}^{(M-1) \times L}$, as was done for $\mathbf{V}$ in Eq. (3.55), resulting in:

$$\mathbf{U}_s = \begin{bmatrix} \mathbf{U}_{s,1} \\ ** \end{bmatrix} = \begin{bmatrix} ** \\ \mathbf{U}_{s,2} \end{bmatrix} . \tag{3.61}$$

Since the columns of $\mathbf{U}_s$ and $\mathbf{V}$ span the same space (i.e. the signal sub-space), then it exists a full rank mapping matrix $\mathbf{T} \in \mathbb{C}^{L \times L}$ which satisfy:

$$\mathbf{V} = \mathbf{U}_s \mathbf{T}, \tag{3.62}$$

which can also be applied to the respective sub-matrices, obtaining:

$$\mathbf{V}_1 = \mathbf{U}_{s,1} \mathbf{T}, \tag{3.63}$$

$$\mathbf{V}_2 = \mathbf{U}_{s,2} \mathbf{T}. \tag{3.64}$$

Based on the observation regarding the rotational invariance of the signal $\boldsymbol{s}[n]$ and similarly to Eq. (3.54), also the matrices $\mathbf{U}_{s,1}$ and $\mathbf{U}_{s,2}$ are related through a rotation matrix $\boldsymbol{\Psi} \in \mathbb{C}^{L \times L}$:

$$\mathbf{U}_{s,2} = \mathbf{U}_{s,1} \boldsymbol{\Psi}. \tag{3.65}$$

Hence, manipulating Eq. (3.63)-(3.65), an estimate for $\boldsymbol{\Phi}$ can be obtained as:

$$\mathbf{V}_2 = \mathbf{U}_{s,2} \mathbf{T} = \mathbf{U}_{s,1} \boldsymbol{\Psi} \mathbf{T}, \tag{3.66}$$

$$\mathbf{V}_2 = \mathbf{V}_1 \boldsymbol{\Phi} = \mathbf{U}_{s,1} \mathbf{T} \boldsymbol{\Phi}, \tag{3.67}$$

$$\boldsymbol{\Psi} \mathbf{T} = \mathbf{T} \boldsymbol{\Phi}, \tag{3.68}$$

and finally:

$$\boldsymbol{\Psi} = \mathbf{T} \boldsymbol{\Phi} \mathbf{T}^{-1}. \tag{3.69}$$

Hence, $\boldsymbol{\Phi}$ can be obtained through an eigendecomposition of $\boldsymbol{\Psi}$. Let ψ_l, $l = 0, \ldots, L-1$, be the L eigenvalues of $\boldsymbol{\Psi}$. Then, the discrete time frequency estimates $\hat{f}_l$ can be calculated as:

$$\hat{f}_l = -\frac{1}{2\pi} \arg \{\psi_l\} \, . \tag{3.70}$$

The last step in the ESPRIT algorithm is the calculation of the matrix $\boldsymbol{\Psi}$ from the eigenvectors $\mathbf{U}_s$. The original approch consists in solving the linear system

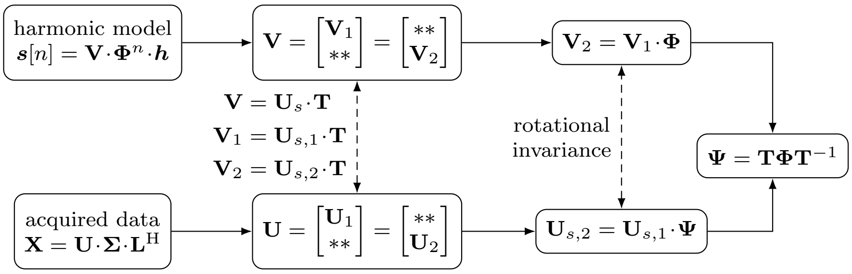

Figure 3.2 – Flowgraph of the derivation of the ESPRIT algorithm.

represented in Eq. (3.65). Since $M-1 \geq L$, then an exact solution for that system might not exist. Hence, the least square solution is given by:

$$\mathbf{\Psi} = \mathbf{U}_{s,1}^{\dagger}\mathbf{U}_{s,2}. \tag{3.71}$$

The literature reports a second and more accurate method for the calculation of $\mathbf{\Psi}$, called total least squares ESPRIT, but its descriptions goes beyond the scope of this thesis. The interested reader may refer to [36] and [43] for further details.

Figure 3.2 summarises the process for the derivation of the ESPRIT algorithm. As one can see, ESPRIT is based on the observation that the signal sub-space has a rotational invariance property, which exists also in the signal sub-space estimated from the data. Since these two spaces are related through a mapping $\mathbf{T}$, then the "rotation" $\mathbf{\Psi}$ that links $\mathbf{U}_{s,1}$ and $\mathbf{U}_{s,2}$ can be used to estimate the actual "rotation" $\mathbf{\Phi}$ that links $\mathbf{V}_1$ and $\mathbf{V}_2$, which contains the discrete time frequencies f_l to be estimated. Figure 3.3 shows the actual implementation of the ESPRIT algorithm. As one can see, the resolution of the estimated discrete time frequencies does not depend on any sampling interval, conversely to what happens for the MUSIC algorithm.

Finally, it should be mentioned that there is another version of the ESPRIT algorithm, called unitary ESPRIT. This version of the ESPRIT algorithm is demonstrated to be more accurate than the legacy one, and also permits to reduce the computational burden by avoiding computations with complex numbers. An interested reader can refer to [44] for further informations about unitary ESPRIT.

3.4 Estimation of the number of multipath components

So far, the number of received multipath components L was assumed to be known at the receiver. However, in real implementations, this assumption is not realizable. As demonstrated in the sections above, L is a parameter of fundamental importance for the implementation and the accuracy of the super-resolution algorithms. Hence, a method for the estimation of L has to be provided.

Consider the signal autocorrelation matrix $\mathbf{R}_x$ of (3.17). As demonstrated in (3.21)-(3.22), the eigenvalues of $\mathbf{R}_x$ can be divided in two sets: L eigenvalues equal to $\lambda_m = M\alpha_l^2 + \sigma_w^2$, $m = 0, \ldots, L-1$, corresponding to the L received paths, and $M-L$

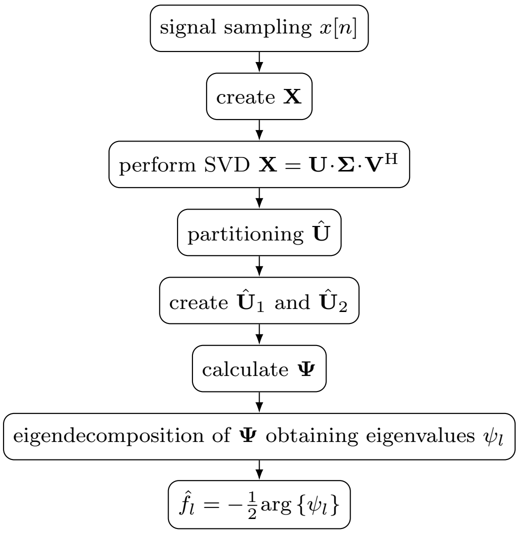

Figure 3.3 – Flowgraph of the implementation of the ESPRIT algorithm.

equal noise eigenvalues $\lambda_m = \sigma_w^2$, $m = L, \ldots, M-1$. If $\mathbf{R}_x$ is known at the receiver, the number of received multipath components L can be easily determined through the calculation of the eigenvalues of $\mathbf{R}_x$: the quantity $M - L$ can be determined by computing the number of equal eigenvalues, and hence L can be calculated as $M - (M - L)$.

However, in real implementations, the actual signal autocorrelation matrix $\mathbf{R}_x$ is not known at the receiver, which can only compute its estimation $\hat{\mathbf{R}}_x$. The estimated autocorrelation matrix has with high probability all different eigenvalues, hence the estimation of the number of multipath components is not as simple as in the case of known $\mathbf{R}_x$. Nevertheless, the eigenvalues of $\hat{\mathbf{R}}_x$ are still a useful mean for understanding the number L of received multipath components. In situations where the square magnitude of all the channel gains $|h_l|^2$ is considerably higher than the noise variance σ_w^2 (i.e. high signal to noise ratio conditions), it is easy to fix a threshold for distinguishing noise eigenvalues and signal eigenvalues, thus determining the value of L. On the other hand, when the values $|h_l|^2$ and σ_w^2 are comparable, then it becomes challenging to distinguish between noise and signal eigenvalues. Hence, a rigorous and reliable method for the estimation of L that relies on the estimated autocorrelation matrix eigenvalues is needed.

3.4.1 The minimum descriptive length method

The authors of [15] propose the minimum descriptive length (MDL) method of [45] for the estimation of the number of multipath components when using super-resolution algorithms for the estimation of the TOAs in a multipath environment.

Consider the eigenvalues λ_m of the autocorrelation matrix $\hat{\boldsymbol{R}}_x \in \mathbb{C}^{M\times M}$, estimated using N snapshots. Suppose that the eigenvalues are sorted in descending

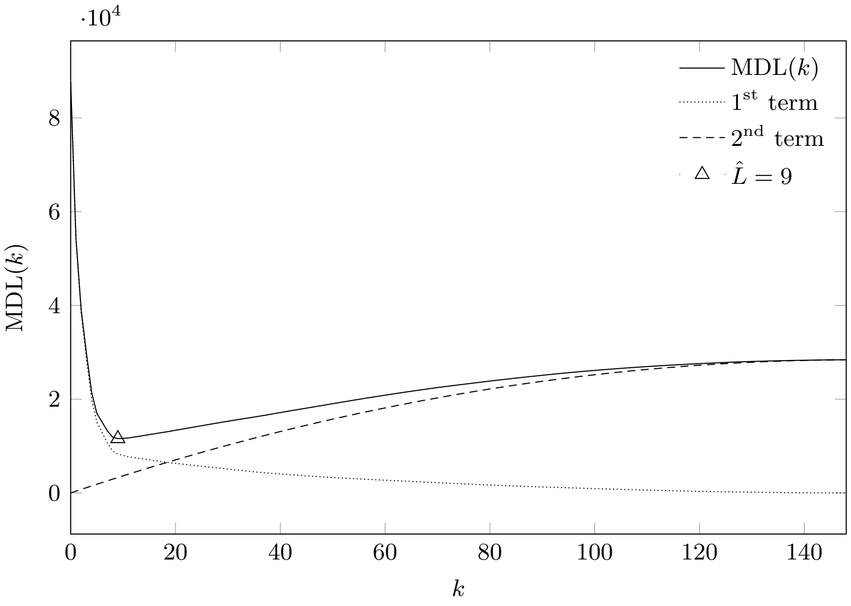

Figure 3.4 – Typical MDL curve. The parameters used for the calculation of this curve are $M = 150$ and $N = 300$. The 1^{st} and 2^{nd} term of (3.72) are also plot.

order, i.e. $\lambda_0 \geq \lambda_1 \geq \cdots \geq \lambda_{M-1}$. The MDL criterion relies on the following metric:

$$\mathrm{MDL}(k) = -N(M-k)\log\left(\frac{\prod_{i=k}^{M-1}\lambda_i^{1/(M-k)}}{\frac{1}{M-k}\sum_{i=k}^{M-1}\lambda_i}\right) + p(k), \quad k = 0,\ldots,M-1, \tag{3.72}$$

where $p(k)$ is given by:

$$p(k) = \frac{1}{2}k(2M-k)\log N. \tag{3.73}$$

Finally, the number of estimated multipath components is obtained by minimizing the metric MDL(k), i.e.:

$$\hat{L} = \arg\min_{k=0,\ldots,M-1}\{\mathrm{MDL}(k)\}. \tag{3.74}$$

A typical shape of the MDL metric is shown in Figure 3.4. A reader who is interested in further details about the theoretical derivation of the MDL criterion should refer to [45] for further details.

Chapter 4

Bounds on TOA estimation

This chapter briefly presents the theoretical performance bounds used for assessing the effectiveness of the various considered signals as reference signals for time of arrival estimation. For having a best case preliminary performance assessment, the considered scenario is the simplest one, i.e., a pulse transmission in the additive white Gaussian noise channel. The used bounds are the Cramér-Rao bound and the Ziv-Zakai bound. The knowledge of such bounds is a matter of interest since they provide a theoretical bound on the performance in terms of root mean square error of any time of arrival estimator over a range of signal-to-noise ratios.

4.1 Problem formulation

4.1.1 Signal parameter estimation problem

Consider a complex signal $s(t; A) \in \mathbb{C}$, $\forall t$, which is a potentially non-linear function of the parameter A. Suppose that the noise $w(t)$ modeled as a zero-mean complex Gaussian random process is added to $s(t; A)$, obtaining the signal:

$$r(t) = s(t; A) + w(t) \in \mathbb{C}. \tag{4.1}$$

The random process $w(t)$ constitutes a zero-mean complex random variable (RV) for every fixed value of t. In particular, $w(t) \sim \mathcal{CN}(0, \sigma_w^2)$, meaning that the RV $w(t)$ has a complex Gaussian distribution with zero mean and σ_w^2 variance, where the real and the imaginary part of $w(t)$ are uncorrelated zero-mean $\sigma_w^2/2$ variance Gaussian RVs. Finally, suppose that $r(t)$ is time-limited to the interval $[0, T_\mathrm{o}[$.

A signal parameter estimation problem consists in the estimation of the parameter A based on the knowledge of the signal $r(t)$. The case where no *a priori* knowledge on the distribution of A is available will be considered. In such a scenario, the optimal estimator for the parameter A is the maximum likelihood (ML) estimator, which requires the knowledge of the likelihood function $\Lambda[r(t); A]$, that expresses the probability of having measured $r(t)$ given that the parameter used in

$s(t;A)$ is A. When $\Lambda[r(t);A]$ is available, then the estimation of A can be performed as:

$$\hat{A} = \arg\max_{A} \left\{\Lambda[r(t);A]\right\}. \tag{4.2}$$

The calculation of the likelihood function is the first problem that has to be faced when performing a signal parameter estimation. This is because $r(t)$ is potentially a function pertaining to an infinite dimensional space [46]. Hence, $\Lambda[r(t);A]$ has to be calculated through an approximation. The procedure of [47] will be used in the following for the explanation of such problem. In particular, consider the K coefficient approximation of $r(t)$:

$$r(t) \simeq r_K(t) = \sum_{k=1}^{K} r_k \psi_k(t), \tag{4.3}$$

where the K functions $\{\psi_k(t)\}_{k=1}^{K}$ defined in $[0, T_\mathrm{o}[$ constitute an orthonormal basis obtained through the Gram - Schmidt process. The parameters r_k can be obtained as:

$$\begin{aligned} r_k &= \int_0^{T_\mathrm{o}} r(t)\psi_k(t)\mathrm{d}t = \int_0^{T_\mathrm{o}} \left(s(t;A) + w(t)\right)\psi_k(t)\mathrm{d}t \\ &= s_k(A) + w_k, \end{aligned} \tag{4.4}$$

where:

$$s_k(A) = \int_0^{T_\mathrm{o}} s(t;A)\psi_k(t)\mathrm{d}t, \tag{4.5}$$

$$w_k = \int_0^{T_\mathrm{o}} w(t)\psi_k(t)\mathrm{d}t. \tag{4.6}$$

Under the assumption of white noise (i.e., if one assumes that the autocorrelation function of the noise is $R_w(\tau) = \sigma_w^2\,\delta(\tau)$), it can be demonstrated that the parameters $\{w_k\}_{k=1}^{K}$ are K $\mathcal{CN}(0, \sigma_w^2)$ distributed uncorrelated (and, since Gaussian, independent) RVs. Using this approach one can define the finite set of parameters:

$$\boldsymbol{r} = [r_1\, r_2\, \ldots\, r_K]^\mathrm{T} \in \mathbb{C}^K, \tag{4.7}$$

which is an equivalent representation of $r_K(t)$ and an approximate representation of $r(t)$, which is more precise as the number K of element of the basis increases, i.e.:

$$\lim_{K\to\infty} r_K(t) = r(t). \tag{4.8}$$

A likelihood function may be easily computed for $\boldsymbol{r}$ as $\Lambda[r_K(t);A] = p_{\boldsymbol{r}|A}(\boldsymbol{r}|A)$, leading to the function:

$$\begin{aligned} \Lambda[r_K(t);A] &= \prod_{k=1}^{K} \frac{1}{\pi\sigma_w^2} \exp\left\{-\frac{|r_k - s_k(A)|^2}{\sigma_w^2}\right\} \\ &= \frac{1}{(\pi\sigma_w^2)^K} \exp\left\{-\frac{1}{\sigma_w^2}\sum_{k=1}^{K} |r_k - s_k(A)|^2\right\}. \end{aligned} \tag{4.9}$$

As one can see, (4.9) is not well defined if $K \to \infty$. Consequently, a different approach has to be followed for the calculation of $\Lambda[r(t); A]$. Looking at (4.2), one can note that $\Lambda[r(t); A]$ may be divided by an arbitrary quantity that does not depend on A, leaving the result of the estimation unchanged. Hence, the likelihood function of (4.9) may be divided by the probability density function (PDF) of measuring $r(t)$ (and hence its approximate K coefficients representation $\boldsymbol{r}$) when there is no signal, i.e.:

$$p(\boldsymbol{r}|\text{no signal}) = p_{\boldsymbol{w}}(\boldsymbol{r}) = \prod_{k=1}^{K} \frac{1}{\sigma_w^2} \exp\left\{-\frac{|r_k|^2}{\sigma_w^2}\right\}, \tag{4.10}$$

which also corresponds to the PDF of the noise vector $\boldsymbol{w} = [w_1 \ldots w_K]^{\mathrm{T}} \in \mathbb{C}^K$. Performing this operations, one obtains:

$$\Lambda_1[r_K(t); A] = \frac{\Lambda[r_K(t); A]}{p_{\boldsymbol{w}}(\boldsymbol{r})} = \exp\left\{-\frac{1}{\sigma_w^2}\sum_{k=1}^{K} |r_k - s_k(A)|^2 + |r_k|^2\right\}. \tag{4.11}$$

Finally, by letting $K \to \infty$ in (4.11), one obtains:

$$\begin{aligned}\Lambda_1[r(t); A] &= \exp\left\{-\frac{1}{\sigma_w^2}\int_0^{T_\mathrm{o}} |r(t) - s(t; A)|^2 + |r(t)|^2 \mathrm{d}t\right\} \\ &= \exp\left\{\frac{2}{\sigma_w^2}\int_0^{T_\mathrm{o}} \mathfrak{Re}\left\{r^*(t)s(t; A)\right\} \mathrm{d}t - \frac{1}{\sigma_w^2}\int_0^{T_\mathrm{o}} |s(t; A)|^2 \mathrm{d}t\right\}\end{aligned} \tag{4.12}$$

By taking its natural logarithm, (4.12) can also be expressed as:

$$\log \Lambda_1[r(t); A] = \frac{2}{\sigma_w^2}\int_0^{T_\mathrm{o}} \mathfrak{Re}\left\{r^*(t)s(t; A)\right\} \mathrm{d}t - \frac{1}{\sigma_w^2}\int_0^{T_\mathrm{o}} |s(t; A)|^2 \mathrm{d}t \tag{4.13}$$

Hence, the ML estimate of A may be obtained using the likelihood function of (4.13) instead of $\Lambda[r(t); A]$, obtaining:

$$\hat{A} = \arg\max_{A}\left\{\frac{2}{\sigma_w^2}\int_0^{T_\mathrm{o}} \mathfrak{Re}\left\{r^*(t)s(t; A)\right\} \mathrm{d}t - \frac{1}{\sigma_w^2}\int_0^{T_\mathrm{o}} |s(t; A)|^2 \mathrm{d}t\right\}. \tag{4.14}$$

The maximization problem of (4.14) is referred to as a parameter estimation problem for a signal corrupted by Gaussian noise.

4.1.2 Time of arrival estimation

Consider the complex baseband representation of a communication system in an additive white Gaussian noise (AWGN) channel given by:

$$r(t) = s(t - \tau) + w(t) \in \mathbb{C},\ t \in [0, T_\mathrm{o}[, \tag{4.15}$$

where $r(t) \in \mathbb{C}$, $s(t) \in \mathbb{C}$ and $w(t) \in \mathbb{C}$ represent respectively the complex envelopes of the received signal, transmitted signal and thermal noise. The thermal noise is modeled as a stationary zero mean $\sigma_w^2 = \mathcal{N}_0$ variance complex Gaussian random process, and hence $w(t) \sim \mathcal{CN}(0, \mathcal{N}_0)$, $\forall t$. In (4.15), the parameter τ models the time that the signal $s(t)$ takes to propagate to the receiver after its transmission, i.e., it models the time of arrival. The signal $s(t)$ is time limited to the interval $[0, T_s[$ with $T_s < T_\mathrm{o}$, i.e., $s(t) \neq 0$ only if $t \in [0, T_s[$. Moreover, $s(t)$ has an energy equal to:

$$\mathcal{E}_s = \int_0^{T_s} |s(t)|^2 \mathrm{d}t. \tag{4.16}$$

The problem of the estimation of τ given the received signal $r(t)$ can be formulated as a signal parameter estimation problem analogous to the one of (4.1), where $A = \tau$ and $s(t; A) = s(t - \tau)$. Suppose that the receiver acquires the received signal in the interval $[0, T_\mathrm{o}[$, where T_o is sufficiently large for the transmitted signal to be completely received. Then there is an *a priori* knowledge on the distribution of τ, which is supposed to be uniformly distributed in the interval $[0, T_\mathrm{o} - T_s[$. Since:

$$\int_0^{T_\mathrm{o}} |s(t; A)|^2 \mathrm{d}t = \int_0^{T_\mathrm{o}} |s(t - \tau)|^2 \mathrm{d}t = \mathcal{E}_s \text{ if } \tau \in [0, T_\mathrm{o} - T_s[, \tag{4.17}$$

is independent from τ, then the optimal estimator for the time of arrival (TOA) of a signal in an AWGN channel is:

$$\hat{\tau} = \arg \max_{\tau \in [0, T_\mathrm{o} - T_s[} \left\{ \int_0^{T_\mathrm{o}} \mathfrak{Re} \left\{ r^*(t) s(t - \tau) \right\} \mathrm{d}t \right\}. \tag{4.18}$$

Upon defining the cross-correlation between the received signal $r(t)$ and the transmitted signal $s(t)$ as:

$$R_{r,s}(\tau) = \int_0^{T_\mathrm{o}} \mathfrak{Re} \left\{ r^*(t) s(t - \tau) \right\} \mathrm{d}t, \quad \tau \in [0, T_\mathrm{o} - T_s[, \tag{4.19}$$

then the estimator of (4.18) becomes:

$$\hat{\tau} = \arg \max_{\tau \in [0, T_\mathrm{o} - T_s[} \left\{ R_{r,s}(\tau) \right\}, \tag{4.20}$$

which is usually referred to as cross-correlation based estimator. Since the cross-correlation $R_{r,s}(\tau)$ can be expressed as:

$$\begin{aligned} R_{r,s}(\tau) &= \int_0^{T_\mathrm{o}} \mathfrak{Re} \left\{ (s^*(t) + w^*(t)) s(t - \tau) \right\} \mathrm{d}t \\ &= \int_0^{T_\mathrm{o}} \mathfrak{Re} \left\{ s^*(t) s(t - \tau) \right\} \mathrm{d}t + \int_0^{T_\mathrm{o}} \mathfrak{Re} \left\{ w^*(t) s(t - \tau) \right\} \mathrm{d}t \\ &= R_{s,s}(\tau) + R_{w,s}(\tau), \end{aligned} \tag{4.21}$$

then it is evident that the performance of the TOA estimation of the signal $s(t)$ in the AWGN channel strongly depends on its shape, and in particular on the shape of its auto-correlation function $R_{s,s}(\tau)$.

4.1.3 The performance of an estimator

As can be seen from (4.14), the result of an estimation is a RV since it is itself a function of a RV (in the case of the TOA estimation, $\hat{\tau}$ is a RV since it is a function of $r(t)$, which is a RV). Hence, the performance of an estimation can only be described statistically [48].

Firstly, the estimators which are usually considered have the property to yield on average the correct value. These estimators are referred to as unbiased estimators. In the case of the TOA estimation, if $\hat{\tau}$ is the result of an unbiased estimation, then:

$$\mathbb{E}\left[\hat{\tau}\right] = \tau \quad \forall \tau. \tag{4.22}$$

But the unbiasedness of an estimator does not imply that this is a good estimator. Hence, a second parameter has to be introduced for quantifying its performance. An optimality criterion which is frequently adopted for searching for good unbiased estimators is the minimum variance criterion. According to this criterion, an unbiased estimator is as good as its variance $\mathrm{Var}(\hat{\tau})$ is small. This criterion is derived from a more general one, which can be applied also to biased estimators, and aims to minimising the mean square error (MSE) that occurs in the estimation. The MSE quantifies the average square distance between the estimation and the real value of the parameter, and is defined as:

$$\mathrm{MSE}\left(\hat{\tau}\right) = \mathbb{E}\left[\left(\hat{\tau} - \tau\right)^2\right]. \tag{4.23}$$

Upon defining the bias $b(\hat{\tau})$ of the estimator $\hat{\tau}$ as:

$$b(\tau) = \mathbb{E}\left[\hat{\tau}\right] - \tau, \tag{4.24}$$

then (4.23) can be expressed as:

$$\begin{aligned}\mathrm{MSE}\left(\hat{\tau}\right) &= \mathbb{E}\left[\left(\hat{\tau} - \mathbb{E}\left[\hat{\tau}\right] + b(\tau)\right)^2\right] \\ &= \mathbb{E}\left[\left(\hat{\tau} - \mathbb{E}\left[\hat{\tau}\right]\right)^2\right] + b^2(\tau) + 2\mathbb{E}\left[b(\tau)\left(\hat{\tau} - \mathbb{E}\left[\hat{\tau}\right]\right)\right] \\ &= \mathrm{Var}\left(\hat{\tau}\right) + b^2(\tau). \end{aligned} \tag{4.25}$$

As one can see, if the estimator is unbiased (i.e. $b(\tau) = 0$, $\forall \tau$), then the minimum MSE criterion corresponds to the minimum variance criterion. A criterion which is equivalent to the minimum MSE criterion is the minimum root mean square error (RMSE) criterion, which aims to minimise:

$$\mathrm{RMSE}\left(\hat{\tau}\right) = \sqrt{\mathrm{MSE}\left(\hat{\tau}\right)}. \tag{4.26}$$

In the particular case of a TOA estimation, the RMSE of $\hat{\tau}$ depends on the signal-to-noise ratio (SNR) of the received signal, defined as:

$$\gamma = \frac{\mathcal{E}_s}{\mathcal{N}_0}. \tag{4.27}$$

Hence, if one wants to evaluate the performance of a TOA estimator, one has to calculate a SNR vs RMSE curve: estimators having smaller values of RMSE for a fixed SNR are better estimators for that SNR.

A lower bound on the RMSE that can be obtained in a given TOA estimation scenario would be a useful benchmark tool for quantifying the effectiveness of an estimator. In particular, a lower bound on the RMSE would quantify the minimum SNR which is required for obtaining a given RSME.

4.2 The Cramér-Rao bound

The Cramér-Rao bound (CRB) is a lower bound on the variance of an unbiased estimator. It is by far the easiest bound to determine [48] and it is widely used in the evaluation of the performance of several types of estimators.

Consider the estimation problem where the scalar parameter ϑ has to be estimated based on the observation $\boldsymbol{x}$. Assume that the likelihood function $p_{\boldsymbol{x}|\vartheta}(\boldsymbol{x}|\vartheta)$ satisfies the condition:

$$\mathbb{E}_{\boldsymbol{x}}\left[\frac{\partial \log p_{\boldsymbol{x}|\vartheta}(\boldsymbol{x}|\vartheta)}{\partial \vartheta}\right] = 0 \quad \forall \vartheta. \tag{4.28}$$

Then, it can be demonstrated that the unbiased estimator $\hat{\vartheta}$ must satisfy the bound:

$$\mathrm{Var}\left(\hat{\vartheta}\right) \geq \frac{1}{-\mathbb{E}_{\boldsymbol{x}}\left[\frac{\partial^2 \log p_{\boldsymbol{x}|\vartheta}(\boldsymbol{x}|\vartheta)}{\partial \vartheta^2}\right]}, \tag{4.29}$$

where the derivative is evaluated at the true value of ϑ [48]. Note that the likelihood function $p_{\boldsymbol{x}|\vartheta}(\boldsymbol{x}|\vartheta)$ can be divided by any arbitrary function f that does not depend on ϑ since:

$$\frac{\partial}{\partial \vartheta} \log \frac{p_{\boldsymbol{x}|\vartheta}(\boldsymbol{x}|\vartheta)}{f} = \frac{\partial}{\partial \vartheta} \log p_{\boldsymbol{x}|\vartheta}(\boldsymbol{x}|\vartheta) - \frac{\partial}{\partial \vartheta} \log f = \frac{\partial}{\partial \vartheta} \log p_{\boldsymbol{x}|\vartheta}(\boldsymbol{x}|\vartheta). \tag{4.30}$$

Consider now the signal parameter estimation problem of (4.1), where A is estimated using the estimator $\hat{A}$, which is a function of the measured signal $r(t)$. The Cramér-Rao bound (CRB) for $\hat{A}$ is given by:

$$\mathrm{Var}\left(\hat{A}\right) \geq \frac{1}{-\mathbb{E}_{r(t)}\left[\frac{\partial^2 \log \Lambda_1[r(t);A]}{\partial A^2}\right]}, \tag{4.31}$$

where $\log \Lambda_1[r(t); A]$ is expressed in (4.13) and can be used instead of the logarithm of the likelihood function thanks to the observation of (4.30). The bound of (4.31) can be simplified by taking the second derivative of $\log \Lambda_1[r(t); A]$, which corresponds to:

$$\frac{\partial}{\partial A}\left[\frac{2}{\mathcal{N}_0}\int_0^{T_\mathrm{o}} \mathfrak{Re}\left\{r^*(t)\frac{\partial}{\partial A}s(t;A)\right\}\mathrm{d}t - \frac{1}{\mathcal{N}_0}\int_0^{T_\mathrm{o}} \frac{\partial}{\partial A}|s(t;A)|^2 \mathrm{d}t\right]. \tag{4.32}$$

Then, since:

$$\frac{\partial}{\partial A}|s(t;A)|^2 = 2\mathfrak{Re}\left\{s^*(t;A)\frac{\partial}{\partial A}s(t;A)\right\}, \tag{4.33}$$

one obtains:

$$\begin{aligned}
\text{Eq. (4.32)} &= \frac{\partial}{\partial A}\left[\frac{2}{\mathcal{N}_0}\int_0^{T_\mathrm{o}} \mathfrak{Re}\left\{(r(t)-s(t;A))^* \frac{\partial}{\partial A}s(t;A)\right\}\mathrm{d}t\right] \\
&= \frac{2}{\mathcal{N}_0}\int_0^{T_\mathrm{o}} \mathfrak{Re}\left\{\frac{\partial}{\partial A}\left[(r(t)-s(t;A))^* \frac{\partial}{\partial A}s(t;A)\right]\right\}\mathrm{d}t \\
&= \frac{2}{\mathcal{N}_0}\int_0^{T_\mathrm{o}} -\left|\frac{\partial}{\partial A}s(t;A)\right|^2 + \mathfrak{Re}\left\{\frac{\partial^2}{\partial A^2}s(t;A)\,(r(t)-s(t;A))^*\right\}\mathrm{d}t.
\end{aligned} \tag{4.34}$$

By taking the expectation over all the possible values of $r(t)$ one obtains:

$$\begin{aligned}
\mathbb{E}_{r(t)}\left[-\frac{\partial^2}{\partial A^2}\log\Lambda_1[r(t);A]\right] &= \frac{2}{\mathcal{N}_0}\int_0^{T_\mathrm{o}}\left|\frac{\partial}{\partial A}s(t;A)\right|^2\mathrm{d}t + \\
&\quad + \int_0^{T_\mathrm{o}} \mathfrak{Re}\left\{\frac{\partial^2}{\partial A^2}s(t;A)\,(\mathbb{E}\left[r(t)\right]-s(t;A))^*\right\}\mathrm{d}t \\
&= \frac{2}{\mathcal{N}_0}\int_0^{T_\mathrm{o}}\left|\frac{\partial}{\partial A}s(t;A)\right|^2\mathrm{d}t,
\end{aligned} \tag{4.35}$$

since $\mathbb{E}[r(t)] = s(t;A)\ \forall t$. Moreover, using the same algebra as above, it can be demonstrated that the regularity condition of (4.28) is also satisfied when using $\log\Lambda_1[r(t);A]$ instead of the likelihood function, at the condition that $s(t;A)$ is a "smooth" function of A. Finally, by substituting (4.35) in (4.31), one obtains the CRB for the estimation of the parameter A in the transmission of the signal $s(t;A)$, which can be expressed as:

$$\mathrm{Var}\left(\hat{A}\right) \geq \frac{1}{\frac{2}{\mathcal{N}_0}\int_0^{T_\mathrm{o}}\left|\frac{\partial}{\partial A}s(t;A)\right|^2\mathrm{d}t}. \tag{4.36}$$

Consider now the case of TOA estimation described in Section 4.1.2, where $A=\tau$ and $s(t;A)=s(t-\tau)$. Then, since:

$$\int_0^{T_\mathrm{o}}\left|\frac{\partial}{\partial\tau}s(t-\tau)\right|^2\mathrm{d}t = \int_0^{T_s}\left|\frac{\mathrm{d}s(t)}{\mathrm{d}t}\right|^2\mathrm{d}t, \tag{4.37}$$

the CRB for a TOA estimation in an AWGN channel becomes:

$$\mathrm{Var}\left(\hat{\tau}\right) \geq \frac{1}{2\frac{\mathcal{E}_s}{\mathcal{N}_0}\beta^2} = \frac{1}{2\gamma\beta^2} = C(\gamma), \tag{4.38}$$

where:

$$\beta^2 = \frac{1}{\mathcal{E}_s}\int_0^{T_s}\left|\frac{\mathrm{d}s(t)}{\mathrm{d}t}\right|^2\mathrm{d}t = \frac{1}{\mathcal{E}_s}\int_{-\infty}^{+\infty}(2\pi f)^2|S(f)|^2 df. \tag{4.39}$$

In (4.39), the Parseval's rule for the continuous time Fourier transform has been invoked. The quantity β of (4.39) is often referred to as Gabor bandwidth (GB), and expresses the root mean square value of the spectral content of the signal $s(t)$. In the TOA estimation case, the regularity condition of (4.28) becomes equivalent to the existence of the derivative $\frac{\mathrm{d}s(t)}{\mathrm{d}t}$, or to the convergence of the integral in the RHS of (4.39).

The CRB can be calculated very easily and gives an accurate prediction on the RMSE performance of unbiased estimators for large SNRs, but has two main limitations. As said, it can be demonstrated that the CRB is accurate only for large values of SNR. This happens mainly because the ML estimator (which represents the optimum if no *a priori* knowledge is available for the parameter to be estimated) is unbiased only for large values of SNR. Moreover, the CRB can be calculated only for certain reference signals $s(t)$. In particular, the CRB is defined only when $s(t)$ is a “smooth” function of t [49], i.e., the regularity condition of (4.28) has to be satisfied.

Modified versions of the CRB (e.g., the bound proposed in [46]) were proposed in the literature for an easy calculation of the bound in presence of nuisance parameters in the estimation problem. This may be useful for evaluating bounds on TOA estimation when other unknown signal paramteres that influence the received signal such Doppler shift or complex channel gains exist but are not estimated.

As one can see from (4.38), the greater the GB of a signal, the smaller will be its CRB and ultimately its RMSE performance for high values of γ. This consideration suggests that a suitable characteristic of a TOA estimation reference signal is to have the greatest possible GB. According to the definition of (4.39), a signal with such properties can be obtained by pushing the available power on the edges of the available bandwidth. The analysis reported in Chapter 5 of this thesis will reveal that designing a reference signal by considering only its GB does not always lead to a good RMSE performance in a wide range of SNR values.

4.3 The Ziv-Zakai bound

The Ziv-Zakai bound (ZZB) was first proposed by J. Ziv and M. Zakai in [50] and then improved by the same authors in [49]. Afterwards, the bound was further improved by the author of [51] thanks to the adoption of the so called Bellini-Tartara valley filling function.

The ZZB is derived specifically for the TOA estimation problem, by using a detection theory approach. Consider the TOA estimation problem of (4.15), which consists on the estimation of the TOA τ of the transmitted signal $s(t)$ using the received signal having a complex baseband representation $r(t)$ given by:

$$r(t) = s(t-\tau) + w(t) \ \in \mathbb{C}, \ t \in [0, T_\mathrm{o}[. \tag{4.40}$$

Let $[0, T_\mathrm{o}[$ denote the *a priori* interval for the estimation problem, i.e., the receiver knows only that $\tau \in [0, T_\text{o}[$. Then, it can be demonstrated that [49,51]:

$$\text{MSE}\,(\hat{\tau}) \geq \frac{1}{T_\text{o}} \int_0^{T_\text{o}} \Delta\,(T_\text{o} - \Delta) Q\left(\sqrt{\gamma\,(1 - \rho_s(\Delta))}\right) d\Delta = Z(\gamma), \tag{4.41}$$

$$\text{MSE}\,(\hat{\tau}) \geq \frac{1}{T_\text{o}} \int_0^{T_\text{o}} \Delta\, G\left\{(T_\text{o} - \Delta) Q\left(\sqrt{\gamma\,(1 - \rho_s(\Delta))}\right)\right\} d\Delta = Z_\text{v}(\gamma), \tag{4.42}$$

where:

- $Q(\cdot)$ denotes the Q-function, which is the complementary cumulative density function for a zero mean unitary variance Gaussian distribution, i.e.:

$$Q(x) = \frac{1}{\sqrt{2\pi}} \int_x^{+\infty} e^{-\frac{u^2}{2}} \,\mathrm{d}u\ ; \tag{4.43}$$

- $G\{\cdot\}$ is the Bellini-Tartara valley filling function [51], defined as:

$$G\{f(x)\} = \begin{cases} \max_{u \in]x,+\infty[} \{f(u)\} & \text{if } f(x) < \max_{u \in]x,+\infty[} f(u) \\ f(x) & \text{otherwise} \end{cases}\ ; \tag{4.44}$$

- $\rho_s(\Delta)$ is the normalized single-sided autocorrelation function of the signal $s(t)$, defined as:

$$\rho_s(\Delta) = \begin{cases} \frac{1}{\mathcal{E}_s} R_{s,s}(\Delta) = \frac{1}{\mathcal{E}_s} \int_0^{T_s} \mathfrak{Re}\left\{s^*(t - \Delta) s(t)\right\} \mathrm{d}t & \Delta \in [0, T_s[\\ 0 & \text{otherwise} \end{cases}\ , \tag{4.45}$$

  and T_s is the duration of $s(t)$, i.e. $s(t)$ is defined in the interval $[0, T_s[$, as detailed in section 4.1.2.

The formulation of $Z(\gamma)$ of (4.41) is the one proposed in [49], while the definition of $Z_\text{v}(\gamma)$ of (4.42) is the one proposed in [51] and employing the valley filling function, and is proved to be a tighter bound.

There is an important remark about the ZZB to take into account, regarding the limit value that the noise variance $\mathcal{N}_0$ can assume. If $\mathcal{N}_0 \to +\infty$ (i.e. when the SNR decreases to zero), then both (4.41) and (4.42) become:

$$\text{MSE}\,(\hat{\tau}) \geq \frac{1}{2T_\text{o}} \int_0^{T_\text{o}} \Delta\,(T_\text{o} - \Delta)\,\mathrm{d}\Delta = \frac{T_\text{o}^2}{12}, \tag{4.46}$$

since $Q(0) = 1/2$. As one can note, $T_\text{o}^2/12$ is the variance of a continuous RV having a uniform distribution in the interval $[0, T_\text{o}[$. This fact has a physical explanation: when the noise level is too high (i.e., when the SNR approaches zero), the best thing that an estimator can do is to randomly select a time of arrival in the *a priori* interval. Hence, at an SNR that approaches zero, the RMSE is greater or equal to the variance of a RV uniformly distributed in the *a priori* interval.

As one can see from (4.41)-(4.42), obtaining a closed form expression of the ZZB can be a challenging task, since it involves the integration of a Q-function that depends on the auto-correlation function of the considered signal. In particular, in the case of the ZZB $Z(\gamma)$ of (4.41), the function to be integrated is $\Delta \cdot \eta(\gamma, \Delta)$, where:

$$\eta(\gamma, \Delta) = \begin{cases} (T_\text{o} - \Delta) \cdot Q\left(\sqrt{\xi(\gamma, \Delta)}\right) & \text{if } \Delta < T_s \\ (T_\text{o} - \Delta) \cdot Q\left(\sqrt{\gamma}\right), & \text{otherwise} \end{cases}, \tag{4.47}$$

and $\xi(\gamma, \Delta) = \gamma \cdot (1 - \rho_s(\Delta))$. The literature presents closed form expressions of the ZZB for only a few simple signals (e.g., the rectangular impulse, in [49]). Hence, in this research work, the ZZB was always computed through numerical integration procedures. The numerical calculation of the integral:

$$\int_0^{T_\text{o}} \Delta \cdot \eta\left(\gamma, \Delta\right) \, \text{d}\Delta, \tag{4.48}$$

is challenging especially for high values of γ, since $\eta(\gamma, \Delta)$ presents an high peak near $\Delta = 0$ and then goes steeply to zero. In oder words, $\eta(\gamma, \Delta)$ is a stiff function for high values of γ, i.e., a function which is hard to be integrated numerically, unless the step size is taken to be extremely small. This is showed in the figures of the examples of Section 4.4.

Although it is difficult to compute, the ZZB has several advantages in respect to the CRB:

- it can be applied to a larger class of functions $s(t)$, e.g., it can be applied for the calculation of a bound for the TOA estimation performance of rectangular pulse shaped orthogonal frequency division multiplexing (OFDM) signals;
- it is a tight bound also for very low values of SNR;
- it takes into account the *a priori* knowledge on the TOA which has to be estimated.

Modified versions of the ZZB (e.g., the one proposed in [52]) were proposed in the literature for an easy calculation of the bound in presence of nuisance parameters in the estimation problem.

4.4 Some examples of bound computations

In this section, the CRB and the ZZB are computed for three test signals, in order to highlight some important behaviours of the bounds in respect to the variation of some signals' properties. The Ziv-Zakai bound $Z_\text{v}(\gamma)$ of [51] is considered, i.e., the one exploiting the valley filling function.

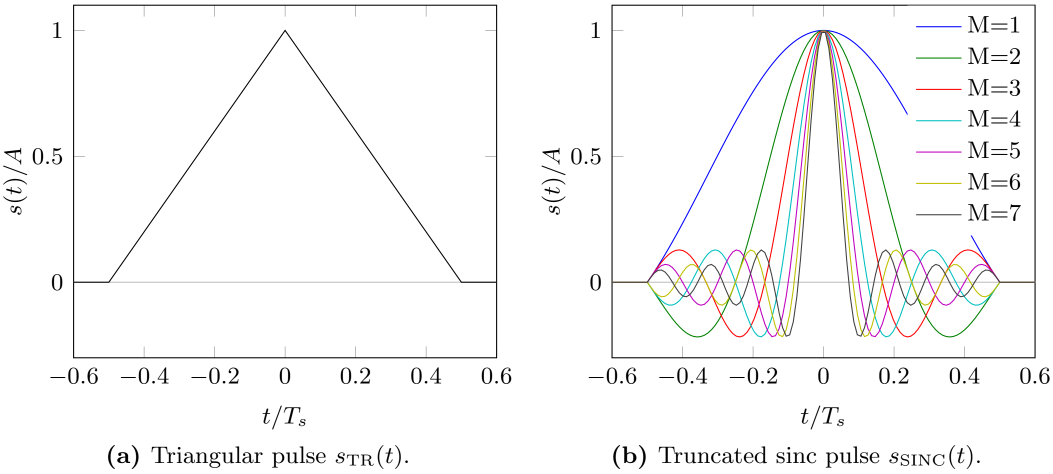

(a) Triangular pulse $s_{\mathrm{TR}}(t)$.

(b) Truncated sinc pulse $s_{\mathrm{SINC}}(t)$.

Figure 4.1 – Some of the test signals used.

Consider a triangular pulse reference signal $s_{\mathrm{TR}}(t)$ having duration T_s and main peak amplitude A, represented in Figure 4.1a and defined as:

$$s_{\mathrm{TR}}(t) = \begin{cases} 2A(\frac{1}{2} + \frac{t}{T_s}) & t \in \left]-\frac{T_s}{2}, 0\right] \\ 2A(\frac{1}{2} - \frac{t}{T_s}) & t \in \left]0, \frac{T_s}{2}\right] \\ 0 & \text{otherwise} \end{cases} . \tag{4.49}$$

This has a squared GB that can be easily evaluated in closed form, equal to:

$$\beta^2_{\mathrm{TR}} = \frac{1}{\mathcal{E}_s} \int_0^{T_s} \left| \frac{\mathrm{d}\, s_{\mathrm{TR}}(t)}{\mathrm{d}t} \right|^2 \mathrm{d}t = \frac{12}{T_s^2}. \tag{4.50}$$

The CRB and the ZZB of $s_{\mathrm{TR}}(t)$ are represented in Figure 4.2. The ZZB is calculated for different values of the *a priori* interval T_{o}. Two points should be noted. Firstly, it is evident that asymptotically, i.e., for high values of SNR, the ZZB and the CRB assume equal values. Secondly, for very low SNRs, the bound curve tends to the value of $T_{\mathrm{o}}/\sqrt{12}$ (which is represented in the figure by a dotted line for every value of T_{o}), according to the asymptotic behaviour described in (4.46). This shows the influence of the *a priori* search interval on the TOA estimation performance: the bigger the observation window, the worse will be the estimation performance for low values of SNR. The normalized auto-correlation function $\rho_s(\Delta)$ for the triangular impulse signal is depicted in Figure 4.3a, while the corresponding integrand function is plotted in Figure 4.3b for different values of the SNR γ. As one can see, for high SNRs the numerical integration of $\eta(\gamma, \Delta)$ may be challenging due to the stiffness of the function.

Consider now a signal defined as a truncated sinc function having a main lobe

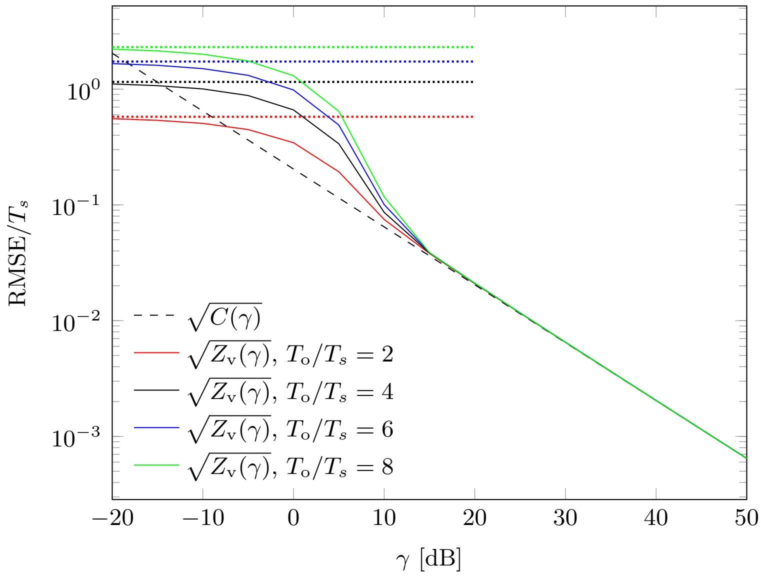

Figure 4.2 – CRB $C(\gamma)$ and ZZB $Z_{\mathrm{v}}(\gamma)$ for the triangular impulse signal $s_{\mathrm{TR}}(t)$ and different values of the *a priori* interval T_{o}. The dotted lines represent the asymptotic value of $T_{\mathrm{o}}/\sqrt{12}$ for every value of T_{o}.

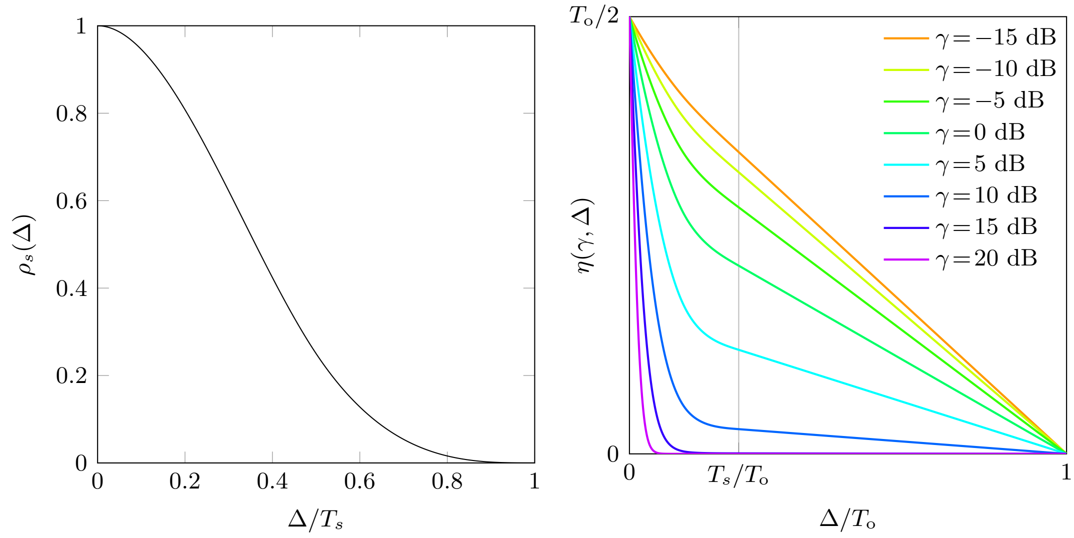

(a) Autocorrelation function of $s_{\mathrm{TR}}(t)$.

(b) ZZB integrand $\eta(\gamma, \Delta)$ for $s_{\mathrm{TR}}(t)$, $T_{\mathrm{o}} = 4T_s$, and various values of SNR.

Figure 4.3 – Autocorrelation and ZZB integrand function for the signal $s_{\mathrm{TR}}(t)$.

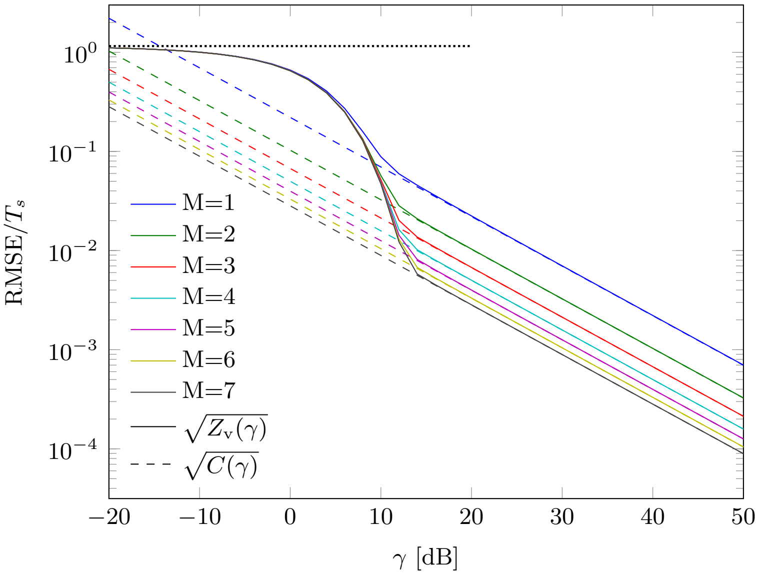

Figure 4.4 – ZZB of the truncated sinc signal $s_{\text{SINC}}(t)$ for different values of the parameter M. The CRBs for the corresponding signals are also plotted as a reference. The *a priori* interval is $T_o = 4T_s$ for all the curves.

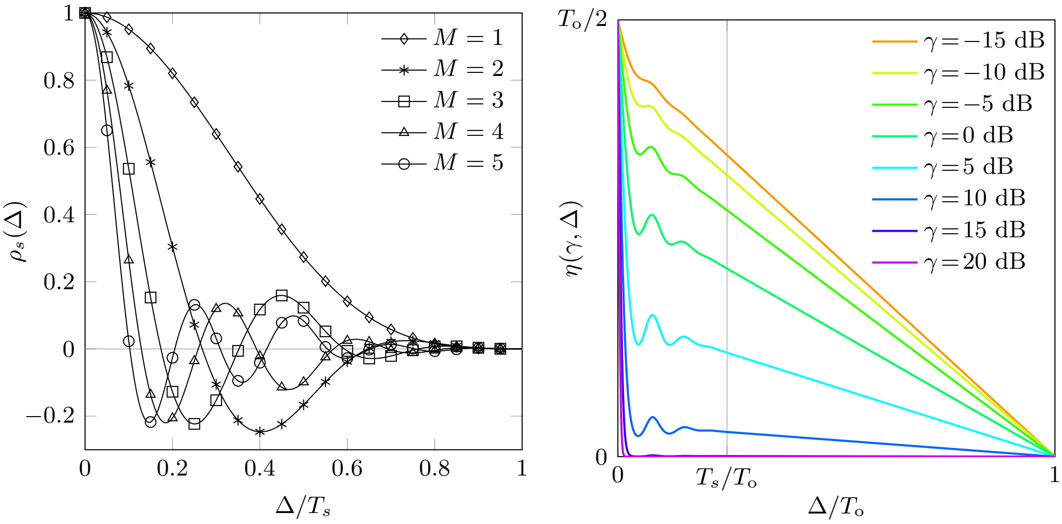

(a) Autocorrelation function of $s_{\text{SINC}}(t)$ for different values of the parameter M.

(b) ZZB integrand $\eta(\gamma, \Delta)$ for $s_{\text{SINC}}(t)$, $T_o = 4T_s$, $M = 4$ and various values of SNR.

Figure 4.5 – Autocorrelation and ZZB integrand function for the signal $s_{\text{SINC}}(t)$.

width that depends on the parameter M, i.e.:

$$s_{\text{SINC}}(t) = \begin{cases} A \operatorname{sinc}\left(\frac{2M}{T_s}t\right) = A\,\dfrac{\sin\left(\pi\frac{2M}{T_s}t\right)}{\pi\frac{2M}{T_s}t} & \text{if } t \in \left]-\frac{T_s}{2}, \frac{T_s}{2}\right] \\ 0 & \text{otherwise} \end{cases} . \tag{4.51}$$

The signal $_{\text{SINC}}(t)$ is represented in Figure 4.1b for different values of M. Differently from the triangular signal, $s_{\text{SINC}}(t)$ does not have a closed form expression for its GB, but the derivative $\frac{\mathrm{d}s_{\text{SINC}}(t)}{\mathrm{d}t}$ exists and it is well defined. The CRB and the ZZB of $s_{\text{SINC}}(t)$ are represented in Figure 4.4 for different values of the parameter M. In Figure 4.4, the dashed lines represent the CRB, and the solid lines represent the ZZB. In this case, the *a priori* interval is assumed to be four times greater than the duration of the impulse, i.e., $T_{\text{o}} = 4T_s$. As one can see, for very low SNRs, the ZZB tends to the value $T_{\text{o}}/\sqrt{12}$, while in the asymptotic region it assumes the same values as the corresponding CRB. The normalized auto-correlation function $\rho_s(\Delta)$ for the truncated sinc impulse signal is depicted in Figure 4.5a for different values of M. As one can see, higher values of M correspond to narrower pulses and hence to narrower autocorrelation functions, leading to a better TOA estimation performance in the high SNR region. This phenomenon can also be analyzed in the frequency domain: a higher value of M leads a narrower pulse, which has a greater bandwidth, and hence a bigger GB, leading to better asymptotic RMSE TOA estimation performance. The integrand function for the $M = 4$ truncated sinc signal is plotted in Figure 4.5b for different values of the SNR γ. Again, for high SNRs the function $\eta(\gamma, \Delta)$ becomes stiff and hence challenging to be numerically integrated.

Finally, the rectangular pulse $s_{\text{R}}(t)$ is considered, defined as:

$$s_{\text{R}}(t) = \begin{cases} A & t \in \left]-\frac{T_s}{2}, \frac{T_s}{2}\right] \\ 0 & \text{otherwise} \end{cases} . \tag{4.52}$$

This type of signal does not admit a finite GB, i.e., the integral that defines β^2 does not converge. Hence, the corresponding CRB can not be evaluated. Fortunately, the ZZB does not have any restriction on the signal regularity, and hence can be evaluated even for the rectangular pulse. Figure 4.6 represents the ZZB of $s_{\text{R}}(t)$ together with ZZBs of the triangular impulse and of the truncated sinc signal with $M = 7$. Again, the *a priori* interval is assumed to be $T_{\text{o}} = 4T_s$ and for very low SNRs the bound attains the value of $T_{\text{o}}/\sqrt{12}$. The normalized auto-correlation function $\rho_s(\Delta)$ for the rectangular impulse signal is depicted in Figure 4.7a while the corresponding integrand function is plotted in Figure 4.7b for different values of the SNR γ. As one can note from Figure 4.6, the asymptotic slopes of the ZZB curves differ. The bounds corresponding to the triangular and the sinc-shaped signal predict a RMSE that requires a 20 dB growth of the SNR for decreasing of a factor ten. Conversely, the bound corresponding to the rectangular signal predict a RMSE that requires a 10 dB growth of the SNR for decreasing of a factor ten. The double slope that characterizes the ZZB of the rectangular impulse signal may be a consequence

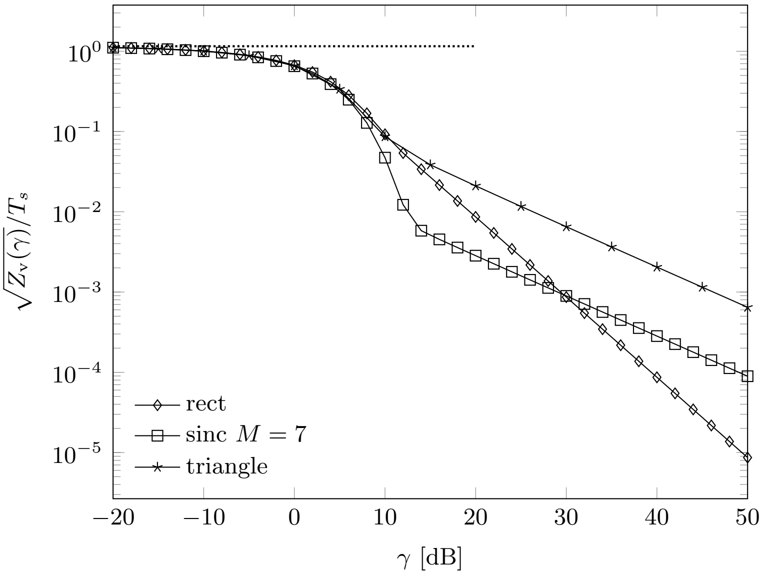

Figure 4.6 – ZZB of the rectangular signal $s_\mathrm{R}(t)$. The ZZBs of the triangular signal and of the truncated sinc signal with $M = 7$ signal are also shown as a comparison. The *a priori* interval is $T_\mathrm{o} = 4T_s$.

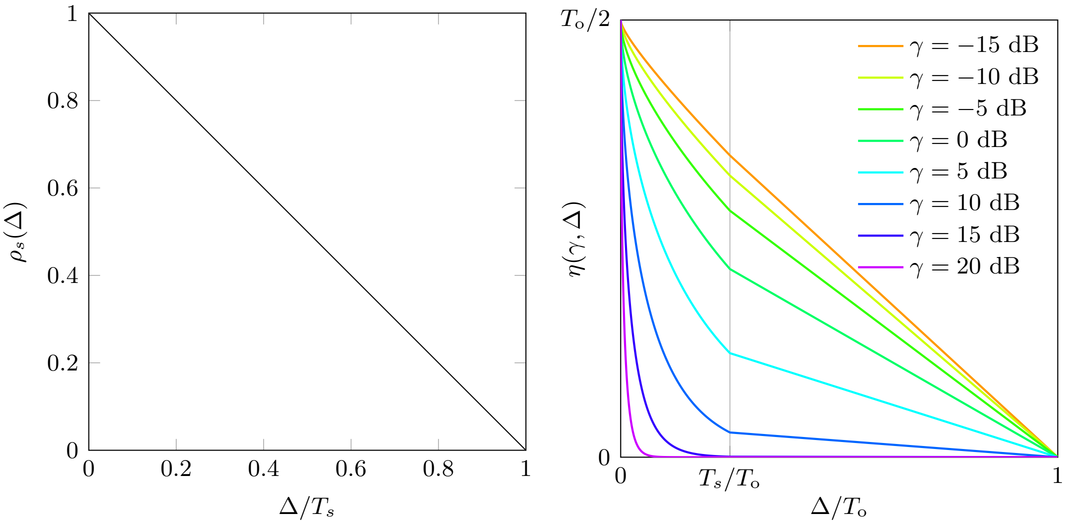

(a) Autocorrelation function of $s_\mathrm{R}(t)$.

(b) ZZB integrand $\eta(\gamma, \Delta)$ for $s_\mathrm{R}(t)$, $T_\mathrm{o} = 4T_s$, and various values of SNR.

Figure 4.7 – Autocorrelation and ZZB integrand function for the signal $s_\mathrm{R}(t)$.

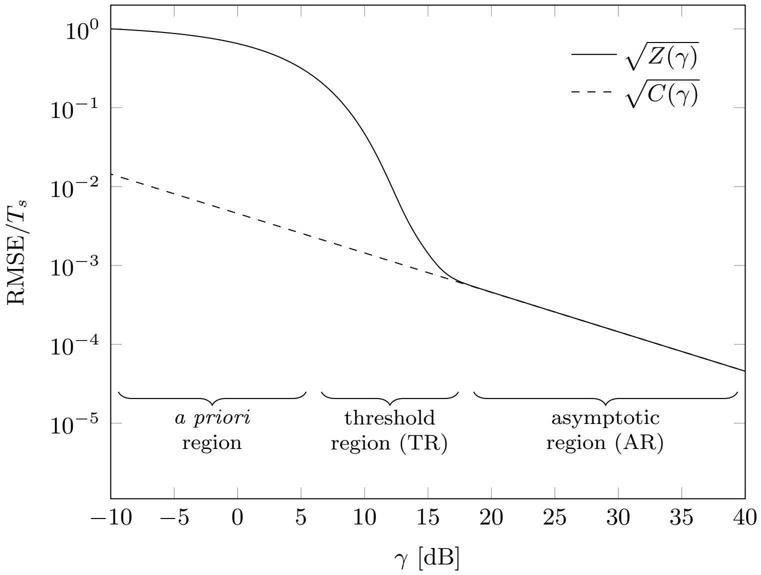

Figure 4.8 – Estimation RMSE characteristic error regions.

of the discontinuities that characterize $s_\mathrm{R}(t)$. Indeed, experimental investigations reported in [53], demonstrated that a single discontinuity in the reference signal is sufficient for producing a double slope in the corresponding ZZB. Since the signals with discontinuities are not physically realizable, they have not been considered in the remainder of the thesis, and hence only signals having a "normal" slope have been analyzed.

4.5 Estimation error regions

As one can note from Figure 4.2, Figure 4.4 and Figure 4.6, the ZZB curve may be divided in three principal regions [54, 55]. A first region, corresponding to low SNR values, corresponds to a RMSE which is mainly determined by the length of the *a priori* interval T_o in respect to the signal duration T_s. This region is referred to as the *a priori* region. The second region, which is referred to as the threshold region, usually corresponds to low-to-medium values of the SNR. In this region, the RMSE curve detaches from the *a priori* value $T_\mathrm{o}/\sqrt{12}$ for reaching the asymptotic behaviour of the RMSE performance, which corresponds to the CRB. The shape and the slope of the threshold region is characteristic of each signal, and mainly depends on the shape of its autocorrelation function $\rho_s(\Delta)$. Signals exhibiting a faster transition between the threshold and the asymptotic region will be preferred for TOA estimation systems that have to work in the low-to-medium SNR range. Finally, the third region is referred to as the asymptotic region or error floor region, and corresponds to high values of SNR. In this region, the ZZB curve overlaps the CRB. These three regions are depicted in Figure 4.8, where the borders between these regions are only qualitative.

Part II

Original results

Chapter 5

Bounds on TOA estimation of LTE OFDM signals

This chapter presents a study of the performance of the orthogonal frequency division multiplexing (OFDM) signals when used as reference signals for time of arrival estimation. A model for physically realizable signals is exploited to address the root mean square error (RMSE) performance of realistic OFDM waveforms. Thanks to the adoption of different sub-carriers power distributions and of a new performance figure, the estimation RMSE is studied both in the threshold and asymptotic signal-to-noise ratio regions, where a performance trade-off is revealed. Finally, different Long Term Evolution OFDM reference signals are compared as reference signals for time of arrival estimation, in order to establish the best signal to use for such purpose.[1]

5.1 Introduction

As has already been mentioned, orthogonal frequency division multiplexing (OFDM) has become a successful and widely used wireless communication technique, which, thanks to its robustness and low complexity, has been adopted in a conspicuous number of wireless communication standards, including Third Generation Partnership Project (3GPP) Long Term Evolution (LTE), terrestrial digital video broadcasting (DVB-T), digital audio broadcasting (DAB), and IEEE 802.11 a/g/n/ac [31]. The fundamentals of this technique have been described in Section 2.1.

The ubiquity of this communication paradigm has determined an interest in the OFDM technology also in the field of positioning, where the intrinsic characteristics of the OFDM signals may be studied for understanding how to design a proper OFDM waveform suitable for pseudorange calculation. Concerning this aspect, the estimation of the time of arrival (TOA) of a signal is a fundamental topic. Indeed,

---

[1] The content of this chapter was partly published on M. Driusso, M. Comisso, F. Babich, and C. Marshall, "Performance Analysis of Time of Arrival Estimation on OFDM Signals," *IEEE Signal Processing Letters*, vol. 22, no. 7, pp. 983–987, Jul. 2015.

there are multiple reasons that make OFDM signals appealing for being used as reference signals in TOA estimation for pseudorange evaluation. Firstly, OFDM waveforms are usually wideband signals, and, as shown in Chapter 4, the wider the bandwidth, the smaller is the error due to noise when estimating the TOA of a signal. Moreover, when the environment is characterized by multipath propagation, signals with a larger bandwidth permit an easier separation of the different received paths' TOA. Secondly, the OFDM waveforms are multi-carrier signals, and hence their spectrum can be easily shaped by differently filling the transmitted sub-carriers, permitting an easy manipulation of the properties of the signal that affect the timing performance.

For this reason, this part of the thesis addresses the issue of assessing the performance of the LTE OFDM signals when used as reference signals in TOA estimation. More particularly, the TOA estimation performance of LTE OFDM waveforms in the additive white Gaussian noise (AWGN) case is analyzed, with the purpose to provide a best-case ranging accuracy indication, in contrast with more severe scenarios, such as the fading multipath channels. Moreover, only physically realizable OFDM signals have been considered for the presented analysis, by taking into account the effect of a realistic digital-to-analog converter (DAC) for the conversion of the OFDM time domain samples to the actual transmitted signal.

The analysis presented is twofold. Firstly, the OFDM waveforms are analyzed from the signal's design point of view. The characterization is performed by properly shaping the power spectral density of the OFDM signals, so as to infer the influence of the sub-carriers' power distribution on the TOA estimation root mean square error (RMSE). The TOA estimation RMSE behavior is explored not only in the asymptotic region, but also in the threshold region, by introducing a novel quantity, which is complementary to the widely adopted Gabor bandwidth (GB). This permitted to reveal a trade-off between asymptotic and threshold performance, showing that the GB is not the only parameter to consider for designing a TOA reference signal. Secondly, the TOA estimation performance of some of the actual LTE OFDM downlink reference signals is compared, in order to understand which of those signals is the most suited to be used for pseudorange measurements, and how the LTE system parameters influence the timing performance.

The remainder of this chapter is organized as follows. Section 5.2 presents a review of the related works found in the literature, together with the motivations of the analysis presented. Section 5.3 introduces the system model used for addressing the performance of the OFDM signals. Section 5.4 analyzes the metrics used for quantifying the TOA estimation performance of the considered signals. Section 5.5 discusses the numerical results obtained through computer simulations. Finally, Section 5.6 summarizes the most relevant conclusions.

5.2 Related works and motivations

The design of TOA-based positioning systems that exploit OFDM waveforms has been addressed in the literature in several works, where both performance analysis and new estimation approaches are proposed. The authors of [56] propose a comprehensive work where OFDM signals are exploited for time difference of arrival (TDOA) measurements in a distributed positioning system. In [57], a system based on OFDM signals TOA measurement is proposed for positioning in WLANs. The authors of [58] exploit the phase rotation induced by the channel delay on the OFDM symbol's sub-carriers for estimating the TOA, and propose this method for the next generation global navigation satellite systems (GNSSs). In [59], a method for positioning by jointly exploiting the direction of arrival (DOA) and the TOA of OFDM signals is proposed. In [60], the LTE positioning reference signal (PRS) signal is exploited for joint time and amplitude channel estimation in multipath scenarios.

Concerning the subject of LTE OFDM signals performance analysis, the authors of [61, 62] proposed an approximated Cramér-Rao bound (CRB) for OFDM signals for assessing the ranging performance obtainable with the LTE PRS under different types of interference. In [63], the same authors propose an analysis of the performance of the same signals under multipath conditions based on the concept of multipath error envelope.

Finally, the subject of OFDM signal design for TOA estimation has been faced in different works. In [17], the authors analyzed the possibility to use band-limited multi-carrier modulations for achieving selective accuracy in GNSSs, by exploiting the Ziv-Zakai bound (ZZB). A method based on the CRB to properly arrange the pilot tones on the sub-carriers of an OFDM symbol in order to achieve an accurate estimation of the timing and amplitude of the channel is proposed in [64]. In [65, 66], the CRB is again exploited for shaping the OFDM symbols' power spectrum, in order to achieve joint capacity maximization and TOA estimation accuracy in multipath channels.

Against this background, a careful investigation that jointly considers the asymptotic and the threshold TOA estimation performance of realistically modelled OFDM signals, and its dependence on the sub-carriers' power distribution, remains a partly unexplored issue. Moreover, a comparison of the TOA estimation performance of all the main LTE reference signals has not been found in the literature. These are the problems that have been addressed in the following sections of the presented work.

5.3 System model

A physically realizable OFDM signal model has been adopted for assessing the performance of different OFDM waveforms when used as reference signals in TOA estimation. In particular, the performed analysis is twofold. Firstly, by exploiting the power distributions defined in Section 5.3.2, the influence of different sub-carriers' arrangements on the TOA estimation RMSE is studied. Secondly, the TOA estimation performance of LTE reference signals described in Section 5.3.3 is compared, in order to determine which of the considered LTE waveforms is the most suited for time based range measurements.

5.3.1 OFDM signal model

The proposed investigation exploits the OFDM signal model described in Section 2.1, i.e., an OFDM signal defined by N_{sc} used sub-carriers out of $N_{\mathrm{dft}} > N_{\mathrm{sc}}$ available ones. The used sub-carriers are arranged symmetrically on each side of the direct current (DC) sub-carrier, $N_{\mathrm{sc}}/2$ on each side. As explained in Section 2.1, the DC sub-carrier is left empty and the reminder of the spectrum is padded out with empty sub-carriers, $(N_{\mathrm{dft}}-N_{\mathrm{sc}})/2$ in the negative range and $(N_{\mathrm{dft}}-N_{\mathrm{sc}})/2-1$ in the positive range. As a consequence, the parameter N_{sc} controls the available bandwidth for each considered OFDM waveform. The ideal complex baseband representation of the adopted OFDM signal is the same as (2.3), i.e.:

$$s(t) = \sum_{k=-N_{\mathrm{sc}}/2}^{N_{\mathrm{sc}}/2} g(t)\, S[k]\, e^{j2\pi k\Delta f t}\ , \quad t \in [0, T_s[, \tag{5.1}$$

where $g(t)$ is the shaping impulse, $S[k] \in \mathbb{C}$ is the symbol transmitted on the k^{th} sub-carrier (with $S[0] = 0$), $\Delta f = 1/T_s$ is the frequency separation between sub-carriers, and T_s is the OFDM symbol duration. Here, the OFDM symbol is considered without the corresponding cyclic prefix (CP), since this is usually discarded by the receiver as it contains the inter-symbol interference due to the previous transmitted symbols. The vector $\boldsymbol{S} = \left[S[-N_{\mathrm{sc}}/2], \ldots, S[k], \ldots, S[N_{\mathrm{sc}}/2]\right]^{\mathrm{T}} \in \mathbb{C}^{N_c+1}$, which contain the sub-carriers' content including the empty DC, is defined in order to satisfy the energy constraint $\|\mathbf{S}\|^2 = 1$.

Ideally, as explained in Section 2.1, $g(t)$ should be the rectangular function. However, in real world implementations, the actual shape of $g(t)$ is determined by the DAC, which generates the continuous time signal:

$$s_{\mathrm{c}}(t) = \sum_{n=0}^{N_{\mathrm{dft}}-1} s[n]\, p_w\!\left(t - \frac{n}{f_s}\right), \tag{5.2}$$

where $s[n] = s(t{=}n/f_s)$ is the sampled ideal OFDM signal, $f_s = N_{\mathrm{dft}}/T_s$ is the sampling frequency, and $p_\omega(t)$ is the impulse response of the DAC used for generating $s_{\mathrm{c}}(t)$ out of the samples $s[n]$. An ideal DAC is a low pass filter with a rectangular frequency response having the cut-off frequency set to match half the sampling frequency of the input discrete time signal. This corresponds to a DAC with an impulse response given by $\mathrm{sinc}\,(t \cdot f_s)$. Physically realizable DACs may be modeled as filters having a truncated sinc-shaped impulse response, i.e., $p_\omega(t) = \omega(t) \cdot \mathrm{sinc}\,(t \cdot f_s)$, with $\omega(t)$ denoting the windowing function that limits in time the sinc interpolating function. The set of the N_{dft} samples $\boldsymbol{s} = \left[s[0], \ldots, s[N_{\mathrm{dft}}-1]\right]^{\mathrm{T}} \in \mathbb{C}^{N_{\mathrm{dft}}}$ is usually

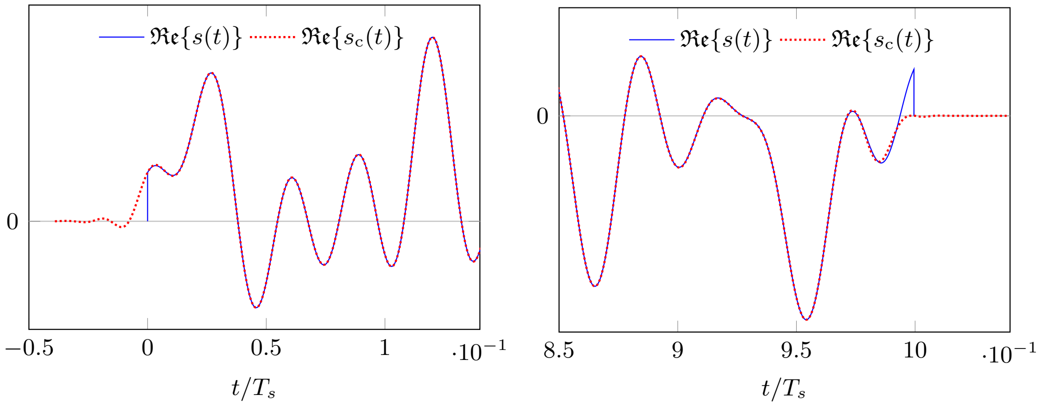

(a) Interval $[0, 0.1T_s]$.

(b) Interval $[0.9T_s, T_s]$.

Figure 5.1 – Comparison between the ideal rectangular pulse shaped OFDM signal $s(t)$ and the real DAC filtered signal $s_c(t)$. The Gibbs oscillations are evident in $t = 0$ and $t = T_s$.

obtained through a length N_{dft} inverse discrete Fourier transform (IDFT) operation on the sequence $\boldsymbol{S}$. More particularly, $\boldsymbol{s} = N_{\text{dft}} \cdot \text{IDFT}\{\tilde{\boldsymbol{S}}\}$, where:

$$\tilde{\boldsymbol{S}} = \left[0, S[1], \ldots, S[N_{\text{sc}}/2], \mathbf{0}^{\text{T}}_{N_{\text{dft}}-N_{\text{sc}}-1}, S[-N_{\text{sc}}/2], \ldots, S[-1]\right]^{\text{T}} \in \mathbb{C}^{N_{\text{dft}}}, \tag{5.3}$$

is a shifted and zero-padded version of $\boldsymbol{S}$. According to [67, p. 533], $\omega(t)$ may be defined by a Hamming windowing function, thus:

$$\omega(t) = \begin{cases} \alpha + (1-\alpha)\cos\left(2\pi t/T_\omega\right) & t \in [-T_\omega/2, T_\omega/2] \\ 0 & \text{otherwise} \end{cases}, \tag{5.4}$$

where $\alpha = 0.54$ and $T_\omega = 10/f_s$ is the adopted window width, which yields to an overall duration of $T_c = T_s + 10/f_s$ for $s_c(t)$.

Thus, instead of using the widely adopted ideal model in (5.1), this study adopts the realistic OFDM waveform in (5.2), hence considering the actual output of the DAC, that is, a physically realizable signal. Figure 5.1 shows an example of an OFDM signal obtained implementing a real digital to analog conversion. As one can see, the discontinuities due to the rectangular shaping function are smoothed by the DAC. In particular, the OFDM signal generated through the simulation of a real DAC shows the classical Gibbs oscillations in correspondence of the time instants where the ideal signal $s(t)$ presents discontinuities.

5.3.2 Sub-carrier power distributions

The OFDM framework is exploited for creating TOA reference signals having different power spectral densities. This is achieved by considering two sets of power distributions: $\mathcal{U}_{d,N_{\mathrm{sc}}}$ and $\mathcal{O}_{N_{\mathrm{a}},N_{\mathrm{sc}}}$. An $\mathcal{U}_{d,N_{\mathrm{sc}}}$ distribution defines the sub-carrier content $S[k]$, according to the sub-carrier distance d, as:

$$S[k] = \frac{1}{\sqrt{2N_{\mathrm{a}}}} \cdot \begin{cases} 1 & k \in \{\pm\left[N_{\mathrm{sc}}/2 - l(d+1)\right], l \in \mathcal{L}_{d,N_{\mathrm{sc}}}\} \\ 0 & \text{otherwise} \end{cases}, \tag{5.5}$$

where $N_{\mathrm{a}} = \lfloor N_{\mathrm{sc}}/[2(d+1)]\rfloor$ is half the number of non-null sub-carriers, and $\mathcal{L}_{d,N_{\mathrm{sc}}} = \{0, 1, \cdots, N_{\mathrm{a}} - 1\}$. Each distribution consists of a set of $2N_{\mathrm{a}}$ active equal power and equal initial phase sub-carriers separated by d empty sub-carriers, which are placed symmetrically with respect to the DC starting from the edges of the available bandwidth (i.e., from the sub-carrier index $k = N_{\mathrm{sc}}/2$). Hence, the parameter d controls the density of the active sub-carriers, with higher values of d corresponding to a lower density of active sub-carriers. The value of d is selected from the set $\mathcal{D}_{N_{\mathrm{sc}}} = \{d \in \mathbb{N} : 0 \leq d < N_{\mathrm{sc}}/2,\ I_{N_{\mathrm{sc}}}(d) = 2d + 1\}$, where:

$$I_{N_{\mathrm{sc}}}(d) = N_{\mathrm{sc}} - 2\,(d+1)\left(\left\lfloor \frac{N_{\mathrm{sc}}}{2(d+1)} \right\rfloor - 1\right) - 1, \tag{5.6}$$

is the number of empty sub-carriers determined by the adopted power distribution around the DC sub-carrier. By this choice, increasing the value of $d \in \mathcal{D}_{N_{\mathrm{sc}}}$, leads to larger spacing between the used sub-carriers and to a higher energy towards the edge of the band. For each $\mathcal{U}_{d,N_{\mathrm{sc}}}$ distribution, a corresponding $\mathcal{O}_{N_{\mathrm{a}},N_{\mathrm{sc}}}$ distribution can be derived by defining $S[k]$ as:

$$S[k] = \frac{1}{\sqrt{2N_{\mathrm{a}}}} \cdot \begin{cases} 1 & k \in \{\pm l : l \in [N_{\mathrm{sc}}/2 - N_{\mathrm{a}} + 1, N_{\mathrm{sc}}/2]\} \\ 0 & \text{otherwise} \end{cases}, \tag{5.7}$$

where, as previously outlined, N_{a} and d are related. Hence, each $\mathcal{O}_{N_{\mathrm{a}},N_{\mathrm{sc}}}$ distribution consists of N_{a} sub-carriers contiguously placed both at the negative and positive edges of the available bandwidth. As an example, Figure 5.2 shows the $\mathcal{U}_{d,N_{\mathrm{sc}}}$ and the corresponding $\mathcal{O}_{N_{\mathrm{a}},N_{\mathrm{sc}}}$ distributions for $N_{\mathrm{sc}} = 72$, which is the number of total available sub-carriers specified in the 3GPP LTE 1.4 MHz channel configuration [26].

5.3.3 Used LTE synchronization and reference signals

The analyzed LTE signals are LTE type 1 downlink signals with a normal CP and a sub-carriers' frequency separation of $\Delta f = 15\,\mathrm{kHz}$, and hence are designed according to the specifications detailed in Section 2.2. A total of four LTE signals have been considered throughout this analysis.

The first two considered signals are the primary synchronization signal (PSS) and the secondary synchronization signal (SSS). These are synchronization signals, which are designed for the time and frequency synchronization of the user equipment (UE), and for providing the UE with the physical cell identity (PCI) of the cell, which is given by $N_{\mathrm{ID}}^{\mathrm{cell}} = 3\,N_{\mathrm{ID}}^{(1)} + N_{\mathrm{ID}}^{(2)}$, $N_{\mathrm{ID}}^{\mathrm{cell}} \in [0, 504[\cap \mathbb{N}$, as described in Section 2.2.4.

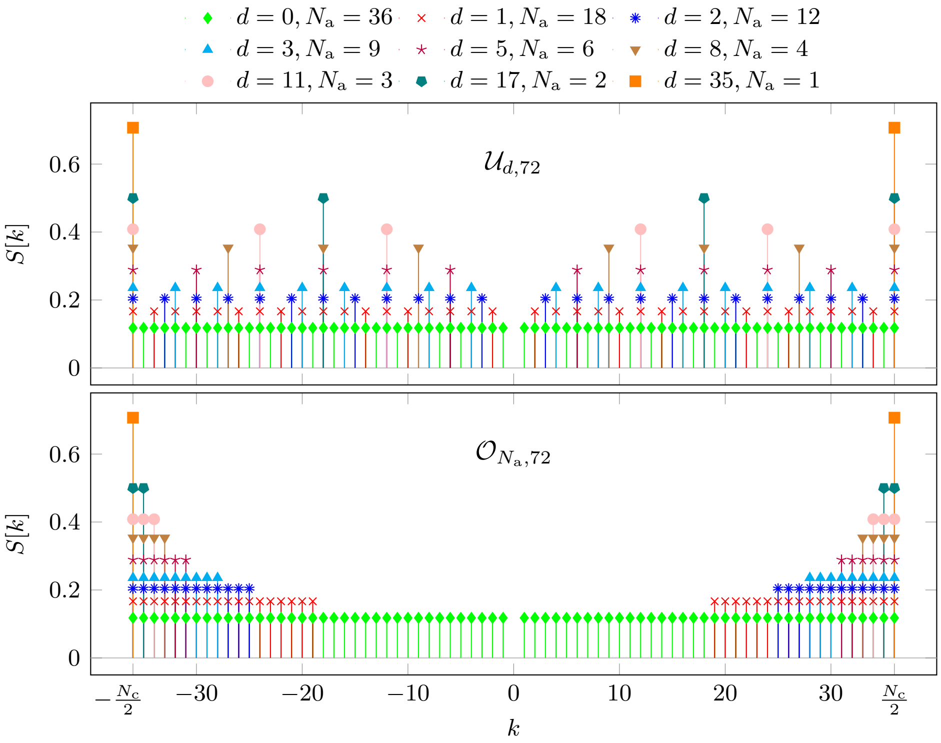

Figure 5.2 – $\mathcal{U}_{d,N_{sc}}$ and $\mathcal{O}_{N_a,N_{sc}}$ power distributions obtained using $N_{sc} = 72$ for $d \in \mathcal{D}_{72} = \{0, 1, 2, 3, 5, 8, 11, 17, 35\}$ and $N_a = \lfloor N_{sc}/[2(d+1)] \rfloor$.

For a detailed description of the synchronization signals and their mapping to the resource elements, the interested reader may refer to [26, p. 95].

The primary synchronization signal consists of a length 62 Zadhoff-Chu sequence having a root sequence index u, which depends on the parameter $N_{ID}^{(2)}$, that identifies a particular cell ID within a physical cell identity group (PCIG). The same PSS is transmitted only in the last OFDM symbol of the slots $n_s = 0$ and $n_s = 10$. The sequence is mapped to the sub-carriers $k = \{-31, \ldots, 31\}$ for all the channel configurations, and hence the PSS has always a rough actual band occupation of $62 \cdot \Delta f = 930\,\text{kHz}$. In our comparisons, the PSS was computed using $N_{ID}^{(2)} = 0$, which corresponds to the Zadhoff-Chu root sequence index $u = 25$. The parameters adopted for the generation of the used PSS are summarized in Table 5.1a.

The secondary synchronization signal is an interleaved concatenation of two length 31 m-sequences. The SSS is transmitted in the slots $n_s = 0$ and $n_s = 10$, in the OFDM symbol that occurs just before the one containing the PSS. Two different SSSs are defined for each slot $n_s \in \{0, 10\}$, and both depends on the PCIG $N_{ID}^{(1)}$. In particular, $N_{ID}^{(1)}$ determines the value of the tuple (m_0, m_1, m', q, q'), which ultimately controls the relative shift of the m-sequences that constitute the SSS. The sequence is mapped to the sub-carriers $k = \{-31, \ldots, 31\}$ for all the channel configurations, and hence also the SSS has always a rough actual bandwidth of $62 \cdot \Delta f = 930\,\text{kHz}$.

ID within the PCIG $N_{\mathrm{ID}}^{(2)}$	2
Zadhoff-Chu root u	20
slot in the LTE radio frame n_{s}	0
considered OFDM symbol in the $n_{\mathrm{s}}^{\mathrm{th}}$ slot l	6
actual bandwidth	930 kHz

(a) Parameters for the considered PSS.

PCIG $N_{\mathrm{ID}}^{(1)}$	62
(m_0, m_1, m', q, q')	$(8, 11, 70, 2, 2)$
slot in the LTE radio frame n_{s}	0
considered OFDM symbol in the $n_{\mathrm{s}}^{\mathrm{th}}$ slot l	5
actual bandwidth	930 kHz

(b) Parameters for the considered SSS.

Table 5.1 – Parameters used for the generation of the considered LTE synchronization signals.

In our comparisons, the SSS positioned in the OFDM symbol $l = 5$ of the slot $n_{\mathrm{s}} = 0$ was used, and it was generated setting $N_{\mathrm{ID}}^{(1)} = 67$ as the physical layer cell identity group. The parameter used for the generation of the used SSS are summarized in Table 5.1b.

The other two considered signals are the reference signals described in Section 2.2.2, namely, the positioning reference signal (PRS) and the cell specific reference signal (CRS). For a detailed description of the composition of the reference signals and their mapping to the resource elements, the interested reader may refer to [26, p. 76]. In our comparisons, the CRS signal pertaining to antenna port $p = 0$ (of a two antenna ports configuration), time slot $n_{\mathrm{s}} = 0$, OFDM symbol $l = 0$, and $N_{\mathrm{ID}}^{\mathrm{cell}} = 3$, and the PRS pertaining to time slot $n_{\mathrm{s}} = 1$, OFDM symbol $l = 1$ and $N_{\mathrm{ID}}^{\mathrm{cell}} = 3$ were considered. The parameter used for the generation of those signals are summarized in Table 5.2a and Table 5.2b, respectively. As described in Section 2.2.2, the symbols of both the PRS and the CRS occur every 6 sub-carriers in the frequency domain, i.e., twice per resource block (RB). Hence, the bandwidth that those reference signals occupy depends on the adopted channel bandwidth configuration, and is given by $[6(2\,N_{\mathrm{DL}}^{\mathrm{RB}} - 1) + 1]\Delta f = (N_{\mathrm{sc}}^{\mathrm{RB}}\,N_{\mathrm{DL}}^{\mathrm{RB}} - 5)\Delta f = (N_{\mathrm{sc}} - 5)\Delta f$, which is slightly less than the actual channel bandwidth $N_{\mathrm{sc}}\Delta f$.

5.4 TOA estimation performance evaluation

Consider the estimation of the TOA τ of the signal $s_{\mathrm{c}}(t)$ in an AWGN channel, given the received signal:

$$r(t) = s_{\mathrm{c}}(t - \tau) + w(t)\ , \quad t \in [0, T_{\mathrm{o}}[, \tag{5.8}$$

PCI $N_{\mathrm{ID}}^{\mathrm{cell}}$	3
slot in the LTE radio frame n_{s}	0
considered OFDM symbol in the $n_{\mathrm{s}}^{\mathrm{th}}$ slot l	0
antenna port p	0
actual bandwidth	$(N_{\mathrm{DL}}^{\mathrm{RB}} N_{\mathrm{sc}}^{\mathrm{RB}} - 5)\Delta f$

(a) Parameters for the considered CRS.

PCI $N_{\mathrm{ID}}^{\mathrm{cell}}$	3
slot in the LTE radio frame n_{s}	1
considered OFDM symbol in the $n_{\mathrm{s}}^{\mathrm{th}}$ slot l	1
actual bandwidth	$(N_{\mathrm{DL}}^{\mathrm{RB}} N_{\mathrm{sc}}^{\mathrm{RB}} - 5)\Delta f$

(b) Parameters for the considered PRS.

Table 5.2 – Parameters used for the generation of the considered LTE reference signals.

where the observation interval $[0, T_{\mathrm{o}}[$ is assumed *a priori* known to the receiver [49], and $w(t)$ is the zero mean complex Gaussian white noise. Defining the signal energy as $\mathcal{E}_s = \int_0^{T_{\mathrm{c}}} |s_{\mathrm{c}}(t)|^2 \mathrm{d}t$ and the noise power spectral density as $\mathcal{N}_0$, the signal-to-noise ratio (SNR) at the receiver is $\gamma = \mathcal{E}_s/\mathcal{N}_0$. If $\hat{\tau}$ is the result of the estimation of τ given $r(t)$, then the estimation mean square error (MSE) is given by $\mathrm{MSE}(\hat{\tau}) = \mathbb{E}\left[(\tau - \hat{\tau})^2\right]$. Now, as the main objective of this study, the TOA estimation root mean square error $\mathrm{RMSE}(\hat{\tau}) = (\mathrm{MSE}(\hat{\tau}))^{1/2}$ obtainable employing the OFDM signal model described in Section 5.3.1, is characterized through the sub-carrier power distributions described in Section 5.3.2 using the widely adopted CRB, and the tighter ZZB. Moreover, the same tools are exploited for comparing the performance of the LTE signals of Section 5.3.3.

5.4.1 Bounds on the estiomation RMSE

If an un-biased estimator is considered, then $\mathbb{E}[\hat{\tau}] = \tau$ and the estimation MSE is equal to the variance of the estimator $\mathrm{Var}(\hat{\tau}) = \mathbb{E}\left[(\hat{\tau} - \mathbb{E}[\hat{\tau}])^2\right]$, which can be lower-bounded using the CRB, as explained in Section 4.2. Identifying $S_{\mathrm{c}}(f) = \mathcal{F}\{s_{\mathrm{c}}(t)\}$ as the spectrum of $s_{\mathrm{c}}(t)$, the CRB, which can be computed only if $s_{\mathrm{c}}(t)$ satisfies some regularity conditions [48], can be expressed as $\mathrm{Var}(\hat{\tau}) \geq C(\gamma) = 1/(2\gamma\beta^2)$, where:

$$\beta^2 = \frac{1}{\mathcal{E}_s} \int_{-\infty}^{\infty} (2\pi f)^2 |S_{\mathrm{c}}(f)|^2 \mathrm{d}f, \tag{5.9}$$

is the squared Gabor bandwidth (GB) of $s_{\mathrm{c}}(t)$. It can be proved that the CRB is tight only in the asymptotic region, that is, for high values of γ [48,49]. Observe that, intuitively, to increase the GB in (5.9), one should increase the power concentration at the edges of the available bandwidth. This is the reason for the adoption of the distributions $\mathcal{U}_{d,N_{\mathrm{sc}}}$ and $\mathcal{O}_{N_{\mathrm{a}},N_{\mathrm{sc}}}$ defined in Section 5.3.2, which allow one to control the GB simultaneously reducing the active sub-carriers' density.

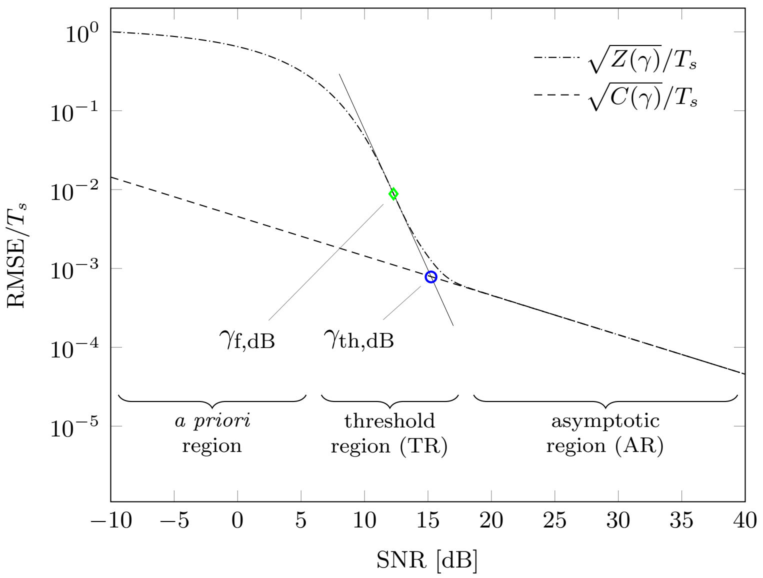

Figure 5.3 – Normalized estimation RMSE and corresponding bounds for $T_\mathrm{o} = 4T_s$ using the $\mathcal{U}_{2,72}$ power distribution.

A bound on the estimation MSE, tighter than the CRB for a wide range of SNR values and holding for all estimators and signals, is the ZZB, which is described in Section 4.3. Here, the bound of (4.41) is adopted, i.e., the one derived in [49], which does not exploit the valley filling function. The ZZB can be expressed as $\mathrm{MSE}(\hat{\tau}) \geq Z(\gamma)$, with:

$$Z(\gamma) = \frac{1}{T_\mathrm{o}} \int_0^{T_\mathrm{o}} \Delta\,(T_\mathrm{o} - \Delta) Q\Big(\sqrt{\gamma\,[1-\rho_s(\Delta)]}\Big)\,\mathrm{d}\Delta, \tag{5.10}$$

where $Q(x) = (2\pi)^{-1/2} \int_x^\infty e^{-u^2/2}\mathrm{d}u$ and:

$$\rho_s(\Delta) = \frac{1}{\mathcal{E}_s} \cdot \begin{cases} \int_0^{T_\mathrm{c}} \mathfrak{Re}\left\{s_\mathrm{c}^*(t-\Delta)s_\mathrm{c}(t)\right\}\mathrm{d}t & \Delta \in [0, T_\mathrm{c}] \\ 0 & \text{otherwise} \end{cases}, \tag{5.11}$$

is the normalized single-sided autocorrelation function of the reference signal $s_\mathrm{c}(t)$, with $\mathfrak{Re}\{\cdot\}$ and $(\cdot)^*$ denoting the real part and the complex conjugate, respectively.

The bounds on the estimation RMSE obtainable from the CRB and the ZZB are $\sqrt{C(\gamma)}$ and $\sqrt{Z(\gamma)}$, respectively. These bounds, normalized to the ideal signal duration T_s, are shown in Figure 5.3 for the $\mathcal{U}_{2,72}$ distribution. The qualitative boundaries between *a priori*, threshold and asymptotic regions are also highlighted, together with the quantities that are proposed for determining a bound between the threshold and the asymptotic region, and that are described in the following section.

5.4.2 Estimation RMSE performance figures

Two quantities are considered for the evaluation of the TOA estimation performance of each power distribution. As one can see from Figure 5.3, the asymptotic estimation RMSE performance is identified by the CRB, which directly depends on the GB β. Hence, the first considered metric is the normalized GB βT_s, which is a dimensionless parameter that quantifies the TOA estimation performance for high SNR values and does not depend on the signal duration.

In addition, for characterizing the signal performance in the threshold region, a novel performance figure is introduced. Define $\gamma_{\mathrm{dB}} = 10 \log_{10} \gamma$ as the SNR expressed in dB, and let $\gamma_{\mathrm{f,dB}} = 10 \log_{10} \gamma_{\mathrm{f}}$ be the maximum value of SNR expressed in dB for which the logarithmic plot of $\sqrt{Z(10^{\gamma_{\mathrm{dB}}/10})}$ has a convex to concave point of inflection. Defining $\Xi(\gamma_{\mathrm{dB}}) = Z(10^{\gamma_{\mathrm{dB}}/10})$, the value $\gamma_{\mathrm{f,dB}}$ can be found by taking the highest solution of:

$$\frac{\partial^2}{\partial \gamma_{\mathrm{dB}}^2} \left[\log_{10} \sqrt{\Xi(\gamma_{\mathrm{dB}})} \right] = 0, \tag{5.12}$$

for which the left hand side of (5.12) changes sign from minus to plus. Using the ZZB definition of (5.10) and defining the auxiliary function:

$$\xi\left(\gamma_{\mathrm{dB}}, \Delta\right) = 10^{\gamma_{\mathrm{dB}}/10} \left[1 - \rho_s(\Delta)\right], \tag{5.13}$$

the equation of (5.12) can be rewritten, after some manipulations, as:

$$\dot{\Xi}^2(\gamma_{\mathrm{dB}}) = \Xi(\gamma_{\mathrm{dB}}) \cdot \ddot{\Xi}(\gamma_{\mathrm{dB}}), \tag{5.14}$$

where:

$$\begin{aligned} \dot{\Xi}(\gamma_{\mathrm{dB}}) &= \frac{\partial}{\partial \gamma_{\mathrm{dB}}} [\Xi(\gamma_{\mathrm{dB}})] \\ &= -\frac{\log 10}{20\sqrt{2\pi} T_{\mathrm{o}}} \int_0^{T_{\mathrm{o}}} \left\{ \Delta\, (T_{\mathrm{o}} - \Delta) e^{-\frac{\xi(\gamma_{\mathrm{dB}}, \Delta)}{2}} \sqrt{\xi\left(\gamma_{\mathrm{dB}}, \Delta\right)} \right\} \mathrm{d}\Delta, \end{aligned} \tag{5.15}$$

$$\begin{aligned} \ddot{\Xi}(\gamma_{\mathrm{dB}}) &= \frac{\partial^2}{\partial \gamma_{\mathrm{dB}}^2} [\Xi(\gamma_{\mathrm{dB}})] \\ &= \frac{\log^2 10}{20^2 \sqrt{2\pi} T_{\mathrm{o}}} \int_0^{T_{\mathrm{o}}} \left\{ \Delta\, (T_{\mathrm{o}} - \Delta) e^{-\frac{\xi(\gamma_{\mathrm{dB}}, \Delta)}{2}} \sqrt{\xi\left(\gamma_{\mathrm{dB}}, \Delta\right)} \left[\xi\left(\gamma_{\mathrm{dB}}, \Delta\right) - 1\right] \right\} \mathrm{d}\Delta. \end{aligned} \tag{5.16}$$

Hence, $\gamma_{\mathrm{f,dB}}$ can be obtained as the highest numerical solution of (5.14). As depicted in Figure 5.3, the novel performance figure is referred to as $\gamma_{\mathrm{th,dB}} = 10 \log_{10} \gamma_{\mathrm{th}}$ and is defined as the intersection between the logarithmic plot of the CRB, i.e., of $\sqrt{C(10^{\gamma_{\mathrm{dB}}/10})}$, and the tangent to the logarithmic plot of $\sqrt{Z(10^{\gamma_{\mathrm{dB}}/10})}$ at $\gamma_{\mathrm{f,dB}}$.

In other words, consider the linear equation that defines the logarithmic plot of the CRB as a function of γ_{dB}, which is:

$$y = -\frac{1}{20} \gamma_{\mathrm{dB}} - \frac{1}{2} \log_{10}\left(2\beta^2\right), \tag{5.17}$$

and the linear equation that defines the tangent to the logarithmic plot of the ZZB as a function of γ_{dB} at $\gamma_{\mathrm{f,dB}}$, which is:

$$y = \frac{1}{2\log 10} \cdot \frac{\dot{\Xi}(\gamma_{\mathrm{f,dB}})}{\Xi(\gamma_{\mathrm{f,dB}})} \cdot (\gamma_{\mathrm{dB}} - \gamma_{\mathrm{f,dB}}) + \frac{1}{2}\log_{10}\left[\Xi(\gamma_{\mathrm{f,dB}})\right]. \tag{5.18}$$

Hence, the value of $\gamma_{\mathrm{th,dB}}$ can be found as the intersection between (5.17) and (5.18), which is given by:

$$\gamma_{\mathrm{th,dB}} = \frac{\gamma_{\mathrm{f,dB}}\dot{\Xi}\left(\gamma_{\mathrm{f,dB}}\right) - \log 10 \cdot \Xi\left(\gamma_{\mathrm{f,dB}}\right) \cdot \log_{10}\left[2\,\Xi\left(\gamma_{\mathrm{f,dB}}\right)\beta^2\right]}{\dot{\Xi}\left(\gamma_{\mathrm{f,dB}}\right) + \frac{1}{10}\log 10 \cdot \Xi\left(\gamma_{\mathrm{f,dB}}\right)}. \tag{5.19}$$

This SNR value may be used to reliably approximate the transition point between the threshold region and asymptotic region, where the ZZB becomes tight to the CRB. Hence, signals having a small value of γ_{th} are considered as signals achieving a good estimation RMSE performance in the threshold region.

In Section 5.5, the SNR threshold δ_2 of [18, 68] is also used as a benchmark of the proposed threshold γ_{th}. The threshold δ_2 is evaluated as the highest solution of the equation:

$$Z(\delta_2) = 2 \cdot C(\delta_2), \tag{5.20}$$

which corresponds to the SNR value for which the ZZB value is twice the value assumed by the CRB.

5.5 Results

In this section, the results obtained with the described OFDM signals are presented. Section 5.5.1 analyzes the dependence of the RMSE performance of the sub-carriers' power distributions of Section 5.3.2 on the parameters d and N_{a}. Moreover, the effectiveness of the proposed SNR threshold γ_{th} in determining the boundaries between threshold and asymptotic RMSE regions is addressed. Finally, Section 5.5.2 presents the results obtained by comparing the different LTE signals explained in Section 5.3.3.

5.5.1 Power distributions comparison

This section discusses the numerical results which are obtained using $T_{\mathrm{o}} = 4T_s$ and considering the two cases $(N_{\mathrm{sc}}, N_{\mathrm{dft}}) = (72, 128)$ and $(N_{\mathrm{sc}}, N_{\mathrm{dft}}) = (300, 512)$, corresponding to the 3GPP LTE specifications for the 1.4 MHz and 5 MHz channel configurations, respectively, as detailed in Section 2.2.

Figure 5.4 depicts the normalized ZZBs obtained for different $\mathcal{U}_{d,N_{\mathrm{sc}}}$ distributions, selecting, for readability purposes, four representative values of d for each value of N_{sc}. More specifically, the $d = \{0, 3, 11, 35\}$ cases (corresponding to $N_{\mathrm{a}} = \{36, 9, 3, 1\}$) are presented for $N_{\mathrm{c}} = 72$ and the $d = \{0, 9, 49, 149\}$ cases (corresponding to $N_{\mathrm{a}} = \{150, 15, 3, 1\}$) are presented for $N_{\mathrm{c}} = 300$. Moreover, Figure 5.5 depicts

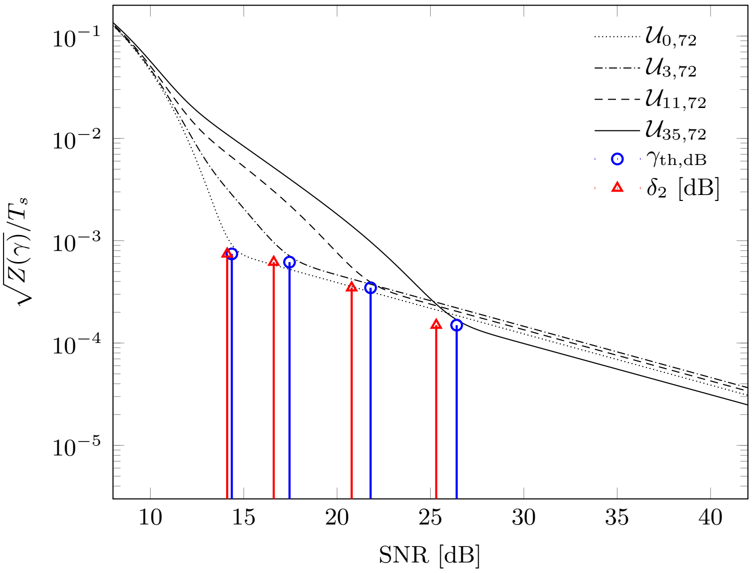

(a) $N_{\mathrm{sc}} = 72$.

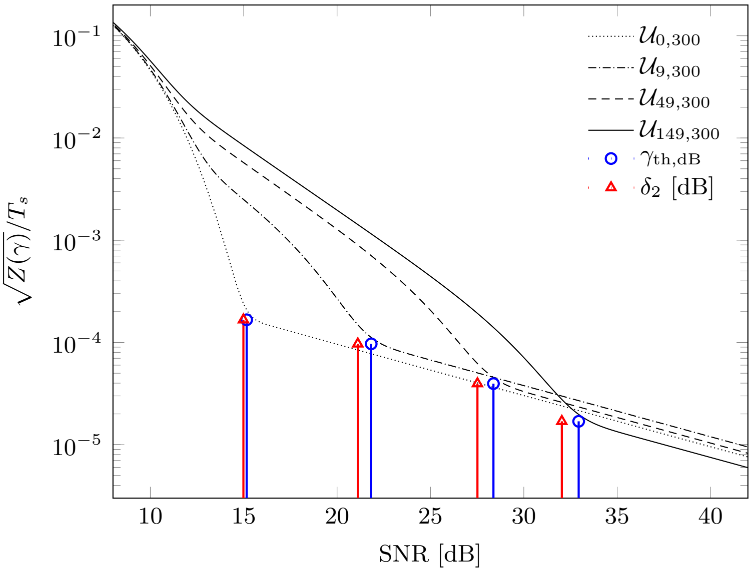

(b) $N_{\mathrm{sc}} = 300$.

Figure 5.4 – Plots of $\sqrt{Z(\gamma)}/T_s$ for selected distributions $\mathcal{U}_{d,N_{\mathrm{sc}}}$. The proposed performance figure $\gamma_{\mathrm{th,dB}}$ and the threshold metric δ_2 of [18, 68] are also shown for each curve.

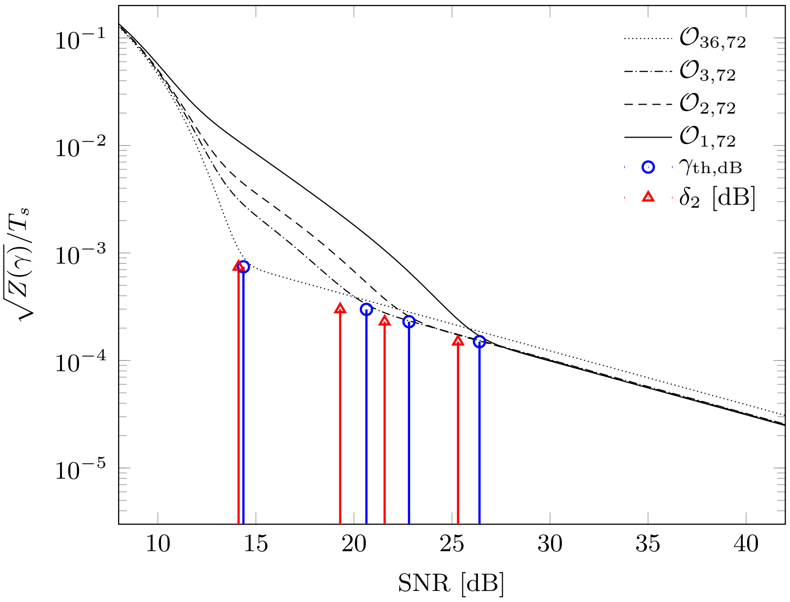

(a) $N_{\mathrm{c}} = 72$.

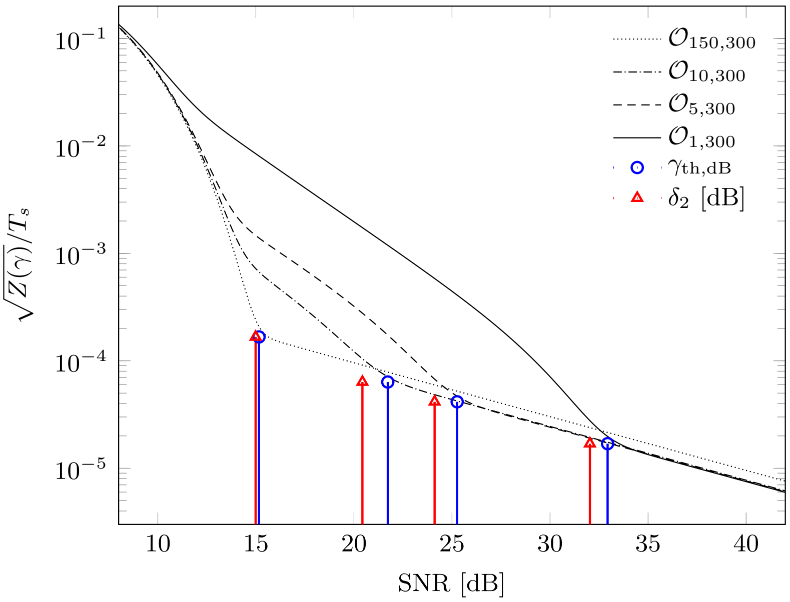

(b) $N_{\mathrm{c}} = 300$.

Figure 5.5 – Plots of $\sqrt{Z(\gamma)}/T_s$ for selected distributions $\mathcal{O}_{N_{\mathrm{a}},N_{\mathrm{c}}}$. The proposed performance figure $\gamma_{\mathrm{th,dB}}$ and the threshold metric δ_2 of [18, 68] are also shown for each curve.

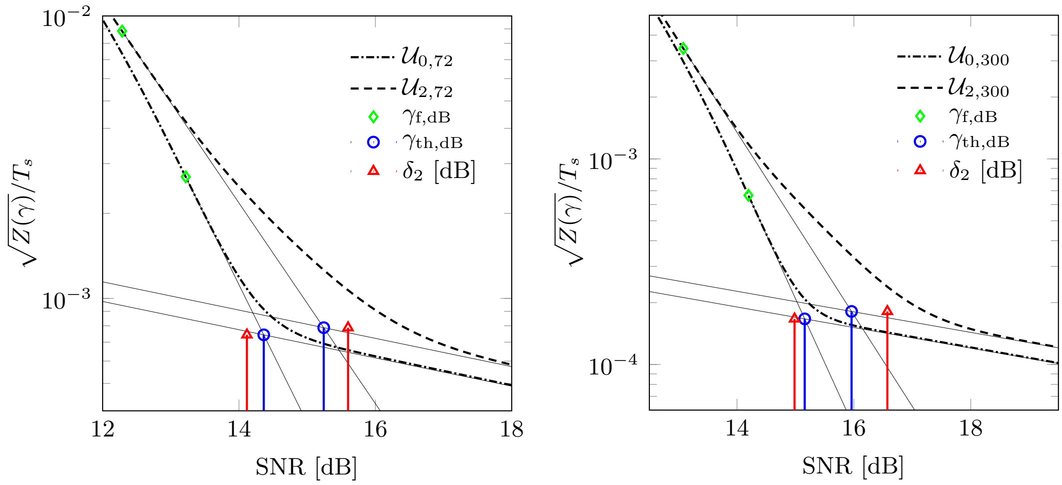

(a) Selected $\mathcal{U}_{d,72}$ distributions.

(b) Selected $\mathcal{U}_{d,300}$ distributions.

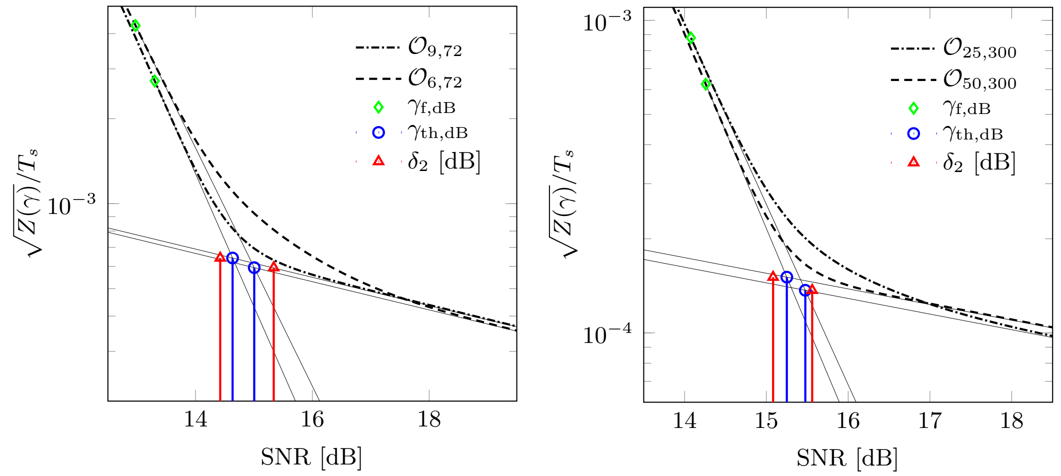

(c) Selected $\mathcal{O}_{N_\text{a},72}$ distributions.

(d) Selected $\mathcal{O}_{N_\text{a},300}$ distributions.

Figure 5.6 – Plots of $\sqrt{Z(\gamma)}/T_s$ for selected U_{d,N_c} and $\mathcal{O}_{N_\text{a},N_\text{c}}$ distributions in the surroundings of the boundary between threshold and asymptotic RMSE region. The thresholds γ_{th} and δ_2 are compared.

the ZZB curves relative to the $\mathcal{O}_{N_\text{a},N_\text{c}}$ distribution. The $N_\text{a} = \{36, 3, 2, 1\}$ cases are presented for $N_\text{c} = 72$ and the $N_\text{a} = \{150, 10, 5, 1\}$ cases are presented for $N_\text{c} = 300$. In both Figure 5.4 and Figure 5.5, for each plotted curve, the circle marker identifies the SNR threshold $\gamma_{\text{th,dB}}$ evaluated by (5.19), while the triangle marker identifies, for comparison purposes, the usual SNR threshold δ_2. For readability purposes, the benchmark threshold δ_2 is reported in dB at the same ordinate of the corresponding $\gamma_{\text{th,dB}}$ value. Three aspects may be outlined from these figures. Firstly, it is evident that the novel performance figure $\gamma_{\text{th,dB}}$ effectively evaluates the estimation RMSE threshold performance of a signal by properly locating the boundary between threshold and asymptotic regions. Secondly, N_{sc} strongly influences the asymptotic estimation RMSE performance, since higher values of N_{sc} lead to an increase of the bandwidth occupied by the sub-carriers with the same inter-channel spacing Δf. This ultimately determines an increased GB and hence a smaller asymptotic estimation RMSE. And thirdly, the adopted value of sub-carriers' spacing d strongly influences the RMSE behavior in the threshold region. Interestingly, the signal obtaining the best asymptotic performance shows the worst threshold behavior.

A direct comparison between $\gamma_{\mathrm{th,dB}}$ and δ_2 shows a satisfactory agreement between the two definitions of the SNR threshold. However, the agreement between $\gamma_{\mathrm{th,dB}}$ and δ_2 depends on the steepness of the ZZB curve in the boundary between threshold region and asymptotic region. When this transition is sufficiently steep, $\gamma_{\mathrm{th,dB}}$ is able to better capture the point at which the threshold region actually ends. Conversely, when the ZZB curve has a flatter transition from the threshold region to the asymptotic region, δ_2 better captures the actual end of the threshold region. This is represented in Figure 5.6, where, for each plot, two cases are depicted, where the novel metric $\gamma_{\mathrm{th,dB}}$ performs better and worse than the metric δ_2 of [18, 68] in identifying the boundary between threshold and asymptotic performance region.

To explore the estimation RMSE behavior of the different OFDM signals with the spectra determined by the parameters d and N_{a}, consider now the threshold gain $G_{\mathrm{th}} = \gamma_{\mathrm{th}}^{\max}/\gamma_{\mathrm{th}}$. This parameter is defined as the hypothetical amount of power that a signal permits to save in respect to $\gamma_{\mathrm{th}}^{\max}$ for attaining the RMSE convergence to the boundary between threshold and asymptotic RMSE region. Here, $\gamma_{\mathrm{th}}^{\max}$ is the value of γ_{th} when $d = N_{\mathrm{sc}}/2-1$, that is when $N_{\mathrm{a}} = 1$, for which the highest normalized GB βT_s is attained. Figure 5.7 shows how the values of βT_s and G_{th} vary depending on the values of N_{a} obtained using $d \in \mathcal{D}_{N_{\mathrm{sc}}}$. As one can see, for the distributions $\mathcal{U}_{d,N_{\mathrm{sc}}}$ and a fixed N_{sc}, the value of βT_s that results from a decrease of the number of active sub-carriers N_{a} (i.e., an increase of the sub-carriers' spacing d), is not associated with an improvement in the threshold gain G_{th}, and hence with a reduction of $\gamma_{\mathrm{th,dB}}$. This reveals a trade-off between βT_s and G_{th}, that is, between asymptotic and threshold performance, which is even more evident for the distributions $\mathcal{O}_{N_{\mathrm{a}},N_{\mathrm{sc}}}$. This demonstrates that the GB is not the only parameter that should be considered when designing a TOA reference signal [48], since the maximization of the GB does not directly guarantee a satisfactory threshold performance. Finally, these results show that an acceptable estimation RMSE performance in the threshold region can be achieved using a sufficiently high density of active sub-carriers for the equispaced $\mathcal{U}_{d,N_{\mathrm{sc}}}$ distributions, or a sufficiently high number of contiguous active sub-carriers at the edges of the bandwidth for the $\mathcal{O}_{N_{\mathrm{a}},N_{\mathrm{sc}}}$ distributions.

5.5.2 LTE signals comparison

In this section, the LTE synchronization and reference signals described in Section 5.3.3 are compared in terms of estimation RMSE performance when employed for TOA measurements in the AWGN channel. The tools exploited for the comparison are the ZZB of (5.10) and the SNR threshold γ_{th} explained in Section 5.4.2. Dif-

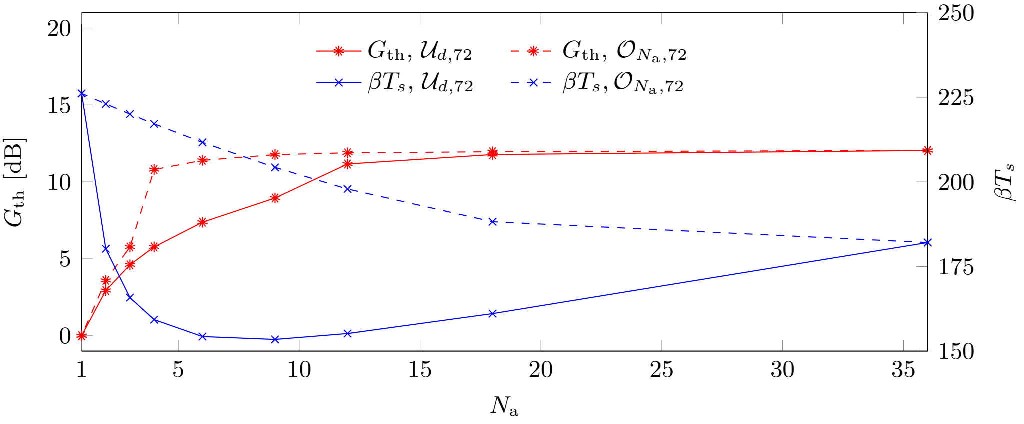

(a) $N_{\text{sc}} = 72$.

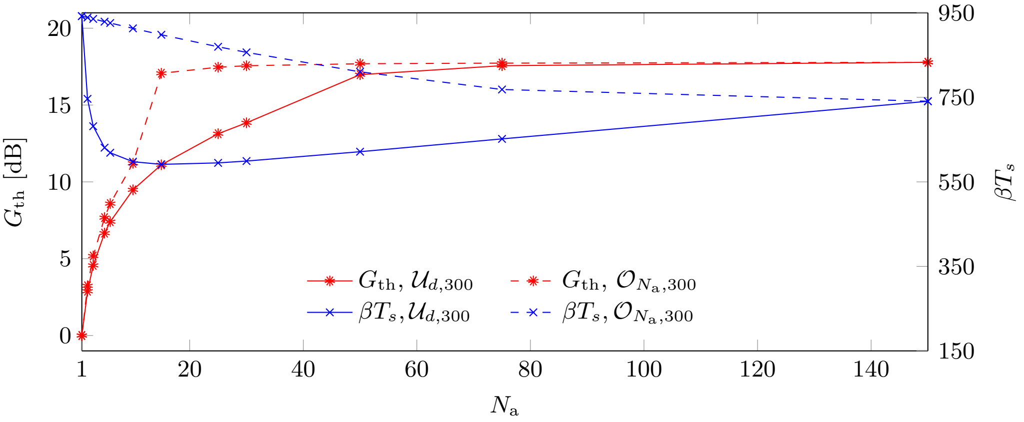

(b) $N_{\text{sc}} = 300$.

Figure 5.7 – Plots of G_{th} (star markers) and βT_s (cross markers) for the distributions $\mathcal{U}_{d,N_{\text{sc}}}$ (solid lines) and $\mathcal{O}_{N_{\text{a}},N_{\text{sc}}}$ (dashed lines) with respect to $N_{\text{a}} = \lfloor N_{\text{sc}}/[2(d+1)]\rfloor$, where $d \in \mathcal{D}_{N_{\text{sc}}}$.

ferently from the previous figures, the bounds on the TOA estimation RMSE are represented as distances, obtained as $c \cdot \sqrt{Z(\gamma)}$, with c being the speed of light.

The results of the comparison are depicted in Figure 5.8, where the ZZBs are evaluated using $T_{\text{o}} = 4T_s$. The signals considered are the PSS, the SSS, and the CRS and PRS for all the possible LTE channel bandwidth configurations, i.e., for all the possible numbers of resource blocks $N_{\text{DL}}^{\text{RB}} \in \{6, 15, 25, 50, 75, 100\}$. There are four aspects to be highlighted. Firstly, the influence of the LTE channel bandwidth configuration, i.e., of the number of resource blocks $N_{\text{DL}}^{\text{RB}}$, on the estimation RMSE performance is evident: the signals with the greatest bandwidth attain the best asymptotic performance. This was expected, since signal with a widest band have a greater GB. Secondly, the performance obtained by the two synchronization signals, namely the PSS and the SSS, is very similar, and is worse than the performance of all the other considered signals. This is because they have the smallest bandwidth

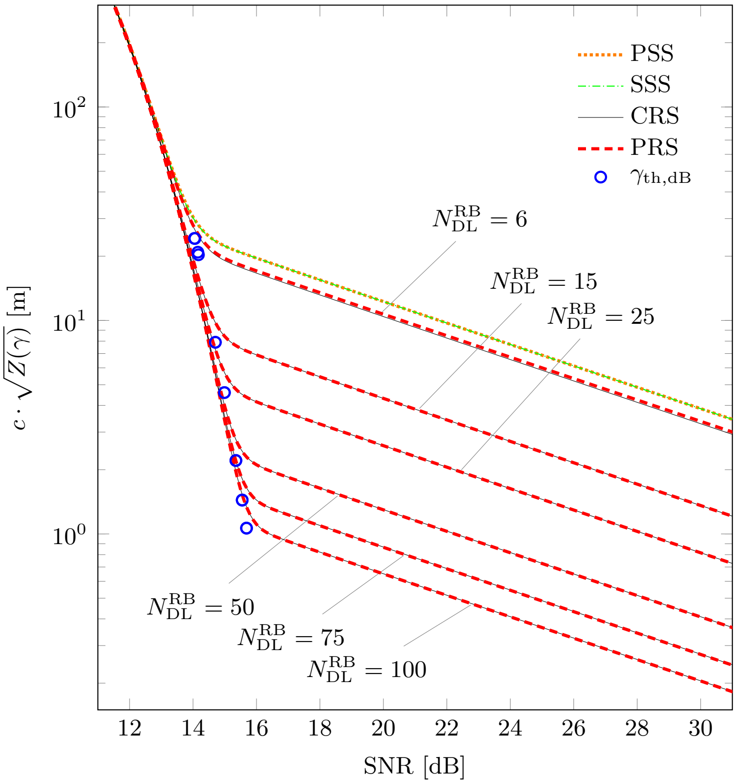

Figure 5.8 – Plots of $c \cdot \sqrt{Z(\gamma)}$ for the considered LTE reference signals and various bandwidth configurations $N_{\mathrm{DL}}^{\mathrm{RB}}$. The SNR threshold γ_{th} is also shown.

occupation, equal to 930 kHz, which is even smaller than the bandwidth of the reference signals with $N_{\mathrm{DL}}^{\mathrm{RB}} = 6$, which is equal to $(N_{\mathrm{DL}}^{\mathrm{RB}} N_{\mathrm{sc}}^{\mathrm{RB}} - 5)\Delta f = 1005\,\mathrm{kHz}$. Thirdly, the performance of the CRS and of the PRS is equal for all the channel bandwidth configurations. The only slight difference that one can notice for the value $N_{\mathrm{DL}}^{\mathrm{RB}} = 6$ is due to the frequency domain (FD) misalignment of the two sets of pilots, which results in the CRS having a pilot at a slightly higher frequency than the PRS's highest frequency pilot. As one can see, this phenomenon is less evident at higher bandwidths, i.e., for $N_{\mathrm{DL}}^{\mathrm{RB}} > 6$. Finally, consider the SNR thresholds achieved by the various LTE signals. As one can see, the values of γ_{th} for signals having the same bandwidth configuration (i.e., the same value of $N_{\mathrm{DL}}^{\mathrm{RB}}$) are very similar (even not distinguishable in the plot).

5.6 Conclusions

The TOA estimation RMSE performance of realistically modelled OFDM signals has been investigated in the AWGN channel, using a model that considers the waveform directly at the output of the DAC.

Firstly, the usage of OFDM waveforms for TOA estimation have been studied from a signal design point of view. Two sets of power distributions on the available sub-carriers have been defined to evaluate the estimation RMSE performance both in the asymptotic and threshold regions by using the CRB and the ZZB. The developed analysis has confirmed that, for a given maximum bandwidth, the power distribution influences the estimation RMSE both in the asymptotic and threshold regions. Analysis using a novel performance figure, introduced to quantify the estimation RMSE threshold behavior, has revealed the existence of a trade-off in the performance of the timing measurements of OFDM signals. More precisely, a widely spaced power distribution, concentrated on the edges of the available bandwidth, has the positive effect of determining a small asymptotic estimation RMSE but the negative effect of giving a poor estimation RMSE threshold behavior. The analysis has also shown that, to obtain a satisfactory threshold performance with an equispaced sub-carrier power distribution, a high density of active sub-carriers is required. Similarly, a certain number of active sub-carries has to be employed if they have to be placed contiguously on the edges of the available bandwidth. Future work aims to extend the TOA performance analysis to multipath channels, by exploiting the bounds of [18, 68], and adopting the presented framework as a reference best-case indication.

Secondly, the framework developed for the asymptotic and threshold performance analysis of physically realizable OFDM waveforms has been exploited for a brief comparison between the available LTE reference signals. While the synchronization signals are characterized by a small bandwidth, which corresponds to a poor performance, the CRS and the PRS resulted equally good as TOA estimation reference signals, achieving identical performance both in the threshold and asymptotic RMSE regions for all the channel bandwidth configurations.

Chapter 6

Algorithms for TOA estimation of real LTE signals

This chapter presents the results of work undertaken in close collaboration with the Hochschule für Technik Rapperswil and with the support of u-blox UK Ltd. Datasets of real Long Term Evolution (LTE) signals collected from the commercial network of the town of Rapperswil, Switzerland, have been processed for extracting time-based pseudorange measurements. Different measurements environment have been tested, including an outdoor vehicular and an indoor scenario, both characterized by strong multipath propagation. Algorithms have been developed for effectively separating multipath and tracking the direct path, in order to estimate unbiased pseudoranges, which have been then used for evaluating position fixes. This demonstrated the feasibility of a positioning system based solely on the use of LTE signals.[1]

6.1 Introduction

The estimation of the distance between a mobile receiver and a base station (BS) performed by measuring the time of arrival (TOA) of the transmitted signals is a difficult task in harsh propagation environments. This is because the reception of several differently delayed paths influences the estimated TOA and ultimately the estimated distance. Indeed, only the direct path (DP) TOA provides an unbiased

---

[1] The content of this chapter was partly published on F. Knutti, M. Sabathy, M. Driusso, H. Mathis, and C. Marshall, "Positioning Using LTE Signals," in *European Navigation Conference (ENC 2015)*, Apr. 2015, and on M. Driusso, F. Babich, F. Knutti, M. Sabathy, and C. Marshall, "Estimation and tracking of LTE signals time of arrival in a mobile multipath environment," in *9th International Symposium on Image and Signal Processing and Analysis*, pp. 276–281, Sep. 2015, and has been submitted for second review in M. Driusso, F. Babich, F. Knutti, M. Sabathy, H. Mathis and C. Marshall, "Vehicular position tracking using LTE signals," *IEEE Transactions on Vehicular Technology*, Feb. 2016. Moreover, a patent on some of the topics described has been submitted as C. Marshall and M. Driusso, "Calculating a ranging measurement in a cellular communications network," EPO application 15195460.9, filed on Nov. 2015, assigned to u-blox AG.

estimate of the distance between the transmitter and the receiver, which is crucial for obtaining a precise position fix. Hence, appropriate processing is needed for identifying the DP among the different received paths.

In this part of the thesis, the topic of the TOA estimation of real Third Generation Partnership Project (3GPP) Long Term Evolution (LTE) signals for positioning in multipath conditions is addressed. The effectiveness of sub-space based super-resolution algorithms (SRAs) when employed for multipath separation is investigated. Several approaches have been developed in the presented work for combining the received LTE signals in order to improve the TOA estimates' quality. Moreover, a DP TOA tracking technique has been tested on real LTE signal samples for performing range estimations along subsequent measurement. All the developed algorithms have been applied to real LTE data collected in the field. The obtained results demonstrated the effectiveness of the SRAs for tackling multipath and the feasibility of a positioning system that relies on TOA measurements of LTE signals.

The work described in this chapter has been realized in close collaboration with the Institute for Communication Systems (ICOM) of the Hochschule für Technik Rapperswil (HSR), Switzerland, and with u-blox UK Ltd. In particular, the ICOM team realized the setup used for the different measurement campaigns in which the real LTE data fed into the developed algorithms was gathered. Moreover, the actual measurements and the preprocessing software needed for storing and sorting the gathered data were realized at the HSR. Finally, the ranges evaluated by running the developed algorithms on the measured data were passed back to the ICOM team, who performed the positioning. The work coming from HSR is briefly presented in Section 6.3 and Section 6.8.

The remainder of the chapter is organized as follows. In Section 6.2, a review of the related works found in the literature is presented, together with a motivation for the presented approach. The setup used for the in-the-field measurements developed at the HSR is described in Section 6.3, together with the measurement locations and with the parameters of the LTE signals received. Section 6.4 explains the different signal combining strategies adopted to improve the quality of the TOA estimates together with the SRAs. Section 6.5 introduces some simple TOA estimators that were used for benchmarking the proposed approach. Section 6.6 describes the main developed algorithm, referred to as EKAT, which was used to identify the DP TOA and track it along subsequent measurements. Section 6.7 explains how the timing measurements obtained with EKAT and with other simpler benchmark algorithms are converted to actual ranges. This section includes the description of the algorithm adopted to combine the measurements from multiple cells pertaining to the same BS, and the description of the procedure used for the estimation of the clock bias and drift of the BSs. Section 6.8 briefly illustrates the adopted positioning algorithm, developed at the HSR for assessing the validity of the estimated ranges at a positioning level. Finally, Section 6.9 comments the obtained ranging and positioning results, followed by some final considerations, in Section 6.10.

6.2 Related works and motivations

As has already mentioned in Chapter 2, the LTE standard itself offers positioning capabilities, providing the so-called positioning reference signal (PRS) and network-centered procedures for localizing the user equipment by exploiting PRS time difference of arrival (TDOA) measurements [24, 26]. Several works, based on computer simulations or experimental evaluations, have been published on the subject of TDOA based positioning systems that exploit LTE signals in harsh propagation environments. The work in [62] evaluates through computer simulations the accuracy of the PRS when used in TDOA-based localization systems under different types of interference. In [63], the same authors extend the timing performance analysis to multipath channels. In [60], the PRS is exploited for realizing a joint time and amplitude multipath channel estimation. An experimental evaluation is presented in [69], where the timing performance of different hardware platforms is compared by using emulated LTE signals in line of sight (LOS) multipath-free channels. In [70, 71], different LTE signals generated with prototyping hardware are exploited for assessing the feasibility of indoor positioning based on LTE signals TDOA measurements. In [72], an opportunistic approach for positioning that exploits the LTE cell specific reference signal (CRS) is proposed. The authors of [73] proposed a passive radar system exploiting the LTE CRS and the LTE base stations as illuminators of opportunity. The work described in [74] proposes a method for pseudorange measurements with LTE signals that is robust in detecting the first received path. In [75], an opportunistic BSs synchronization method is proposed, that exploits the LTE CRS and the *a priori* knowledge of the BSs' positions.

Interestingly, the authors of [75] recognized that newly deployed LTE commercial networks are not mature yet for TDOA based positioning, mainly because of a lack of PRS transmission and because of non-synchronized BSs. This is in accordance with the early measurements performed at the HSR and documented in [76]. The limited operators' efforts in deploying services and infrastructure needed for performing positioning with LTE signals may be mainly motivated by the fact that the PRS transmission reduces the resources available to transport customers' data. Consequently, new approaches are needed in order to enable LTE-based positioning services that are more appealing for use in practice in operators' networks.

The approach followed in this part of the thesis moves from these motivations. The proposed system is mobile-centered and uses the signals transmitted by the currently deployed commercial LTE networks. The LTE CRS is exploited for estimating the ranges between the BSs and the mobile receiver. Differently from the majority of the existing literature, the proposed system is based on TOA measurements, avoiding any BSs synchronization requirement. However, it relies on two assumptions. Firstly, the positions of the BSs have to be known to the receiver. Secondly, each BS has to make its clock properties available to the positioning engine (PE) which performs the location estimation, enabling a reasonably approximate knowledge of each BS's clock offset and drift in respect to a reference time. The PE might be internal within the network, or located on the mobile receiver. In the presented experiments, the BSs positions were acquired from a public database, and the BSs' clock properties were estimated in a preliminary phase.

Within this approach, the algorithms developed during the activities of the PhD mainly focus on the TOA estimation of the LTE CRS in multipath conditions. Several works have been realized on the subject of multipath-robust TOA estimation. The authors of [70] proposed a cross-correlation based TOA estimator with non line of sight (NLOS) mitigation together with a particle filter for performing indoor positioning with LTE signals generated ad-hoc using prototyping hardware. In [15,16], super-resolution algorithms and frequency diversity techniques are employed for indoor static ranging measurements using wideband sounding signals. State-space approach algorithms specifically designed for channel sounding can also been employed for TOA estimation in multipath environments, such as the ones of [77–79]. However, specific hardware is required for these algorithms, which is usually too complex for real time consumer product implementation.

In the proposed algorithm, the TOA estimation is performed by using the estimation of signal parameters via rotational invariance techniques (ESPRIT) algorithm and by exploiting opportunistically the CRS pilot tones. The LTE CRS was chosen as the reference signal for TOA estimation, because it is mandatory to be transmitted, and because occupies the full channel bandwidth, offering high resolution for multipath separation. The ESPRIT algorithm was previously used in [37] for parametric channel estimation. A state-space approach similar to [78] is then adopted for tracking the estimated DP TOA. Moreover, a novel measurement noise covariance estimation is performed, using the ESPRIT performance bound of [80]. The capabilities of the developed algorithm were explored using the real LTE data gathered with a portable setup at the HSR, both in outdoor and indoor multipath scenarios. To the best of the author's knowledge, there are no works in the literature that propose an experimental in-the-field validation of a multipath-robust LTE signals TOA estimation system for positioning.

6.3 Measurements in real conditions

The proposed approach has been tested with a live data set of commercial LTE signals recorded in Rapperswil, Switzerland. The measurement setup was developed at the HSR by the ICOM team, and is documented in [76,81–83]. In the following, a brief review of the used test-beds and of the three considered measurement scenarios is presented. Moreover, details on the particular LTE parameters found during the measurements in Rapperswil are given. This does not limit the generality of the obtained results.

Note that the first of these three measurement sessions consists of small preliminary datasets. Conversely, the latter two measurement sessions, held in an outdoor vehicular and in an indoor scenario, respectively, are those on which the proposed TOA estimation algorithm has been actually applied. Hence, with the exception of the preliminary results presented in Section 6.9.3, the rest of the chapter always

parameter	**operator 1**	**operator 2**
B	15 MHz	10 MHz
$N_{\mathrm{DL}}^{\mathrm{RB}}$	75	50
$N_{\mathrm{sc}} = N_{\mathrm{sc}}^{\mathrm{RB}}\, N_{\mathrm{DL}}^{\mathrm{RB}}$	900	600
carrier frequency f_{C}	1815.1 MHz	1869 MHz
N_{dft}	1024	
$\Delta f = 1/T_{\mathrm{s}}$	15 kHz	
$N_{\mathrm{sc}}^{\mathrm{RB}}$	12	
$N_{\mathrm{symb}}^{\mathrm{DL}}$	7	
base time unit $T_{\mathrm{s},0}$	$T_{\mathrm{s}}/2048$	
$l = 0$ cyclic prefix (CP) length $T_{\mathrm{cp},0}$	$160 \cdot T_{\mathrm{s},0}$	
$l > 0$ CP length $T_{\mathrm{cp},l}$	$144 \cdot T_{\mathrm{s},0}$	

Table 6.1 – LTE physical layer parameters - outdoor measurements (28 August 2014)

refers to the two main datasets.

6.3.1 Measurement scenarios

The first measurement session consisted of a preliminary test held at the HSR with a basic version of the measurement setup, documented in [76]. During this test, only the LTE signals coming from a single BS of a single operator in LOS conditions were continuously recorded. The test-bed was placed in a corridor inside the university building, as shown in Figure 6.1, where just a large glass wall separated the receiver and the BS. Figure 6.1c shows both the test-bed in the corridor and the transmitting base station where the recorded signals came from. Two measurements were realized. In the first one, 120 seconds of data were acquired leaving fixed the receiver in the "Start" position indicated in the map of Figure 6.1d. In the second one, the receiver was moved as depicted in the map of Figure 6.1d, resting for 15 seconds at each of the "Start", "Stopover" and "Final" positions. The acquired signal data was analyzed off line. Two cell IDs were detected, respectively $N_{\mathrm{ID}}^{\mathrm{cell}} = 84$ and $N_{\mathrm{ID}}^{\mathrm{cell}} = 86$, which correspond to the sectors highlighted in Figure 6.1d. The recorded LTE signals pertain to a normal CP 15 MHz LTE channel configuration with 2 antenna ports, which corresponds to the signal parameters that are summarized for operator 1 in Table 6.1. The goal of this preliminary set of measurements was to have a clear set of LTE signals to be used for testing the TOA estimation algorithms.

The second dataset was acquired during a vehicular data gathering session, documented in [81]. LTE signals were recorded in the area of Rapperswil SG, Switzerland, with the equipment installed in a van. The route was chosen such as to include urban, sub-urban, and open-field areas, as the Global Positioning System (GPS) track in Figure 6.2a suggests. This routing allows the performance of the proposed system to be analyzed in different mixed propagation environments. The time needed for driving the route shown was about 20 minutes, at speeds up to 50 km/h. This session

(a) First part of the path. **(b)** Second part of the path.

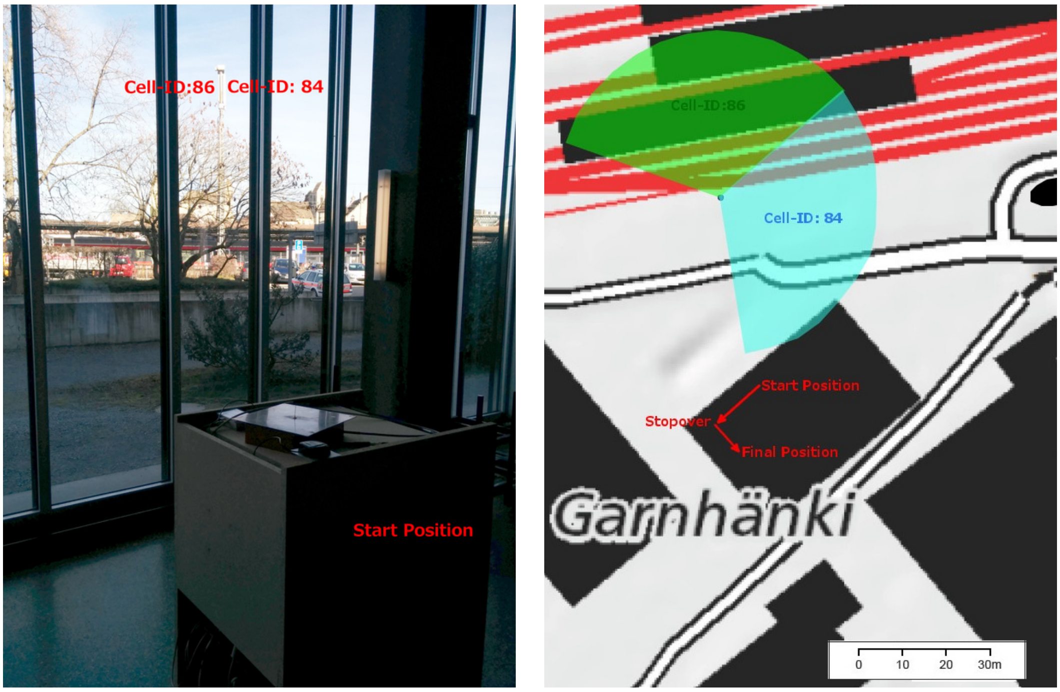

(c) Start position with base station view. **(d)** Map of the measurement scenario.

Figure 6.1 – Photos and map of the preliminary measurement scenario [76].

parameter	**operator 1**	**operator 2**	**operator 3**
B	20 MHz	15 MHz	15 MHz
$N_{\mathrm{DL}}^{\mathrm{RB}}$	100	75	75
$N_{\mathrm{sc}} = N_{\mathrm{sc}}^{\mathrm{RB}}\, N_{\mathrm{DL}}^{\mathrm{RB}}$	1200	900	900
carrier frequency f_{C}	1815.1 MHz	1870 MHz	1850.1 MHz
N_{dft}	1536		
$\Delta f = 1/T_{\mathrm{s}}$	15 kHz		
$N_{\mathrm{sc}}^{\mathrm{RB}}$	12		
$N_{\mathrm{symb}}^{\mathrm{DL}}$	7		
base time unit $T_{\mathrm{s},0}$	$T_{\mathrm{s}}/2048$		
$l = 0$ CP length $T_{\mathrm{cp},0}$	$160 \cdot T_{\mathrm{s},0}$		
$l > 0$ CP length $T_{\mathrm{cp},l}$	$144 \cdot T_{\mathrm{s},0}$		

Table 6.2 – LTE physical layer parameters - indoor measurements (18 June 2015)

was held on the 28th August 2014. At that time, two operators were found in the LTE network of Rapperswil, which was set to frequency domain duplexing (FDD), with a normal CP and a two antenna port configuration. Table 6.1 summarizes all the useful LTE parameters found during the measurements. Because of the channel bandwidths used, a sample rate of 25 MSPS is enough for an un-aliased reception of the LTE signals from both operators. Given the length of the measurement session and the big amount of data to be stored (1 second at 25 MSPS with 16 bit I/Q samples corresponds to 100 MB of data), only 10 ms of data were recorded every second.

The third dataset was acquired during an indoor NLOS data gathering session, documented in [82]. LTE signals were recorded in building 2 of the HSR, with the equipment installed on a trolley. The test route started outdoors, in the area in front of building 2, which is slightly below the ground level, and surrounded by concrete facilities. As the laser track of Figure 6.2b shows, the route continued following a square shaped path inside the HSR building 2, and returned outdoors, with a duration of approximately 15 minutes. This routing allows the performance of the proposed system to be analyzed in indoor propagation environments, characterized by NLOS propagation and strong multipath. This session was held on the 18th June 2015. At that time, three operators were found in the LTE network of Rapperswil, which was set to FDD, with a normal CP and a two antenna port configuration. Table 6.2 summarizes all the useful LTE parameters found during this last set of measurements. Again, the sample rate used is 25 MSPS, and only 10 ms of data were recorded every second.

6.3.2 Measurement setup

The setup used to gather the live data consists of a set of universal software radio peripheral (USRP) N210 software defined radios (SDRs), which use a high precision

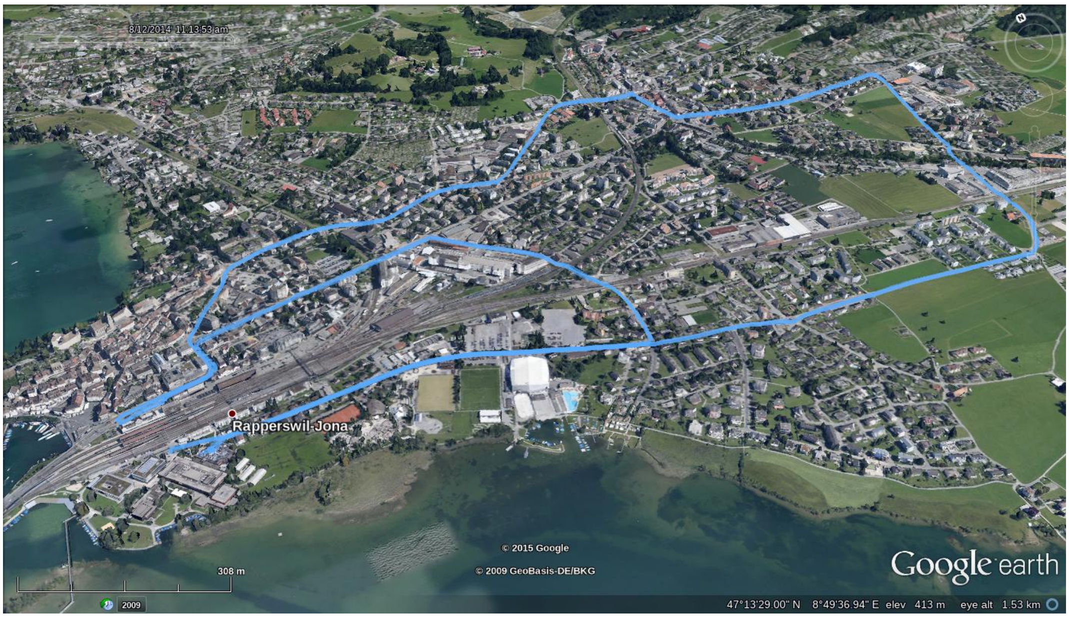

(a) Outdoor scenario.

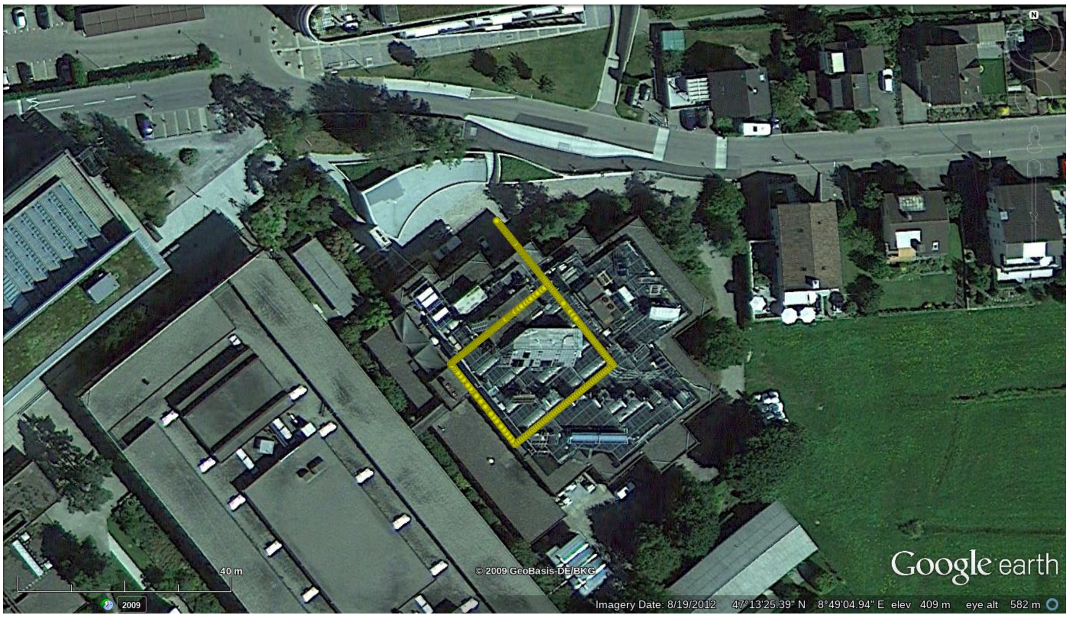

(b) Indoor scenario.

Figure 6.2 – Ground truth and satellite views for the outdoor and indoor measurement scenarios. In the outdoor case, the ground truth is assumed to be the measured GPS track, while in the indoor case, the ground truth is assumed to be given by the positions measured using a laser distance sensor.

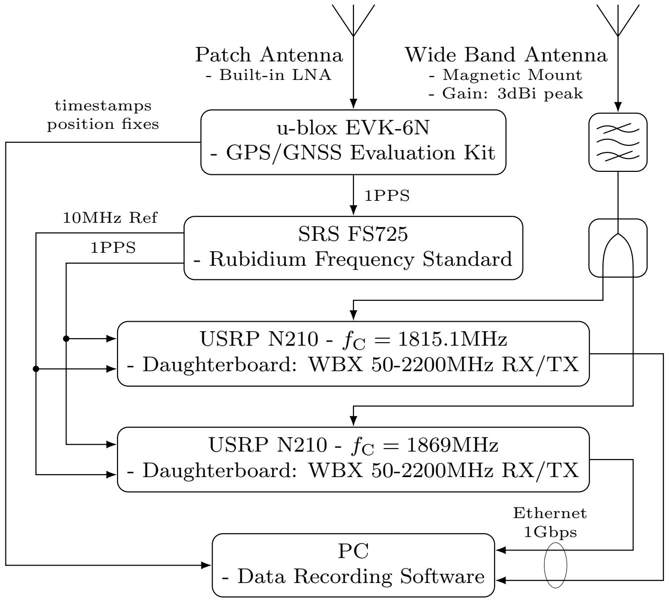

Figure 6.3 – Flow graph of the portable measurement setup used in the outdoor vehicular scenario. The setup was installed in a van.

10 MHz reference clock of a GPS-locked Rubidium frequency standard. A conventional personal computer was used as a system controller and for data storage. The data recording equipment was installed on a trolley and energy was supplied by a battery-powered DC to AC converter, allowing field usage. In the case of the preliminary measurements, no further instruments were used, and, given the short duration of the session, the LTE signals were recorded continuously [76].

For the outdoor and indoor datesets, the setup used was more elaborated, also because the goal of the measurements was to receive the highest possible number of different operators and cells. For this reason, a dedicated USRP was used for each operator to cover the different downlink carrier frequencies f_C. The recorded data was GPS time stamped and therefore coherent sampling between the USRPs was guaranteed. This allows the LTE signals of the different operators to be used in combination. As said previously, to reduce the amount of data to be saved, only 10 ms chunks of contiguous data were stored every second. Two versions of the measurement setup were realized. The first version, used in the outdoor vehicular measurements session, consisted of two USRPs, since two operators were detected at that time, and is shown in Figure 6.3. When available, the GPS fix corresponding to the reception position of each recorded chunk was saved, to be used as a ground truth. The second version of the measurement setup, used in the indoor measurements session, consisted of three USRPs, since three operators were detected at that time, and is shown in Figure 6.4. Again, the GPS fix corresponding to the reception position of each recorded chunk was saved when available. Data analysis reported in [82] showed that GPS position fixes were available only in the outdoor portion

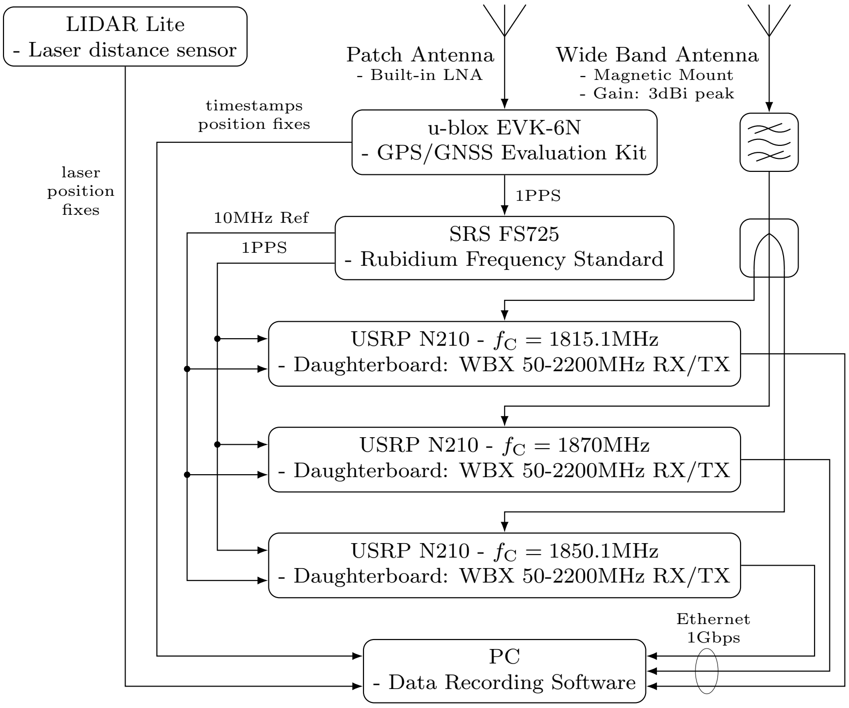

Figure 6.4 – Flow graph of the portable measurement setup used in the indoor scenario. The setup was installed on a trolley.

of the route of Figure 6.2b. Hence, a further position sensor was required in this measurement session, in order to ensure ground truth data collection even in indoor areas. As the setup of Figure 6.4 shows, a laser distance sensor was used for this purpose.

6.3.3 Cell search and coarse synchronization

The preliminary dataset was processed by the ICOM team with the simple steps described in [76]. Indeed, this dataset contained the LTE signals coming from a single very close BS transmitting with known cell IDs. Moreover, the signals were recorded continuously throughout the measurement session. Hence, the cell search and symbol-level synchronization were realized using the canonical method based on the correlation of the received signal with the primary synchronization signal (PSS) and the secondary synchronization signal (SSS). Further details on this technique are available in [35].

The procedure followed for the outdoor and indoor datasets is different, and is described in [83]. In this case, the measured datasets were searched for signals from available BSs by means of an exhaustive search against a list of cell identities of all BSs in the area. Since the BS locations were assumed to be known, the location information provided by the Swiss Federal Office of Communications (OFCOM) was

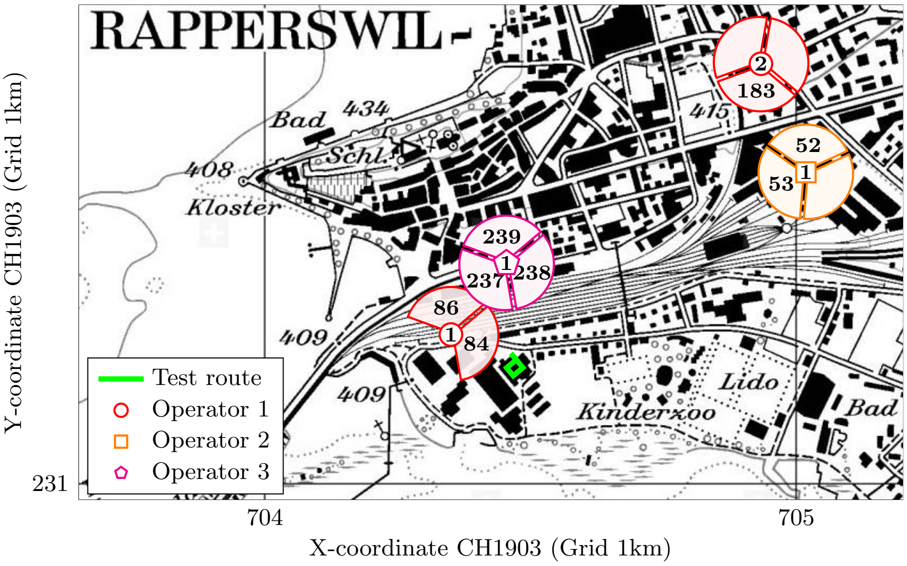

Figure 6.5 – Test route and detected LTE cells for the indoor dataset. Each indexed marker corresponds to a BS, which transmits on several cells, having the indicated $N_{\mathrm{ID}}^{\mathrm{cell}}$. The orientation of the cells is approximate. The cells of a third BS pertaining to operator 2 ($N_{\mathrm{ID}}^{\mathrm{cell}} = 459$ and $N_{\mathrm{ID}}^{\mathrm{cell}} = 460$), located souther across the lake, were also detected.

used [84]. After discovering all available base stations, frame and symbol timing for each base station were acquired correlating the received signal with the CRS. This method is suited for discovering all the cells of the surroundings, and not only the one received with the highest power. Afterwards, the 10 ms chunks which contain the signal of a certain BS were marked per BS. From every chunk of raw data, for every BS received in that chunk and every cell pertaining to each BS, all the orthogonal frequency division multiplexing (OFDM) symbols containing the CRS were saved for further processing. Since the duration of each chunk is 10 ms, roughly 40 OFDM symbols were saved for each detected cell in each chunk. Together with each chunk, also the Coordinated Universal Time (UTC) timestamp $t^{(\mathrm{U})}$ of its reception and the offset Δt_{s} introduced in respect to $t^{(\mathrm{U})}$ for synchronizing at a symbol level were saved.

In the case of the indoor dataset, the recorded samples contained signals from a total of 5 BSs, with 2 BSs from operator 1, 2 BSs from operator 2 and 1 BS from operator 3. Figure 6.5 shows the locations of the BSs used, except for a distant BS across the lake in south-southwesterly direction (BS 3 operator 2). The cells detected during the indoor measurements are shown in Figure 6.5, where each marker identifies one of the three active operators.

Similarly, in the case of the outdoor dataset, the recorded samples contained signals from a total of 9 BSs, with 6 BSs from operator 1 and 3 BSs from operator 2. Figure 6.6 shows the locations of the BSs used, except for a distant BS across

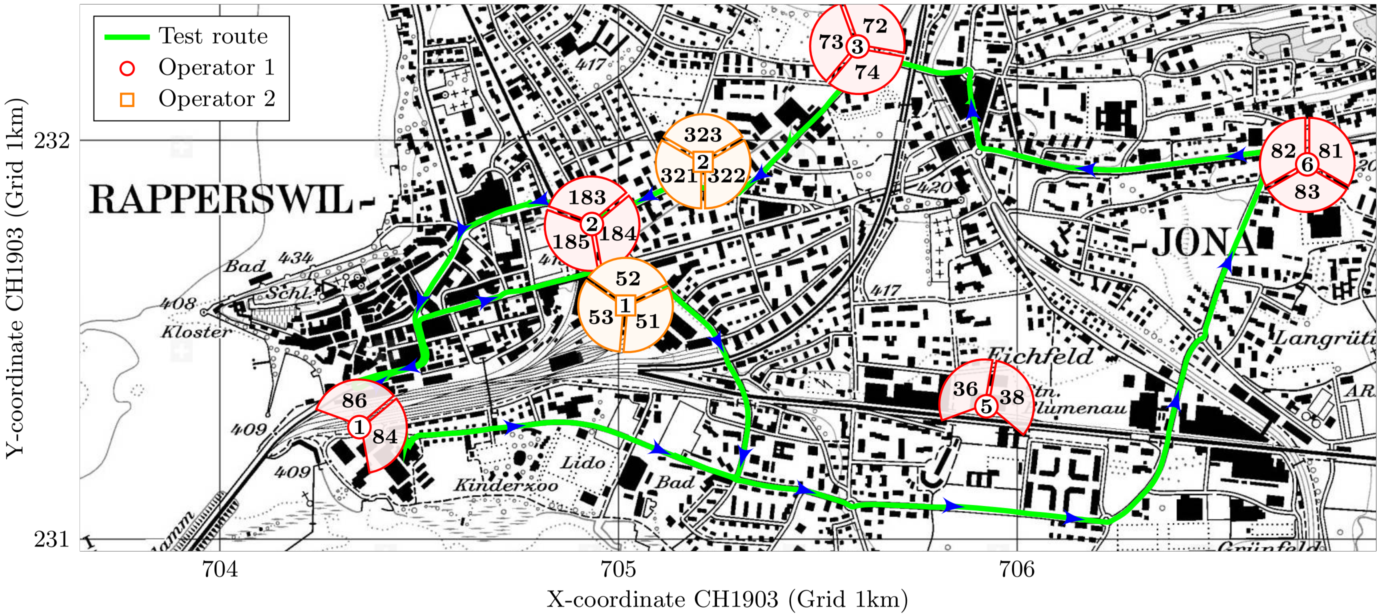

Figure 6.6 – Test route and detected LTE cells for the outdoor vehicular dataset. Each indexed marker corresponds to a BS, which transmits on several cells, having the indicated $N_{\text{ID}}^{\text{cell}}$. The orientation of the cells is approximate. The cells of a third BS pertaining to operator 2 ($N_{\text{ID}}^{\text{cell}}=460$ and $N_{\text{ID}}^{\text{cell}}=461$), located souther across the lake, were also detected.

the lake in south-southwesterly direction (BS 3 operator 2) and another BS situated on a hill to the north (BS 4 operator 1, not considered for positioning). Moreover, the cells detected during the outdoor measurements are also shown, with a different marker identifying one of the two active operators.

6.4 Time-frequency combining of the received signals

Notation. In the remainder of this chapter, the index t is generally employed as a discrete time index identifying the t^{th} performed measurement either in the outdoor vehicular or in the indoor scenario, with $t^{(\text{U})}$ being the corresponding UTC epoch.

As explained in Section 3.1, the multipath channel encountered by a signal propagating from a BS to a mobile receiver may be modeled with the following channel impulse response (CIR) and channel frequency response (CFR) [20]:

$$h(\tau) = \sum_{l=0}^{L-1} h_l \delta(\tau - \tau_l), \tag{6.1}$$

$$H(f) = \sum_{l=0}^{L-1} h_l e^{-j2\pi f \tau_l}. \tag{6.2}$$

Using an estimate $\hat{\tau}_0$ of the DP TOA τ_0, the pseudorange $\hat{\rho} = c \cdot \hat{\tau}_0$ can be evaluated, from which a distance estimate $\hat{d}$ can be calculated. The relation between the pseudorange $\hat{\rho}$ and the distance estimate $\hat{d}$ between the BS and the receiver is discussed in Section 6.7. Thanks to the OFDM modulation that underlies their physical layer, LTE downlink signals offer a very convenient way of estimating the CFR using the CRS pilot tones. This CFR estimate constitutes a convenient and substantial basis for the DP TOA estimation.

Let $r^i_{t,l,n_s}[n]$, $n = 0, \ldots, N_{\text{dft}}-1$ be the result of the analog-to-digital conversion of the l^{th} OFDM symbol (after CP removal) received in the slot n_s at the measurement time t from cell i. Just the OFDM symbols carrying the CRS were saved, hence $l \in \{0, 4\}$. Moreover, since a measurement index t corresponds to a 10 ms chunck of saved data, approximately 20 slots are contained in each chunk, and hence $n_s \in \{0, \ldots, 19\}$.

Using the OFDM demodulation principles explained in Section 2.1, the content of the sub-carriers in the received signal can be easily accessed as $R^i_{t,l,n_s}[k] = \text{DFT}\{r^i_{t,l,n_s}[n]\}$. Hence, a simple least squares (LS) CFR estimation [33] is possible thanks to the knowledge of the CRS symbols $S^{i,p}_{t,l,n_s}[k]$, $k \in \mathcal{C}^{i,p}_{t,l,n_s}$, where $\mathcal{C}^{i,p}_{t,l,n_s} = \{6k + \kappa^{i,p}_l, k = 0, \ldots, N_{\text{tot}} - 1\}$ is the set of equispaced sub-carrier indices occupied by a CRS symbol, and $\kappa^{i,p}_l \in \mathbb{N} \cap [0, 5]$ is the frequency domain (FD) shift that characterizes each CRS mapping depending on $N^{\text{cell}}_{\text{ID}}$, p, and l. More particularly:

$$\hat{H}^{i,p}_{t,l,n_s}[k] = \frac{R^i_{t,l,n_s}[6k + \kappa^{i,p}_l]}{S^{i,p}_{t,l,n_s}[6k + \kappa^{i,p}_{t,l}]}, \ k = 0, \ldots, N_{\text{tot}} - 1. \tag{6.3}$$

for $p = \{0, 1\}$. As one can see, this procedure leads to a total of four CFR LS estimates for every slot in every measurement chunk t, one per antenna port for each OFDM symbol carrying CRS (two antenna ports $p = \{0, 1\}$, two symbols carrying CRS per slot). These CFR estimates are used in the presented framework for estimating the DP TOA τ_0.

This approach is particularly useful because it permits a convenient integration of the proposed positioning approach into LTE communication modules. Indeed, the CFR LS estimation of (6.3) is commonly performed by LTE receivers for coherently demodulating the user data [85], and can be passed, without additional computations, to a ranging module, that performs the processing required for the estimation of τ_0.

6.4.1 CFR estimates time-frequency merging

As explained in Section 6.3, only the two OFDM symbols of a slot containing the CRSs are stored during the preprocessing for every chunk of saved data. According to the mapping depicted in Figure 2.7b, the two CRSs of a slot pertaining to the same antenna port p occupy different sub-carriers. More particularly, $|\kappa_0^{i,p} - \kappa_4^{i,p}| = 3$, meaning that the sub-carriers of the two CRSs of a slot are characterized by a relative FD shift of $3\Delta f$. If the propagation channel is sufficiently correlated, i.e., the relative speed v between the transmitter and the receiver is sufficiently low, this aspect of the CRS design may be exploited by merging the two estimates $\hat{H}^{i,p}_{t,0,n_s}[k]$ and $\hat{H}^{i,p}_{t,4,n_s}[k]$ pertaining to the same slot n_s, as shown in Figure 6.7. This time-frequency combination permits to obtain the CFR estimate $\hat{H}^{i,p}_{t,n_s}[k]$, which is characterized by a frequency separation of $\Delta f_{\text{mCRS}} = 3\Delta f$ between samples (the subscript mCRS stands for "merged CRS"). More particularly, $\hat{H}^{i,p}_{t,n_s}[k] = \hat{H}^{i,p}_{t,l(k),n_s}[\lfloor k/2 \rfloor]$, where the function $l(k)$ selects the CFR estimate to assign to the index k according to:

$$l(k) = \begin{cases} 4 \cdot \langle k \rangle_2 \,, & \text{if } \kappa_0^{i,p} < \kappa_4^{i,p} \\ 4 \cdot \langle k+1 \rangle_2 \,, & \text{if } \kappa_0^{i,p} > \kappa_4^{i,p} \end{cases}, \tag{6.4}$$

and $k = 0, \dots, 2N_{\text{tot}} - 1$. An example result of this merging procedure applied to real data is shown in Figure 6.8.

A wireless fading channel tap h_l can be considered correlated both in envelope $|h_l|$ and phase $\phi_h = \arg\{h_l\}$ in the time interval Δt if its amplitude and phase correlation coefficients are above a certain threshold ρ_{th}. According to the Jakes' model, the envelope and phase normalized time correlation coefficients are a function of both the time interval Δt and Doppler frequency f_{D}, and are equal to [86]:

$$\rho_{|h|}(f_{\text{D}}\Delta t) \simeq J_0^2\left(2\pi f_{\text{D}}\Delta t\right), \tag{6.5}$$

$$\rho_{\phi_h}(f_{\text{D}}\Delta t) = 3 \cdot \Gamma(f_{\text{D}}\Delta t) \cdot [1 + \Gamma(f_{\text{D}}\Delta t)] - \frac{1}{8} \cdot \Omega(f_{\text{D}}\Delta t). \tag{6.6}$$

In (6.5)-(6.6), $J_0(\cdot)$ is the zero-order Bessel function of the first kind, $\Gamma(x) = \frac{1}{2\pi}\sin^{-1}(|J_0(2\pi x)|)$, and $\Omega(x) = \frac{6}{\pi^2}\sum_{n=1}^{\infty} n^{-2} \cdot J_0^{2n}(2\pi x)$. The curves of Figure 6.9

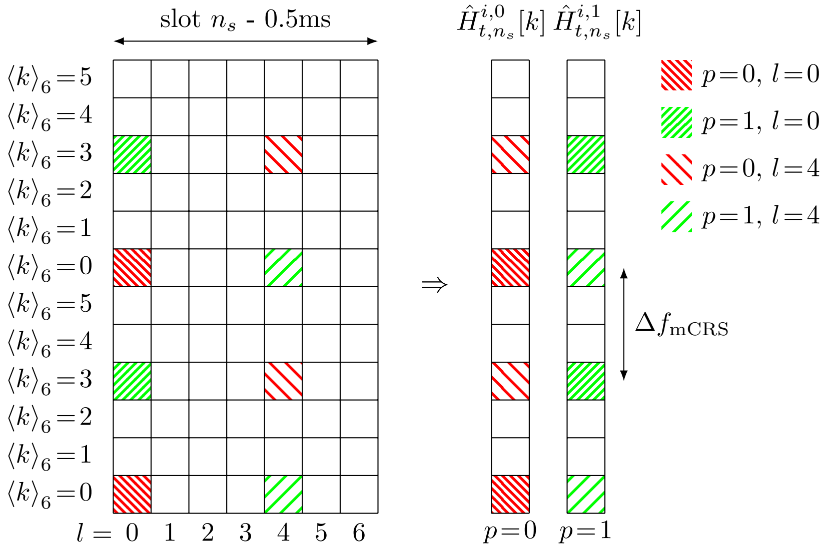

Figure 6.7 – Example of merging the CFR LS estimates evaluated using the two CRSs of a slot, for each antenna port.

depict the expressions above. As one can see, a correlation threshold of $\rho_{\mathrm{th}} = 0.9$ approximately imply $f_{\mathrm{D}}\Delta t < 0.025$ for having correlated envelope and phase, with $f_{\mathrm{D}} = f_{\mathrm{C}} \cdot v/c$ and f_{C} being the carrier frequency. Without loss of generality, and using the LTE system parameters measured in Rapperswil, the time interval between two CRSs in a slot is equal to $\Delta t = 4T_{\mathrm{s}} + \sum_{l=0}^{3} T_{\mathrm{cp},l} \simeq 285\,\mu\mathrm{s}$, and the carrier frequency may be assumed equal to $f_{\mathrm{C}} = 1850\,\mathrm{MHz}$. Then, the relative speed between transmitter and receiver must be $v < 51.2\,\mathrm{km/h}$ in order to have correlated channel gains. At a speed of $v = 51.2\,\mathrm{km/h} = 14.2\,\mathrm{m/s}$, the distance covered in $\Delta t = 285\,\mu\mathrm{s}$ is $d = 4\,\mathrm{mm}$, which correspond to a negligible difference in the signal TOA (only $d/c \simeq 0.013\,\mathrm{ns}$). Hence, if the speed constraint that ensures the channel gains correlation is respected, the CFR estimates merging of (6.4) has negligible consequences on the signal TOA, while decreases the FD sampling interval.

Since $v = 51.2\,\mathrm{km/h}$ is higher than the achieved maximum speed in both the outdoor vehicular and the indoor measurement scenarios, the CFR time-frequency combining strategy was adopted in the proposed work. The benefits of merging the CFR estimates $\hat{H}^{i,p}_{t,l,n_s}[k]$ consist in an increased number of samples for each CFR estimate $\hat{H}^{i,p}_{t,n_s}[k]$ and in a smaller frequency separation $\Delta f_{\mathrm{mCRS}} < \Delta f_{\mathrm{CRS}}$ between adjacent samples. Depending on the TOA estimation algorithm adopted, this may correspond to increased resolution and increased maximum TOA computable.

6.4.2 Combining CFR estimates from multiple slots

After the merging procedure described above, the merged CFR estimates $\hat{H}^{i,p}_{t,n_s}[k]$ of all the slots pertaining to each measured 10 ms chunk are available. Hence, an appropriate method for combining these estimates is needed, in order to obtain a

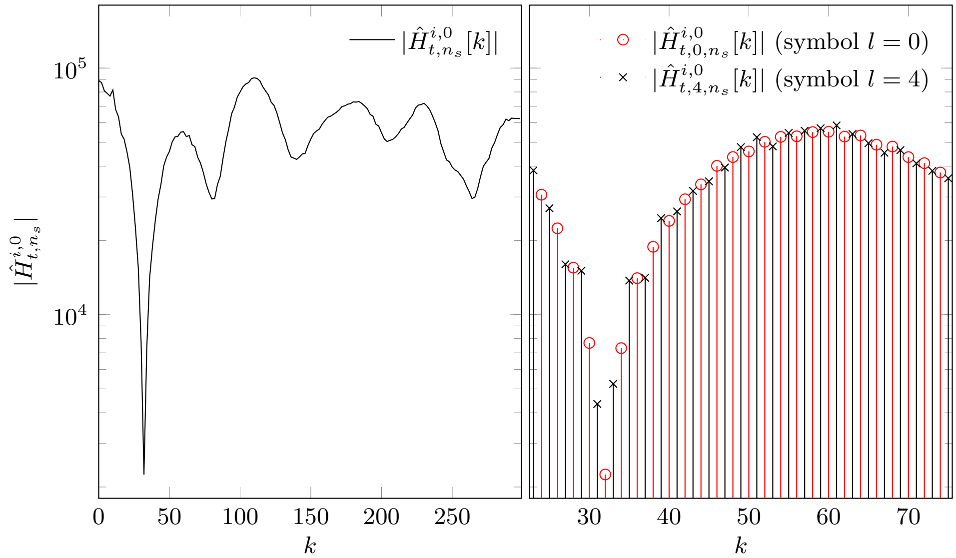

Figure 6.8 – Result of the merging procedure for the CFR estimated during the outdoor vehicular measurements using the CRSs of antenna port $p = 0$, cell ID $N^{\text{cell}}_{\text{ID}} = 84$, base station 1, operator 1, measurement time $t = 1$, slot $n_s = 4$. The plot on the right is a particular of the plot on the left.

single CFR estimate representative of the measurement time t, one per antenna port p and per detected cell i. In the presented approach, two methods are proposed. The application of one particular method depends on the type of mobility that characterize the measurement environment to which the analyzed signals pertain.

In high mobility environments, such as the vehicular outdoor measurement scenario of Figure 6.2a - Figure 6.6, a selection method based on the signal-to-noise ratio (SNR) is proposed. A selection method is preferred to a combining method since in a high mobility environment the correlation between subsequent CFR estimates, which would be required by a combining method, cannot be ensured. The CFR estimate between the $\hat{H}^{i,p}_{t,n_s}[k]$, $n_s = 0, \ldots, 19$ corresponding to the highest received SNR is chosen as representative of the chunk acquired at measurement time t, i.e. $\hat{H}^{i,p}_{t}[k] = \hat{H}^{i,p}_{t,\bar{n}_s}[k]$, where:

$$\bar{n}_s = \arg\max_{n_s} \left\{ \gamma\left(\hat{H}^{i,p}_{t,n_s}[k] \right) \right\}. \tag{6.7}$$

In (6.7), the operator $\gamma(\cdot)$ associates to the CFR $\hat{H}^{i,p}_{t,n_s}[k]$ the corresponding estimated instantaneous SNR. Several estimators designed for the estimation of the SNR of OFDM signals may be employed, such as [87,88]. However, the methods proposed in these papers are more suited for average SNR estimation, and require a long training before producing reliable estimates. That is why, in the presented results, the fast heuristic SNR estimator inspired by [89,90] has been employed, which is based on a χ^2 statistical analysis of each power delay profile (PDP). For the estimated merged

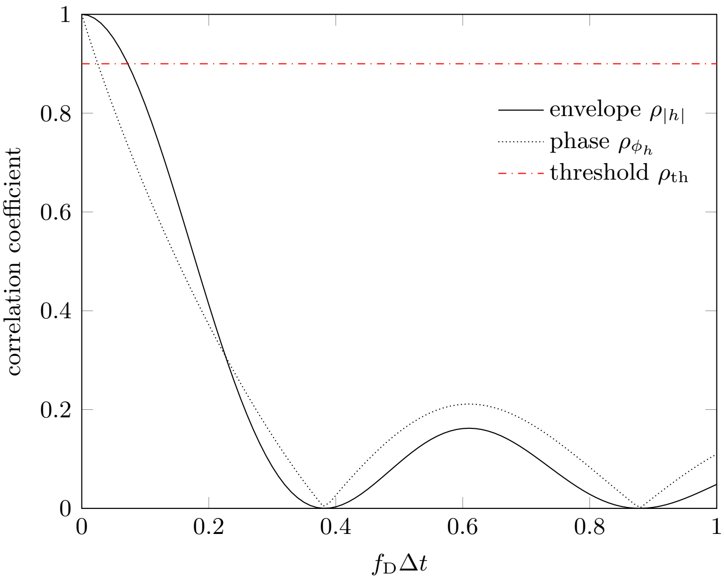

Figure 6.9 – Normalized correlation coefficients for envelope and phase of a wireless fading channel gain as a function of time and Doppler frequency.

CFR pertaining to each slot n_s, the corresponding CIR is first computed as:

$$\hat{h}^{i,p}_{t,n_s}[n] = \mathrm{IDFT}\{\hat{H}^{i,p}_{t,n_s}[k]\},\ n = 0, \dots, 2N_\mathrm{tot} - 1. \tag{6.8}$$

Then, the PDP is computed as $|\hat{h}^{i,p}_{t,n_s}[n]|^2$, and the heuristic SNR estimator is defined as:

$$\gamma\left(\hat{H}^{i,p}_{t,n_s}[k]\right) = \max\left\{0, \frac{\sum_{n\in\mathcal{N}_\mathrm{th}} |\hat{h}^{i,p}_{t,n_s}[n]|^2 - N^+_\mathrm{th}\cdot\hat{\sigma}^2_w}{N^-_\mathrm{th}\cdot\hat{\sigma}^2_w}\right\}, \tag{6.9}$$

where $\mathcal{N}_\mathrm{th}$ is the set having cardinality $N^+_\mathrm{th} = \mathrm{n}\left[\mathcal{N}_\mathrm{th}\right]$ of the indexes n for which the PDP is above the noise threshold w_th, $N^-_\mathrm{th} = 2\cdot N_\mathrm{tot} - N^+_\mathrm{th}$, and $\hat{\sigma}^2_w$ is an estimate of the mean square value of the noise $w[n]$ that corrupts the CIR estimate. Under the assumption of complex Gaussian noise, $\hat{\sigma}^2_w$ and w_th can be evaluated by exploiting some statistical properties of the χ^2 distribution. In particular, the square magnitude W^2 of a complex Gaussian random variable $\mathcal{CN}(0,1)$ is χ^2 distributed with $k = 2$ degrees of freedom, and has average $\mathbb{E}[W^2] = k$ and median $\{W^2\} \simeq k\cdot\left(1 - \frac{2}{9k}\right)^3$. Under the assumption that median$\{|w[n]|^2\} \simeq$ median$\{|\hat{h}^{i,p}_{t,n_s}[n]|^2\}$, which holds if the duration of the actual CIR is much shorter than the observation window, the noise mean square value can be estimated as:

$$\hat{\sigma}^2_w \simeq \mathrm{median}\left\{|\hat{h}^{i,p}_{t,n_s}[n]|^2\right\}\frac{\mathbb{E}\left[W^2\right]}{\mathrm{median}\left\{W^2\right\}}. \tag{6.10}$$

Similarly, the noise threshold value w_th can be estimated as:

$$w_\mathrm{th} \simeq \mathrm{median}\left\{|\hat{h}^{i,p}_{t,n_s}[n]|^2\right\}\frac{F^{-1}_{\chi^2(2)}(p)}{\mathrm{median}\left\{W^2\right\}}, \tag{6.11}$$

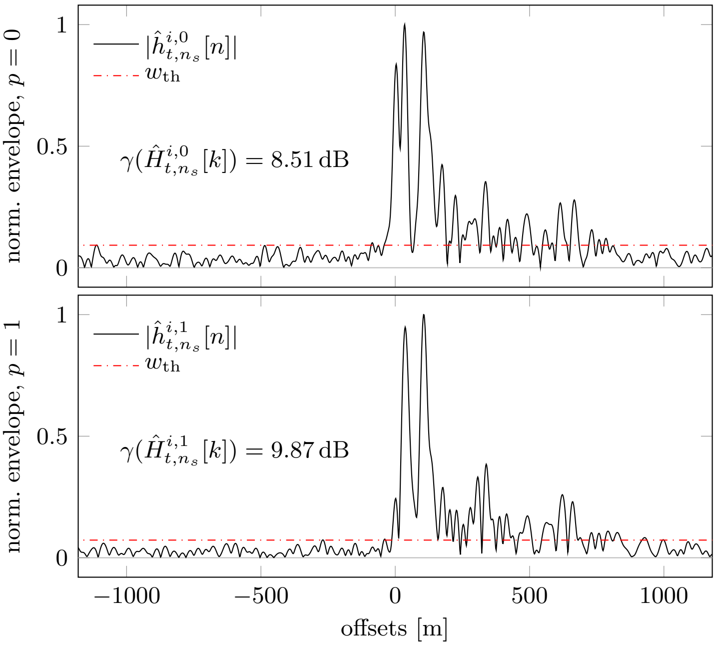

Figure 6.10 – Example of an SNR estimation using the fast heuristic estimator of (6.9). The merged CRSs used for the estimation pertain to the outdoor dataset, and have been received from the antenna ports of cell ID $N^{\text{cell}}_{\text{ID}} = 72$, BS 3, operator 1, at measurement time $t = 600$, slot $n_s = 17$. The time axes is expressed as distance offsets.

where $F^{-1}_{\chi^2(2)}(\cdot)$ is the inverse cumulative density function (CDF) of the $\chi^2(2)$ distribution. In the proposed results, a value of $p = 0.99$ has been used. An example of SNR estimation performed with (6.9) is shown in Figure 6.10.

On the other hand, for low mobility environments such as the indoor scenario of Figures 6.2b - Figure 6.5, a combining method can be employed, since low mobility ensures a certain degree of correlation between subsequent CFR estimates. Even a simple average between subsequent slots' CFR estimates can increase the SNR thanks to the averaging of noise, and this gives rise to substantial improvements in the channel estimation. Since the duration of a slot is of 0.5 ms, under the same assumptions of Section 6.4.1, the relative speed between transmitter and receiver must be $(N_s - 1)\cdot 0.5\cdot 10^{-3}\cdot v\cdot f_{\text{C}}/c < 0.025 \Leftrightarrow v < \frac{1}{(N_s-1)} 8.11\,\text{m/s}$ in order to combine N_s slots. If this constraint is satisfied, then the estimated CFR representative of the measurement time t can be obtained as a coherent average of $N_s \leq 20$ CFRs pertaining to subsequent slots, as:

$$\hat{H}^{i,p}_{t} = \frac{1}{N_s} \sum_{n_s=0}^{N_s-1} \hat{H}^{i,p}_{t,n_s}. \tag{6.12}$$

Given the very low speeds that characterize the indoor measurement scenario, the averaging method of (6.12) has been used for the indoor dataset, with a number of $N_s = 18$ slots to be combined. Again, such an average has negligible consequences from the TOA estimation point of view, since the distance traveled for $\Delta t = 17 \cdot 0.5\,\text{ms} = 8.5\,\text{ms}$ at $v = 8.11/17 \simeq 0.48\,\text{m/s}$ is $d \simeq 4\,\text{mm}$, which corresponds to a TOA variation of $d/c \simeq 0.013\,\text{ns}$.

6.5 Some basic TOA estimators

By exploiting the CFR estimates obtained after time-frequency merging (Section 6.4.1) and time combining (Section 6.4.2), denoted as $\hat{H}_t^{i,p}[k]$, $k = 0, \ldots, 2N_{\text{tot}} - 1$, a simple TOA estimation may be realized using an approach similar to [91]. Following that approach, a discrete CIR estimate is first computed as:

$$\hat{h}_t^{i,p}[n] = \text{IDFT}\{\hat{H}_t^{i,p}[k]\},\ n = 0, \ldots, 2N_{\text{tot}} - 1, \tag{6.13}$$

and then the TOA is obtained with a parabolic interpolation around the maximum of (6.13), as:

$$\hat{n}_0 = \arg\max_n \big\{ \big|\hat{h}[n]\big| \big\}, \tag{6.14}$$

$$\hat{\tau}_0 = T_{\text{CIR}} \left(\hat{n}_0 + \frac{\frac{1}{2}\big(|\hat{h}[\hat{n}_0 - 1]| - |\hat{h}[\hat{n}_0 + 1]|\big)}{|\hat{h}[\hat{n}_0 + 1]| - 2|\hat{h}[\hat{n}_0]| + |\hat{h}[\hat{n}_0 - 1]|} \right), \tag{6.15}$$

where the indices i, p, t have been omitted for notational simplicity and T_{CIR} is the time resolution of the computed CIR, which can be increased with straightforward up-sampling techniques. Throughout the remainder of the chapter, this method will be referred to as *IDFT-MAX* (IM). Since $T_{\text{CIR}} = \frac{1}{2N_{\text{tot}}\Delta f_{\text{mCRS}}}$ and since $\hat{h}_t^{i,p}[n]$ is made of $2N_{\text{tot}}$ samples, then the CIR of (6.13) spans the time interval $\big[-\frac{1}{2\Delta f_{\text{mCRS}}}, \frac{1}{2\Delta f_{\text{mCRS}}}\big) = \big[-11.11\,\mu\text{s}, 11.11\,\mu\text{s}\big)$. It is evident that the reduced FD separation between the CFR samples due to the merging procedure of Section 6.4.1 permits a widening of the interval observable for TOA estimation.

Although attractive for its computational simplicity, the method of (6.13)-(6.15) is not robust against multipath, because harsh propagation environments are typically characterized by a DP which is not necessarily the strongest path. A simple countermeasure consists in the computation of the N_{IL} highest CIR peaks, where N_{IL} is a parameter subject to empirical tuning. The measure is considered as a LOS case only if the maximum of the CIR is the earliest peak between the N_{IL}. In this case, the DP TOA is assumed to be the interpolated CIR maximum, similarly to (6.15). Otherwise, the measurement is discarded. This method is referred to as *IDFT-LOS* (IL), it is quite robust in identifying NLOS measurements, but it has the drawback of discarding measurements without producing TOA estimates.

Other TOA estimation methods based on the CIR evaluation are the threshold based methods of [92–94]. However, these have not been considered in the presented work because of the difficulties encountered in defining a threshold selection method that suited all the different propagation environments encountered during the test route.

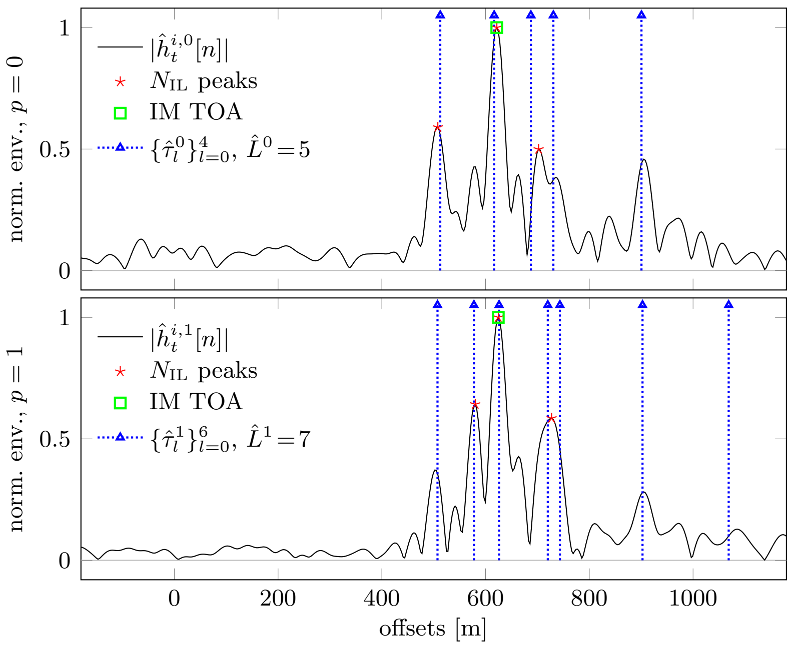

(a) Outdoor vehicular dataset, $N_{\mathrm{ID}}^{\mathrm{cell}} = 51$, BS 1, operator 2, $t = 2561$.

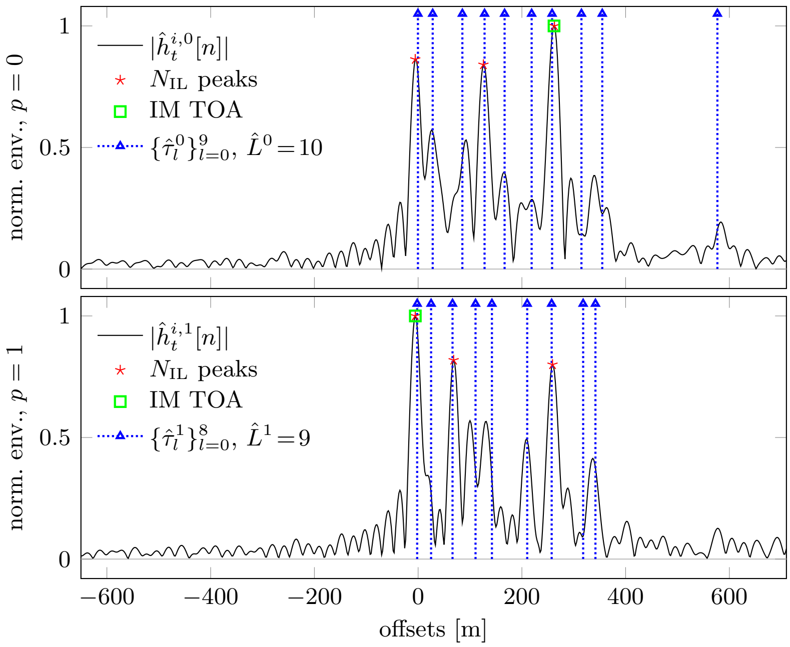

(b) Indoor dataset, $N_{\mathrm{ID}}^{\mathrm{cell}} = 237$, BS 1, operator 3, $t = 290$.

Figure 6.11 – Examples of CIRs and simple TOA estimations. Both the estimations pertaining to antenna ports $p = 0$ and $p = 1$ are shown. The DP TOA estimates obtained with IM are also shown, together with the multipath TOA estimates obtained with ESPRIT, indicated with $\{\hat{\tau}_l^p\}_{l=0}^{\hat{L}^p - 1}$ (where $\hat{L}^p$ is the estimated number of multipath components). The IL estimator uses $N_{\mathrm{IL}} = 3$. All time estimates are expressed as distance offsets.

Examples of IM and IL TOA estimates are shown in Figure 6.11. The estimates are obtained exploiting the CRSs transmitted from the two antenna ports of cell $N_{\mathrm{ID}}^{\mathrm{cell}} = 51$, BS 1, operator 2 of the outdoor dataset, shown in Figure 6.11a, and of cell $N_{\mathrm{ID}}^{\mathrm{cell}} = 237$, BS 1, operator 3 of the indoor dataset, shown in Figure 6.11b. The ESPRIT multipath TOA estimates, computed as described in Section 6.6.1, are also shown as a reference, since they constitute a more precise estimate. As one can note, the CIRs pertaining to different antenna ports exhibit different multipath, but similar DP TOA. In the cases of Figure 6.11a and Figure 6.11b antenna port $p = 0$, the IM estimations fails to locate what appears to be the DP (i.e., the path at offset around 500 m for Figure 6.11a and the path at offset around 0 m for Figure 6.11b). In all these three cases, the IL estimator correctly recognizes the measurements as NLOS cases, and discards them.

These simple CIR based estimators were considered as a benchmark of the proposed algorithm, also because similar estimators are being considered by standards committees for modeling LTE receivers in positioning applications [95].

6.6 The EKAT algorithm

The main contribution of this part of the thesis work consists of a DP TOA estimator which is robust against multipath and that enables further insights on the effects of multipath on TOA based ranging. The algorithm is shown to overcome the detrimental effects of multipath suffered by the simple algorithms considered in Section 6.5. The proposed method is referred to as "ESPRIT and Kalman filter for time of Arrival Tracking" (EKAT). Briefly, EKAT relies on the ESPRIT SRA for separating multipath and performing the TOA estimation, and on a Kalman filter (KF) for tracking the estimated pseudorange along subsequent measurements. Moreover, EKAT exploits a bound-based estimation of the measurements reliability for filling the KF measurement covariance matrix, and an empirical selection of the DP TOA among the estimates produced by ESPRIT. Its flow graph is represented in Figure 6.12, with the blocks described in the following sections.

6.6.1 ESPRIT-based multipath TOA estimation

As shown in Section 3.1, the CFR of a mobile multipath channel, expressed in (6.2), can be seen as a sum of L complex sinusoids, having "frequency" equal to τ_l, $\forall l$. After sampling this CFR with interval Δf_{mCRS}, one obtains the discrete signal $H[k] = \sum_{l=0}^{L-1} h_l e^{j2\pi k \Delta f_{\mathrm{mCRS}} \tau_l}$, which is a so-called harmonic model [36]. Hence, as explained in Section 3.1, sub-space based SRAs can be employed for the estimation of the delays $\tau_l, \forall l$, provided that an estimate of $H[k]$ is available.

EKAT uses for this purposes the CFR estimates $\hat{H}_t^{i,p}[k]$, $k = 0, \ldots, 2N_{\mathrm{tot}} - 1$, obtained with the merging and combining methods explained in Section 6.4. The minimum descriptive length (MDL) criterion is applied for the estimation of L, and the ESPRIT algorithm is then used for the estimation of the τ_l, $\forall l$. More

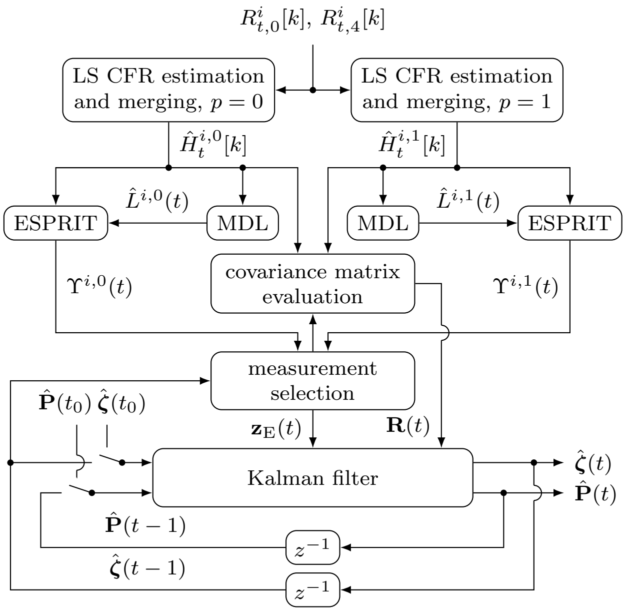

Figure 6.12 – Flow graph of the EKAT algorithm applied to the signals measured from the cell i.

particularly, for each detected cell i, measurement instant t, and antenna port p, MDL and ESPRIT are applied to $\hat{H}^{i,p}_t[k]$ as follows.

The samples of $\hat{H}^{i,p}_t[k]$ are arranged in length M snapshots $\boldsymbol{x}^{i,p}_t[k]$, which are used to build the so-called data matrix $\mathbf{X}^{i,p}_t$:

$$\mathbf{X}^{i,p}_t = \frac{1}{\sqrt{N}}\left[\boldsymbol{x}^{i,p}_t[0], \cdots, \boldsymbol{x}^{i,p}_t[N-1]\right] \in \mathbb{C}^{M\times N}, \tag{6.16}$$

$$\boldsymbol{x}^{i,p}_t[k] = \left[\hat{H}^{i,p}_t[k], \cdots, \hat{H}^{i,p}_t[k+M-1]\right]^{\mathrm{T}} \in \mathbb{C}^{M}, \tag{6.17}$$

where $N = 2N_{\mathrm{tot}} - M + 1$ and M is a design parameter of the SRA. M is usually chosen as $M = m \cdot N_{\mathrm{tot}} \cdot 2$, with m being a parameter subject to empirical tuning, as shown in Section 6.9.2. Higher values of M ensures increased resolution in multipath separation, at the cost of decreased averaging of noise [15].

In the remainder of this section, the indices i, t, p will be omitted for notational simplicity. As explained in Section 3.1, the data matrix $\mathbf{X}$ is related to an estimate of the auto-correlation matrix $\mathbf{R}_x$ of $\boldsymbol{x}[k]$ by the relation $\hat{\mathbf{R}}_x = \mathbf{X}\cdot\mathbf{X}^{\mathrm{H}} \in \mathbb{C}^{M\times M}$. Hence, estimates of the eigenvalues of $\mathbf{R}_x$, denoted with $\lambda_1 \geq \cdots \geq \lambda_M$, can be obtained by taking the square of the singular values of $\mathbf{X}$, obtained with a singular values decomposition (SVD) as $\mathbf{X} = \mathbf{U}\cdot\boldsymbol{\Sigma}\cdot\mathbf{L}^{\mathrm{H}}$. The matrices $\mathbf{U} \in \mathbb{C}^{M\times M}$ and $\mathbf{L} \in \mathbb{C}^{N\times N}$ are unitary, and $\boldsymbol{\Sigma} \in \mathbb{C}^{M\times N}$ is a diagonal matrix with the singular values $\sigma_1 \geq \cdots \geq \sigma_M$ in the main diagonal, where $(\sigma_i)^2 = \lambda_i$, $i = 1, \ldots, M$. Using the estimated eigenvalues, the MDL criterion can be applied for the estimation of L in the considered CFR, by calculating the metric [15, 37]:

$$\mathrm{MDL}(k) = -N(M-k)\log\left\{\frac{\prod_{i=k}^{M-1}\lambda_i^{1/(M-k)}}{\frac{1}{M-k}\sum_{i=k}^{M-1}\lambda_i}\right\} + p(k), \tag{6.18}$$

where $p(k) = \frac{1}{2}k(2M-k)\log N$. Then, L is estimated by minimizing the metric of (6.18), i.e., as $\hat{L} = \arg\min_{k\in\{0,\dots,M-1\}}\mathrm{MDL}(k)$. Once the number of multipath components has been estimated, the ESPRIT algorithm is applied by using the following matrix computations on the singular vectors of $\mathbf{U}$, as:

$$\mathbf{U}_s = \mathbf{U}\cdot[\mathbf{I}_{\hat{L}}\mathbf{0}_{\hat{L}\times(M-\hat{L})}]^{\mathrm{T}} \in \mathbb{C}^{M\times\hat{L}}, \tag{6.19a}$$

$$\mathbf{U}_{s,1} = [\mathbf{I}_{M-1}\mathbf{0}_{M-1}]\cdot\mathbf{U}_s \in \mathbb{C}^{M-1\times\hat{L}}, \tag{6.19b}$$

$$\mathbf{U}_{s,2} = [\mathbf{0}_{M-1}\mathbf{I}_{M-1}]\cdot\mathbf{U}_s \in \mathbb{C}^{M-1\times\hat{L}}, \tag{6.19c}$$

$$\boldsymbol{\Psi} = \mathbf{U}_{s,1}^{\dagger}\cdot\mathbf{U}_{s,2} \in \mathbb{C}^{\hat{L}\times\hat{L}}. \tag{6.19d}$$

Finally, the $\hat{L}$ eigenvalues $\psi_0, \dots, \psi_{\hat{L}-1}$ of $\boldsymbol{\Psi}$ are computed, and then used to evaluate the multipath TOA as:

$$\hat{\tau}_l = -\frac{1}{2\pi\Delta f_{\mathrm{mCRS}}}\arg\{\psi_l\}, \; l = 0, \cdots, \hat{L}-1. \tag{6.20}$$

From the fact that $\arg\{\psi_l\} \in [-\pi, \pi)$, $\forall l$, it follows that ESPRIT is capable of estimating a TOA in the interval $\left[-\frac{1}{2\Delta f_{\mathrm{mCRS}}}, \frac{1}{2\Delta f_{\mathrm{mCRS}}}\right) = \left[-11.11\,\mu\mathrm{s}, 11.11\,\mu\mathrm{s}\right)$ around the instant of measure t. Again, it is evident that the decrease in the FD separation between the CFR samples due to the merging procedure described in Section 6.4.1 permits a widening of the interval observable for TOA estimation.

As a result of the whole procedure described above, a set of $\hat{L}^{i,p}(t)$ multipath TOA $\Upsilon^{i,p}(t) = \{\hat{\tau}_0^{i,p}(t) < \cdots < \hat{\tau}_{\hat{L}^{i,p}(t)-1}\}$ is produced using the merged CFR estimate corresponding to the antenna port p of the i^{th} sector at each measurement time t. It has to be noted that a well known shortcoming of the MDL criterion is that it tends to overestimate L in case of large snapshot lengths M and high SNR values (i.e., low σ_w^2 values) [96–98]. Hence, overestimated values of L may cause ESPRIT to produce TOA outliers, which may be even smaller than the actual DP TOA τ_0. EKAT overcomes this weakness using the measurement selection strategy described in Section 6.6.4.

An example of the results obtained with the described multipath TOA estimation procedure is depicted in the plots of Figure 6.13. There, for each measurement index t, up to the first 4 paths estimated using the CRSs of cell $N_{\mathrm{ID}}^{\mathrm{cell}} = 52$ operator 2 (Figure 6.13a) and of cell $N_{\mathrm{ID}}^{\mathrm{cell}} = 52$ operator 2 (Figure 6.13b) pertaining to the outdoor vehicular dataset are shown for each antenna port. All the values are expressed as pseudoranges, obtained as $c\cdot(\hat{\tau}_l^{i,p}(t) + \Delta t_{\mathrm{s}}^i)$, where Δt_{s}^i is the time offset introduced in respect to t for the cell i symbol level coarse synchronization, as explained in Section 6.3.3. As one can see, the first detected path has almost the same

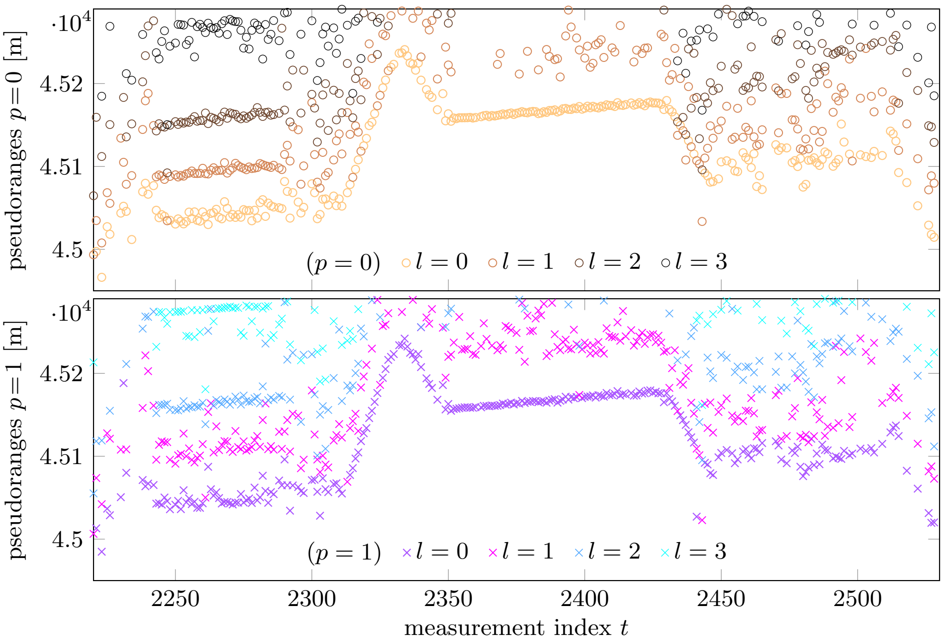

(a) $N_{\mathrm{ID}}^{\mathrm{cell}} = 52$, BS 1, operator 2 (outdoor vehicular scenario).

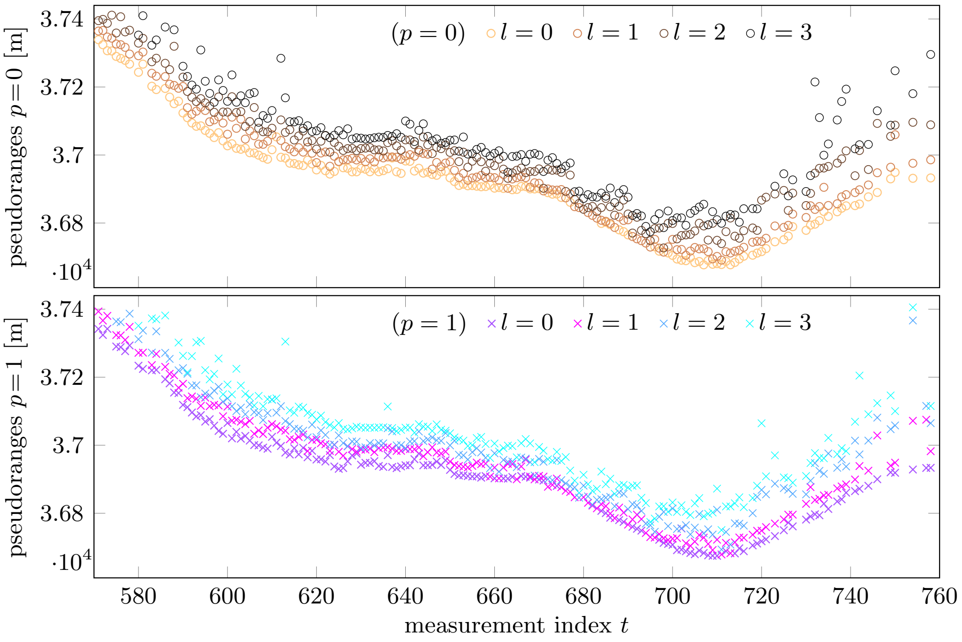

(b) $N_{\mathrm{ID}}^{\mathrm{cell}} = 72$, BS 3, operator 1 (outdoor vehicular scenario).

Figure 6.13 – Results of the ESPRIT multipath TOA estimations in representative time intervals of the outdoor vehicular dataset. All the plotted values are pseudoranges obtained multiplying by c the estimated TOA. The multipath estimates of both antenna ports $p = 0$ and $p = 1$ are shown.

TOA for the two antenna ports, while the other paths are different. This is evident in the interval $[2350, 2430]$ of Figure 6.13a, where there is almost no multipath from $p = 0$, while from $p = 1$ at least a second multipath component is received after the first. Another important aspect to highlight is the constant slope of all paths that is visible across the whole displayed measurement interval of Figure 6.13a, which is a detrimental consequence of the BS clock drift.

6.6.2 State-space model

The estimation of the multipath TOA described in Section 6.6.1 is needed for separating the delayed paths from the DP, which is then tracked for positioning purposes with the procedure described in the following. For each detected cell i, EKAT performs the tracking of the DP TOA along the different measurement times t using a state-space approach similar to [78]. More specifically, consider the state vector defined as the DP TOA $\tau_0^i(t)$ of cell i and its rate of change $\Delta\tau_0^i(t)$, i.e.:

$$\boldsymbol{\zeta}^i(t) = \left[\tau_0^i(t), \Delta\tau_0^i(t)\right]^{\mathrm{T}} \in \mathbb{R}^2. \tag{6.21}$$

In the following, the index i will be dropped for notational simplicity. The evolution in time of $\boldsymbol{\zeta}(t)$ is modeled as described in [77], with the following recursive relation:

$$\boldsymbol{\zeta}(t) = \mathbf{F}\cdot\boldsymbol{\zeta}(t-1) + \boldsymbol{q}(t-1), \quad \mathbf{F} = \begin{bmatrix} 1 & 1 \\ 0 & 1 \end{bmatrix}, \tag{6.22}$$

where the entries of the vector $\boldsymbol{q}(t) \in \mathbb{R}^2$, that models the process noise, are zero mean white Gaussian processes. The covariance matrix of $\boldsymbol{q}(t)$, according to the model of [77], is chosen to be constant and equal to:

$$\mathbf{Q} = \mathbb{E}\left[\boldsymbol{q}(t)\boldsymbol{q}^{\mathrm{H}}(t)\right] = q \begin{bmatrix} \frac{1}{3} & \frac{1}{2} \\ \frac{1}{2} & 1 \end{bmatrix}, \tag{6.23}$$

where $q \in \mathbb{R}^+$ is a design parameter that is proportional to some increasing function of the receiver speed. Consider then the following measurement equation:

$$\boldsymbol{z}_{\mathrm{E}}(t) = \mathbf{F}\cdot\boldsymbol{\zeta}(t) + \boldsymbol{r}(t), \quad \mathbf{F} = \begin{bmatrix} 1 & 0 \\ 1 & 0 \end{bmatrix}, \tag{6.24}$$

where the entries of the vector $\boldsymbol{r}(t) \in \mathbb{R}^2$, that models the measurement noise, are zero mean white Gaussian processes. The covariance matrix $\mathbf{R}(t) = \mathbb{E}[\boldsymbol{r}(t)\boldsymbol{r}^{\mathrm{H}}(t)] \in \mathbb{R}^{2\times 2}$ is evaluated according to the procedure described in Section 6.6.5. As one can see, (6.24) defines two available measurements for the first component of $\boldsymbol{\zeta}(t)$, i.e., two measurements of the DP TOA. The approach of EKAT is to exploit the two TOA estimates corresponding to the CRSs received from the two antenna ports $p = 0$ and $p = 1$ as the two DP TOA measurements contained in $\boldsymbol{z}_{\mathrm{E}}(t)$.

As a final note, the transmit antenna ports are usually positioned in a way to provide a certain degree of diversity to the receiver. As an example, when two antenna ports are configured, these usually provide polarization diversity [76], i.e., the two antennas transmit electromagnetic fields with orthogonal polarizations. As a consequence, the signals received from the two antenna ports travel through different multipath channels, though sharing the same DP delay. Consequently, the DP TOA measurements from the two antenna ports can be threated as affected by uncorrelated noise, and hence $\mathbf{R}(t)$ is diagonal.

Thanks to the linear dynamic system defined by (6.22)-(6.24) it is possible, using a conventional KF, to evaluate an estimate of the state vector, and ultimately track the DP TOA [28]. As one can see from Figure 6.12, the KF takes as an input a selection $\boldsymbol{z}_{\mathrm{E}}(t)$ of the TOA measurements performed with ESPRIT, together with the matrix $\mathbf{R}(t)$, and outputs an estimate of the state, denoted with $\hat{\boldsymbol{\zeta}}(t) \in \mathbb{R}^2$, and the covariance matrix of the estimated state, denoted with $\hat{\mathbf{P}}(t) \in \mathbb{R}^{2\times 2}$. As a consequence of the definition in (6.21), the tracked DP TOA is the first component $\hat{\zeta}_0(t)$ of the estimated state $\hat{\boldsymbol{\zeta}}(t) = [\hat{\zeta}_0(t), \hat{\zeta}_1(t)]^{\mathrm{T}}$. Moreover, the upper left element of the estimated state covariance $\hat{\mathbf{P}}(t)$, denoted with $\hat{P}_{0,0}(t)$, corresponds to the variance of the tracked DP TOA.

6.6.3 DP TOA tracking with a Kalman filter

The Kalman filtering for the estimation of the state $\boldsymbol{\zeta}(t)$ pertaining to the i^{th} BS sector follows the approach of [28] and consists of the following set of recursive matrix equations:

$$\hat{\boldsymbol{\zeta}}^{-}(t) = \mathbf{F}\cdot\hat{\boldsymbol{\zeta}}(t-1), \tag{6.25}$$

$$\hat{\mathbf{P}}^{-}(t) = \mathbf{F}\cdot\hat{\mathbf{P}}(t-1)\cdot\mathbf{F}^{\mathrm{T}} + \mathbf{Q}, \tag{6.26}$$

$$\mathbf{W}(t) = \hat{\mathbf{P}}^{-}(t)\cdot\mathbf{H}^{\mathrm{T}}\cdot\left[\mathbf{R}(t) + \mathbf{H}\cdot\hat{\mathbf{P}}^{-}(t)\cdot\mathbf{H}^{\mathrm{T}}\right]^{-1}, \tag{6.27}$$

$$\hat{\boldsymbol{\zeta}}(t) = \hat{\boldsymbol{\zeta}}^{-}(t) + \mathbf{W}(t)\cdot\left[\boldsymbol{z}_{\mathrm{E}}(t) - \mathbf{H}\cdot\hat{\boldsymbol{\zeta}}^{-}(t)\right], \tag{6.28}$$

$$\hat{\mathbf{P}}(t) = \left[\mathbf{I}_2 - \mathbf{W}(t)\cdot\mathbf{H}\right]\cdot\hat{\mathbf{P}}^{-}(t), \tag{6.29}$$

where $\hat{\boldsymbol{\zeta}}^{-}(t)$, $\hat{\mathbf{P}}^{-}(t)$, $\hat{\boldsymbol{\zeta}}(t)$, $\hat{\mathbf{P}}(t)$ and $\mathbf{W}(t)$ correspond to the predicted state, the predicted state covariance, the estimated state, the estimated state covariance, and the KF gain, respectively. The calculation of the first estimated state $\hat{\boldsymbol{\zeta}}(t_0)$ and the corresponding covariance $\hat{\mathbf{P}}(t_0)$ is performed in a similar way to the two step initialization procedure of [28], by exploiting the measurements $\boldsymbol{z}_{\mathrm{E}}(t_0)$, $\boldsymbol{z}_{\mathrm{E}}(t_{-1})$, where t_0 and t_{-1} are two time measurement indexes not displaced more than D_{init} measurement instants, i.e., $t_0 - t_{-1} \leq D_{\mathrm{init}}$. This is for allowing KF initialization even in the case of measurements not being continuous. This is important as a particular cell i is not necessarily received continuously in all measurement instants due to obstacles in the propagation environment or because of deep fades.

During initialization, the measurement vector $\boldsymbol{z}^{i}_{\mathrm{E}}(t) = [z^{i,0}_{\mathrm{E}}(t),\, z^{i,1}_{\mathrm{E}}(t)]^{\mathrm{T}}$ for cell i

is filled with the smallest TOA estimated by ESPRIT from each antenna port, i.e.:

$$\begin{aligned} \boldsymbol{z}_{\mathrm{E}}^{i}(t_0) &= \left[z_{\mathrm{E}}^{i,0}(t),\, z_{\mathrm{E}}^{i,1}(t)\right]^{\mathrm{T}} = \left[\Delta t_{\mathrm{s}}^{i} + \min\{\Upsilon^{i,0}(t_0)\},\, \Delta t_{\mathrm{s}}^{i} + \min\{\Upsilon^{i,1}(t_0)\}\right]^{\mathrm{T}} \\ &= \left[\Delta t_{\mathrm{s}}^{i} + \hat{\tau}_0^{i,0}(t_0),\, \Delta t_{\mathrm{s}}^{i} + \hat{\tau}_0^{i,1}(t_0)\right]^{\mathrm{T}} \in \mathbb{R}^2. \end{aligned} \tag{6.30}$$

As one can note, the ESPRIT estimates are saved in $\boldsymbol{z}_{\mathrm{E}}(t)$ after being added to the time offset $\Delta t_{\mathrm{s}}^{i}$ introduced in respect to $t^{(\mathrm{U})}$ by the coarse symbol level synchronization to cell i. The initial measurement covariance matrix $\mathbf{R}^{i}(t_0)$ is filled accordingly, as described in Section 6.6.5. Then, upon defining the mean measured TOA at t_0 and t_{-1}, and the variance of the former, as (the index i being dropped for simplicity):

$$z_0 = \tfrac{1}{2}\left(z_{\mathrm{E}}^{0}(t_0) + z_{\mathrm{E}}^{1}(t_0)\right), \tag{6.31}$$

$$z_{-1} = \tfrac{1}{2}\left(z_{\mathrm{E}}^{0}(t_{-1}) + z_{\mathrm{E}}^{1}(t_{-1})\right), \tag{6.32}$$

$$r_0 = \tfrac{1}{4}\left(R^{0}(t_0) + R^{1}(t_0)\right), \tag{6.33}$$

the initial state and the corresponding covariance matrix are evaluated as [28, p.247]:

$$\hat{\boldsymbol{\zeta}}(t_0) = [z_0,\, (z_0 - z_{-1})/\Delta T]^{\mathrm{T}} \in \mathbb{R}^2, \tag{6.34}$$

$$\hat{\mathbf{P}}(t_0) = \begin{bmatrix} r_0 & r_0/\Delta T \\ r_0/\Delta T & 2r_0/(\Delta T)^2 \end{bmatrix} \in \mathbb{R}^{2\times 2}, \tag{6.35}$$

where $\Delta T = T(t_0 - t_{-1})$, and T is the interval between two measurements ($T = 1\,\mathrm{s}$ in the proposed outdoor vehicular and indoor setups). The measurement vector of the time instants following the initialization phase is filled as described in the following section.

6.6.4 DP TOA measurement selection

The measurements passed to the KF are selected from the results of the ESPRIT based multipath TOA estimation of Section 6.6.1. Indeed, for each cell i and measurement time t, ESPRIT produces one set of TOA estimates per antenna port, i.e. $\Upsilon^{i,0}(t)$ and $\Upsilon^{i,1}(t)$. Each set of multipath TOA estimates contains $\hat{L}^{i,p}(t)$ TOA measurements, $p \in \{0, 1\}$. Hence, a selection mechanism which chooses the DP TOA among the $\hat{L}^{i,p}(t)$ time measurements in each set $\Upsilon^{i,p}(t)$ has to be implemented. This choice permits the selection of the entries $z_{\mathrm{E}}^{i,p}(t)$, $p \in \{0, 1\}$, of the measurement vector $\boldsymbol{z}_{\mathrm{E}}^{i}(t) = [z_{\mathrm{E}}^{i,0}(t), z_{\mathrm{E}}^{i,1}(t)]^{\mathrm{T}}$ that feeds the KF, as Figure 6.12 depicts. Unfortunately, the selection mechanism cannot be a simple choice of the earliest TOA because of the possible estimated TOA outliers mentioned in Section 6.6.1.

During the initialization of the KF (i.e., for $t \leq t_0$), the value of $z_{\mathrm{E}}^{i,p}(t)$, $p \in \{0, 1\}$, is selected taking the smallest TOA in the set $\Upsilon^{i,p}(t)$, i.e., $z_{\mathrm{E}}^{i,p}(t) = \Delta t_{\mathrm{s}}^{i} + \hat{\tau}_0^{i,p}(t)$, $t \leq t_0$, as described in (6.30). After initialization (i.e., for $t > t_0$), $z_{\mathrm{E}}^{p}(t)$ is selected from

$\Upsilon^{i,p}(t)$ according to:

$$z_{\mathrm{E}}^{i,p}(t) = \Delta t_{\mathrm{s}}^{i} + \begin{cases} \min\{\Theta^{i,p}(t)\} & \mathrm{n}[\Theta^{i,p}(t)] > 0 \\ \hat{\tau}_0^{i,p}(t) & \mathrm{n}[\Theta^{i,p}(t)] = 0, \hat{L}^{i,p}(t) > 0 \\ z_{\mathrm{E}}^{p}(t-1) & \hat{L}^{i,p}(t) = 0 \\ [1\ 0]\cdot\hat{\boldsymbol{\zeta}}^{-}(t) & \text{sparse missing measure} \end{cases}. \tag{6.36}$$

In (6.36), $\hat{\boldsymbol{\zeta}}^{-}(t)$ is the predicted state of the KF and $\Theta^{i,p}(t)$ is the subset of the ESPRIT estimates containing only the time values that, compared to the previous KF estimation of the DP TOA $\hat{\zeta}_0(t-1)$, do not imply a receiver movement with a speed higher than $v_{\max}^{(1)}$, i.e.:

$$\Theta^{i,p}(t) = \left\{\tau \in \Upsilon^{i,p}(t) : \frac{c}{T}|\tau - \hat{\zeta}_0(t-1)| < v_{\max}^{(1)}\right\} \subseteq \Upsilon^{i,p}(t), \tag{6.37}$$

where $v_{\max}^{(1)}$ is a design parameter representing the maximum allowed receiver speed. The set of (6.37) may be non-empty only if $\hat{\boldsymbol{\zeta}}(t-1)$ and hence $\hat{\zeta}_0(t-1)$ exist, otherwise is left empty, i.e., $\Theta^{i,p}(t) = \varnothing$. Again, as one can note from (6.36), the time offset $\Delta t_{\mathrm{s}}^{i}$ introduced in respect to $t^{(\mathrm{U})}$ by the coarse symbol level synchronization is added to the actual ESPRIT estimates.

The measurement selection strategy of (6.36) is needed for dealing with the following three problems. Firstly, the ESPRIT multipath TOA estimation may produce outliers with TOA much earlier than the real DP TOA, and these are discarded according to a maximum allowed receiver speed $v_{\max}^{(1)}$, by comparing the estimated TOA in $\Upsilon^{i,p}(t)$ with the previous DP TOA estimation $\hat{\zeta}_0(t-1)$. This happens especially when the MDL criterion overestimates the number of receiver multipath components. Secondly, it may happen that, in a particular measurement, despite a particular cell ID being detected, the MDL criterion fails to find multipath components in the considered signal, producing $\hat{L}^{i,p}(t) = 0$. In this case, the value of the previous measurement is used. Thirdly, as already explained in Section 6.6.3, the CRS from a particular cell may not be detected continuously through the measurement period. It may in practice happen that at a certain t the receiver suffers of a deep fade or shadowing, resulting in a sparse missing measure.

For managing the discontinuity of the measurements, a states machine has been defined for each cell, which is represented in Figure 6.14. In this state machine, the state transitions depend on the time Δt_z elapsed from the last measurement available for the particular cell. The initial state $\mathbf{q}_0$ corresponds to a first measure available for a certain cell. As explained in Section 6.6.3, if a second measurement is available before D_{init} measurement times, the initial state is evaluated, and the KF enters the state $\mathbf{q}_1$. Afterwards, if there is a third measurement available in $\Delta t_z \leq D_{\mathrm{init}}$, the state $\mathbf{q}_2$ is entered and the first run of the KF is performed using the initial state $\hat{\boldsymbol{\zeta}}(t_0)$, previously evaluated in the state $\mathbf{q}_1$. Then, the KF stays in the state $\mathbf{q}_2$ if the measurements are discontinuous, with Δt_z being less than D_{init}, otherwise reinitialization occurs. Conversely, if the measurements are continuous,

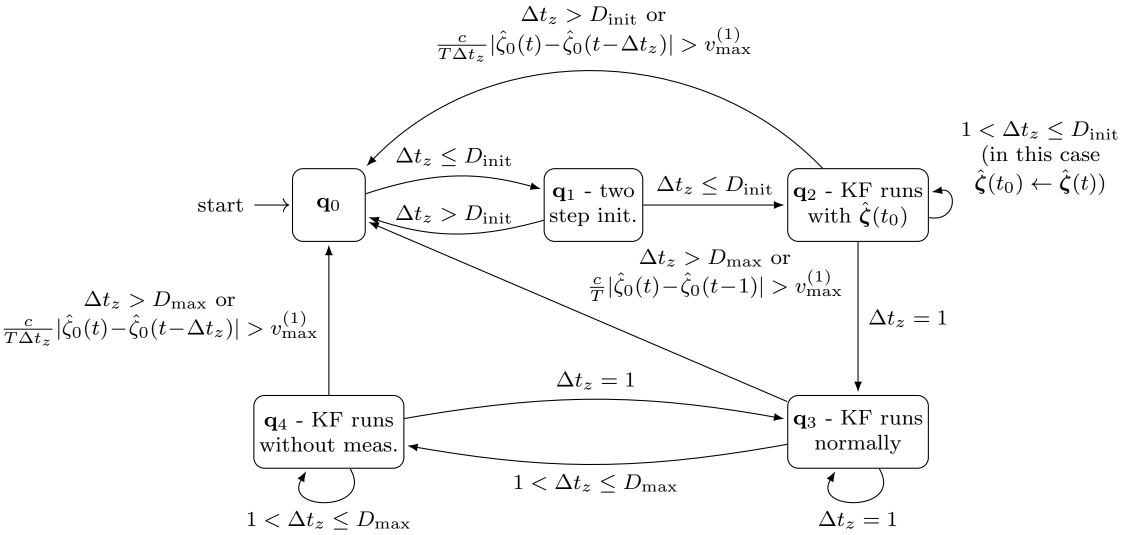

Figure 6.14 – States diagram showing how the discontinuous measurements are managed during the run of the Kalman filter. Every state transition happens when a TOA measurement is available, and the destination state depends on the discrete time interval Δt_z elapsed since the last measurement, and on the fulfillment of the speed constraint $\frac{c}{T\Delta t_z}|\hat{\zeta}_0(t) - \hat{\zeta}_0(t-\Delta t_z)| \leq v_{\max}^{(1)}$.

i.e., if $\Delta t_z = 1$, the KF goes in the state $\mathbf{q}_3$ and runs normally according to the equations of Section 6.6.3. In this state, if the CRS from the particular cell is not received for more than $D_{\max}$ consecutive measurements (e.g., when the BS is too far for being detected), the tracking is stopped and the KF reinitialized to state $\mathbf{q}_0$. On the other hand, if the step between two discontinuous measurements is less than $D_{\max}$ measurement instants, the KF enters the state $\mathbf{q}_4$. Here, the filter runs in the usual way, and substitutes the missing measurements with the measurement prediction $[1\ 0] \cdot \hat{\boldsymbol{\zeta}}^{-}(t)$, until the actual real measurement index is reached. There, the KF runs with the real estimates, and then returns to $\mathbf{q}_3$ in case of continuous measurements, or stays in $\mathbf{q}_4$ in case of further discontinuities.

At each state transition from $\mathbf{q}_i$, $i \geq 2$, the new estimated state $\hat{\boldsymbol{\zeta}}(t)$ is compared to the previous state estimate $\hat{\boldsymbol{\zeta}}(t - \Delta t_z)$ ($\Delta t_z = 1$ in the case of $\mathbf{q}_3$). If the new state imply a receiver movement with a speed higher than $v_{\max}^{(1)}$, i.e., if $\frac{c}{T\Delta t_z}|\hat{\zeta}_0(t) - \hat{\zeta}_0(t-\Delta t_z)| > v_{\max}^{(1)}$, the KF is reinitialized to state $\mathbf{q}_0$. This is an heuristic check for avoiding the KF to start a wrong track. This may happen when the measurement selection process fail in passing to the KF the correct path, and the received multipath times of arrival are mismatched.

An example of the measurement selection is depicted in Figure 6.15, where the selected values $z_{\text{E}}^{p}(t)$ are represented as pseudoranges after being multiplied by c, and showed together with the pseudorange $c \cdot \hat{\zeta}_0(t)$ tracked by EKAT. The represented data is the same of Figure 6.13. The measurement intervals in which the KF is reinitialized to state $\mathbf{q}_0$ due to discontinuous measurements are also highlighted.

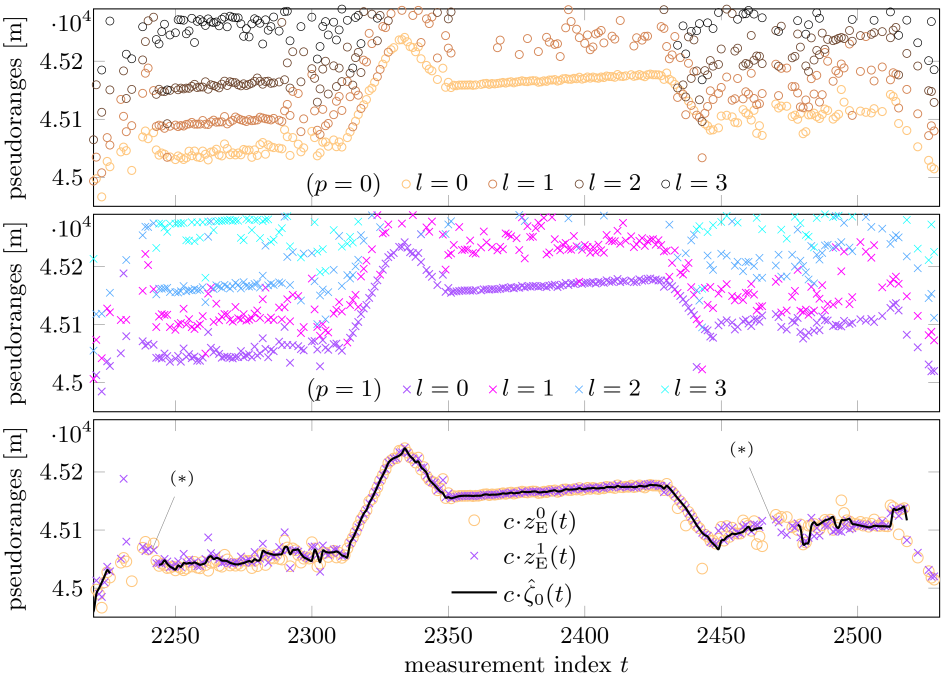

(a) $N_{\mathrm{ID}}^{\mathrm{cell}} = 52$, BS 1, operator 2 (outdoor vehicular scenario).

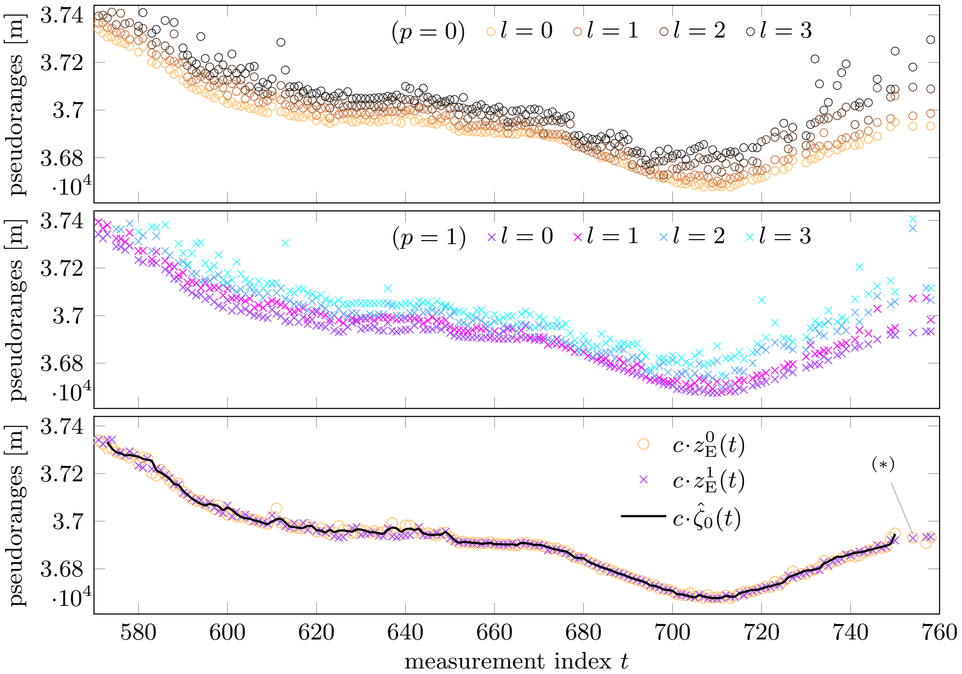

(b) $N_{\mathrm{ID}}^{\mathrm{cell}} = 72$, BS 3, operator 1 (outdoor vehicular scenario).

Figure 6.15 – Example of measurement selection. In each figure, the two upper plots depicts the results of the ESPRIT TOA estimation from antenna ports $p = 0$ and $p = 1$, and the bottom plot shows the selected measurements $z_{\mathrm{E}}^{p}(t)$, $p = \{0, 1\}$, together with the tracked DP TOA. All the plotted values are pseudoranges obtained multiplying by c the estimated TOA. The $(*)$ highlights intervals where the KF is reinitialized to state $\mathbf{q}_0$ due to more than $D_{\max}$ consecutive missing measurements.

6.6.5 Measurement noise variance evaluation

As mentioned in Section 6.6.2, EKAT evaluates the measurement noise covariance matrix $\mathbf{R}(t)$ assuming that the two measurements of the DP TOA $z_{\mathrm{E}}^{0}(t)$ and $z_{\mathrm{E}}^{1}(t)$ are subject to independent Gaussian noise. This results in a diagonal measurement covariance matrix, i.e., $\mathbf{R}(t) = \mathrm{diag}\{[R^0(t), R^1(t)]\}$. The values of the two measurement noise variances $R^p(t), p \in \{0,1\}$, pertaining to each DP TOA estimate, are evaluated with the approach of [80], that permits the computation of the variance of the error $\epsilon_l = \tau_l - \hat{\tau}_l$ relative to the l^{th} TOA estimated with ESPRIT. Indeed, equation (39) of [80] expresses the error variance of ESPRIT when used for estimating the angle of arrival (AOA) of narrowband waveforms on a linear uniform array. This equation exploits the knowledge of the true number of incoming waves, together with the singular vectors and singular values of the exact data matrix, which is built in the same way as (6.16)-(6.17), except that the real data values are used instead of the noisy ones. However, this approach is not feasible for real scenarios, since the real data is unknown.

In contrast, EKAT relies on the use of the noisy data matrix $\mathbf{X}$ and of the estimated value $\hat{L}$ of received multipath components. More particularly, to estimate the measurement noise variance $\mathrm{Var}(\epsilon_l)$ of the l^{th} detected path by using the noisy data matrix and the approach of [80], consider, in addition to the matrices (6.19a)-(6.19d), the following matrix decompositions of $\mathbf{U}$ and $\mathbf{\Sigma}$:

$$\mathbf{U}_o = \mathbf{U}\cdot[\mathbf{0}_{(M-\hat{L})\times\hat{L}}\mathbf{I}_{M-\hat{L}}]^{\mathrm{T}} \in \mathbb{C}^{M\times(M-\hat{L})}, \tag{6.38a}$$

$$\mathbf{U}_{o,1} = [\mathbf{I}_{M-1}\mathbf{0}_{M-1}]\cdot\mathbf{U}_o \in \mathbb{C}^{(M-1)\times(M-\hat{L})}, \tag{6.38b}$$

$$\mathbf{U}_{o,2} = [\mathbf{0}_{M-1}\mathbf{I}_{M-1}]\cdot\mathbf{U}_o \in \mathbb{C}^{(M-1)\times(M-\hat{L})}, \tag{6.38c}$$

$$\mathbf{\Sigma} = \begin{bmatrix} \mathbf{\Sigma}_{\hat{L}} & * \\ * & * \end{bmatrix}, \ \mathbf{\Sigma}_{\hat{L}} \in \mathbb{C}^{\hat{L}\times\hat{L}}. \tag{6.38d}$$

Then, the error variance relative to the l^{th} ESPRIT estimate can be calculated by exploiting the approach of [80] as:

$$\mathrm{Var}\left(\epsilon_l\right) = \frac{C_l^2\hat{\sigma}_w^2}{2}\left\|\boldsymbol{v}_l\mathbf{U}_{s,1}^{\dagger}\left(\mathbf{U}_{o,2} - \psi_l\mathbf{U}_{o,1}\right)\right\|^2\left\|\mathbf{\Sigma}_{\hat{L}}^{-1}\boldsymbol{u}_l\right\|^2, \tag{6.39}$$

where $\hat{\sigma}_w^2$ is an estimate of the variance of the noise affecting the CFR samples $\hat{H}[k]$ and $\boldsymbol{u}_l$, $\boldsymbol{v}_l$, ψ_l are respectively the l^{th} left eigenvector, right eigenvector and eigenvalue of the ESPRIT rotational matrix $\mathbf{\Psi}$ of (6.19d). The parameter C_l in (6.39) is defined in [80] for the case of AOA estimation as a constant that relates the first order perturbation $\Delta\vartheta_l$ on the l^{th} AOA, to the corresponding eigenvalue of the ESPRIT rotational matrix. More particularly:

$$\Delta\vartheta_l = C_l \cdot \mathfrak{Im}\left\{\frac{\Delta\psi_l}{\psi_l}\right\}, \tag{6.40}$$

where: ψ_l is the l^{th} eigenvalue of the ESPRIT rotational matrix $\mathbf{\Psi}$; $\Delta\vartheta_l$ and $\Delta\psi_l$ are the first order perturbations due to noise on the l^{th} AOA and on the corresponding eigenvalue, respectively. Similarly, C_l can also be defined for the ESPRIT TOA estimation case. In this case, the noise-less ESPRIT rotational matrix is given by $\mathrm{diag}\{\psi_1, \ldots, \psi_L\}$, where $\psi_l = e^{-j2\pi\Delta f_{\mathrm{mCRS}}\tau_l}$ [80]. Hence, from the perturbation equation:

$$\psi_l + \Delta\psi_l = e^{-j2\pi\Delta f_{\mathrm{mCRS}}(\tau_l + \Delta\tau_l)}, \tag{6.41}$$

it follows that:

$$\frac{\Delta\psi_l}{\psi_l} = e^{-j2\pi\Delta f_{\mathrm{mCRS}}\Delta\tau_l} - 1. \tag{6.42}$$

By considering the imaginary part of (6.42) one obtains:

$$\mathfrak{Im}\left\{\frac{\Delta\psi_l}{\psi_l}\right\} = -\sin\left(2\pi\Delta f_{\mathrm{mCRS}}\Delta\tau_l\right) \simeq -2\pi\Delta f_{\mathrm{mCRS}}\Delta\tau_l, \tag{6.43}$$

where the approximation $\sin(x) \simeq x$ was used, which holds since $\Delta\tau_l$ is a small value. Then, from (6.43) one obtains:

$$\Delta\tau_l = -\frac{1}{2\pi\Delta f_{\mathrm{mCRS}}}\mathfrak{Im}\left\{\frac{\Delta\psi_l}{\psi_l}\right\}, \tag{6.44}$$

which implies that, in the case of TOA estimation, $C_l = -1/(2\pi\Delta f_{\mathrm{mCRS}})$, $\forall l$. Finally, the noise variance estimation $\hat{\sigma}_w^2$ is obtained exploiting the eigenvalues of $\hat{\mathbf{R}}_x$, which are already available since they have been used in previous stages of the system for feeding the MDL algorithm. More particularly, the approach of [99] is used, which exploits the $M - \hat{L}$ smaller eigenvalues of $\hat{\mathbf{R}}_x$ as:

$$\hat{\sigma}_w^2 = \frac{1}{M - \hat{L}} \sum_{i=\hat{L}+1}^{M} \lambda_i. \tag{6.45}$$

The error variances $\mathrm{Var}(\epsilon_l)$ are evaluated using (6.39) for each multipath TOA estimate $\hat{\tau}_l^{i,p}(t) \in \Upsilon^{i,p}(t)$ obtained at t for the CRS of sector i, antenna port p.

Finally, the value of the measurement error variance $R^p(t)$ is determined in accordance with the choice of (6.36), i.e.:

$$R^p(t) = \begin{cases} \mathrm{Var}\left(\epsilon_{l'}\right) & \mathrm{n}[\Theta^{i,p}(t)] > 0 \\ \gamma_0 \cdot \mathrm{Var}\left(\epsilon_0\right) & \mathrm{n}[\Theta^{i,p}(t)] = 0, \hat{L}^{i,p}(t) > 0 \\ \gamma_1 \cdot R^p(t-1) & \hat{L}^{i,p}(t) = 0 \\ \gamma_2 \cdot R^p(t-1) & \text{sparse missing measure} \end{cases}. \tag{6.46}$$

In (6.46), l' is the index corresponding to the TOA selected by the $\min\{\Theta^{i,p}(t)\}$, and $\gamma_1, \gamma_2, \gamma_0 > 1$ are design parameters used to increase the unreliability due to the use of a previous measurement, of a predicted measurement, and of a measurement implying a receiver speed higher than $v_{\max}^{(1)}$, respectively. As one can see, the variance choices of (6.46) reflect the measurement choices of (6.36).

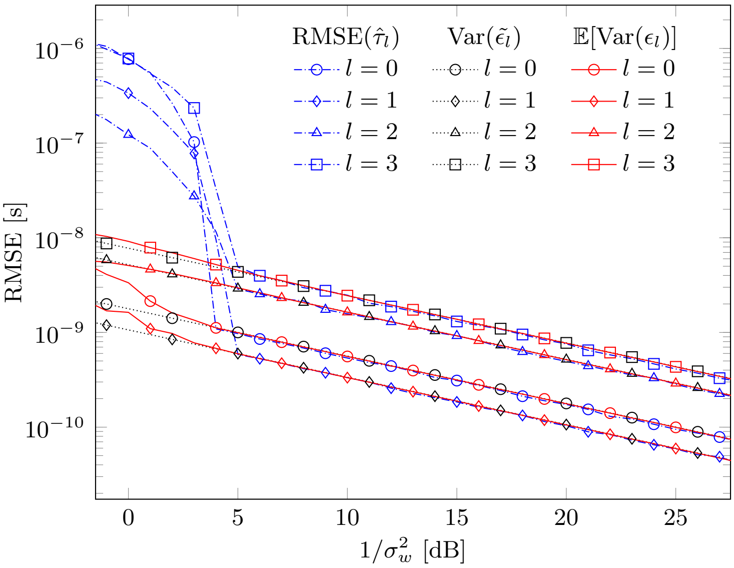

Figure 6.16 – Comparison between the average value of Var(ϵ_l) (red solid lines) and Var($\tilde{\epsilon}_l$) (black dotted lines). The RMSE of an ESPRIT estimation (blue dash-dotted lines) is also shown as a reference.

Monte Carlo simulations were performed to assess the effectiveness of this approach. The simulations showed a substantial agreement between the values of error variance calculated using the exact data matrix, denoted with Var($\tilde{\epsilon}_l$), and the values Var(ϵ_l) obtained using the noisy data $\mathbf{X}$, provided that the noise variance σ_w^2 determines a signal-to-noise ratio corresponding to an above-threshold estimation. Since Var(ϵ_l) is evaluated using a noisy data matrix, its value depends on the particular noise realization, and hence the average value $\mathbb{E}[\text{Var}(\epsilon_l)]$ has been considered in the simulations. As an example, consider Figure 6.16, where the values of error variance are calculated for different values of noise variance σ_w^2 and using the $L = 4$ paths channel defined as:

$$\tau_0 = -1.075\,\mu\text{s}, \qquad h_0 = 0.4 + j0.5\,, \tag{6.47a}$$

$$\tau_1 = 0.006\,\mu\text{s}, \qquad h_1 = 1 + j0.39\,, \tag{6.47b}$$

$$\tau_2 = 0.358\,\mu\text{s}, \qquad h_2 = 0.2 + j0.1\,, \tag{6.47c}$$

$$\tau_3 = 1.369\,\mu\text{s}, \qquad h_3 = 0.15\,. \tag{6.47d}$$

The root mean square estimation error $\text{RMSE}(\hat{\tau}_l) = (\mathbb{E}[(\tau_l - \hat{\tau}_l)^2])^{1/2}$ obtained with an ESPRIT estimation of the multipath TOA is also shown, revealing the correctness of the error variance estimation.

6.7 Ranges evaluation

After the estimation of the DP TOA for each detected cell i at each measurement index t, a pseudorange can be easily evaluated. Indeed, depending on the adopted DP TOA estimator, the pseudorange for the i^{th} detected cell ID at measurement time t was evaluated as:

$$\hat{\rho}_i(t) = c \cdot \begin{cases} \Delta t_{\text{s}}^i + \hat{\tau}_{\text{IM}}^i(t) & \text{IM (Section 6.5)} \\ \Delta t_{\text{s}}^i + \hat{\tau}_{\text{IL}}^i(t) & \text{IL (Section 6.5)} \\ \hat{\zeta}_0^i(t) & \text{EKAT (Section 6.6)} \end{cases} . \tag{6.48}$$

In (6.48), Δt_{s}^i is the delay introduced in respect to $t^{(\text{U})}$ during the preprocessing phase of Section 6.3 for synchronizing to cell i, and:

$$\hat{\tau}_x^i(t) = \min_{p \in \{0,1\}} \left\{ \hat{\tau}_x^{i,p}(t) \right\}, \; x \in \{\text{IM}, \text{IL}\}, \tag{6.49}$$

where $\hat{\tau}_x^{i,p}(t)$ denotes the IM or IL TOA estimate at time t from antenna port p. Note that Δt_{s}^i is not added in the case of the EKAT estimator because it is already considered during the DP tracking, as one can see from (6.36).

The plots of Figure 6.17 depict the results of a range estimation from selected cells using the three considered methods on the CRSs collected during the outdoor vehicular measurements. For a clearer understanding of each estimator's performance, all the plotted values are not pseudoranges but actual ranges, thanks to the application of the clock correction explained later in Section 6.7.2. The ESPRIT multipath ranges are also shown for each transmitted antenna port in the two top plots of each figure, for a clearer understanding of the multipath influence in the performance of each estimator. The GPS measured distance is also shown as a reference. As one can see, the benefits of the EKAT algorithm are evident, since it correctly tracks the DP, determining a consistent range estimate, which is almost equal to the GPS range measure. Conversely, the IM estimator is biased by multipath, especially in the interval $[2250, 2300]$ of Figure 6.17a, where the fourth received path (clearly visible in the two top plots) is mismatched with the DP. This can be seen also in the interval $[600, 640]$ of Figure 6.17b. Finally, it is evident that the IL estimator gives substantial benefits compared to IM, being more robust against multipath detrimental effects, at the cost of discarding suspect NLOS measurements and hence producing fewer estimates.

In Figure 6.18, similar results are shown in the case of the indoor measurements. Again, all the plotted values are actual ranges, which are obtained by applying the correction explained in Section 6.7.2 to the pseudoranges evaluated as in (6.48). The ESPRIT estimates are also shown in the two upper plots of each figure, together with the laser and the GPS ranges. In the indoor case, the ranges evaluated with the laser distance sensor are necessary beyond the GPS ranges, since GPS reception is absent in indoor environments, as the discontinuities of the GPS track in Figures 6.18a-6.18b demonstrate. Indeed, at $t \simeq 750$ of Figure 6.18a, the receiver exits from

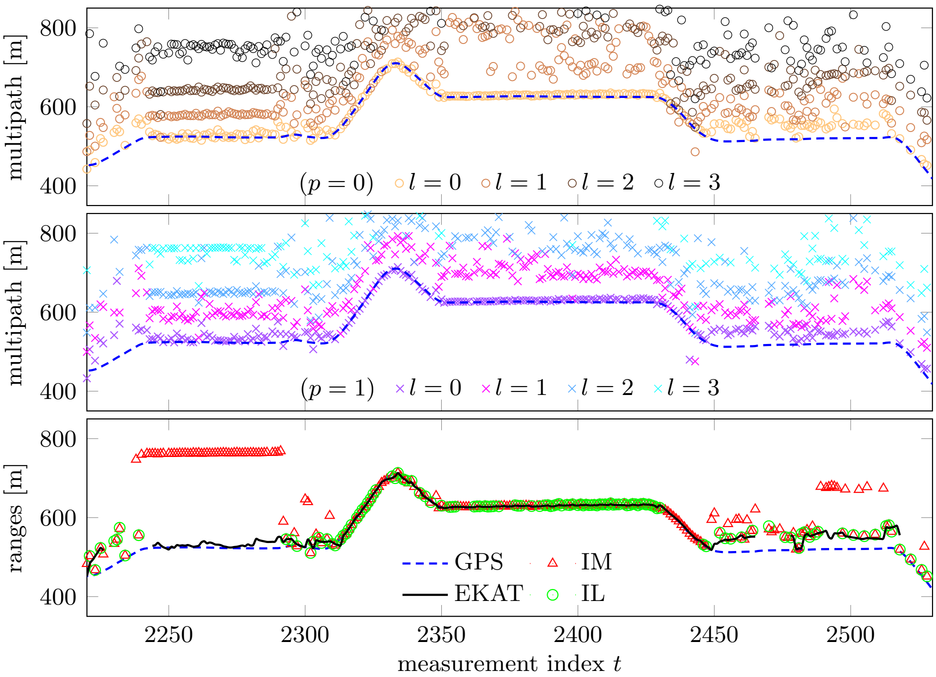

(a) $N_{\mathrm{ID}}^{\mathrm{cell}} = 52$, BS 1, operator 2 (outdoor vehicular scenario).

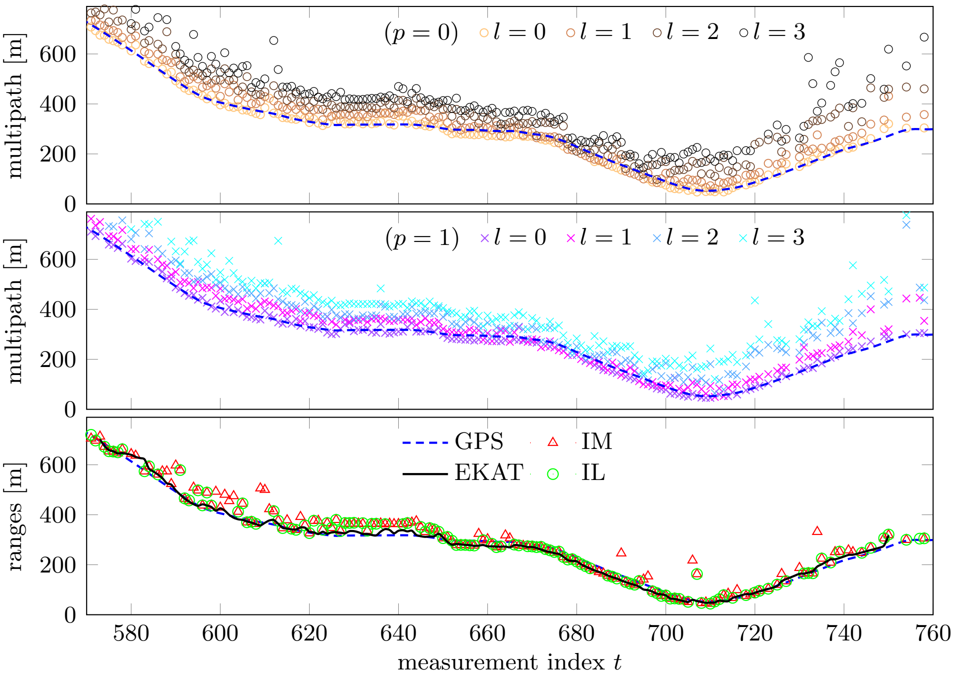

(b) $N_{\mathrm{ID}}^{\mathrm{cell}} = 72$, BS 3, operator 1 (outdoor vehicular scenario).

Figure 6.17 – Examples of range estimations on selected portions of the outdoor vehicular dataset. All the plotted values are actual ranges since already corrected for bias and drift. The upper two plots show the ESPRIT estimates, while the bottom plot depicts the ranging results of the three considered algorithms (i.e., EKAT, IM and IL). The GPS range is also shown as a reference.

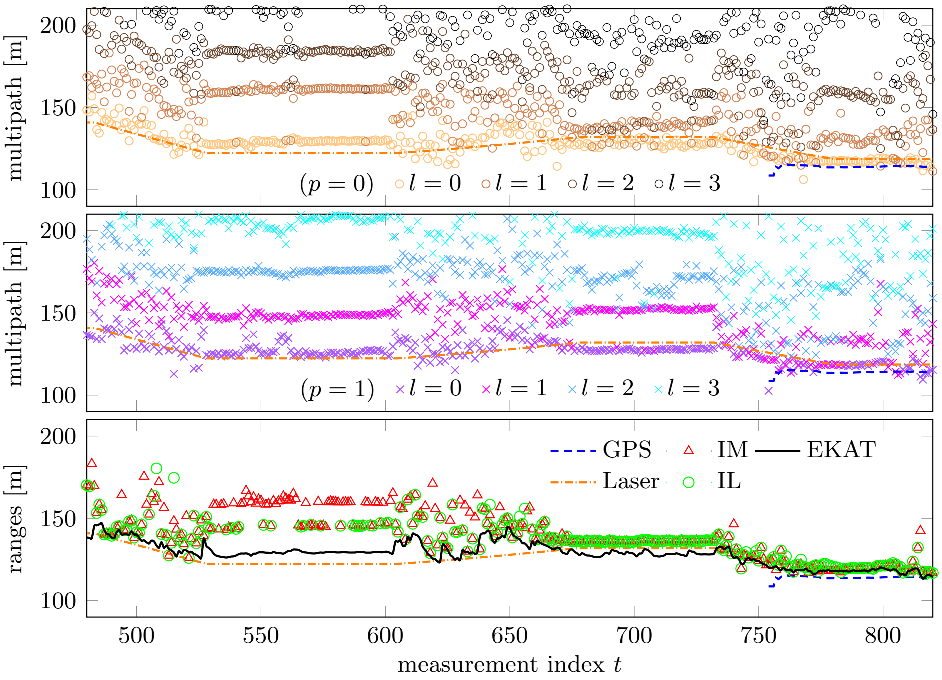

(a) $N_{\mathrm{ID}}^{\mathrm{cell}} = 84$, BS 1, operator 1 (indoor scenario).

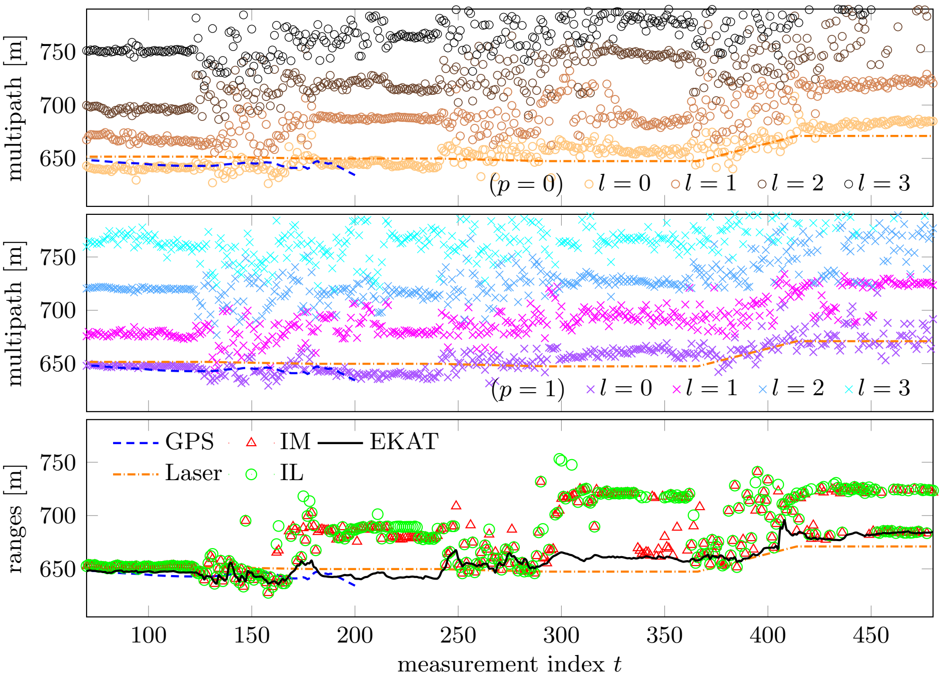

(b) $N_{\mathrm{ID}}^{\mathrm{cell}} = 53$, BS 1, operator 2 (indoor scenario).

Figure 6.18 – Examples of range estimations on selected portions of the indoor dataset. All the plotted values are actual ranges since already corrected for bias and drift. The upper two plots show the ESPRIT estimates, while the bottom plot depicts the ranging results of the three considered algorithms (i.e., EKAT, IM and IL). The GPS and laser ranges are also shown as a reference.

the HSR building (and the GPS track reappears), and at $t \simeq 200$ of Figure 6.18b, the receiver enters the HSR building (and the GPS track disappears). Similarly to the outdoor case, these indoor examples show the robustness of the EKAT algorithm against multipath. This is particularly evident in the interval $[530, 600]$ of Figure 6.18a, where the EKAT tracked DP TOA is close to the laser track, while the IM estimator selects the second path received from antenna port $p = 1$ as the signal TOA. Similarly, in the intervals $[160, 240]$ and $[300, 350]$ of Figure 6.18b, the IM estimator fails in recognizing the DP TOA, while the EKAT track is very close to the laser ground truth.

6.7.1 Combining cells of the same base station

Since the aim of the performed pseudorange measurements is to calculate a position fix based on the BS position knowledge, a single range per BS is needed, instead of multiple ranges corresponding to each cell controlled by every BS. Hence, a method for selecting a single measurement from multiple cells controlled by the same BS is needed. More particularly, let $\bar{\mathcal{K}}_j$ be the set of the cell IDs controlled by BS j, and let $\mathcal{K}_j(t) \subseteq \bar{\mathcal{K}}_j$ be the set of BS j cell IDs that are visible by the receiver at the measurement time t. Given the pseudoranges $\{\hat{\rho}_i(t)\}_{i\in\mathcal{K}_j(t)}$, the selection method has to define a strategy for selecting the cell index $i'(t) \in \mathcal{K}_j(t)$ that selects the per-BS pseudorange $\hat{\rho}_j^{\mathrm{BS}}(t) = \hat{\rho}_{i'(t)}(t)$ for the measurement time t. Without loss of generality, a generic selection method can be defined as the choice of an index that minimizes a specific metric, as:

$$\mathcal{K}_j(t) \ni i'(t) = \begin{cases} \arg\min_{i\in\Lambda_j(t)}\{m_i(t)\} & \mathrm{n}[\Lambda_i(t)] > 0 \\ \arg\min_{i\in\mathcal{K}_j(t)}\{m_i(t)\} & \mathrm{n}[\Lambda_i(t)] = 0 \end{cases}, \tag{6.50}$$

where $m_i(t)$ is the metric to be minimized, which depends on the specific method adopted.

In (6.50), the set $\Lambda_j(t)$ is defined as the collection of cell IDs corresponding to the cells having pseudoranges that, compared to the previous estimation of the per-BS pseudorange $\hat{\rho}_j^{\mathrm{BS}}(t-1)$, do not imply a receiver movement with a speed higher than $v_{\max}^{(2)}$, i.e.:

$$\Lambda_j(t) = \left\{ i \in \mathcal{K}_j(t) : \frac{1}{T} |\hat{\rho}_j^{\mathrm{BS}}(t-1) - \hat{\rho}_i(t)| < v_{\max}^{(2)} \right\} \subseteq \mathcal{K}_j(t), \tag{6.51}$$

where T is the interval between two measurements ($T = 1\,\mathrm{s}$ in the proposed setup). Similarly to (6.37), also the set $\Lambda_j(t)$ may be non-empty only if $\hat{\rho}_j^{\mathrm{BS}}(t-1)$ exists, otherwise is set to $\Lambda_j(t) = \varnothing$. The parameter $v_{\max}^{(2)}$ has to be set according to the expected receiver's maximum speed, which is determined by the environment and type of mobility (e.g., pedestrian, vehicular), and is subject to empirical tuning. Similarly to (6.36), the method of (6.50) is needed for guaranteeing robustness against estimated TOA outliers.

A simple selection method is to choose the cell corresponding to the earliest estimated pseudorange, i.e., $m_i(t) = \hat{\rho}_i(t)$. This method is the more intuitive, and it is used for combining pseudoranges evaluated with the IM and IL algorithms. It has the drawback of not being robust against earlier-than-LOS TOA outliers. A better method, which is used for combining the EKAT pseudoranges, is based on the exploitation of the estimated variance of the tracked DP TOA. At every measurement time, for each BS, the cell corresponding to the measured range with the smallest estimated variance at that particular time is selected. In other words, the metric to be minimized is the estimated TOA variance, i.e., $m_i(t) = \hat{P}^i_{0,0}(t)$. This method may be more robust against TOA outliers, since usually they have a high estimated variance.

An example of the combination of multiple cell estimates pertaining to the same BS is shown in Figure 6.19 for some BSs received in the outdoor vehicular dataset, and in Figure 6.20 for some BSs received in the indoor dataset. Again, for a clearer understanding of the combining performance, all the plotted values are actual ranges, corrected for transmitter time offset as explained in Section 6.7.2. All the figures represent the EKAT estimates obtained from each cell and combined according the variance method described above. In other words, the EKAT estimates pertaining to each BS's cells, shown in the upper plot, are selected on the basis of their variance $\hat{P}^i_{0,0}(t)$, which is shown in the form of distance standard deviation $c \cdot (\hat{P}^i_{0,0}(t))^{1/2}$ in the bottom plot.

Figure 6.19a represents the result of the cell combining corresponding to BS 1 operator 2, which controls the cell IDs $\{51, 52, 53\}$. This is a typical case of dominant cell ID received through all the measurement interval, that is $N^{\text{cell}}_{\text{ID}} = 53$, and the other sectors received occasionally, e.g., thanks to back-lobes and/or side-lobes of the transmitting antenna. As one can see, the earlier-than-LOS TOA outliers are discarded, e.g., at $t \simeq 2610$ and $t \simeq 2635$.

Figure 6.19b represents the result of the multi-cell combining corresponding to BS 2 operator 1, which controls the cell IDs $\{183, 184, 185\}$. In this case, the receiver is probably moving from a zone covered by cell $N^{\text{cell}}_{\text{ID}} = 184$ (where cell $N^{\text{cell}}_{\text{ID}} = 185$ is still visible), to a zone dominated by cell $N^{\text{cell}}_{\text{ID}} = 183$. Considering multiple sectors permits here to select the best cell ID to use for ranging during this sort of handover, which occurs around measurement index $t \simeq 2160$. Moreover, the tracked range from $N^{\text{cell}}_{\text{ID}} = 184$ at $t \simeq 2230$ is correctly ignored regardless of its slightly lower variance, thanks to the outliers discarding strategy of (6.51).

Finally, Figure 6.19c represents the result of the multi-cell combining corresponding to BS 3 operator 1, which controls the cell IDs $\{183, 184, 185\}$. Here, the TOA outliers at $t \simeq 730$ and $t \simeq 750$ are successfully discarded.

The benefits of the cell combining method are evident also in indoor propagation scenarios. Consider as an example Figure 6.20a, where the results pertaining to BS 1 operator 1 in a representative time interval are depicted. As one can see, $N^{\text{cell}}_{\text{ID}} = 84$ is received with the highest SNR and hence it is the cell that produces the more reliable estimates, which are correctly selected by the combining algorithm. This is in accordance with the cell orientation depicted in Figure 6.5. Note also the

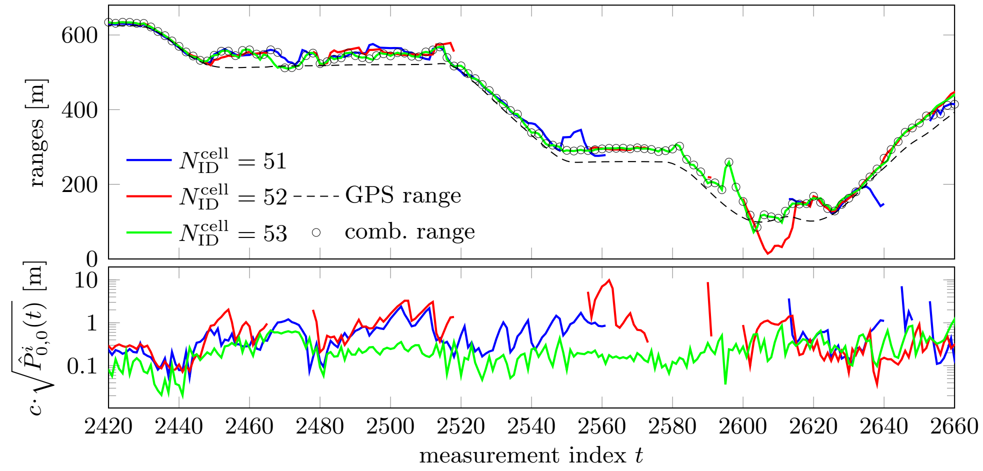

(a) BS 1, operator 2 (outdoor vehicular scenario).

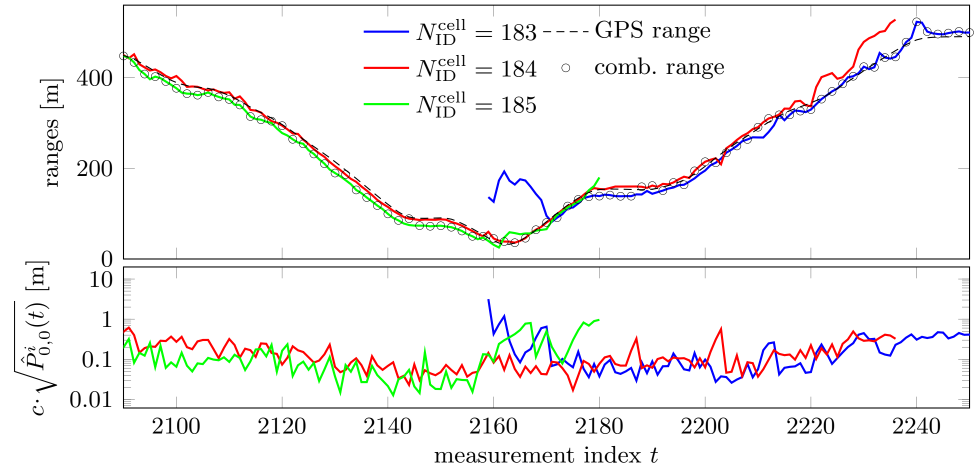

(b) BS 2, operator 1 (outdoor vehicular scenario).

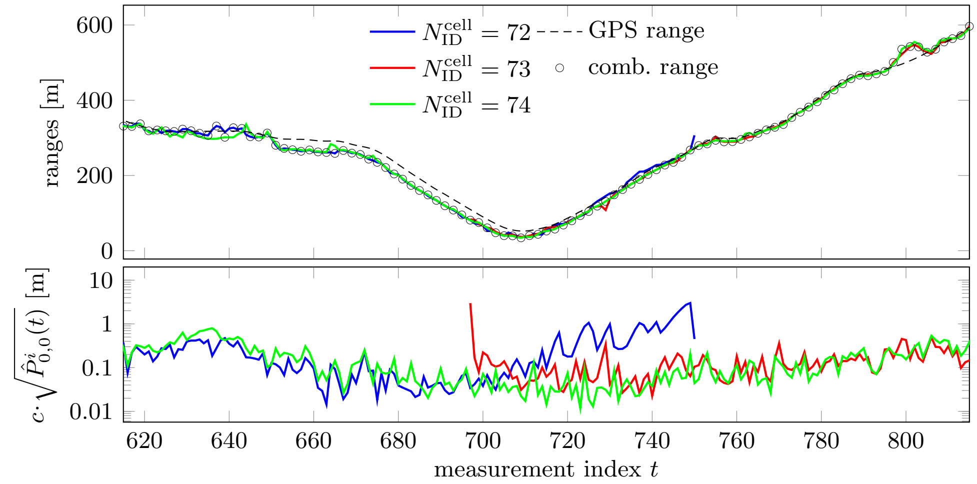

(c) BS 3, operator 1 (outdoor vehicular scenario).

Figure 6.19 – Examples of multiple cell combining of the EKAT pseudoranges in selected time intervals from the outdoor vehicular dataset. All the plotted values are actual ranges since already corrected for bias and drift.

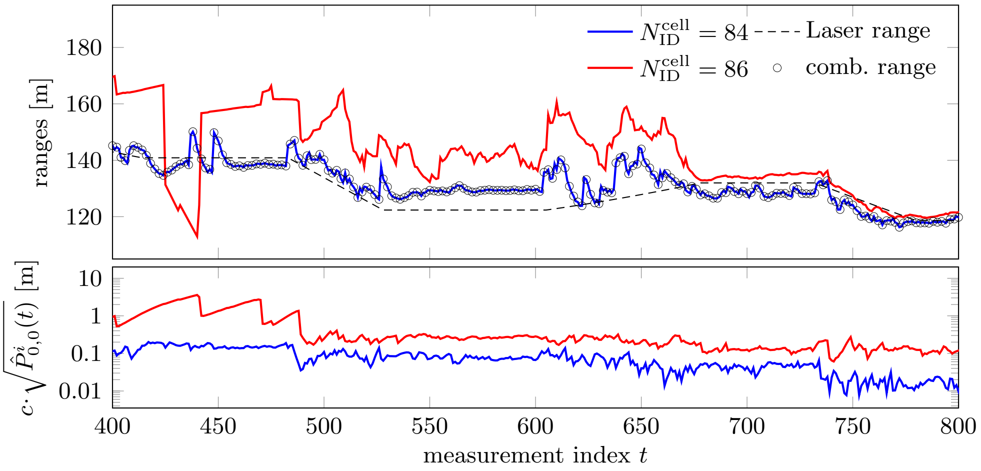

(a) BS 1, operator 1 (indoor scenario).

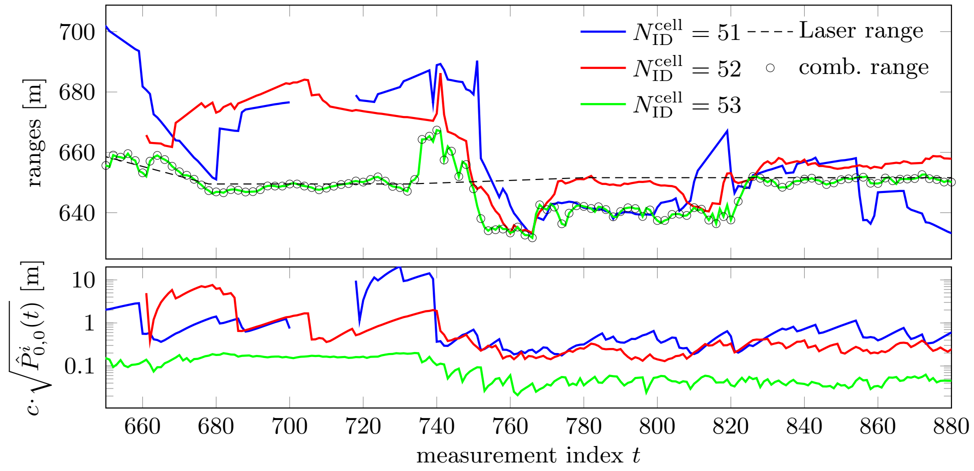

(b) BS 1, operator 2 (indoor scenario).

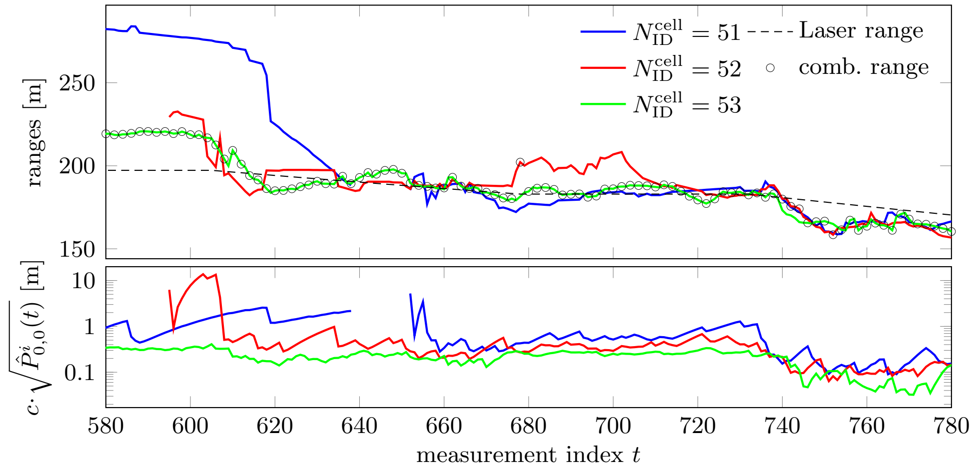

(c) BS 1, operator 3 (indoor scenario).

Figure 6.20 – Examples of multiple cell combining of the EKAT pseudoranges in selected time intervals from the indoor dataset. All the plotted values are actual ranges since already corrected for bias and drift.

outlier from cell $N_{\mathrm{ID}}^{\mathrm{cell}} = 86$ that is discarded at $t \simeq 430$. Similarly, Figure 6.20b and Figure 6.20c show the results pertaining to BS 1 operator 2 and BS 1 operator 3, respectively. As one can see from Figure 6.20b, cell $N_{\mathrm{ID}}^{\mathrm{cell}} = 53$ is likely received with the highest SNR, and hence it produces the estimates with the lowest variance. This causes a successful outlier rejection from cell $N_{\mathrm{ID}}^{\mathrm{cell}} = 51$ at $t \simeq 860$.

6.7.2 Correction for base station bias and drift

In this section, the relation between the measured pseudoranges and actual distances is discussed, for applying the general concepts of Section 1.2.2 to the specific case of the used LTE measurements. Suppose that the propagation channel is observed at the receiver, thanks to a LTE CRS transmission from BS j, at the UTC epoch $t^{(\mathrm{U})}$. The corresponding estimated pseudorange is $\hat{\rho}_j^{\mathrm{BS}}(t)$, which is evaluated in respect to $t^{(\mathrm{U})}$, and hence corresponds to the UTC estimated DP TOA:

$$\mathrm{TOA}_j(t) = t^{(\mathrm{U})} + \hat{\rho}_j^{\mathrm{BS}}(t)/c. \tag{6.52}$$

Consider then the unknown UTC epoch at which the CRS exploited for the TOA estimation was transmitted from the BS j, referred to as time of transmit (TOT), that can be expressed as:

$$\mathrm{TOT}_j(t) = t^{(\mathrm{U})} + \varrho_j(t)/c + k\cdot\Delta T_{\mathrm{CRS}}, \tag{6.53}$$

where the parameter $\varrho_j(t)/c$ is the unknown offset of the BS clock in respect to UTC time $t^{(\mathrm{U})}$, and $k \cdot \Delta T_{\mathrm{CSR}} = k \cdot 10\,\mathrm{ms}$, $k \in \mathbb{Z}$, is the ambiguity due to the CRS transmission periodicity. This ambiguity can be easily solved since the introduced offset is very large, i.e., $c\cdot\Delta T_{\mathrm{CRS}} = 3\cdot 10^6$ m, and hence the value $k = 0$ is set. Finally, the actual distance estimate between the receiver and the transmitter, referred to as range, is given by:

$$\hat{d}_j(t) = c\cdot(\mathrm{TOA}_j(t) - \mathrm{TOT}_j(t)) = \hat{\rho}_j^{\mathrm{BS}}(t) - \varrho_j(t). \tag{6.54}$$

Hence, the clock offset $\varrho_j(t)/c$ of the BS j must be known to the receiver in order to calculate the actual range estimate $\hat{d}_j(t)$.

6.7.3 Base station bias and drift estimation

The proposed approach assumes that each BS makes available parameters such as clock drift and bias in respect to UTC, enabling the receiver to evaluate the clock offset $\varrho_j(t)/c$ with a reasonable accuracy for every t. Unfortunately, in our real field test, $\varrho_j(t)$ is unknown, so it is estimated by exploiting the GPS position fixes available for the receiver. Indeed, the knowledge of both the BS and the receiver position permits a straightforward calculation of the distance $d_j(t)$, which can be used to estimate $\varrho_j(t)$.

The instantaneous BS clock offset (expressed as a distance) $\varrho_j(t)$ is an unknown function of time t, and depends on several parameters, including the deviation of the

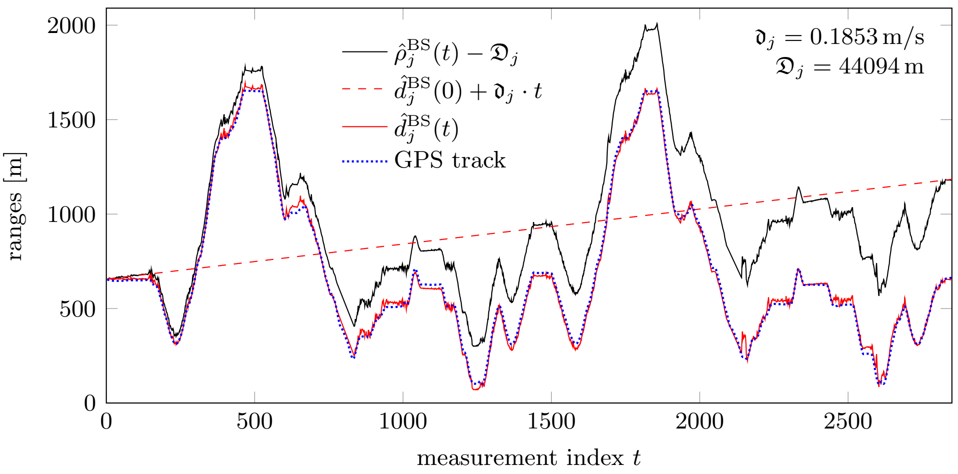

(a) BS 1, operator 2, outdoor vehicular dataset.

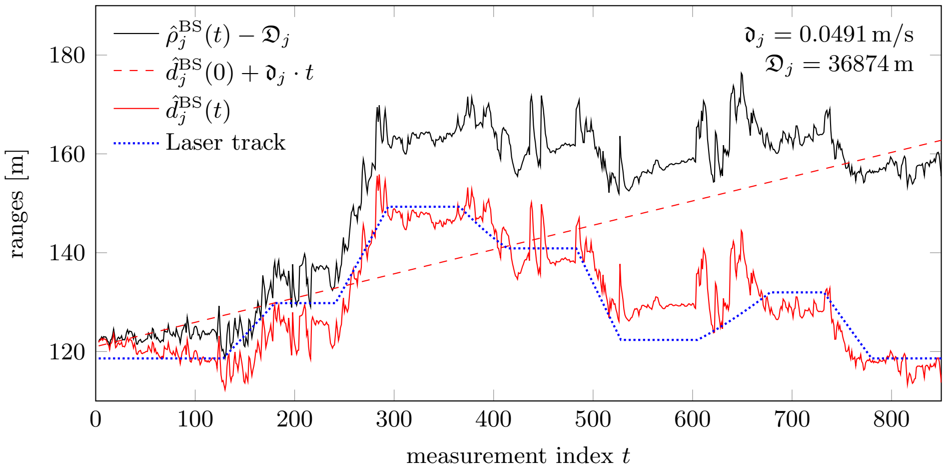

(b) BS 1, operator 1, indoor dataset.

Figure 6.21 – Examples of pseudoranges correction for BS's clock bias and drift.

BS clock to the ideal frequency, and environmental parameters such as temperature, power voltage, and pressure [100]. The BS clock offset is estimated by assuming a linear model for $\varrho_j(t)$, namely $\varrho_j(t) = \mathfrak{D}_j + t \cdot \mathfrak{d}_j$, where $\mathfrak{D}_j$ represents the clock bias (measured in meters) and $\mathfrak{d}_j$ represents the clock drift (measured in meters per second), which is assumed to be constant.

Let $\bar{\mathcal{T}}_j$ be the set of all measurement times in which both a receiver GPS fix (and hence the distance $d_j(t)$) and an LTE pseudorange $\hat{\rho}_j^{\text{BS}}(t)$ from BS j were available during the real field test. In the case of the outdoor vehicular test, at almost every instant in which a certain BS was received, also a GPS position fix was available. Conversely, in the case of the indoor test, position fixes were available only in the part of the test route outside the HSR building 2, i.e., at the beginning and at the end of the test.

Op.	BS	$\mathfrak{D}_j$ [m]	$\mathfrak{d}_j$ [m/s]
1	1	56871	0.0051
	2	2968	-0.0111
	3	36649	-0.0117
	5	8033	-0.0104
	6	67855	-0.0186
2	1	44094	0.1853
	2	54029	-0.0612
	3	-1242	0.0346

(a) Outdoor scenario

Op.	BS	$\mathfrak{D}_j$ [m]	$\mathfrak{d}_j$ [m/s]
1	1	36874	0.0491
	2	72273	0.0216
2	1	45533	-0.0564
	3	22715	-2.7759
3	1	52456	-0.0006

(b) Indoor scenario

Table 6.3 – Complete results of bias and drift estimation.

A simple least squares approach permits to estimate the bias $\mathfrak{D}_j$ and the drift $\mathfrak{d}_j$ for any sub-set $\mathcal{T}_j \subseteq \bar{\mathcal{T}}_j$ as:

$$(\hat{\mathfrak{D}}_j, \hat{\mathfrak{d}}_j) = \arg\min_{\mathfrak{D},\mathfrak{d}} \left\{ \sum_{t\in\mathcal{T}_j} \left| d_j(t) - \hat{\rho}_j^{\mathrm{BS}}(t) + \mathfrak{D} + t\cdot\mathfrak{d} \right|^2 \right\}. \tag{6.55}$$

The accuracy of the estimation of (6.55) depends on both the accuracy of the LTE pseudoranges $\hat{\rho}_j^{\mathrm{BS}}(t)$ and on the number and distribution of the considered measurement instants $\mathcal{T}_j$. Indeed, a low number of observations sufficiently spaced in time may be more effective for the estimation of the drift than a high number of subsequent measurements concentrated in a small time interval. For both the outdoor vehicular and indoor datasets, the whole set $\bar{\mathcal{T}}_j$ and the EKAT pseudoranges were used in order to obtain the most precise bias and drift estimates.

Examples of corrected EKAT pseudoranges are depicted in Figure 6.21. In each plot, the pseudoranges corrected for bias only $\hat{\rho}_j^{\mathrm{BS}}(t) - \mathfrak{D}_j$ and for both bias and drift $\hat{d}_j^{\mathrm{BS}}(t)$ are shown together with the ground truth. The drift term $\hat{d}_j^{\mathrm{BS}}(0) + \mathfrak{d}_j \cdot t$ is also shown, where the term $\hat{d}_j^{\mathrm{BS}}(0)$ is added just for a clearer understanding of the drift effects on the range estimates. Figure 6.21a depicts the complete estimated range pertaining to BS 1 operator 2 of the outdoor vehicular dataset, where the GPS track is used as the ground truth. Figure 6.21b depicts the complete estimated range pertaining to BS 1 operator 1 of the indoor dataset. Here, the laser track is used as the ground truth.

Finally, all the complete results obtained for the bias and drift estimation in the cases of the outdoor vehicular and indoor measurement scenarios are summarized in Table 6.3a and in Table 6.3b, respectively. As one can note from the table pertaining to the outdoor scenario, BSs pertaining to operator 2 generally exhibit heavier drift effects. This is in accordance with the clock properties measurements reported in [101].

6.8 Estimating receiver position

The ranges calculated with the procedures described in the previous sections are exploited for estimating and tracking the receiver position in both the outdoor vehicular and the indoor measurement scenarios. The ICOM team of the HSR implemented the positioning engine needed for such purpose, which was then fed with the ranges produced by the proposed TOA estimation algorithms, and particularly with the EKAT algorithm. In this section, a brief review of the adopted positioning techniques is presented. An interested reader may find additional details in [82].

An extended Kalman filter (EKF) is used to estimate the receiver position. Analyzing the geographical properties of the base stations used, shows that their heights differ only slightly. In conjunction with the base station spread, which is large compared to the height differences, the situation is close to all base stations lying in one plane. Hence, the rover position is solved in two dimensions only. The problem space is constrained to two dimensions by using local east-north-up coordinates (ENU), with the up component set to zero. A second order model is used to describe the rover position. Hence, the state vector is $\boldsymbol{\xi}(t) = [\boldsymbol{p}(t)^{\mathrm{T}}, \dot{\boldsymbol{p}}(t)^{\mathrm{T}}, \ddot{\boldsymbol{p}}(t)^{\mathrm{T}}]^{\mathrm{T}} \in \mathbb{R}^6$, containing the 2D rover position $\boldsymbol{p}(t) = [x(t), y(t)]^{\mathrm{T}} \in \mathbb{R}^2$, the 2D rover speed $\dot{\boldsymbol{p}}(t) = [\dot{x}(t), \dot{y}(t)]^{\mathrm{T}} \in \mathbb{R}^2$, and the 2D rover acceleration $\ddot{\boldsymbol{p}}(t) = [\ddot{x}(t), \ddot{y}(t)]^{\mathrm{T}} \in \mathbb{R}^2$. Whenever measurements to at least two base stations are available a measurement update is performed. The constant acceleration second order model leads to the following state transition model:

$$\boldsymbol{\xi}(t) = \begin{bmatrix} 1 & 0 & \Delta t_{\mathrm{p}} & 0 & \frac{1}{2}\Delta t_{\mathrm{p}}^2 & 0 \\ 0 & 1 & 0 & \Delta t_{\mathrm{p}} & 0 & \frac{1}{2}\Delta t_{\mathrm{p}}^2 \\ 0 & 0 & 1 & 0 & \Delta t_{\mathrm{p}} & 0 \\ 0 & 0 & 0 & 1 & 0 & \Delta t_{\mathrm{p}} \\ 0 & 0 & 0 & 0 & 1 & 0 \\ 0 & 0 & 0 & 0 & 0 & 1 \end{bmatrix} \cdot \boldsymbol{\xi}(t-1) + \boldsymbol{q}_{\mathrm{p}}(t-1) \tag{6.56}$$

where Δt_{p} is the elapsed time since the last position estimate at $t-1$, and $\boldsymbol{q}_{\mathrm{p}}(t) \in \mathbb{R}^6$ is the zero mean white Gaussian process noise of the position state equation, having constant covariance matrix $\mathbf{Q}_{\mathrm{p}} = \mathbb{E}\left[\boldsymbol{q}_{\mathrm{p}}(t)\boldsymbol{q}_{\mathrm{p}}^{\mathrm{H}}(t)\right]$. In the case of (6.56), the discrete time index t does not identify subsequent measurements, as in the previous sections, but identify subsequent measurement times characterized by a number of visible BSs $N(t) \geq 2$. The measurement vector is $\boldsymbol{z}_{\mathrm{p}}(t) = [z_{\mathrm{p},1}(t), \ldots, z_{\mathrm{p},N(t)}]^{\mathrm{T}}$, where $N(t)$ is the number of received BSs at time t, and each component $z_{\mathrm{p,n}}(t)$ is the measured range between the receiver and the n^{th} BS, which is given by the non-linear observation model:

$$z_{\mathrm{p},n}(t) = \left\|\boldsymbol{p}_{\mathrm{BS}}^{n} - \boldsymbol{p}(t)\right\|, \quad n = 1, \ldots, N(t), \tag{6.57}$$

with the vector $\boldsymbol{p}_{\mathrm{BS}}^{n} \in \mathbb{R}^2$ representing the known 2D location of the n^{th} received BS. According to [28], the linearization of (6.57) around the predicted position $\hat{\boldsymbol{p}}^{-}(t)$, which is produced by the EKF, leads to the following linear observation model:

$$\mathbf{H}_{\mathrm{p}}(t) = \begin{bmatrix} (\hat{\boldsymbol{p}}^{-}(t) - \boldsymbol{p}_{\mathrm{BS}}^{1})^{\mathrm{T}}/\|\boldsymbol{p}_{\mathrm{BS}}^{1} - \hat{\boldsymbol{p}}^{-}(t)\| & \mathbf{0}_2^{\mathrm{T}} & \mathbf{0}_2^{\mathrm{T}} \\ (\hat{\boldsymbol{p}}^{-}(t) - \boldsymbol{p}_{\mathrm{BS}}^{2})^{\mathrm{T}}/\|\boldsymbol{p}_{\mathrm{BS}}^{2} - \hat{\boldsymbol{p}}^{-}(t)\| & \mathbf{0}_2^{\mathrm{T}} & \mathbf{0}_2^{\mathrm{T}} \\ \vdots & \vdots & \vdots \\ (\hat{\boldsymbol{p}}^{-}(t) - \boldsymbol{p}_{\mathrm{BS}}^{N(t)})^{\mathrm{T}}/\|\boldsymbol{p}_{\mathrm{BS}}^{N(t)} - \hat{\boldsymbol{p}}^{-}(t)\| & \mathbf{0}_2^{\mathrm{T}} & \mathbf{0}_2^{\mathrm{T}} \end{bmatrix} \in \mathbb{R}^{N(t)\times 6}. \tag{6.58}$$

The matrix of (6.58) is evaluated at every iteration of the EKF, which produces at each step an estimate $\hat{\boldsymbol{p}}(t)$ of the receiver position at time t. Again, the measurements are supposed to be corrupted by a zero mean Gaussian noise vector $\boldsymbol{r}_{\mathrm{p}}(t) \in \mathbb{R}^{N(t)}$, having covariance matrix $\mathbf{R}_{\mathrm{p}} = \mathbb{E}\left[\boldsymbol{r}_{\mathrm{p}}(t)\boldsymbol{r}_{\mathrm{p}}^{\mathrm{H}}(t)\right]$. The process noise matrix $\mathbf{Q}_{\mathrm{p}}$ and the measurement uncertainty matrix $\mathbf{R}_{\mathrm{p}}$ were supposed time invariant and were tuned empirically. When using pseudoranges obtained with the EKAT algorithm, a time variant measurement uncertainty matrix $\mathbf{R}_{\mathrm{p}}(t)$ may be adopted, and populated on the diagonal with the estimated pseudorange variances. This should help in reducing the effects on the position estimate of the ranging outliers.

6.9 Results

This section summarizes the ranging and positioning results obtained with the live data captured by using the setup of Section 6.3. Pseudorange estimations were firstly performed from the detected cells with the algorithms of Sections 6.4-6.6, namely IDFT-MAX (IM), IDFT-LOS (IL) and EKAT (E). Then, cell pseudoranges were combined with the method of Section 6.7.1, in order to obtain a single pseudorange for each BS, which was corrected for clock bias and drift, according to the procedure of Section 6.7.2. Finally, these range estimates were used in the positioning filter of Section 6.8 to evaluate a position estimate. Before the presentation of the obtained results, a brief review of the parameters used in the exploited algorithms is offered in Sections 6.9.1-6.9.2. Moreover, some of the preliminary results obtained in the first phases of the work by applying the plain ESPRIT algorithm to the preliminary measurement dataset are shown in Section 6.9.3.

6.9.1 Parameters used

The IM estimator was run as described in Section 6.5, while for the IL algorithm the number of searched CIR peaks was set to $N_{\mathrm{IL}} = 3$. The EKAT algorithm was run with two different sets of parameter depending on the type of mobility in the particular measurement scenario of application. For the outdoor vehicular scenario, the following parameters were used: $D_{\mathrm{init}} = 1$, $D_{\mathrm{max}} = 3$, $q = 5 \cdot 10^{-19}$, $v_{\mathrm{max}}^{(1)} = 70\,\mathrm{m/s}$, $v_{\mathrm{max}}^{(2)} = 30\,\mathrm{m/s}$, $\gamma_0 = \gamma_1 = 100$, $\gamma_2 = 10$. For the indoor scenario, the following parameters were used: $D_{\mathrm{init}} = 8$, $D_{\mathrm{max}} = 10$, $q = 5 \cdot 10^{-21}$, $v_{\mathrm{max}}^{(1)} = 40\,\mathrm{m/s}$, $v_{\mathrm{max}}^{(2)} = 30\,\mathrm{m/s}$, $\gamma_0 = \gamma_1 = 100$, $\gamma_2 = 10$. Moreover, a value of $m = 0.48$ was chosen for setting the dimensions of the data matrix $\mathbf{X}$, with the particular procedure described in Section 6.9.2. For the outdoor vehicular scenario, the positioning EKF used a process covariance matrix given by:

$$\mathbf{Q}_{\mathrm{p}} = \mathrm{diag}\{[q_1 \Delta t_{\mathrm{p}}^2,\ q_1 \Delta t_{\mathrm{p}}^2,\ q_2 \Delta t_{\mathrm{p}}^2,\ q_2 \Delta t_{\mathrm{p}}^2,\ q_3,\ q_3]\} \in \mathbb{C}^{6\times 6}, \tag{6.59}$$

where $q_1 = (6\,\mathrm{m})^2$, $q_2 = (0.5\,\mathrm{m/s})^2$, $q_3 = (0.0092\,\mathrm{m/s^2})^2$, and $\Delta t_{\mathrm{p}} \geq 1$ is used here as a dimensionless scaling factor that has the purpose of increasing the uncertainty, i.e., the more time has passed since the last measurement update the more the measurement variances are increased. Conversely, the process covariance matrix used by the positioning EKF in the indoor scenario is:

$$\mathbf{Q}_{\mathrm{p}} = \mathrm{diag}\{[q_1 \Delta t_{\mathrm{p}}^2,\ q_1 \Delta t_{\mathrm{p}}^2,\ q_2,\ q_2,\ q_3,\ q_3]\} \in \mathbb{C}^{6\times 6}. \tag{6.60}$$

where $q_1 = (0.1\,\mathrm{m})^2$, $q_2 = (0.01\,\mathrm{m/s})^2$, $q_3 = (0.001\,\mathrm{m/s^2})^2$, and, again, $\Delta t_{\mathrm{p}} \geq 1$ is used as a dimensionless scaling factor. In (6.60), the uncertainty q_2 corresponding to the speed is not scaled by Δt_{p} because of the limited speeds involved in the indoor scenario. Finally, the positioning EKF used the following measurement noise covariance matrix:

$$\mathbf{R}_{\mathrm{p}} = \mathrm{diag}\{[r, r, ..., r]\}\ \in \mathbb{C}^{N(t)\times N(t)}, \tag{6.61}$$

where, the values of r differ depending on the adopted ranging algorithm. The value of $r = (40\,\mathrm{m})^2$ was set in the IL/IM case. In the EKAT case, a smaller value of $r = (10\,\mathrm{m})^2$ was used, in order to give more trust to the ranges evaluated by this algorithm.

6.9.2 SRA tuning

Carefully selecting the value of the M parameter is of crucial importance for the super-resolution algorithm to give reliable and accurate results. As pointed out in [15], the value of M determines a trade-off between resolution and stability of the SRA estimation results.

In the ESPRIT-based approach proposed in Section 6.6.1, a single length $2 \cdot N_{\mathrm{tot}}$ CFR estimate $\hat{H}_t^{i,p}[k]$, $k = 0, \ldots, 2 \cdot N_{\mathrm{tot}} - 1$, feeds the SRA. Because overlapped length M snapshots are used to build up the data matrix $\mathbf{X} \in \mathbb{C}^{M\times N}$ of (6.16), its dimensions are related through the equation $N = 2 \cdot N_{\mathrm{tot}} - M + 1$. Hence, increasing M corresponds to decreasing N, which ultimately means that the data matrix is made of less overlapped snapshots. This corresponds to less reliable estimates, since the autocorrelation matrix estimate is calculated using a lower number of snapshots and hence is more sensible to the fluctuations due to noise. On the other hand, increasing M determines an increased resolution of the SRA [36, 43], i.e. the SRA is able to distinguish closer instant of arrivals. Hence, M has to be carefully selected for achieving the best trade-off between resolution and reliability. Usually, M is chosen as some fraction of the length of the initial CFR sampling, i.e., $M = m \cdot 2 \cdot N_{\mathrm{tot}}$. Consequently, selecting a value for M is equivalent to selecting a value for m.

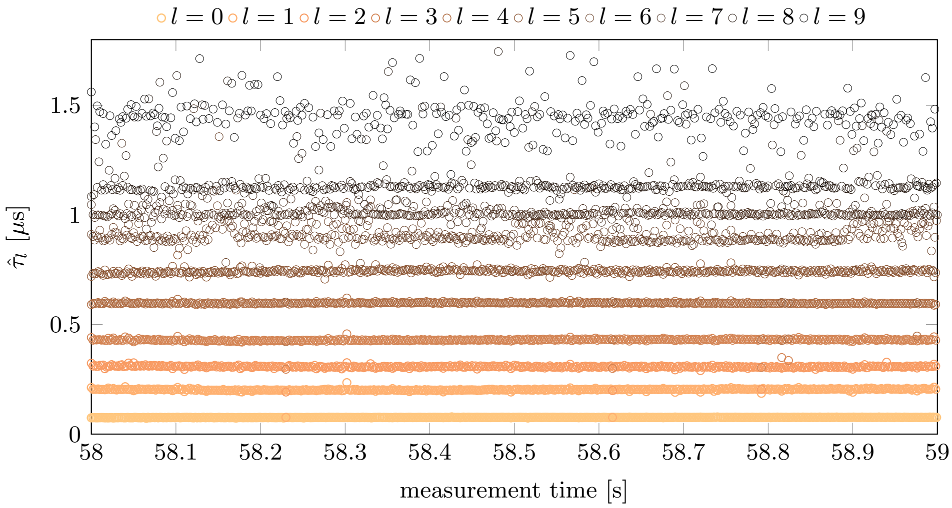

Figure 6.22 – Multipath TOA of the first $L_{\max} = 10$ detected paths in the interval [58 s, 59 s] of the preliminary measurements dataset, antenna port $p = 0$, cell $N_{\text{ID}}^{\text{cell}} = 84$. Here, the ESPRIT TOA estimation has been used with $M = 144$ on the merged CFR estimates. For a clearer visualization, just one estimation every four performed estimations is shown.

For choosing the most appropriate value of m to be used in the presented measurements, the following method has been used (further considerations on the SRA tuning can be found in [15, 102] and references therein). By inspecting the results derived from the application of ESPRIT to the signal coming from antenna port $p = 0$, cell $N_{\text{ID}}^{\text{cell}} = 84$, of the preliminary measurements, an interval of 1 s containing constant multipath was selected. This interval is shown in Figure 6.22, where an ESPRIT TOA estimation is applied using the length $2 \cdot N_{\text{tot}} = 300$ merged CFR estimations and a value of $M = 144$. Several ESPRIT TOA estimations were then run on that interval using different values of M. More particularly, M was set to $M = m \cdot 2 \cdot N_{\text{tot}}$ with $m \in \mathcal{M} = \{0.01, 0.02, \ldots, 0.6\}$. Then, a number of $L_{\max} = 10$ paths was fixed, and, for each value of M and for each estimation, the first $L_{\max}$ estimated paths' TOA were stored, namely:

$$\hat{\tau}_0^{(m)}[n], \hat{\tau}_1^{(m)}[n], \ldots, \hat{\tau}_{L_{\max}-1}^{(m)}[n], \quad m \in \mathcal{M},\ n = 0, \ldots, \tilde{N} - 1, \tag{6.62}$$

where $\tilde{N}$ is the number of estimations performed in the 1 s considered interval. The values of $L_{\max} = 10$ was chosen since in the considered interval at least 10 multipath components were always detected at every estimation. Then, for each value of $m \in \mathcal{M}$, the statistical average and variance of each estimated TOA were computed, namely:

$$\mu_{\tau_l}^{(m)} = \frac{1}{\tilde{N}} \sum_{n=0}^{\tilde{N}-1} \hat{\tau}_l^{(m)}[n], \tag{6.63}$$

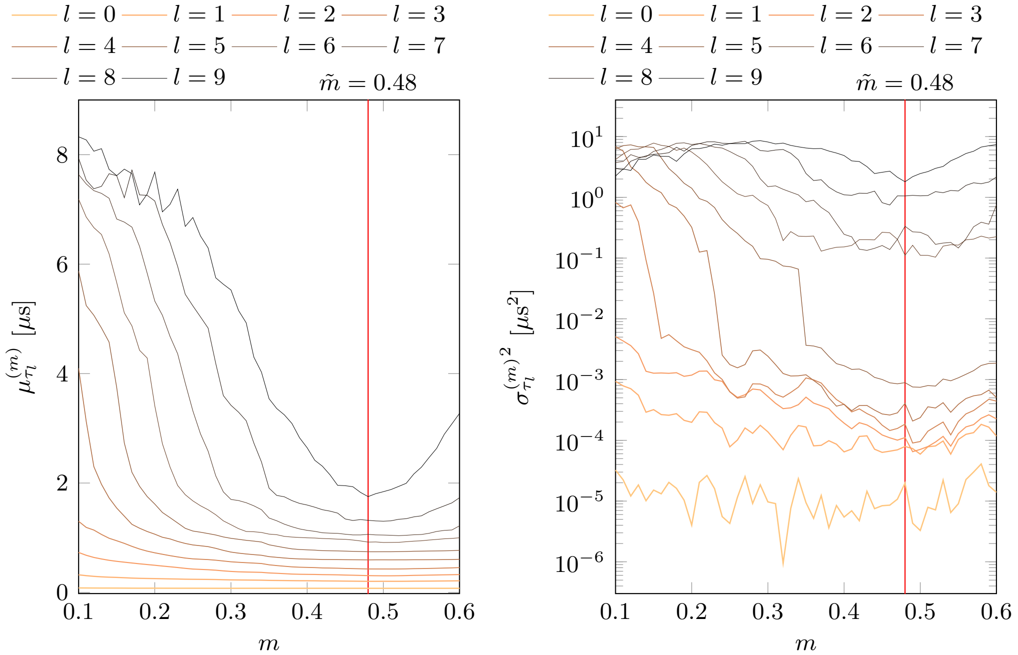

(a) Mean multipath TOA. **(b)** Multipath TOA variance.

Figure 6.23 – Calculation of $\tilde{m}$ using the length $2 \cdot N_{\text{tot}} = 300$ merged CFR estimates obtained with the CRS of a single slot.

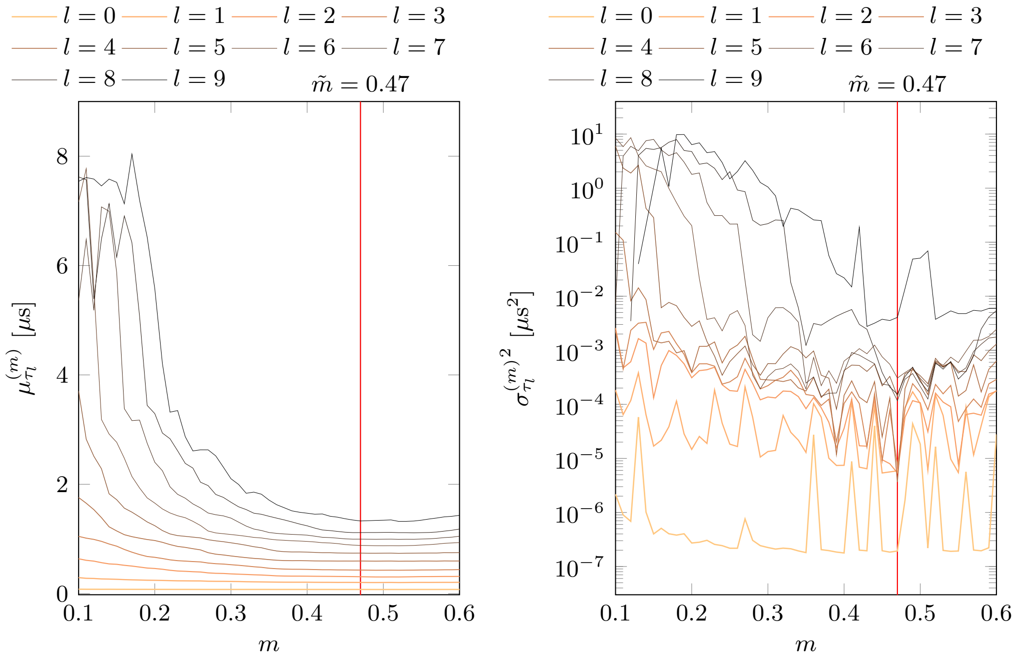

(a) Mean multipath TOA. **(b)** Multipath TOA variance.

Figure 6.24 – Calculation of $\tilde{m}$ using the length $2 \cdot N_{\text{tot}} = 300$ merged CFR obtained by averaging the estimates of $N_s = 10$ subsequent slots' CRSs.

$$\sigma_{\tau_l}^{(m)^2} = \frac{1}{\tilde{N}-1} \sum_{n=0}^{\tilde{N}-1} \left(\hat{\tau}_l^{(m)}[n] - \mu_{\tau_l}^{(m)} \right)^2 . \tag{6.64}$$

Finally, the value of m that minimized the sum of the empirical multipath TOA variances was chosen, i.e.:

$$\tilde{m} = \arg \min_{m \in \mathcal{M}} \left\{ \sum_{l=0}^{L_{\max}-1} \sigma_{\tau_l}^{(m)^2} \right\} . \tag{6.65}$$

This procedure was performed twice. In the first run, which results are represented in Figure 6.23, the ESPRIT TOA estimation was applied to the merged CFR estimates of all the received slots in the analyzed interval. This led to a total of $\tilde{N} = 2000$ estimations, since 1 s of continuous data corresponds to 100 frames, which contain 20 slots each, hence $\tilde{N} = 100 \cdot 20 = 2000$. In the second run, which results are represented in Figure 6.24, the ESPRIT TOA estimation was applied to groups of $N_s = 10$ merged CFR estimates combined with the averaging method of (6.12). In this case, $\tilde{N} = 200$ estimations were performed, since a TOA estimate is computed every $N_s = 10$ slots (1 s corresponds to 100 frames, which contain 20 slots each, hence $\tilde{N} = 100 \cdot 20/10 = 200$). As can be seen from Figures 6.23b-6.24b, the value of $\tilde{m}$ was near 0.5 in both cases. Hence, the value of $m = 0.48$ has been selected to be used in the EKAT algorithm.

6.9.3 Preliminary TOA estimation results

The preliminary measurements from cell IDs $N_{\mathrm{ID}}^{\mathrm{cell}} = 84$ and $N_{\mathrm{ID}}^{\mathrm{cell}} = 86$ of BS 1 operator 1 described in Section 6.3 were used to asses the feasibility of multipath TOA estimation of real LTE signals by means of super-resolution algorithms. The ESPRIT TOA estimation described in Section 6.6.1 was applied to the CFR estimates evaluated exploiting the received CRS and combined in time and frequency as described in Section 6.4. During these preliminary experiments, only the TOA estimation was performed on the real data, with no tracking of the DP nor bias and drift correction.

As explained in Section 6.3, differently from the two main datasets used to evaluate the performance of the EKAT algorithm, the preliminary dataset is made of continuous recorded samples. Hence, after coarse frame and symbol timing, the subsequent received CRSs were used to evaluate the CFR estimates pertaining to each received cell and antenna port, and were then merged as described in Section 6.4.1. Ten subsequent merged channel estimates were then averaged as described in Section 6.4.2, i.e., $N_s = 10$. Finally, each merged and averaged CFR estimate was used to feed the ESPRIT multipath TOA estimation of Section 6.6.1, where m was set to $m = 0.48$. Since during the preliminary measurements operator 1 had an LTE channel bandwidth configuration of 15 Mhz, corresponding to $N_{\mathrm{sc}} = 900$ subcarriers, then each merged CFR estimate contained $2 \cdot N_{\mathrm{tot}} = 300$ samples, which correspond $M = 144$ and $N = 157$ if $m = 0.48$ is used. These settings correspond

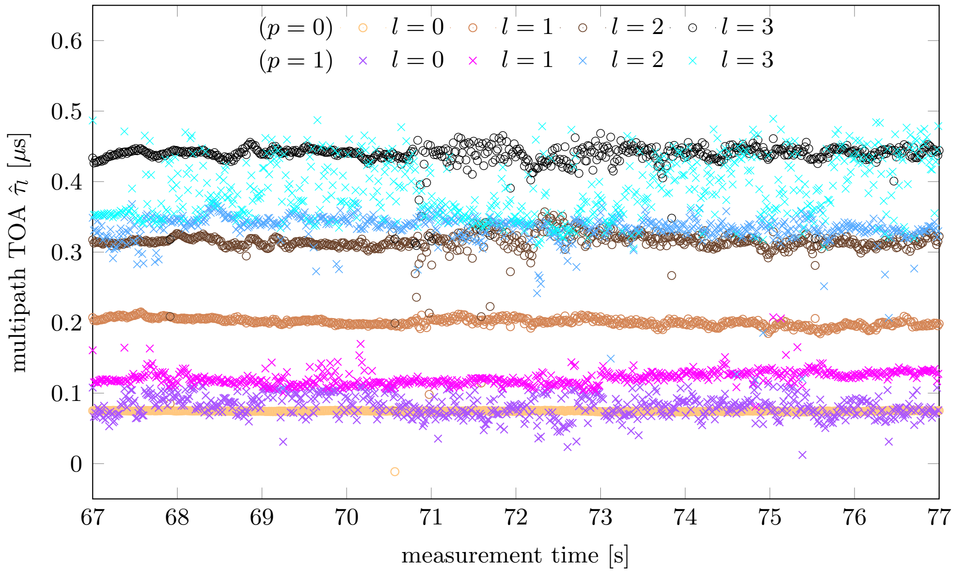

(a) Static dataset.

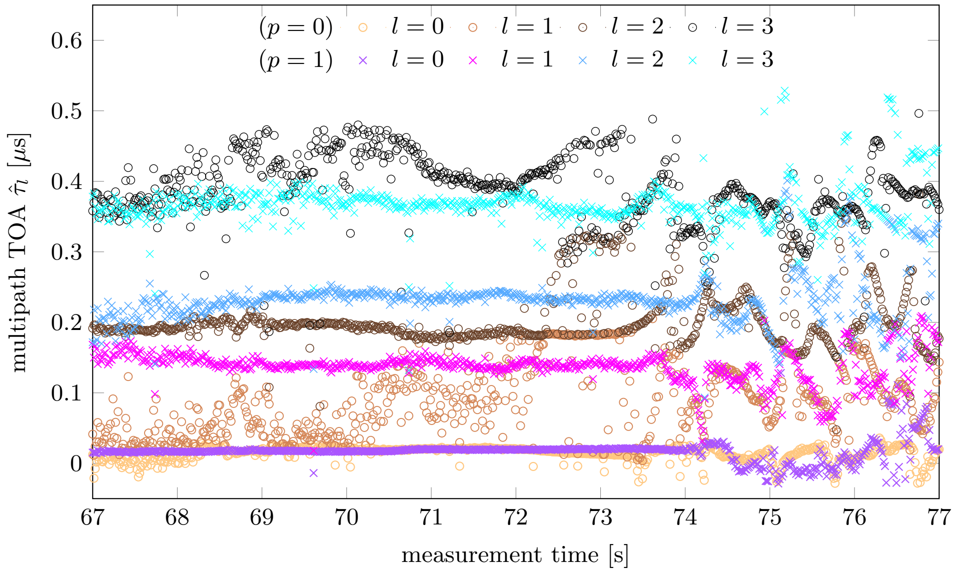

(b) Moving dataset.

Figure 6.25 – Results of ESPRIT multipath TOA estimation using the CRSs of $N_{\text{ID}}^{\text{cell}} = 84$ from the preliminary measurement dataset in a representative time interval. Both the received antenna ports are shown in the same plot.

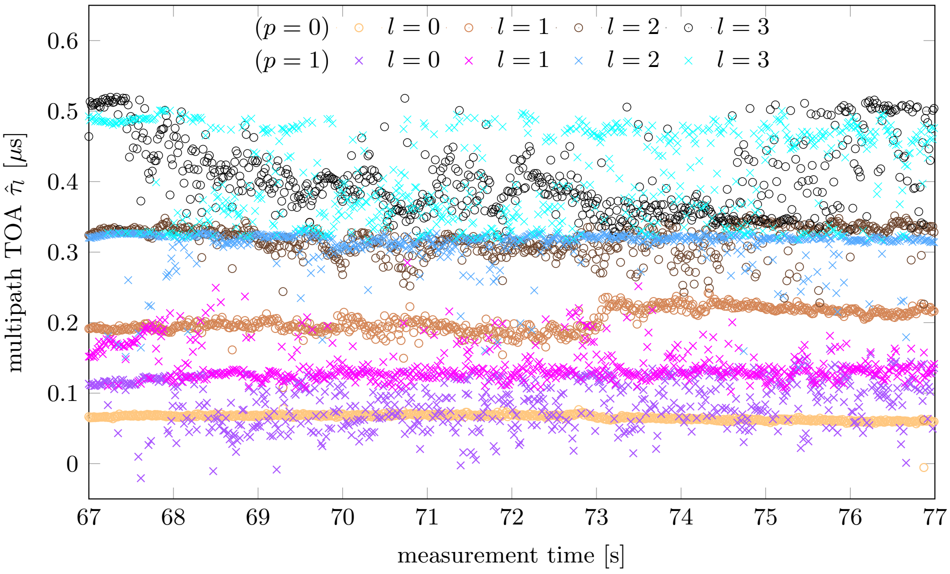

(a) Static dataset.

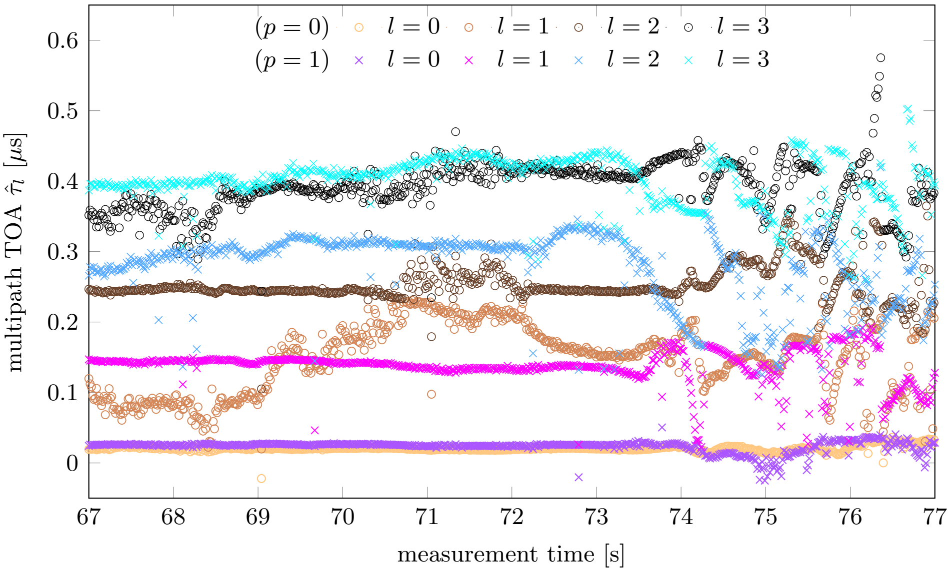

(b) Moving dataset.

Figure 6.26 – Results of ESPRIT multipath TOA estimation using the CRSs of $N_{\mathrm{ID}}^{\mathrm{cell}} = 86$ from the preliminary measurement dataset in a representative time interval. Both the received antenna ports are shown in the same plot.

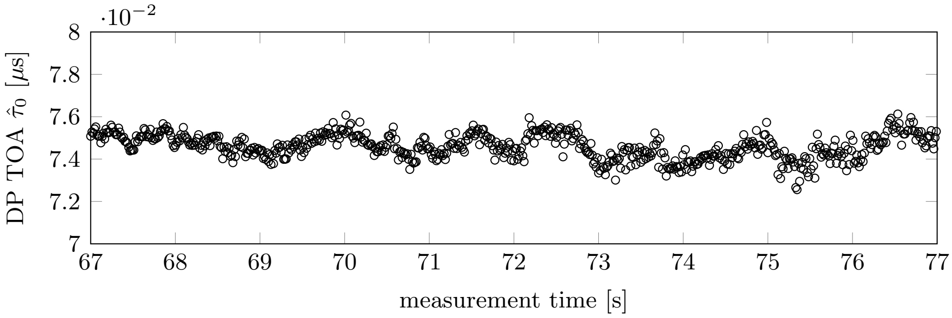

Figure 6.27 – First estimated path (likely the direct path) from antenna port $p = 0$ of cell $N_{\text{ID}}^{\text{cell}} = 84$, "Start" position, static measurements.

to a TOA estimation every $N_s = 10$ slots, which correspond to 200 estimations per second.

The estimation procedure was applied to both the static and the moving preliminary datasets, and both $p = 0$ and $p = 1$ antenna ports were considered. Moreover, the CRSs coming from both $N_{\text{ID}}^{\text{cell}} = 84$ and $N_{\text{ID}}^{\text{cell}} = 86$ were taken into account for the estimation.

Figure 6.25 shows the results obtained using the CRS of cell ID $N_{\text{ID}}^{\text{cell}} = 84$, for both the static and moving scenarios. As one can see, especially for $p = 0$ in Figure 6.25a and for $p = 1$ in Figure 6.25b, the estimation of the DP as well as the multipath components is quite clear and continuous along subsequent measurements. The static case of Figure 6.25a correctly exhibits almost constant multipath behaviour, and fluctuations probably imputable to noise. The multipath TOA estimated in the moving case, represented in Figure 6.25b, exhibits time variant multipath from time 73.5 s, which roughly corresponds to the time where the received started moving from the "Stopover" position. Equivalently, Figure 6.26 shows the results obtained using the CRS of cell ID $N_{\text{ID}}^{\text{cell}} = 86$, for both the static and moving scenarios, for which considerations similar to the ones done for $N_{\text{ID}}^{\text{cell}} = 84$ hold.

Comparing the cases of the two different cell IDs $N_{\text{ID}}^{\text{cell}} = 84$ and $N_{\text{ID}}^{\text{cell}} = 86$, it is evident that the estimations for $N_{\text{ID}}^{\text{cell}} = 84$ are more stable in the static case, while the estimations for $N_{\text{ID}}^{\text{cell}} = 86$ are more stable in the case of the moving scenario. This means that likely in the "Start" position (where all whole static measurement was conducted, refer to Figure 6.1d), the signal coming from the cell having $N_{\text{ID}}^{\text{cell}} = 84$ is stronger than the $N_{\text{ID}}^{\text{cell}} = 86$ signal. Conversely, the results suggest that in the "Stopover" position (where the receiving station is in the considered measurement time interval $[67\,\text{s}, 77\,\text{s}]$) the signal coming from the cell having $N_{\text{ID}}^{\text{cell}} = 86$ is stronger than the $N_{\text{ID}}^{\text{cell}} = 84$ signal. Moreover, using analogous considerations, one can note that the signal coming from antenna port $p = 0$ is stronger in the static case (hence in the "Start" position) while the signal coming from antenna port $p = 1$ is stronger in the moving case (hence in the "Stopover" position), both in the case of $N_{\text{ID}}^{\text{cell}} = 84$ and $N_{\text{ID}}^{\text{cell}} = 86$.

The results of this preliminary set of measurements demonstrated the feasibility

Op.	BS	n_{tot}	n_{E}	$P^{\mathrm{r}}_{\mathrm{E}}$	$P^{\mathrm{o}}_{\mathrm{E}}$	n_{IL}	$P^{\mathrm{r}}_{\mathrm{IL}}$	$P^{\mathrm{o}}_{\mathrm{IL}}$
1	1	905	887	0.98	0.02	640	0.71	0.29
	2	1604	1569	0.98	0.02	898	0.56	0.44
	3	1067	947	0.89	0.11	720	0.67	0.33
	5	909	876	0.96	0.04	531	0.58	0.42
	6	359	347	0.97	0.03	236	0.66	0.34
2	1	2730	2730	1.00	0.00	1918	0.70	0.30
	2	534	458	0.86	0.14	282	0.53	0.47
	3	2292	2270	0.99	0.01	1320	0.58	0.42

(a) Outdoor vehicular measurement scenario.

Op.	BS	n_{tot}	n_{E}	$P^{\mathrm{r}}_{\mathrm{E}}$	$P^{\mathrm{o}}_{\mathrm{E}}$	n_{IL}	$P^{\mathrm{r}}_{\mathrm{IL}}$	$P^{\mathrm{o}}_{\mathrm{IL}}$
1	1	902	900	0.99	0.01	657	0.72	0.28
	2	516	627	1.00	0.00	261	0.50	0.50
2	1	902	900	0.99	0.01	586	0.64	0.36
	3	554	713	1.00	0.00	356	0.64	0.36
3	1	867	888	1.00	0.00	504	0.58	0.42

(b) Indoor measurement scenario.

Table 6.4 – Coverage statistics for the different employed estimators.

of LTE timing measurements with SRAs for ranging purposes, with the DP TOA being estimated within the remarkably small interval of 3 ns in the best case, as shown in Figure 6.27.

6.9.4 Ranging results

After the preliminary assessment of the capabilities of the ESPRIT algorithm on real LTE signals described in the previous section, the EKAT algorithm was developed, which is capable of detecting and tracking the DP TOA, to be used for the actual pseudorange estimations. EKAT was applied to the outdoor vehicular and indoor datasets described in Section 6.3, which are more complete and comprehensive datasets, more suited for the testing of positioning applications. To assess its effectiveness, EKAT was also compared to the simpler pseudorange estimators of Section 6.5.

Firstly, the employed pseudorange estimators, namely IM, IL and EKAT, were compared in terms of coverage. Indeed, differently from the IM estimator, EKAT and IL do not produce an estimate for each input measurement. EKAT requires measurements displaced by less than $D_{\mathrm{max}} \cdot T$ in order to produce pseudoranges, and it may happen that a measurement does not correspond to an estimate. Similarly, IL discards a measurement if one of the N_{IL} CIR highest peaks appears before the CIR maximum. Tables 6.4 show, for each BS and each operator in each measure-

Op.	BS	$\varepsilon_{0.5}^{\mathrm{IM}}$ [m]	$\varepsilon_{0.95}^{\mathrm{IM}}$ [m]	$\varepsilon_{0.5}^{\mathrm{IL}}$ [m]	$\varepsilon_{0.95}^{\mathrm{IL}}$ [m]	$\varepsilon_{0.5}^{\mathrm{E}}$ [m]	$\varepsilon_{0.95}^{\mathrm{E}}$ [m]
1	1	11.49	56.47	8.65	53.34	10.16	50.68
	2	13.67	127.20	9.20	63.97	8.26	23.24
	3	18.51	175.26	11.62	107.99	8.94	47.96
	5	16.07	107.38	12.73	41.06	11.86	37.64
	6	3.37	65.26	3.03	19.53	3.40	12.20
2	1	20.52	102.74	17.82	61.71	14.21	35.90
	2	17.07	208.17	12.16	59.68	11.19	51.59
	3	23.12	140.02	15.92	51.09	17.36	43.53

(a) Outdoor vehicular measurement scenario.

Op.	BS	$\varepsilon_{0.5}^{\mathrm{IM}}$ [m]	$\varepsilon_{0.95}^{\mathrm{IM}}$ [m]	$\varepsilon_{0.5}^{\mathrm{IL}}$ [m]	$\varepsilon_{0.95}^{\mathrm{IL}}$ [m]	$\varepsilon_{0.5}^{\mathrm{E}}$ [m]	$\varepsilon_{0.95}^{\mathrm{E}}$ [m]
1	1	6.20	50.45	3.43	28.83	3.19	9.21
	2	23.21	89.81	22.99	89.64	7.98	17.42
2	1	21.19	97.97	19.52	76.76	5.02	14.62
	3	17.51	49.98	14.67	27.57	8.64	46.01
3	1	25.91	79.17	12.79	90.87	8.83	22.16

(b) Indoor measurement scenario.

Table 6.5 – Ranging error statistics for the different employed estimators.

ment scenario, the total number of available measurements n_{tot}, and the number of produced estimates n_x, $x \in \{\mathrm{E}, \mathrm{IL}\}$. The corresponding probabilities of having a range estimate $P_x^{\mathrm{r}} = \min\{n_x/n_{\mathrm{tot}}, 1\}$ and of a ranging outage $P_x^{\mathrm{o}} = 1 - P_x^{\mathrm{r}}$ are also shown. This particular definition of P^{r} is necessary because it may happen that EKAT is run with no input measurements (state $\mathbf{q}_4$ of the state machine in Figure 6.14), and hence it is possible that EKAT produces more estimates than the number of input measurements. Note that the number of estimates produced by IM is always equal to n_{tot}, hence $P_{\mathrm{IM}}^{\mathrm{r}} = 1$ and $P_{\mathrm{IM}}^{\mathrm{o}} = 0$. As one can see from the results of Table 6.4, the discarding policy of IL results in a considerably lower number of estimates than the total number of measurements available. Conversely, EKAT delivers output results with a low outage probability, i.e., it almost always produces an output result. Moreover, as one can note from Table 6.4b, in the indoor measurement scenario EKAT produced a number of estimates often higher than the number of input measurements. This is due to the high value for $D_{\max}$ used for the indoor measurements. A high value for $D_{\max}$ can be used because of the low speeds involved in the indoor measurements, which ensure a slowly changing propagation environment.

Secondly, the range estimates $\hat{d}_j(t)$ were compared to the recorded ground truth $d_j(t)$ in order to produce error statistics, and ultimately to evaluate the performance of each used pseudorange estimator. As already shown in the previous sections, the

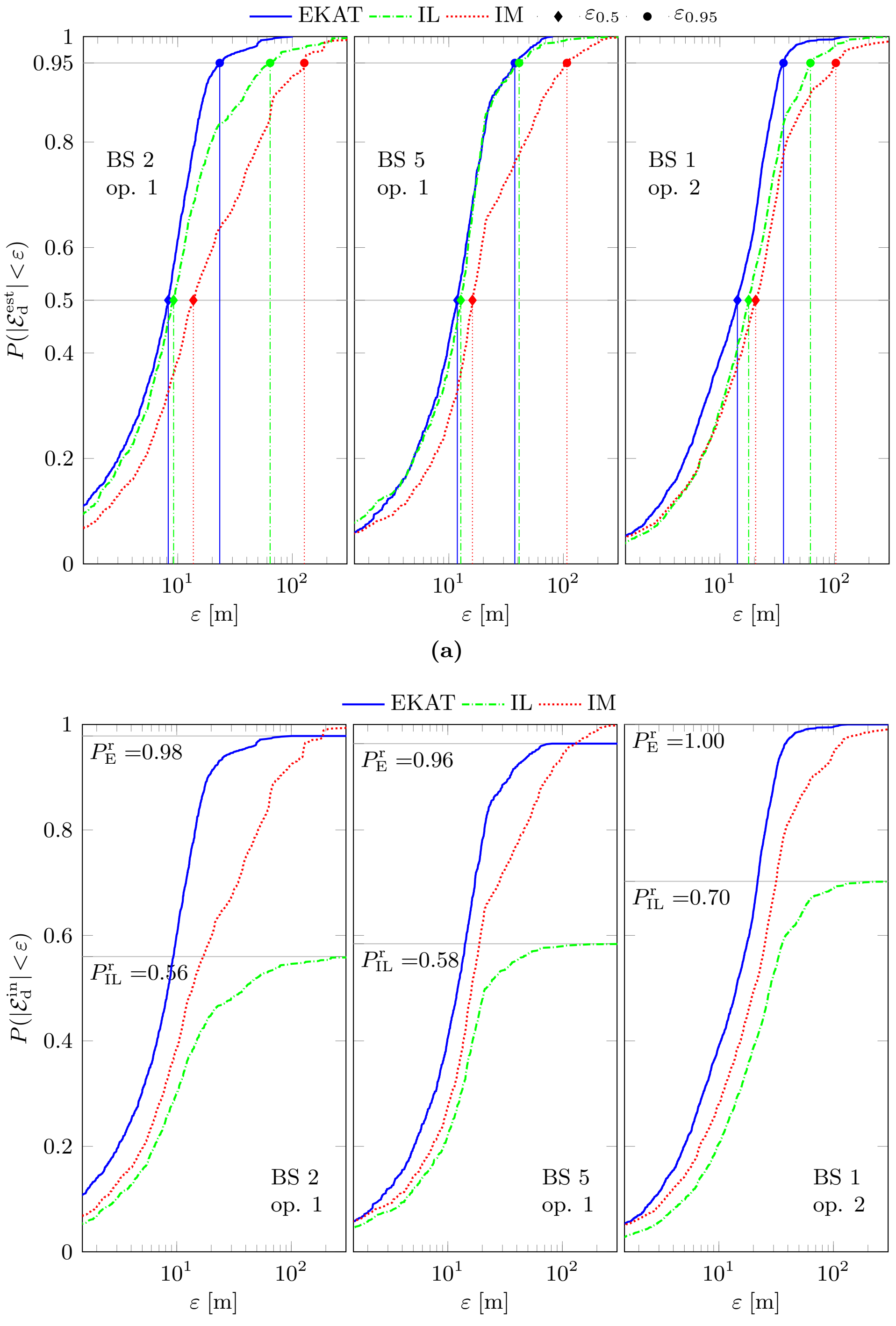

(a)

(b)

Figure 6.28 – CDFs of the ranging error $\mathcal{E}_{\mathrm{d}}^{\mathrm{est}}$ (a) and $\mathcal{E}_{\mathrm{d}}^{\mathrm{in}}$ (b) for selected base stations of the outdoor vehicular measurement scenario. In (a), the values ε_p for $p = \{0.5, 0.95\}$ are also highlighted. In (b), the values of P_x^{r}, $x \in \{\mathrm{E}, \mathrm{IL}\}$, are also shown.

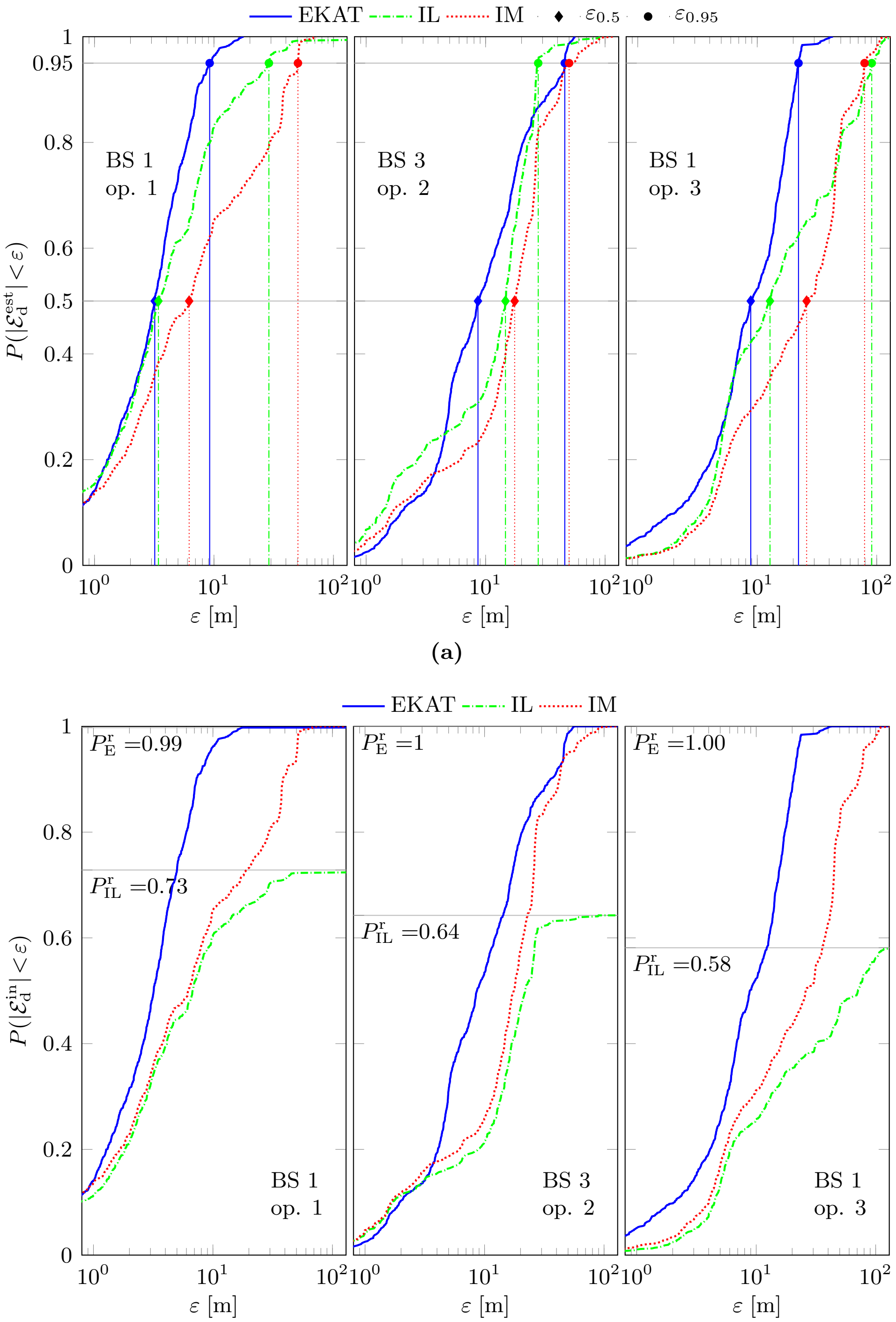

(a)

(b)

Figure 6.29 – CDFs of the ranging error $\mathcal{E}_{\rm d}^{\rm est}$ (a) and $\mathcal{E}_{\rm d}^{\rm in}$ (b) for selected base stations of the indoor measurement scenario. In (a), the values ε_p for $p = \{0.5, 0.95\}$ are also highlighted. In (b), the values of $P_x^{\rm r}$, $x \in \{\rm E, IL\}$, are also shown.

GPS-based ranges were used as ground truth for the outdoor vehicular measurement scenario, while the laser-based ranges were used as ground truth for the indoor measurement scenario. Empirical cumulative density functions (CDFs) of the ranging absolute error were evaluated as $P(|\mathcal{E}_\mathrm{d}| < \varepsilon)$ for each BS and each estimator, where $\mathcal{E}_\mathrm{d} = \hat{d} - d$. Since there may be measurement instants for which all three estimators produce a pseudorange, and other instants in which just a sub-set of the estimators outputs a pseudorange, two different criteria were adopted in order to evaluate the CDF of $\mathcal{E}_\mathrm{d}$.

The CDFs for the first type of error, denoted with $\mathcal{E}_\mathrm{d}^\mathrm{est}$, are calculated considering separately all the estimates produced by the three algorithms. The corresponding error probability abscissas, defined as the value ε_p such that $P(|\mathcal{E}_\mathrm{d}^\mathrm{est}| < \varepsilon_p) = p$, for $p = \{0.5, 0.95\}$, were also evaluated. The results are shown for selected BSs of the outdoor vehicular dataset in Figure 6.28a, and for selected BSs of the indoor dataset in Figure 6.29a. The best error performance is always obtained by the EKAT estimator, which exhibits an $\varepsilon_{0.5}$ and an $\varepsilon_{0.95}$ that are always smaller than the corresponding values of the other estimators. This is particularly true in the case of the indoor dataset of Figure 6.29a, mostly because EKAT is designed to cope with obstructed LOS scenarios, which characterize indoor propagation. Moreover, it is evident that the IL estimator obtains a better estimation of the range than the IM estimator, sometimes even comparable with that of EKAT (e.g., for BS 5 operator 1 outdoor dataset, shown in Figure 6.28a). A complete comparison is shown in Table 6.5, where the values of ε_p obtained for all the BSs are reported for the two examined datasets. The results show that in the outdoor case of Table 6.5a, the $p = 0.5$ performance of EKAT and IL are comparable, while at $p = 0.95$ IL presents a higher error, probably because it cannot completely handle multipath effects. Finally, as expected, the IM estimator shows the worst results, since by definition it cannot face multipath effects. Conversely, in the indoor case of Table 6.5b, EKAT always obtains the best results, with the exception of the $p = 0.95$ case of BS 3 operator 2, where the performance is worse than the IL one.

The CDFs for the second type of error, denoted with $\mathcal{E}_\mathrm{d}^\mathrm{in}$, are calculated similarly to the ones of $\mathcal{E}_\mathrm{d}^\mathrm{est}$, with the exception that they are plotted as a percentage of the common number of input data. More particularly, $P(|\mathcal{E}_\mathrm{d}^\mathrm{in}| < \varepsilon) = P(|\mathcal{E}_\mathrm{d}^\mathrm{est}| < \varepsilon)/\min\{n_\mathrm{tot}, n\}$, where n is the number of estimates produced by the considered algorithm. The corresponding results are shown in Figure 6.28b for the outdoor dataset and the same cases considered in Figure 6.28a, and in Figure 6.29b for the indoor dataset and the same cases considered in Figure 6.29a. For each estimator, this type of error definition combines the error performance and the ranging outage probability P^o, namely, the probability of not having a range estimation when a measurement from a BS is available. As one can see, EKAT obtains the better trade off between small error performance and an unlikely outage, while IL suffers from a high outage probability. This probably happens because IL tends to produce an estimate only in LOS conditions, which do not occur too frequently in the considered scenarios. As an example, consider the case of BS 5 operator 1 outdoor dataset, represented in the middle plots of Figure 6.28. According to $\mathcal{E}_\mathrm{d}^\mathrm{est}$ (Figure 6.28a), IL and EKAT exhibit almost the same performance. Considering $\mathcal{E}_{\mathrm{d}}^{\mathrm{in}}$ (Figure 6.28b), it is evident that the statistics of IL pertain just to 58% of the possible range estimations, while EKAT produces estimates of the same quality in 96% of cases. Similar considerations hold for BS 3 operator 2 of the indoor dataset. Here, IL obtains an error $\varepsilon_{0.95}^{\mathrm{IL}} = 27.57\,\mathrm{m}$ in just the 64% of the possible range estimations, while EKAT produces always an estimate, at a cost of an increased error $\varepsilon_{0.95}^{\mathrm{E}} = 46.01\,\mathrm{m}$. Nevertheless, EKAT has still a better $p = 0.5$ error of $\varepsilon_{0.5}^{\mathrm{E}} = 8.64\,\mathrm{m}$ compared to $\varepsilon_{0.5}^{\mathrm{IL}} = 14.67\,\mathrm{m}$.

6.9.5 Positioning results

The ranges evaluated from both the outdoor vehicular dataset and the indoor dataset were used in the positioning algorithm described in Section 6.8. The results obtained are depicted in Figure 6.30 for the outdoor vehicular dataset, and in Figure 6.31 for the indoor dataset. In both cases, each plot corresponds to a different ranging technique. Each marker in each plot is a position estimate, where the different marker types represent the number of BSs $N(t)$ used for evaluating that particular position fix. By using the ground truth data gathered during the live measurements (GPS position fixes in the outdoor vehicular scenario, and laser positions in the indoor scenario) as the true positions $\boldsymbol{p}$, a positioning error was defined as $\mathcal{E}_{\mathrm{p}} = \|\hat{\boldsymbol{p}} - \boldsymbol{p}\|$. Error CDFs were evaluated as $P(\mathcal{E}_{\mathrm{p}} < \varepsilon)$, which are shown in Figure 6.33 and Figure 6.34 for the outdoor vehicular scenario and the indoor scenario, respectively. The same two error definitions of the ranging results section are adopted, namely the error $\mathcal{E}_{\mathrm{p}}^{\mathrm{est}}$, that considers all the estimates produced by the positioning algorithm, and the error $\mathcal{E}_{\mathrm{p}}^{\mathrm{in}}$, that represents the results as a percentage of the common number of inputs. In other words, $P(\mathcal{E}_{\mathrm{p}}^{\mathrm{in}} < \varepsilon)$ is obtained by scaling $P(\mathcal{E}_{\mathrm{p}}^{\mathrm{est}} < \varepsilon)$ for the ratio between the number of produced position fixes and the total number of instants for which at least one range is available. Using the error definition of $\mathcal{E}_{\mathrm{p}}^{\mathrm{est}}$, error probability abscissas were also evaluated as $P(\mathcal{E}_{\mathrm{p}}^{\mathrm{est}} < \varepsilon_p) = p$, $p = \{0.5, 0.95\}$, and a root mean square (RMS) positioning error was evaluated as $(\mathbb{E}[(\mathcal{E}_{\mathrm{p}}^{\mathrm{est}})^2])^{1/2}$. As usually done in positioning contexts, $\varepsilon_{0.5}$ and $\varepsilon_{0.95}$ are referred to as circular error probability (CEP) and 95% radius (R95), respectively. Similarly to Section 6.9.5, the error definition $\mathcal{E}_{\mathrm{p}}^{\mathrm{in}}$ permits to highlight a position fix probability P^{p} and a positioning outage probability $P^{\mathrm{o}} = 1 - P^{\mathrm{p}}$.

Figure 6.30a represents the positioning result obtained with the IM range estimator applied to the data collected in the outdoor vehicular scenario. As explained in Section 6.5, the IM estimator produces the typical timing outputs of a communications module. Hence, the corresponding bad positioning results demonstrate the need for appropriate processing at the receiver in order to correctly extract the TOA of a signal for positioning purposes. However, some good fixes are obtained in the southern part of the route, which corresponds to open field regions, where the propagation occurs mainly with LOS between the BSs and the receiver.

The need of appropriate signal processing for positioning is further evident in the results of Figure 6.31a, where the position fixes obtained with the IM ranges extracted from the indoor data are presented. In indoor environments, the propa-

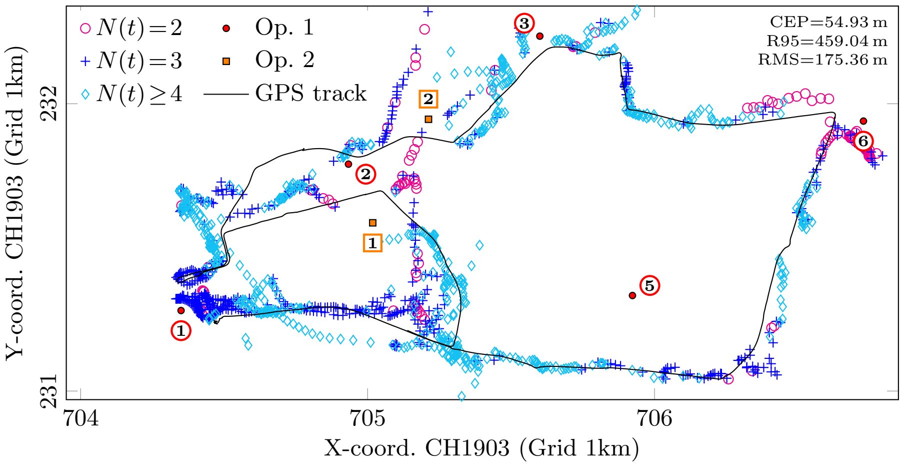

(a) IM algorithm's ranges.

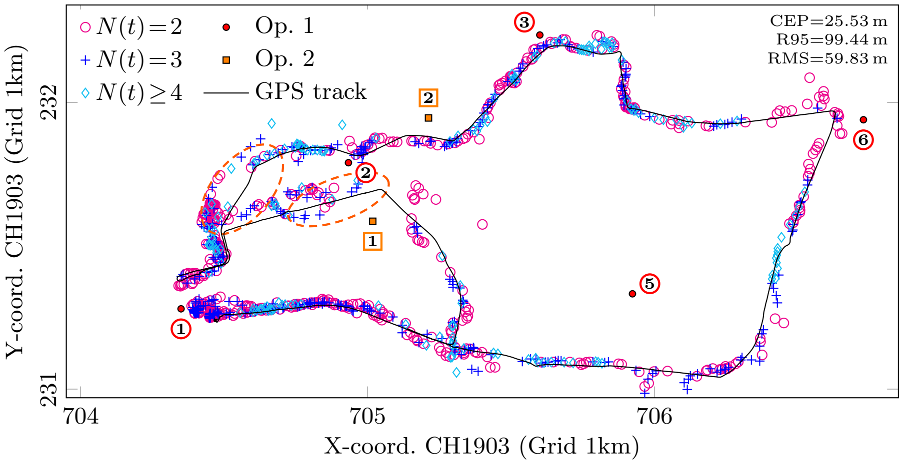

(b) IL algorithm's ranges.

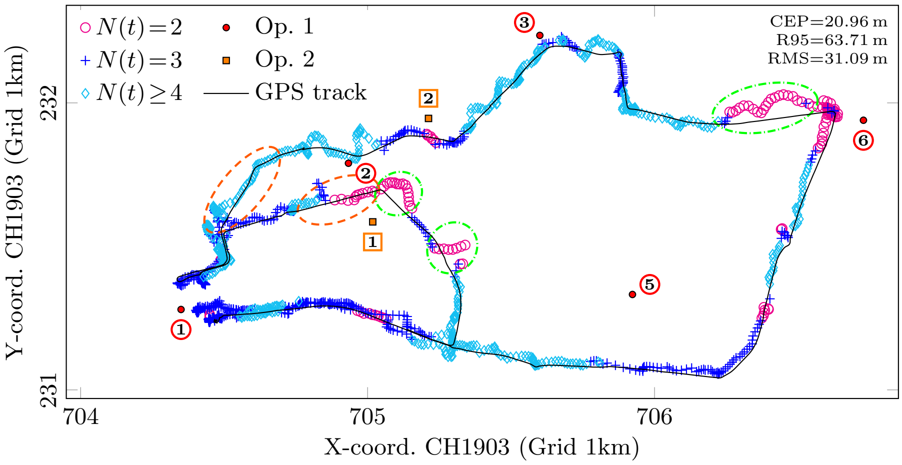

(c) EKAT algorithm's ranges.

Figure 6.30 – Positioning solution for the considered ranging techniques applied to the outdoor dataset. One marker corresponds to a position estimate, obtained with a number $N(t)$ of detected BSs. The ground truth is represented by the black solid line.

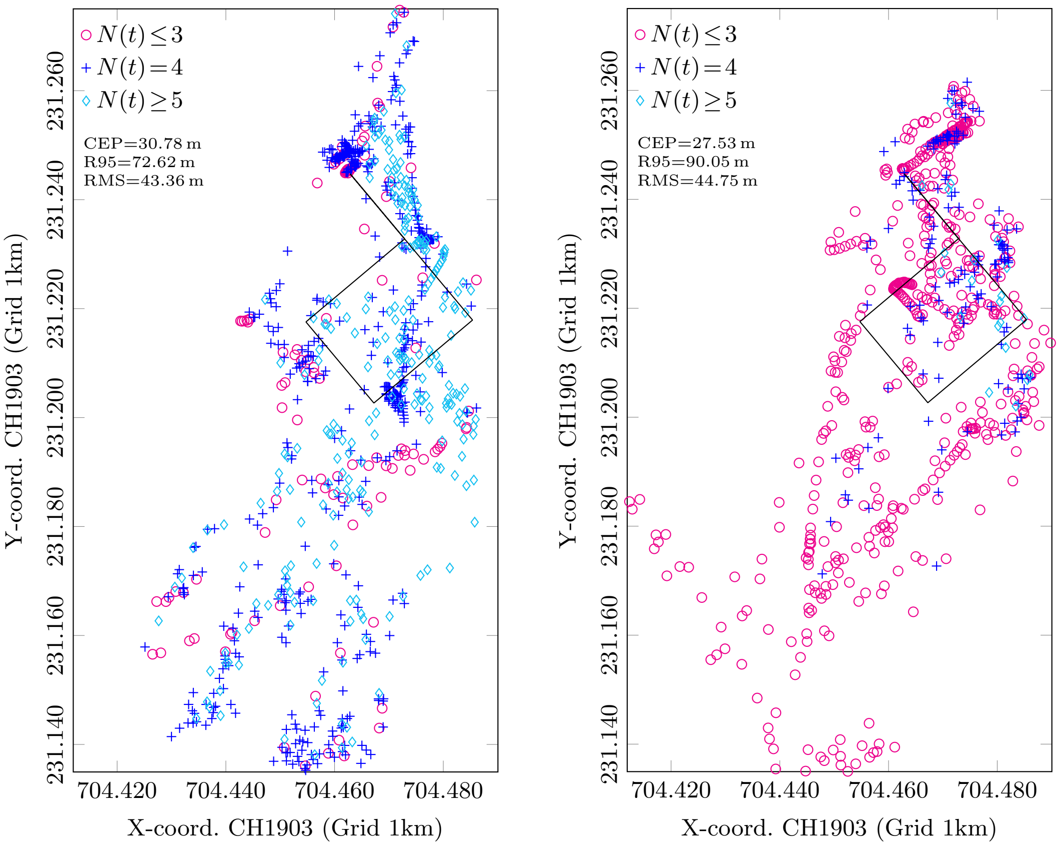

(a) IM algorithm's ranges.

(b) IL algorithm's ranges.

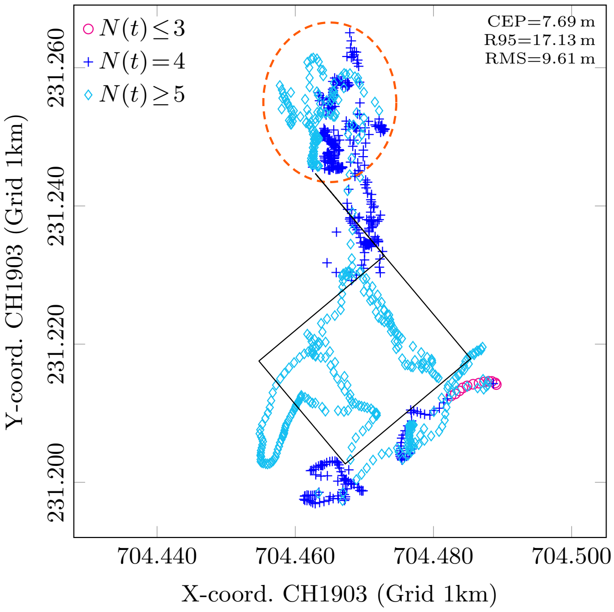

(c) EKAT algorithm's ranges.

Figure 6.31 – Positioning solution for the considered ranging techniques applied to the indoor dataset. One marker corresponds to a position estimate, obtained with a number $N(t)$ of detected BSs. The ground truth is represented by the black solid line.

gation mainly occurs by multiple reflections, and the LOS path is often obstructed. This badly affects the performance of the IM estimator, indeed most of the position fixes are outside the building, in south western direction, and the achieved RMS is of 43 m, which is quite large for an indoor pedestrian scenario.

Figure 6.30b presents the positioning results obtained using the IL ranges extracted from the outdoor vehicular dataset. This results demonstrate that the very simple NLOS detection algorithm of the IL pseudorange estimator is sufficient to drastically improve the quality of the position fixes in outdoor environments, were a nice CEP of 25.53 m is achieved. However, IL has the drawback of discarding all the measurements detected as potential NLOS reception. The consequence of this fact at a positioning level, is a reduced coverage, as can be seen by the low number of position fixes produced with $N(t) \geq 4$ BSs. Moreover, the low coverage of IL is also highlighted by its position fix probability $P_{\mathrm{IL}}^{\mathrm{p}} = 0.72$, as shown in the bottom plot of Figure 6.33. As one can see from the orange dashed ellipses of Figure 6.30b, the main positioning failures for IL happen in the north-western part of the route, and in the region between BS 2 operator 1 and BS 1 operator 2. An inspection of the CIRs measured in these areas revealed that these suffered the typical behaviours of NLOS propagation and strong multipath. This explains the poor performance and low coverage of IL in that regions.

Figure 6.31b presents the positioning results obtained using the IL ranges extracted from the indoor dataset. In this case, the NLOS detection strategy of IL is not sufficient for producing reliable range estimates, probably because almost all the measured CIRs correspond to NLOS cases. This results in bad position fixes, with an RMS of 44.75 m, and a large set of the position estimates outside the building. Hence, performing range estimations with the IL algorithm may be sufficient in outdoor vehicular scenarios with open fields regions, but is not enough for a good positioning in indoor environments.

Figure 6.30c represents the positioning results obtained using the ranges estimated with the EKAT algorithm applied to the outdoor vehicular dataset, and a satellite view of the same results is shown in Figure 6.32a. The plots show a notable adherence of the estimated positions to the actual path. As one can see from the top plot of Figure 6.33, EKAT achieves the best performance among the considered ranging techniques, with a CEP of 20.96 m, an R95 of 63.71 m, and an RMS of 31.09 m. Moreover, EKAT offers the best coverage, achieving a null outage probability, and the highest number of position fixes obtained with $N(t) \geq 4$ BSs. The quality of the position fixes achieved by EKAT in the regions where IL fails is remarkable, thanks to the ability of EKAT to cope with the detrimental effects of multipath. Finally, most of the regions where the positioning fixes produced with the EKAT ranges have a low quality, are characterized by a low number of BSs visible, as the green dash-dotted ellipses of Figure 6.30c highlight.

Finally, Figure 6.31c represents the positioning results obtained using the ranges estimated with the EKAT algorithm applied to the indoor dataset, and a satellite view of the same results is shown in Figure 6.32b. As one can see from the top plot of Figure 6.34, also in this case EKAT achieves the best performance among the

(a) Outdoor vehicular dataset. The red markers are the position solutions. The blue line is the ground truth.

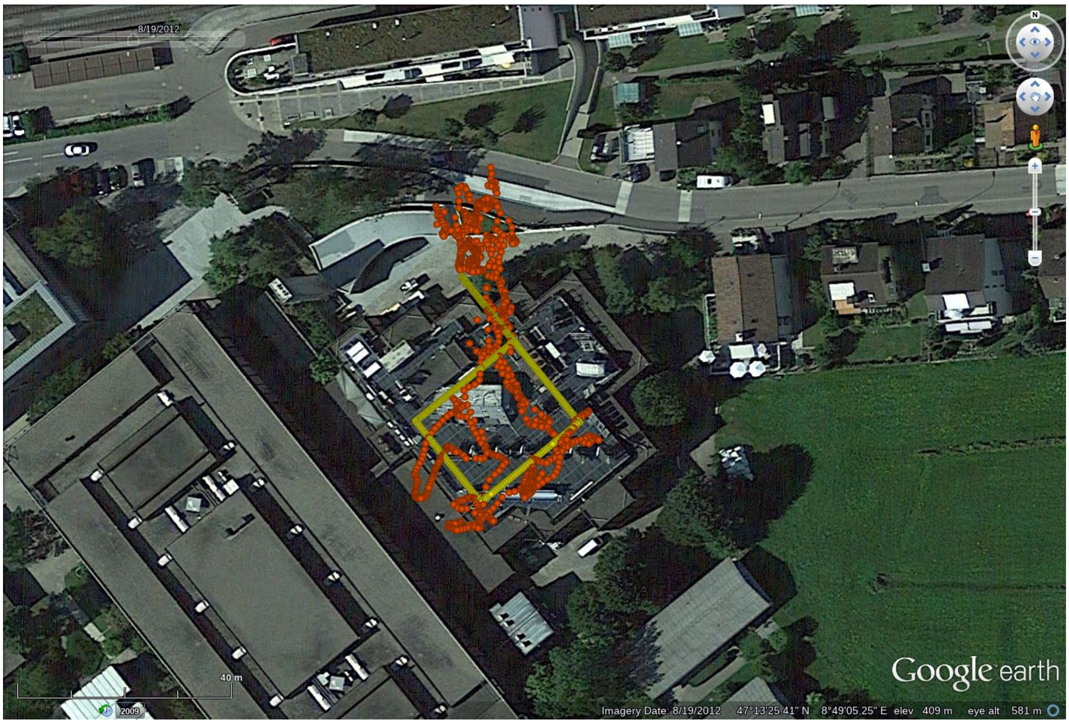

(b) Indoor dataset. The orange markers are the position solutions. The yellow markers show the ground truth.

Figure 6.32 – Satellite views of the positioning results achieved with the EKAT ranges for the considered datasets. The ground truths are shown as a reference.

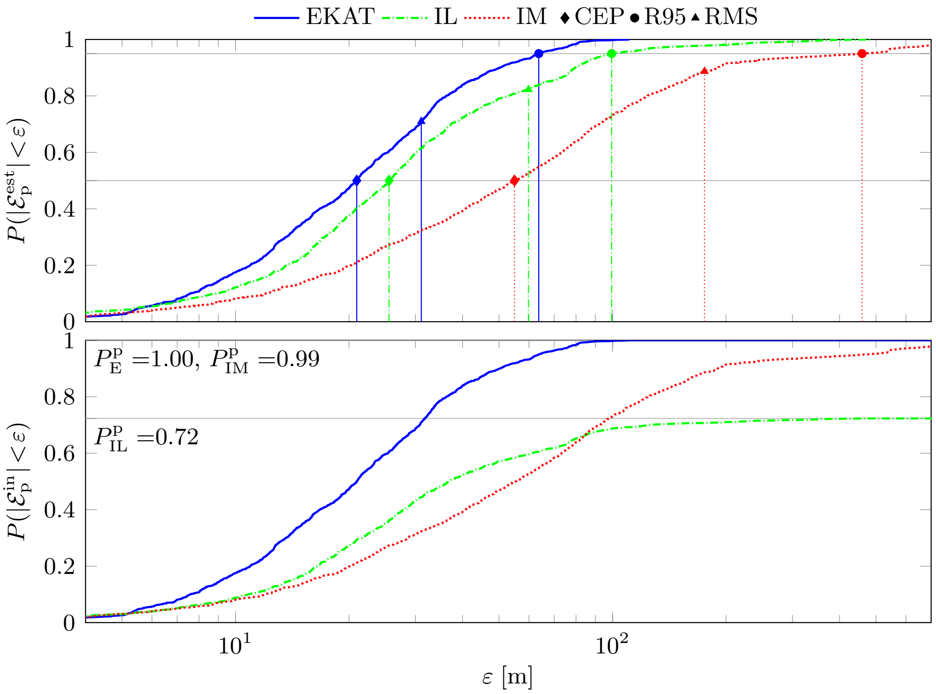

Figure 6.33 – CDFs of the positioning errors $\mathcal{E}_\mathrm{p}^\mathrm{est}$ and $\mathcal{E}_\mathrm{p}^\mathrm{in}$ for the considered ranging techniques applied to the outdoor vehicular dataset. The CEP, R95 and RMS statistics are highlighted for $\mathcal{E}_\mathrm{p}^\mathrm{est}$, and the position fix probability P^p is highlighted in the $\mathcal{E}_\mathrm{p}^\mathrm{in}$ plot.

considered ranging techniques, with a CEP of 7.69 m, an R95 of 17.13 m, and an RMS of 9.61 m. Again, EKAT also offers the best coverage, achieving an outage probability of $P_\mathrm{E}^\mathrm{o} = 0.01$, and the highest number of position fixes obtained with $N(t) \geq 5$ BSs. The quality of the position fixes achieved by EKAT in the indoor scenario is remarkable, with a maximum error of approximately 20 m, and the trajectory performed by the received which is clearly visible and always inside the HSR building (Figure 6.32b). Notably, the region where the worst positioning fixes are achieved is the first part of the indoor dataset, which is highlighted with an orange ellipse in Figure 6.31c. This part of the route is located outdoor of the HSR building, below the ground level, and surrounded by massive concrete facilities. Hence, it is likely that in this position, some of the LOS paths coming from the received BSs are completely obstructed, leading to biased range estimations and consequently to wrong position fixes. Interestingly, the positioning results achieved for the indoor dataset are even better than the positioning results achieved with the outdoor dataset. This may be due to the reduced mobility of the indoor dataset, that permitted to apply the averaging technique described in Section 6.4.2, which drastically improved the quality of the estimated ranges.

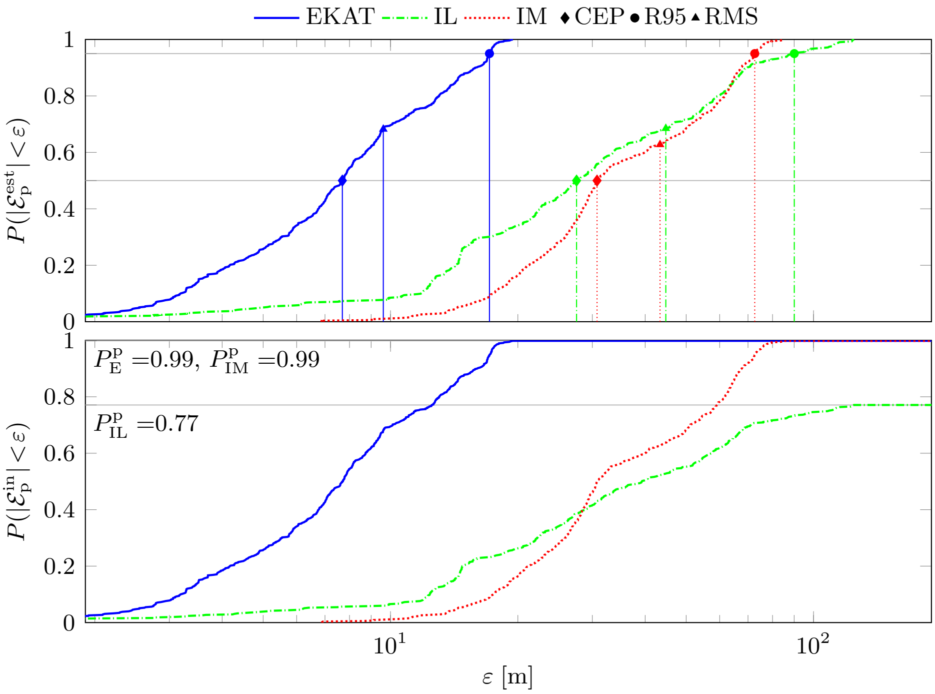

Figure 6.34 – CDFs of the positioning errors $\mathcal{E}_{\mathrm{p}}^{\mathrm{est}}$ and $\mathcal{E}_{\mathrm{p}}^{\mathrm{in}}$ for the considered ranging techniques applied to the indoor dataset. The CEP, R95 and RMS statistics are highlighted for $\mathcal{E}_{\mathrm{p}}^{\mathrm{est}}$, and the position fix probability P^{p} is highlighted in the $\mathcal{E}_{\mathrm{p}}^{\mathrm{in}}$ plot.

6.10 Conclusions

An LTE downlink signals time of arrival estimation and tracking method has been proposed and validated in the field, by using real measurements gathered in different propagation scenarios. The considered cases are an outdoor vehicular dataset, collected during a car drive in the town of Rapperswil, Switzerland, and an indoor pedestrian dataset, collected in a test route through a building of the Hochschule für Technik Rapperswil, Switzerland.

Preliminary measurements demonstrated the feasibility of extracting multipath time of arrival measurements by using super resolution algorithms applied on real LTE signals. In particular, time of arrival measurements of the LTE cell specific reference signal have been exploited. Then, the EKAT algorithm has been developed, which exploits the ESPRIT super-resolution algorithm for separating multipath, and a Kalman filter together with a novel bound-based uncertainty estimation method for tracking the direct path time of arrival. The use of experimental data collected in the field has demonstrated that EKAT is capable of effectively reducing the detrimental effects of multipath.

A combination of the received signals in the time and frequency has been exploited for improving the timing estimates. Furthermore, the estimates pertaining to the signals coming from the multiple base stations' antenna ports have been combined in the EKAT's Kalman filter, realizing also a spatial combining, in addition to the aforementioned time and frequency combining. The pseudoranges calculated with EKAT have been then combined on a cell ID basis, in order to produce a single pseudorange for every received BS. Hence, a combination of the signals on time, frequency, spatial and cell ID domains has been exploited for improving the range estimates. Finally, the pseudoranges evaluated with EKAT have been corrected for base stations' clock bias and drift, previously estimated. At a ranging level, the performance of EKAT is always superior in respect to the one of the other considered TOA estimators, achieving CEP values ranging from 3.19 m (best case, indoor dataset, BS 1, operator 1) to 17.36 m (worst case, outdoor vehicular dataset, BS 3, operator 2).

The evaluated ranges have been then used to feed a positioning filter. A CEP of 25.53 m and an RMS of 59.83 m with a coverage of the 72% have been obtained using a simple CIR based timing algorithm with NLOS detection on the outdoor vehicular dataset. This demonstrates the feasibility of LTE-based positioning systems, even with simple signal processing at the receiver, at a cost of a limited coverage. Improved CEP, RMS (20.96 m and 31.09 m, respectively), and universal coverage throughout the test have been obtained with the more powerful EKAT algorithm, demonstrating its benefits in correctly detecting the direct path in environments characterized by multipath propagation. The benefits of the EKAT algorithm were particularly evident when the algorithm was applied to the indoor dataset. In this case, a CEP of 7.69 m and an RMS of 17.13 m were achieved, and almost all the position estimates were inside the HSR building in which the measurements took place, with a clearly visible estimated receiver trajectory.

The proposed approach demonstrates that positioning with LTE signals is possible, even without transmission of the LTE positioning reference signal. Improvements are easily achievable in the positioning performance, e.g., by employing a better navigation filter, and by exploiting the wider deployment of LTE cells/micro-cells/pico-cells, and the transmission of LTE channels with a wider bandwidth. To the best of the author's knowledge, this is the first contribution proposing a real field validation of a positioning approach that uses opportunistically the LTE downlink signals.

Chapter 7

Conclusions and future work

This thesis presented a research work on the estimation of the time of arrival (TOA) of modern cellular systems downlink signals for positioning purposes. The Third Generation Partnership Project (3GPP) Long Term Evolution (LTE) signals have been considered, and the underlying orthogonal frequency division multiplexing (OFDM) based physical layer has been exploited. The original contribution presented in the thesis is twofold.

The first addressed topic concerns the TOA estimation of OFDM waveforms from a reference signal design perspective. A framework has been developed for assessing the performance of OFDM signals used for TOA estimation. The simple case of the additive white Gaussian noise (AWGN) channel has been considered, in order to obtain performance assessments to be used as best case indications in more complex propagation environments. The considered OFDM signals have been modeled avoiding the use of the popular rectangularly shaped pulse, which determines a non physically realizable signal, and considering the OFDM signal at the output of the transmitting digital-to-analog converter (DAC). Then, different power distributions on the available OFDM sub-carriers have been carefully defined, and used to explore the TOA estimation performance both in the asymptotic and in the threshold root mean square error (RMSE) regions. Moreover, a novel performance metric based on the shape of the Ziv-Zakai bound (ZZB) curve has been defined, and exploited to precisely evaluate the boundaries between the threshold and the asymptotic RMSE regions. By using this metric, which targets the threshold RMSE, and the popular Gabor bandwidth (GB), which targets the asymptotic RMSE, the TOA estimation performance of the considered OFDM signals has been studied. As a final topic of this thesis part, the developed framework has been applied to the most common LTE reference signals, for establishing the most suited waveforms to be used as reference signal for time based range measurements.

The analysis revealed a trade-off between the threshold and the asymptotic RMSE, with the signal achieving the best asymptotic RMSE exhibiting also the worst signal-to-noise ratio (SNR) threshold. This suggested that the Gabor bandwidth is not the only parameter to consider for designing TOA reference signals, and that the SNR threshold should also be taken into account. The analysis also showed that, to obtain a satisfactory threshold performance with an equispaced active sub-carrier power distribution, a high density of active sub-carriers is required. Similarly, a certain number of active sub-carriers has to be employed if they have to be placed contiguously on the edges of the available bandwidth. Finally, the analysis of the LTE reference signals revealed that from the point of view of fundamental TOA measurement accuracy the normal cell specific reference signal (CRS) is as good as the dedicated positioning reference signal (PRS).

Future works on the topic of the OFDM signals performance assessment may include the extension of the proposed framework to more severe channels, like the multipath fading channels, by using the ZZBs of [18, 68]. Moreover, optimization tools such as the genetic algorithms may be employed for finding power distributions on the OFDM sub-carriers that maximize some objective function that jointly consider the threshold and the asymptotic RMSE performance.

The second addressed topic concerns the development of a TOA estimation algorithm and its application to real LTE OFDM signals collected in the town of Rapperswil, Switzerland, in harsh propagation environments. This part of the research work has been undertaken in close collaboration with the Hochschule für Technik Rapperswil (HSR), Switzerland, and with the support of u-blox UK Ltd. The used datasets were collected from the team of the Institute for Communication Systems (ICOM) of the HSR, by using a software defined radio (SDR) based portable setup, which also collected ground truth data. The measurements took place in an outdoor vehicular and in an indoor scenario, both characterized by strong multipath propagation. The developed algorithm is referred to as ESPRIT and Kalman filter for time of Arrival Tracking (EKAT), and combines a super-resolution algorithm (SRA), which performs the multipath separation, with a Kalman filter (KF), which tracks the estimated direct path (DP) TOA. SRAs were chosen for the TOA estimation task since they naturally exploit the OFDM based physical layer of the LTE downlink signals. More particularly, the estimation of signal parameters via rotational invariance techniques (ESPRIT) algorithm has been used, in conjunction with the LTE CRS, which was exploited as the reference signal. Techniques for combining the received LTE pilot tones in the time, frequency, spatial and cell ID domains have been adopted, which were used to exploit the intrinsic diversity offered by the CRS, and to improve the robustness and the quality of the TOA estimates. The employed KF has been designed in order to cope with the discontinuities typical of the real datasets, and also features an heuristic selection of the DP among the measured multipath TOA values, and a novel bound-based estimation of the measurements reliability. By exploiting the developed EKAT algorithm, several DP TOA values have been tracked from the dataset measured at the HSR. The corresponding pseudoranges have been converted to actual ranges by correcting the transmitter clock bias and drift, which were estimated in a previous phase for each received base station (BS). Moreover, for analyzing the EKAT performance from a positioning point of view, the evaluated ranges have been used to feed a positioning filter (implemented by the HSR team).

To the best of the author's knowledge, this is the first real field validation of a positioning approach that uses opportunistically the LTE downlink signals. By comparing the estimated ranges with the ground truth data, the performance of EKAT has been assessed, achieving error values (50%) ranging from 3.19 m (best case, indoor dataset) to 17.36 m (worst case, outdoor vehicular dataset, BS 3, operator 2). Concerning the positioning results, the ranges calculated with EKAT outperformed the considered benchmark algorithms. In the outdoor vehicular scenario, EKAT achieved a circular error probability (CEP) and a root mean square (RMS) error of 20.96 m and 31.09 m, respectively. In the indoor case, a remarkably small CEP of 7.69 m and RMS of 17.13 m were achieved, and almost all the position estimates were inside the HSR building in which the measurements took place, with a clearly visible estimated receiver trajectory. The results obtained demonstrated that useful positioning can be achieved with LTE signals in harsh propagation environments, even indoors.

Multiple further developments are possible concerning the topic of real LTE signals TOA estimation in harsh propagation environments. Firstly, a tracking of all the multipath components estimated by the ESPRIT algorithm may be realized, similarly to the approach of [78]. The tracked multipath components may be exploited, together with the tracked DP TOA, for improving the positioning, thanks to the concept of virtual sources, as explained in [79]. Finally, the TOA estimation part of the EKAT algorithm may be replaced with simpler threshold based TOA estimation algorithms, in order to reduce the computational burden caused by the ESPRIT matrix manipulations.

List of publications

Journal papers

- M. Driusso, F. Babich, F. Knutti, M. Sabathy, H. Mathis and C. Marshall, “Vehicular position tracking using LTE signals,” under second review, *IEEE Transactions on Vehicular Technology*, Feb. 2016.

- M. Driusso, M. Comisso, F. Babich, and C. Marshall, “Performance Analysis of Time of Arrival Estimation on OFDM Signals,” *IEEE Signal Processing Letters*, vol. 22, no. 7, pp. 983–987, Jul. 2015.

- F. Babich, A. Crismani, M. Driusso, and L. Hanzo, “Design Criteria and Genetic Algorithm Aided Optimization of Three-Stage-Concatenated Space-Time Shift Keying Systems,” *IEEE Signal Processing Letters*, vol. 19, no. 8, pp. 543–546, Aug. 2012.

- F. Babich, M. Comisso, A. Dorni, F. Barisi, M. Driusso, and A. Manià, “Discrete-time simulation of smart antenna systems in Network Simulator-2 Using MATLAB and Octave,” *SIMULATION: Transactions of The Society for Modeling and Simulation International*, vol. 87, pp. 932–946, Dec. 2010.

Patents

- C. Marshall and M. Driusso, “Calculating a ranging measurement in a cellular communications network,” EPO application 15195460.9, filed on 19 November 2015, assigned to u-blox AG.

Conference proceedings

- M. Driusso, F. Babich, F. Knutti, M. Sabathy, and C. Marshall, “Estimation and tracking of LTE signals time of arrival in a mobile multipath environment,” in *9th International Symposium on Image and Signal Processing and Analysis*, pp. 276–281, September 2015.

- F. Knutti, M. Sabathy, M. Driusso, H. Mathis, and C. Marshall, "Positioning Using LTE Signals," in *European Navigation Conference (ENC 2015)*, Apr. 2015.

- M. Driusso, F. Babich, M. Kadir, and L. Hanzo, "OFDM Aided Space-Time Shift Keying for Dispersive Downlink Channels," in *IEEE Vehicular Technology Conference (VTC Fall 2012)*, Sep. 2012, pp. 1–5.

- F. Babich, M. Comisso, A. Dorni, and M. Driusso, "Open source simulation of smart antenna systems in network simulator-2 using Octave," in *5th IEEE International Symposium on Wireless Pervasive Computing (ISWPC 2010)*, May 2010, pp. 51–56.

Conference presentations

- M. Driusso, F. Barisi, F. Babich, and C. Marshall, "Super Resolution Algorithm Based Estimation of LTE PRS Time of Arrivals in Multipath Channels," in *RIN International Navigation Conference (INC 2015).* Manchester (UK). Feb. 2015.

- M. Driusso, F. Barisi, F. Babich, and C. Marshall, "Super Resolution Algorithm based Estimation of LTE PRS Time of Arrivals in Multipath Channels," *12th Italian Networking Workshop.* Cavalese (Italy). Jan. 2015.

- M. Driusso and F. Babich, "Performance analysis of LTE downlink signals time of arrival estimation for opportunistic positioning," *11th Italian Networking Workshop.* Cortina d'Ampezzo (Italy). Jan. 2014.

Bibliography

[1] J. Figueiras and S. Frattasi, *Mobile Positioning and Tracking. From Conventional to Cooperative Techniques.* Wiley, 2010.

[2] D. Dardari, E. Falletti, and M. Luise, *Satellite and Terrestrial Radio Positioning Techniques.* Elsevier, 2012.

[3] E. D. Kaplan and C. J. Hegarty, *Understanding GPS, Principles and Applications.* Artech House, 2006.

[4] R. Zekavat and R. Buehrer, *Handbook of Position Location: Theory, Practice and Advances.* Wiley-IEEE Press, 2012.

[5] N. Patwari, J. Ash, S. Kyperountas, A. Hero, R. Moses, and N. Correal, "Locating the nodes: cooperative localization in wireless sensor networks," *IEEE Signal Processing Magazine*, vol. 22, pp. 54–69, July 2005.

[6] H. Wymeersch, J. Lien, and M. Win, "Cooperative Localization in Wireless Networks," *Proceedings of the IEEE*, vol. 97, pp. 427–450, Feb 2009.

[7] M. Harris, "The way through the flames," *IEEE Spectrum*, vol. 50, pp. 30–35, September 2013.

[8] D. Schneider, "You are here," *IEEE Spectrum*, vol. 50, pp. 34–39, December 2013.

[9] N. O. Tippenhauer, C. Pöpper, K. B. Rasmussen, and S. Capkun, "On the Requirements for Successful GPS Spoofing Attacks," in *Proceedings of the 18th ACM Conference on Computer and Communications Security*, CCS '11, (New York, NY, USA), pp. 75–86, ACM, 2011.

[10] M. Psiaki, B. O'Hanlon, J. Bhatti, D. Shepard, and T. Humphreys, "GPS Spoofing Detection via Dual-Receiver Correlation of Military Signals," *IEEE Transactions on Aerospace and Electronic Systems*, vol. 49, pp. 2250–2267, October 2013.

[11] Z. F. Syed, P. Aggarwal, X. Niu, and N. El-Sheimy, "Civilian Vehicle Navigation: Required Alignment of the Inertial Sensors for Acceptable Navigation

Accuracies," *IEEE Transactions on Vehicular Technology*, vol. 57, pp. 3402–3412, Nov 2008.

[12] C. Yang and H. rong Shao, "WiFi-based indoor positioning," *IEEE Communications Magazine*, vol. 53, pp. 150–157, March 2015.

[13] F. Gustafsson and F. Gunnarsson, "Mobile positioning using wireless networks: possibilities and fundamental limitations based on available wireless network measurements," *IEEE Signal Processing Magazine*, vol. 22, pp. 41–53, July 2005.

[14] Open Signal, "The State of LTE (September 2015)." URL: `http://opensignal.com/reports/2015/09/state-of-lte-q3-2015/`. Accessed on: 2016-01-07.

[15] X. Li and K. Pahlavan, "Super-resolution TOA estimation with diversity for indoor geolocation," *IEEE Transactions on Wireless Communications*, vol. 3, pp. 224–234, Jan 2004.

[16] N. Alsindi, X. Li, and K. Pahlavan, "Analysis of Time of Arrival Estimation Using Wideband Measurements of Indoor Radio Propagations," *IEEE Transactions on Instrumentation and Measurements*, vol. 56, pp. 1537–1545, Oct 2007.

[17] A. Emmanuele, M. Luise, F. Zanier, and M. Crisci, "Selective accuracy and multiresolution capabilities are intrinsic features of multicarrier waveforms for GNSS," in *ESA Workshop on Satellite Navigation Technology & European Workshop on GNSS Signals and Signal Processing*, pp. 1–8, Dec 2012.

[18] Z. Xu and B. M. Sadler, "Time delay estimation bounds in convolutive random channels," *IEEE Journal of Selected Topics in Signal Processing*, vol. 1, pp. 418–430, Oct 2007.

[19] A. Goldsmith, *Wireless Communications.* Cambridge University Press, 2005.

[20] G. L. Stüber, *Principles of Mobile Communication.* Kluwer Academic, second ed., 2001.

[21] S. Mazuelas, A. Bahillo, R. Lorenzo, P. Fernandez, F. Lago, E. Garcia, J. Blas, and E. Abril, "Robust Indoor Positioning Provided by Real-Time RSSI Values in Unmodified WLAN Networks," *IEEE Journal of Selected Topics in Signal Processing*, vol. 3, pp. 821–831, Oct 2009.

[22] Y. Xu, J. Zhou, and P. Zhang, "RSS-Based Source Localization When Path-Loss Model Parameters are Unknown," *IEEE Communications Letters*, vol. 18, pp. 1055–1058, June 2014.

[23] S. Fischer, “Observed Time Difference Of Arrival (OTDOA) Positioning in 3GPP LTE.” URL: `http://www.qualcomm.com/media/documents/files/otdoa-positioning-in-3gpp-lte.pdf`, Jun. 2014. Accessed on: 2015-12-16.

[24] K. Ranta-aho and Z. Shen, “User Equipment Positioning,” in *LTE - The UMTS Long Term Evolution* (S. Sesia, I. Toufik, and M. Baker, eds.), pp. 423–436, John Wiley & Sons, Ltd, 2009.

[25] 3GPP TS 36.355, *Evolved Universal Terrestrial Radio Access (E-UTRA); LTE Positioning Protocol (LPP) (Release 11).* 3rd Generation Partnership Project, V11.0.0, October 2012.

[26] 3GPP TS 36.211, *Evolved Universal Terrestrial Radio Access (E-UTRA); Physical channels and modulation (Release 11).* 3rd Generation Partnership Project, V11.0.0, October 2012.

[27] S. Gezici, Z. Tian, G. Giannakis, H. Kobayashi, A. Molisch, H. Poor, and Z. Sahinoglu, “Localization via ultra-wideband radios: a look at positioning aspects for future sensor networks,” *IEEE Signal Processing Magazine*, vol. 22, pp. 70–84, July 2005.

[28] Y. Bar-Shalom, X. R. Li, and T. Kirubarajan, *Estimation with Applications to Tracking and Navigation: Theory Algorithms and Software.* John Wiley & Sons, Apr. 2001.

[29] F. Gustafsson, F. Gunnarsson, N. Bergman, U. Forssell, J. Jansson, R. Karlsson, and P.-J. Nordlund, “Particle filters for positioning, navigation, and tracking,” *IEEE Transactions on Signal Processing*, vol. 50, pp. 425–437, Feb 2002.

[30] M. Arulampalam, S. Maskell, N. Gordon, and T. Clapp, “A tutorial on particle filters for online nonlinear/non-Gaussian Bayesian tracking,” *IEEE Transactions on Signal Processing*, vol. 50, pp. 174–188, Feb 2002.

[31] Y. G. Li and G. L. Stuber, *Orthogonal Frequency Division Multiplexing for Wireless Communications.* Springer, 2006.

[32] L. Hanzo and T. Keller, *OFDM and MC-CDMA: A Primer.* Wiley-IEEE Press, 2006.

[33] Y. Liu, Z. Tan, H. Hu, L. Cimini, and G. Li, “Channel Estimation for OFDM,” *IEEE Communications Surveys and Tutorials*, vol. 16, pp. 1891–1908, Fourth quarter 2014.

[34] I. Toufik and R. Knopp, “Multi-User Scheduling and Interference Coordination,” in *LTE - The UMTS Long Term Evolution* (S. Sesia, I. Toufik, and M. Baker, eds.), pp. 285–300, John Wiley & Sons, Ltd, 2009.

[35] F. Tomatis and S. Sesia, "Synchronization and cell search," in *LTE The UMTS Long Term Evolution* (S. Sesia, I. Toufik, and M. Baker, eds.), pp. 151–164, John Wiley & Sons, Ltd, 2009.

[36] D. G. Manolakis, V. K. Ingle, and S. M. Kogon, *Statistical and Adaptive Signal Processing: Spectral Estimation, Signal Modeling, Adaptive Filtering, and Array Processing.* Artech House, 2005.

[37] B. Yang, K. Letaief, R. Cheng, and Z. Cao, "Channel estimation for OFDM transmission in multipath fading channels based on parametric channel modeling," *IEEE Transactions on Communications*, vol. 49, pp. 467–479, Mar 2001.

[38] V. Prabhu and D. Jalihal, "An Improved ESPRIT Based Time-of-Arrival Estimation Algorithm for Vehicular OFDM Systems," in *IEEE 69th Vehicular Technology Conference (VTC Spring)*, pp. 1–4, April 2009.

[39] X. Li and H. Jiang, "Lunar rover positioning based on TOA estimation for UWB signal using unitary-ESPRIT," in *9th International Conference on Electronic Measurement Instruments (ICEMI)*, pp. 2–646–2–650, Aug 2009.

[40] N. Alsindi, X. Li, and K. Pahlavan, "Performance of TOA estimation algorithms in different indoor multipath conditions," in *IEEE Wireless Communications and Networking Conference (WCNC)*, vol. 1, pp. 495–500 Vol.1, March 2004.

[41] M.-A. Pallas and G. Jourdain, "Active high resolution time delay estimation for large BT signals," *IEEE Transactions on Signal Processing*, vol. 39, pp. 781–788, April 1991.

[42] J. Xiong, K. Sundaresan, and K. Jamieson, "ToneTrack: Leveraging Frequency-Agile Radios for Time-Based Indoor Wireless Localization," in *Proceedings of the 21st Annual International Conference on Mobile Computing and Networking*, MobiCom '15, (New York, NY, USA), pp. 537–549, ACM, 2015.

[43] H. L. V. Trees, *Detection, Estimation, and Modulation Theory part IV: Optimum Array Processing.* John Wiley and Sons, 2004.

[44] M. Haardt and J. Nossek, "Unitary ESPRIT: how to obtain increased estimation accuracy with a reduced computational burden," *IEEE Transactions on Signal Processing*, vol. 43, pp. 1232–1242, May 1995.

[45] M. Wax and T. Kailath, "Detection of signals by information theoretic criteria," *IEEE Transactions on Acoustics, Speech and Signal Processing*, vol. 33, pp. 387–392, Apr 1985.

[46] A. D'Andrea, U. Mengali, and R. Reggiannini, "The modified Cramer-Rao bound and its application to synchronization problems," *IEEE Transactions on Communications*, vol. 42, no. 234, pp. 1391–1399, 1994.

[47] H. L. V. Trees, *Detection, Estimation, and Modulation Theory part I: Detection, Estimation and Linear Modulation Theory.* John Wiley and Sons, 2004.

[48] S. M. Kay, *Fundamentals of statistical signal processing, volume I: Estimation theory.* Prentice Hall, 1993.

[49] D. Chazan, M. Zakai, and J. Ziv, "Improved Lower Bounds on Signal Parameter Estimation," *IEEE Transactions on Information Theory*, vol. 21, no. 1, pp. 90–93, 1975.

[50] J. Ziv and M. Zakai, "Some lower bounds on signal parameter estimation," *IEEE Transactions on Information Theory*, vol. 15, no. 3, pp. 386–391, 1969.

[51] S. Bellini and G. Tartara, "Bounds on Error in Signal Parameter Estimation," *IEEE Transactions on Communications*, vol. 22, no. 3, pp. 340–342, 1974.

[52] A. Emmanuele, M. Luise, F. Zanier, and M. Crisci, "Modified Ziv-Zakai bound for Time-Of-Arrival estimation of GNSS Signal-In-Space," in *IEEE International Conference on Acoustics, Speech and Signal Processing (ICASSP)*, pp. 3041–3044, 2012.

[53] M. Driusso, "Bounds for time of arrival estimation in the AWGN channel," internal technical report, Università degli Studi di Trieste, December 2013.

[54] A. Weiss and E. Weinstein, "Fundamental limitations in passive time delay estimation–Part I: Narrow-band systems," *IEEE Transactions on Acoustics, Speech and Signal Processing*, vol. 31, pp. 472–486, Apr 1983.

[55] E. Weinstein and A. Weiss, "Fundamental limitations in passive time-delay estimation–Part II: Wide-band systems," *IEEE Transactions on Acoustics, Speech and Signal Processing*, vol. 32, pp. 1064–1078, Oct 1984.

[56] R. K. Martin, C. Yan, H. H. Fan, and C. Rondeau, "Algorithms and bounds for distributed TDOA-based positioning using OFDM signals," *IEEE Transactions on Signal Processing*, vol. 59, pp. 1255–1268, March 2011.

[57] Z. He, Y. Ma, and R. Tafazolli, "Improved high resolution TOA estimation for OFDM-WLAN based indoor ranging," *IEEE Wireless Communications Letters*, vol. 2, pp. 163–166, April 2013.

[58] L. Dai, Z. Wang, J. Wang, and Z. Yang, "Positioning with OFDM signals for the next-generation GNSS," *IEEE Transactions on Consumer Electronics*, vol. 56, pp. 374–379, May 2010.

[59] O. Bar-Shalom and A. J. Weiss, "Efficient direct position determination of orthogonal frequency division multiplexing signals," *IET Radar, Sonar & Navigation*, vol. 3, pp. 101–111, April 2009.

[60] J. A. del Peral-Rosado, J. A. López-Salcedo, G. Seco-Granados, F. Zanier, and M. Crisci, “Joint maximum likelihood time-delay estimation for LTE positioning in multipath channels,” *EURASIP Journal on Advances in Signal Processing*, vol. 2014, no. 1, p. 33, 2014.

[61] J. A. del Peral-Rosado, J. A. López-Salcedo, G. Seco-Granados, F. Zanier, and M. Crisci, “Preliminary analysis of the positioning capabilities of the positioning reference signal of 3GPP LTE,” in *European Workshop on GNSS Signals and Signal Processing*, December 2011.

[62] J. A. del Peral-Rosado, J. A. López-Salcedo, G. Seco-Granados, F. Zanier, and M. Crisci, “Achievable localization accuracy of the positioning reference signal of 3GPP LTE,” in *International Conference on Localization and GNSS*, pp. 1–6, June 2012.

[63] J. del Peral-Rosado, J. Lopez-Salcedo, G. Seco-Granados, F. Zanier, and M. Crisci, “Evaluation of the LTE positioning capabilities under typical multipath channels,” in *6th Advanced Satellite Multimedia Systems Conference (ASMS) and 12th Signal Processing for Space Communications Workshop (SPSC)*, pp. 139–146, Sept 2012.

[64] M. D. Larsen, G. Seco-Granados, and A. L. Swindlehurst, “Pilot optimization for time-delay and channel estimation in OFDM systems,” in *IEEE International Conference on Acoustics, Speech and Signal Processing*, pp. 3564–3567, May 2011.

[65] R. Montalban, J. A. López-Salcedo, G. Seco-Granados, and A. L. Swindlehurst, “Power allocation method based on the channel statistics for combined positioning and communications OFDM systems,” in *IEEE International Conference on Acoustics, Speech and Signal Processing*, pp. 4384–4388, May 2013.

[66] A. Shahmansoori, R. Montalban, J. A. López-Salcedo, and G. Seco-Granados, “Design of OFDM sequences for joint communications and positioning based on the asymptotic expected CRB,” in *International Conference on Localization and GNSS*, June 2014.

[67] S. K. Mitra, *Digital Signal Processing: A Computer-Based Approach.* McGraw-Hill Education, 2011.

[68] B. M. Sadler, N. Liu, and Z. Xu, “Ziv-Zakai bounds on time delay estimation in unknown convolutive random channels,” *IEEE Transactions on Signal Processing*, vol. 58, pp. 2729–2745, May 2010.

[69] J. A. del Peral-Rosado, J. M. Parro-Jimenez, J. A. López-Salcedo, G. Seco-Granados, P. Crosta, F. Zanier, and M. Crisci, “Comparative results analysis on positioning with real LTE signals and low-cost hardware platforms,” in *7th ESA Workshop on Satellite Navigation Technology and European Workshop on GNSS Signals and Signal Processing*, pp. 1–8, Dec 2014.

[70] C. Gentner, E. Munoz, M. Khider, E. Staudinger, S. Sand, and A. Dammann, "Particle filter based positioning with 3GPP-LTE in indoor environments," in *IEEE/ION Position Location and Navigation Symposium*, pp. 301–308, Apr. 2012.

[71] C. Gentner, S. Sand, and A. Dammann, "OFDM indoor positioning based on TDOAs: Performance analysis and experimental results," in *International Conference on Localization and GNSS*, pp. 1–7, June 2012.

[72] A. Dammann, S. Sand, and R. Raulefs, "On the Benefit of Observing Signals of Opportunity in Mobile Radio Positioning," in *Proceedings of 9th International ITG Conference on Systems, Communications and Coding*, pp. 1–6, Jan 2013.

[73] S. Bartoletti, A. Conti, and M. Win, "Passive radar via LTE signals of opportunity," in *IEEE International Conference on Communications Workshops*, pp. 181–185, June 2014.

[74] M. Huang and W. Xu, "Enhanced LTE TOA/OTDOA estimation with first arriving path detection," in *IEEE Wireless Communications and Networking Conference*, pp. 3992–3997, April 2013.

[75] J. A. del Peral-Rosado, J. A. López-Salcedo, G. Seco-Granados, P. Crosta, F. Zanier, and M. Crisci, "Downlink synchronization of LTE base stations for opportunistic ToA positioning," in *International Conference on Localization and GNSS*, pp. 1–6, June 2015.

[76] N. Ramagnano, F. Knutti, and M. Sabathy, "Information about Positioning from opportunistic LTE Signals Timing (IPoST LTE)," internal technical report, Hochschule für Technik Rapperswil (HSR), May 2014.

[77] J. Salmi, A. Richter, and V. Koivunen, "Detection and Tracking of MIMO Propagation Path Parameters Using State-Space Approach," *IEEE Transactions on Signal Processing*, vol. 57, pp. 1538–1550, Apr. 2009.

[78] T. Jost, W. Wang, U. Fiebig, and F. Perez-Fontan, "Detection and Tracking of Mobile Propagation Channel Paths," *IEEE Transactions on Antennas and Propagation*, vol. 60, pp. 4875–4883, Oct. 2012.

[79] C. Gentner and T. Jost, "Indoor positioning using time difference of arrival between multipath components," in *International Conference on Indoor Positioning and Indoor Navigation*, pp. 1–10, Oct. 2013.

[80] F. Li, R. Vaccaro, and D. Tufts, "Performance analysis of the state-space realization (TAM) and ESPRIT algorithms for DOA estimation," *IEEE Transactions on Antennas and Propagation*, vol. 39, pp. 418–423, Mar. 1991.

[81] M. Sabathy and F. Knutti, "Aquila PLT - Experimental system," internal technical report, Hochschule für Technik Rapperswil (HSR), August 2015.

[82] M. Sabathy and F. Knutti, "Aquila PLT - Forward positioning," internal technical report, Hochschule für Technik Rapperswil (HSR), August 2015.

[83] M. Sabathy and F. Knutti, "Aquila PLT - The LTE-Signal/Cell-Search Procedure," internal technical report, Hochschule für Technik Rapperswil (HSR), August 2015.

[84] Swiss Federal Office of Communications (OFCOM), "OFCOM - Location of radio transmitters." URL: `http://www.bakom.admin.ch/themen/frequenzen/00652/00699/index.html?lang=en`. Accessed on: 2015-11-03.

[85] A. Ancora, S. Sesia, and A. Gorokhov, "Reference Signals and Channel Estimation," in *LTE - The UMTS Long Term Evolution* (S. Sesia, I. Toufik, and M. Baker, eds.), pp. 165–187, John Wiley & Sons, Ltd, 2009.

[86] W. C. Jakes, *Microwave Mobile Communications.* Wiley-IEEE Press, 1994.

[87] F.-X. Socheleau, A. Aissa-El-Bey, and S. Houcke, "Non data-aided snr estimation of ofdm signals," *IEEE Communications Letters*, vol. 12, pp. 813–815, November 2008.

[88] V. Savaux, Y. Louet, M. Djoko-Kouam, M. Djoko-Kouam, and A. Skrzypczak, "An iterative and joint estimation of snr and frequency selective channel for ofdm systems," in *18th European Wireless Conference*, pp. 1–7, April 2012.

[89] S. Lu, "Wide-band Noise, Signal and SNR Estimation," internal technical report, u-blox UK LTD, January 2015.

[90] A. Giorgetti and M. Chiani, "Time-of-arrival estimation based on information theoretic criteria," *IEEE Transactions on Signal Processing*, vol. 61, pp. 1869–1879, April 2013.

[91] F. Benedetto, G. Giunta, and E. Guzzon, "Enhanced TOA-based indoor-positioning algorithm for mobile LTE cellular systems," in *8th Workshop on Positioning Navigation and Communications*, pp. 137–142, April 2011.

[92] E. Staudinger and A. Dammann, "Round-trip delay indoor ranging experiments with OFDM signals," in *IEEE International Conference on Communications Workshops*, pp. 150–156, June 2014.

[93] A.-Z. Xu, E. Au, A.-S. Wong, and Q. Wang, "A Novel Threshold-Based Coherent TOA Estimation for IR-UWB Systems," *IEEE Transactions on Vehicular Technology*, vol. 58, pp. 4675–4681, Oct 2009.

[94] D. Dardari, C.-C. Chong, and M. Win, "Threshold-Based Time-of-Arrival Estimators in UWB Dense Multipath Channels," *IEEE Transactions on Communications*, vol. 56, pp. 1366–1378, August 2008.

[95] Ericsson, "R1-152112: UE Receiver Model for Performance Evaluation," in *3GPP TSG RAN WG1 Meeting 80bis*, April 2015.

[96] A. Liavas and P. Regalia, "On the behavior of information theoretic criteria for model order selection," *IEEE Transactions on Signal Processing*, vol. 49, pp. 1689–1695, Aug 2001.

[97] A. Liavas, P. Regalia, and J.-P. Delmas, "Blind channel approximation: effective channel order determination," *IEEE Transactions on Signal Processing*, vol. 47, pp. 3336–3344, Dec 1999.

[98] J. Via, I. Santamaria, and J. Perez, "Effective channel order estimation based on combined identification/equalization," *IEEE Transactions on Signal Processing*, vol. 54, pp. 3518–3526, Sept 2006.

[99] X. Xu, Y. Jing, and X. Yu, "Subspace-based noise variance and SNR estimation for OFDM systems," in *IEEE Wireless Communications Networking Conference*, vol. 1, pp. 23–26, Mar. 2005.

[100] B. Denis, J.-B. Pierrot, and C. Abou-Rjeily, "Joint distributed synchronization and positioning in UWB ad hoc networks using TOA," *IEEE Transactions on Microwave Theory and Techniques*, vol. 54, pp. 1896–1911, June 2006.

[101] M. Sabathy and F. Knutti, "Aquila PLT - Base Station Situation," internal technical report, Hochschule für Technik Rapperswil (HSR), August 2015.

[102] F. Barisi, "Time of arrival estimation of LTE downlink signals," Master's thesis, Università degli Studi di Trieste, December 2014.